

**ELECTRON BEAM (EB) - ASSISTED  
MATERIALS FABRICATION**

by

**VIVEK RAMESH DAVÉ**

S.B., Engineering and Applied Science  
California Institute of Technology, 1989

S.M., Materials Engineering  
Massachusetts Institute of Technology, 1991

Submitted to the Department of Materials Science and Engineering  
in Partial Fulfillment of the Requirements for the Degree of

**DOCTOR OF PHILOSOPHY**  
in Materials Engineering  
at the  
Massachusetts Institute of Technology

June 1995

© 1995 Vivek Ramesh Davé  
All Rights Reserved

The author hereby grants to MIT permission to reproduce and to distribute  
publicly paper or electronic copies of this thesis document in whole or in part.

Signature Of Author.....  
Department of Materials Engineering  
May 5, 1995

Certified by.....  
Dr. Thomas W. Eagar, Thesis Supervisor  
POSCO Professor of Materials Engineering,  
Department Head, Department of Materials  
Science and Engineering

Accepted by .....  
Dr. Carl V. Thompson II  
Professor of Electronic Materials  
Chair, Departmental Committee on  
Graduate Students

MASSACHUSETTS INSTITUTE  
OF TECHNOLOGY

**JUL 20 1995**

LIBRARIES

v. 1

**ARCHIVES**

# **ELECTRON BEAM (EB) - ASSISTED MATERIALS FABRICATION**

by

**VIVEK RAMESH DAVÉ**

Submitted to the Department of Materials Science and Engineering  
on May 5, 1995 in partial fulfillment of the requirements for  
the Degree of Doctor of Philosophy  
in Materials Engineering

## **ABSTRACT**

The principal contributions of this work to the field of electron beam materials processing are fourfold.

- 1) Electron beam - based materials fabrication was demonstrated using a wire feed technique. The experiments demonstrated the successful deposition of 308 stainless steel onto a 304L stainless base. Crack-free deposits in excess of 1.25 cm thickness were deposited. Layered structures consisting of Al-Bronze deposits on a Monel 400 base were also made. These experiments demonstrate the feasibility of EB-based SFF (Solid Freeform Fabrication).
- 2) A new pressureless technique for the EB-assisted reaction synthesis of aluminide intermetallics was developed. This technique allows control over the position of the reaction front and results in full density and full extent of reaction for such systems as FeAl and Fe<sub>3</sub>Al. The technique was successfully applied to the deposition of fully dense and adherent coatings on steel.
- 3) Several materials processing applications were implemented using high energy electron beams (HEEBs). These include shock surface strengthening, ceramic strengthening, and C/C joining. The potential benefits of HEEB shock processing in SFF (Solid Freeform Fabrication) are discussed. This present work represents one of the most extensive surveys of the applicability of HEEBs to materials processing in existence.
- 4) A thermal model was developed to describe the temperature profiles due to moving distributed volumetric sources. This model takes into account the volumetric penetration effects of electron beams and extends existing models for distributed surface sources. The model is applied to several processing applications and is compared to actual e-beam operating parameters.

Thesis Supervisor : Dr. Thomas W. Eagar

Title: Department Head, Department of Materials Science and  
Engineering and POSCO Professor of Materials Engineering

## Acknowledgments

I would like to thank first and foremost my thesis supervisor, Prof. T. W. Eagar. The *raison d' être* for this project was conceived by him in early 1992, and the subsequent course of evolution has dramatically benefited from his continued input. Also, I would like to thank the other members of my committee, Prof.s K.C. Russell and Y.M. Chiang for their valuable suggestions and their time.

The bulk of this work was funded primarily through ARPA ORDER 7792 and was monitored by the Naval Surface Warfare Center, Dahlgren Division. I would like to thank Dr.s Eugene Nolting and Ralph Schneider and Mr. William Freeman of NSWC for their valuable input and assistance with very high energy shock processing experiments.

This project was a collaboration between MIT and Science Research Laboratory, Inc. in Somerville, MA. My principal collaborator at SRL was Dr. Daniel Goodman. I want to thank Dr. Goodman for his many contributions to this work. My experiences at SRL greatly enriched my professional development and provided me with a preview of the industrial R&D environment. Other people who helped me at SRL include Mr. Jay Freshman, Mr. Sumner Freshman, and Mr. John Gallagher. A special mention also goes to Dr. George Chedid for his excellent suggestions and comments.

The low energy beam work in this thesis was done at PTR - Precision Technologies in Enfield, CT. Mr. Gary LaFlamme was instrumental in scheduling this work, and also made several good suggestions. Also, I would like to thank Mr. Claudio Russo and Mr. Don Powers of PTR for their help.

My fellow welders ( Bryan, Cheryl, Jeff, John, Larry, Mike, Renkae, and Tadashi) of 4-047 deserve a hearty thanks as well for their many technical and non-technical contributions. Also, Denise Wilsey, Staff Assistant to Prof. Eagar, made many valuable administrative contributions. John Matz, graduate student in the MIT Welding Group, will be continuing, improving, and extending this line of work in the future. His assistance in the PTR experiments was greatly appreciated.

## Table of Contents

<b>Title</b>	1
<b>Abstract</b>	2
<b>Acknowledgments</b>	3
<b>Table of Contents</b>	4
<b>List of Figures</b>	9
<b>List of Tables</b>	16
<b>Dedication</b>	23
<b>Chapter 1 Introduction</b>	24
1.1 Historical Background	24
1.2 HEEB - Based Materials Processing	25
1.3 EB - Based Materials Fabrication	26
1.4 Concise Overview of Thesis	32
<b>Chapter 2 E-Beam Thermal Interaction Model Part I :     Presentation of Theory</b>	33
2.1 Overview	33
2.2 EB Irradiation	33
2.3 Surface Heat Sources	38
2.4 Incorporating the Effect of Backscatter	40
2.5 Corrections for Thermal Radiation and Convection	41
2.6 Extension of Model - Preliminary Consideration of Melt Depth	42
2.7 Applicability of Model to Slabs of Finite Thickness	44
2.8 Extension of Model to Thin Slabs	45
2.9 Summary of Model Framework	49

<b>Chapter 2 E-Beam Thermal Interaction Model Part II : Applications</b>	<b>51</b>
2.10 Overview	51
2.11 Power Requirements for Melting	52
2.12 High Energy Beam Effects	56
2.13 Melt Pools and the Efficiency of EB Deposition Processes	60
2.14 EB Deposition Process vs. Conventional Welding Processes	63
2.15 Modeling of 308 Stainless Steel Wirefeed Deposition Process	66
2.16 Estimation of Power Losses due to Vaporization	68
2.17 Summary of Model Applications	73
<b>Chapter 3 E-Beam Based Powder Melting / Sintering</b>	<b>75</b>
3.1 Overview	75
3.2 E-Beam Sintering and Melting of Powders	75
3.3 Properties of Selected Aluminides	79
3.4 Reactive Synthesis of Aluminides	83
3.5 Aluminide Coating Applications	106
3.6 Hardness of Material C ( $\alpha$ Fe) Coating	114
3.7 Summary of EB Powder Processing	114
<b>Chapter 4 EB Material Deposition Utilizing Wirefeed</b>	<b>116</b>
4.1 Overview	116
4.2 Low Energy EB Deposition Apparatus	119
4.3 EB Wirefeed Deposition of 308 Stainless Steel : Experimental Assembly	121
4.4 Concise Review of the Metallurgy of 304 and 308 Stainless Steel	123
4.5 Microstructure of EB - Deposited 308 Stainless Steel	126
4.6 Al - Bronze EB Deposit on Monel	138

4.7	Residual Stresses	145
4.8	Conclusions	151
<b>Chapter 5</b>	<b>High Energy Electron Beam (HEEB) Materials Processing Applications</b>	<b>153</b>
5.1	Overview	153
5.2	C / C Composite Joining	154
5.2.1	Introduction	154
5.2.2	HEEB-Based Joining of Carbon-Carbon Materials : Theory	156
5.2.3	Thermally Induced Residual Stresses	160
5.2.4	Experimental Program	168
5.2.5	Summary of Brazing Applications	170
5.2.6	NDE Analysis Via Thermal Imaging	170
5.3	HEEB - Based Ceramic Strengthening	173
5.3.1	Introduction	173
5.3.2	Thermally - Induced Residual Stresses : Mechanisms of Formation	174
5.3.3	Experimental Program	179
5.3.4	Summary of HEEB Ceramic Strengthening	181
5.4	HEEB - Based Shock Strengthening	181
5.4.1	Introduction	181
5.4.2	Mechanics and Thermodynamics of Shocks	181
5.4.3	Metallurgical Considerations of Shock Deformation	187
5.4.4	Laser - Based Shock Processing	189
5.4.5	HEEB-Based Shock Processing - Experimental Studies	190
5.4.6	Estimate of HEEB - Generated Pressure	191
5.4.7	HEEB Shock Generation vs. Surface Sources	192

5.4.8	Future Prospects of E-Beam Shock Processing	196
5.5	Summary of HEEB - Based Materials Processing	197
<b>Chapter 6</b>	<b>Conclusions and Future Work</b>	198
6.1	Overview	198
6.2	EB Deposition Processes - Performance and Cost	198
6.3	HEEB Materials Processing - Processes other than Deposition	203
6.4	Reaction Synthesis	204
6.5	Conclusions Regarding EB Fabrication	205
6.6	Guidance for Future Work	205
<b>References</b>		208
<b>Appendix A</b>	<b>Background Physics and Beam Technology</b>	220
A.1	Electron Beams and their Interaction with Matter	220
A.1.1	Types of Electron - Material Interactions	220
A.1.2	Backscattering	221
A.1.3	Material Stopping Power, Energy Deposition, and Electron Range	227
A.1.4	Monte Carlo Simulations of Electron Transport	234
A.2	Numerical Data and Source Modeling	237
A.2.1	Spencer's Report - NBS Monograph 1, 1959	237
A.2.2	Form of Source Function	238
A.2.3	Monte Carlo Methods - TIGER / ITS	241
A.3	Electron Accelerators	243
A.3.1	Different Classes of Electron Accelerators	243
A.3.2	Marx Generator - Based Accelerators	244
A.3.3	Induction LINACs (Linear Accelerators)	247
A.3.4	Conventional EB Welding Machines	248

A.4	Cathodes	250
A.4.1	Thermionic Cathodes	250
A.4.2	Plasma or Explosive Emission Cathodes	252
A.4.3	Electron Guns - Vacuum Diodes	254
A.5	Beam Optics - Focusing and Transport of Electron Beams	255
<b>Appendix B</b>	<b>Electron Energy Deposition and Source Terms for Thermal Models</b>	<b>258</b>
B.1	Source Term Information	258
B.2	Backscattering Information	262
<b>Appendix C</b>	<b>Results of Thermal Calculations</b>	<b>264</b>
<b>Appendix D</b>	<b>List of Acronyms Used in this Work</b>	<b>276</b>
	<b>References for the Appendices</b>	<b>277</b>
	<b>Biographical Sketch</b>	<b>280</b>



## List of Figures

Figure 1.1	Ideal Laser or E-Beam Based SFF Process	29
Figure 1.2	More Realistic Representation of E-Beam / Powder Interaction	30
Figure 1.3	E-Beam SFF Using Wire Feedstock	31
Figure 2.1	Coordinate System for Evaluation of Green's Functions	33
Figure 2.2	Terminology for Thin Slab Solution	46
Figure 2.3	Power Needed to Initiate Surface Melt in Fe as a Function of Beam Travel Velocity and Beam Radius, Beam Energy is 0.1 MeV.	53
Figure 2.4	Power Needed to Vaporize Surface of Fe as a Function of Beam Travel Velocity and Beam Radius, Beam Energy is 0.1 MeV.	54
Figure 2.5	Maximum Power Available for Melting and Deposition of Fe as a Function of Beam Travel Velocity and Beam Radius, Beam Energy is 0.1 MeV.	55
Figure 2.6	Processing Space for Fe, Beam Energy is 0.1 MeV, Beam Radius is 0.35 cm.	56
Figure 2.7	Range of Allowable Processing Powers for Fe (Processing Space), Beam Radius is 0.35 cm, Beam Travel Velocity is 5 cm / s.	57
Figure 2.8	Absorbed Power Needed to Initiate Surface Melt in 304 Stainless, Beam Radius is 0.15 cm, Beam Travel Velocity is 5 cm / s.	58
Figure 2.9	Surface Temperature of 304 Stainless, Absorbed Power is 600W, Beam Radius is 0.15 cm, and Beam Travel Velocity is 5 cm / s.	58
Figure 2.10	Temperature Profiles in 304SS when Surface is at Melting Point, Beam Radius is 0.15 cm, Beam Travel Velocity is 5 cm / s	59
Figure 2.11	Temperature Profiles in 304 Stainless Assuming Absorbed Power of 582W, Beam Radius is 0.15 cm, Beam Travel Velocity is 5 cm / s.	60

Figure 2.12	Schematic Representation of Melt Depth Cross - Section	61
Figure 2.13	GMAW Mass Transfer Modes Adapted from HOBART BROTHERS CO. (1980)	64
Figure 3.1	Circular Scan Pattern for Commercial EB Welder - PTR Machine	76
Figure 3.2	"Line Source" Consisting of Scanning Circular Source Commercial EB Welder - PTR Machine	77
Figure 3.3	Microstructure of Primary Melt in HY-100 Steel, 100X EB Melting of HY-100 Powder Compact	78
Figure 3.4	Microstructure of Re-melt Region in HY-100 Steel, 100X EB Melting of HY-100 Powder Compact	79
Figure 3.5	Fe - Al Phase Diagram Reprinted with Permission from MASSALSKI (1990)	87
Figure 3.6	Macrostructure of Material A, 16X EB - Assisted Reaction Synthesis	90
Figure 3.7	Microstructure of Material A, 50X Single-Pass Melt, EB - Assisted Reaction Synthesis	91
Figure 3.8	Microstructure of Material A, 100X Single -Pass Melt, EB - Assisted Reaction Synthesis	92
Figure 3.9	Microstructure of Material A, 200X Single-Pass Melt, EB - Assisted Reaction Synthesis	93
Figure 3.10	Microstructure of Material A, 100 X Multi-Pass Melt, EB Assisted Reaction Synthesis	94
Figure 3.11	Microstructure of Material A, 400X Multi-Pass Melt, EB Assisted Reaction Synthesis	95
Figure 3.12	Surface Melt Features of Material A, 400X Single-Pass Melt, EB Assisted Reaction Synthesis	96
Figure 3.13	Surface Solidification features of Material A, 750X Single-Pass Melt, EB Assisted Reaction Synthesis	97
Figure 3.14	Surface Crack in Material A, 660X Single-Pass Melt, EB Assisted Reaction Synthesis	98
Figure 3.15	Microstructure of Material B, 200X Multi-Pass Melt, EB Assisted Reaction Synthesis	99

Figure 3.16	Microstructure of Material B, 400X Multi-Pass Melt, EB Assisted Reaction Synthesis	100
Figure 3.17	Surface Solidification Features in Material B, 150X Multi-Pass Melt, EB Assisted Reaction Synthesis	101
Figure 3.18	Centerline Porosity in Material B, 200X Multi-Pass Melt, EB Assisted Reaction Synthesis	102
Figure 3.19	Microstructure of Material A + TiC, 400X Multi-Pass Melt, EB Assisted Reaction Synthesis	103
Figure 3.20	Microstructure of Material B + TiC, 400X Multi-Pass Melt, EB Assisted Reaction Synthesis	104
Figure 3.21	TiC Particle Protruding from Surface of Material A, 1800X Multi-Pass Melt, EB Assisted Reaction Synthesis	105
Figure 3.22	Unreacted powders Spot-Welded onto Steel Sheet, 12 X Material C Precursor, Single EB Melt Pattern is Visible, EB Assisted Reaction Synthesis	107
Figure 3.23	Deposited and Fully Melted Fe <sub>3</sub> Al Tracks on Steel, 12 X EB Assisted Reaction Synthesis	108
Figure 3.24	Microstructure of Material C on Steel, 100 X Through Thickness of Melt, Multi-Pass Melt, EB Assisted Reaction Synthesis	109
Figure 3.25	Microstructure of Material C Deposit on Steel, 100X Edge of Melt, Multi-Pass Melt, EB Assisted Reaction Synthesis	110
Figure 3.26	Interface between Material C and Steel Substrate, 400 X EB Assisted Reaction Synthesis	111
Figure 3.27	Schematic of Material C Deposit on Steel, Location of Figures 3.24 and 3.25	112
Figure 3.28	Composition Variation Across Interface, Material C Coating on Steel	113
Figure 4.1	Schematic of EB Wirefeed Deposition Process	116
Figure 4.2	Schematic Representation of Disk Repair	117
Figure 4.3	Schematic of Turbine Blade Repair by Wirefeed Deposition Process, Adapted from WELDING JOURNAL 11 / 92 (1992)	118

Figure 4.4	150kV EB Commercial Welder Located at PTR - Precision Technologies, Enfield, CT.	119
Figure 4.5	Wirefeed Mechanism and XY - Motion Table, PTR - Precision Technologies, Enfield, CT.	120
Figure 4.6	Geometry of Stainless Target, Drawn to 1 / 2 Scale	122
Figure 4.7	Section of Fe-Cr-Ni Phase Diagram at 70 wt. % Fe Reprinted with Permission from VITEK et al (1992)	123
Figure 4.8	Solidification of 304 (308 also) Stainless Steel Adapted from MATSUDA & LEE (1990)	124
Figure 4.9	Schaeffler Diagram Modified to Include Cooling Rate Effect Copied with Permission from DAVID, VITEK & HEEBLE (1987)	125
Figure 4.10	EB Deposit of 308 SS Wire on 304L SS Pipe	127
Figure 4.11	Side View of 308 SS EB Deposit	127
Figure 4.12	Smooth Section of 308 SS EB Deposit	128
Figure 4.13	Disturbed Region on 308 SS EB Deposit	128
Figure 4.14	Smooth 308 EB Deposit	129
Figure 4.15	Macro Close-up of Surface of Smooth Deposit, 25X 308 SS EB Deposit	130
Figure 4.16	Schematic of Defect Formation in EB Wirefeed Deposition	131
Figure 4.17	Multilayer Defect in 308 SS EB Deposit, 10X	132
Figure 4.18	Bottom of 1.25 cm thick 308 SS EB Deposit, 400X	133
Figure 4.19	Top of 1.25 cm thick 308 SS EB Deposit, 400 X	134
Figure 4.20	Interface Between Two Successive Weld Deposits, 308 SS EB Deposit, 400 X	135
Figure 4.21	308 SS EB Deposit, Multipass Nature of Deposits, 12X	136
Figure 4.22	308 SS EB Deposit, Multipass Nature of Deposit, 25 X	137
Figure 4.23	Al - Bronze Deposit on Monel, 16 X	139
Figure 4.24	Mixing Region Between Al - Bronze and Monel, 50 X	140

Figure 4.25	Region of Mixing Between Al - Bronze and Monel, 100X	141
Figure 4.26	Hot Tear Near Bottom of Mixing Region, 400 X	142
Figure 4.27	Hot Tear Near Bottom of Mixing Region, 400 X	143
Figure 4.28	Microstructure of Al - Bronze EB Deposit, 400 X	144
Figure 4.29	Schematic Representation of Residual Stresses for a Single Layer EB Deposit	145
Figure 4.30	Schematic of Residual Stresses in a Multilayer EB Deposit	145
Figure 4.31	Schematic of Targets used for Residual Stress Evaluation, Shown 1/2 Scale	146
Figure 4.32	Coordinate System for Residual Stress Measurement Adapted from CULLITY (1978)	147
Figure 4.33	Microhardness Profile in 308 EB Deposit	150
Figure 5.1	Relative Strength of C/C Materials	155
Figure 5.2	Electron Range in Carbon	157
Figure 5.3	Isothermal Brazing	158
Figure 5.4	Laser / Conventional E-Beam Brazing	159
Figure 5.5	HEEB Brazing	160
Figure 5.6	Coordinate System used for Calculation of Unconstrained Thermal Mismatch Strain	161
Figure 5.7	Interfacial Shear and Peeling Stresses	164
Figure 5.8	Thermal Images of ACC4 - to - MoRe Braze Joints	171
Figure 5.9	Bonded Area of ACC4 - to - MoRe Braze Joints Revealed After Shear Testing	172
Figure 5.10	Schematic of Coordinate System Used to Evaluate Thermal Stresses	174
Figure 5.11	Schematic of Flow in Diffusional Creep Adapted from KINGERY, BOWMAN and UHLMANN (1976)	176
Figure 5.12	Definition of Variables Used in Jump Conditions	182

Figure 5.13	Rankine - Hugoniot Curve in Comparison to Shock Adiabats	183
Figure 5.14	Pressure / Shock Waves Resulting from Pulsed E-Beam Irradiation	184
Figure 5.15	Shock Wave in an Elastic - Perfectly Plastic Material	186
Figure 5.16	Elastic and Plastic Wave Fronts in an Elastic - Perfectly Plastic Material	187
Figure 5.17	Hardness at Irradiated Spots as a Function of Number of Pulses, Weld Centerline in 5086 Aluminum	191
Figure 5.18	Specific Energy Deposition as a Function of Source Energy, Target Material is Aluminum, $\Delta T=100\text{ }^{\circ}\text{C}$	194
Figure 5.19	Maximum Compressive Stress as a Function of Source Energy, Material is Aluminum	195
Figure 6.1	Processing Regimes for Low Energy EBs, High Energy EBs, and Arc Welding Processes.	199
Figure 6.2	Power Required to Melt 304 SS, Beam Radius is 0.25 cm	200
Figure 6.3	Maximum Compressive Stress as a Function of Source Energy, Material is Aluminum	202
Figure A.1	Basic Electron - Material Interactions Adapted from TANIGUCHI (1989)	220
Figure A.2	Backscattered Current as a Function of Incident Electron Energy, 304 SS is Target	222
Figure A.3	Backscattered Power as a Function of Incident Electron Energy, 304 SS is Target	222
Figure A.4	Beam Impinging Upon a Cylindrical Surface Indentation	223
Figure A.5	Diagram Used to Find Backscattering from a Surface Depression	224
Figure A.6	Electron - Electron Scattering : Classical Theory Adapted from JACKSON (1962)	229
Figure A.7	Schematic X-Ray Spectrum Adapted from CULLITY (1978)	232
Figure A.8	Event Probabilities Arranged on Interval (0, 1) Adapted from SHREIDER (1964)	236

Figure A.9	5th-Order Polynomial Fit to Energy Deposition Profile	239
Figure A.10	Schematic of CYLTRAN Input Geometry and Various Calculated Energy Losses	242
Figure A.11	Schematic of Pulsed High Voltage Electron Beam System Based on the Marx Generator Adapted from NATION (1979)	245
Figure A.12	Schematic Circuit of Marx Generator Adapted from MILLER (1982)	245
Figure A.13	Self-Erecting Marx Configuration Adapted from MILLER (1982)	246
Figure A.14	Schematic of an Induction LINAC Acceleration Cell Adapted from HUMPHRIES (1986)	247
Figure A.15	Schematic of Conventional EB Welder LaFLAMME (1994)	248
Figure A.16	Some Possible Scan Patterns for EB Welders LaFLAMME (1994)	249
Figure A.17	Schematic "Richardson Plot"	251
Figure A.18	Schematic of a Dispenser Cathode : View of Cross - Section, Adapted from ANONYMOUS (1977)	251
Figure A.19	Surface "Whisker" on a Plasma Cathode Adapted from MILLER (1982)	253
Figure A.20	Coordinate System for Paraxial Ray Approximation	256

## List of Tables

Table 1.1	Taxonomic Classification of HEEB-Based Processes	26
Table 1.2	Comparison Between Lasers and E-Beams for SFF Applications	27
Table 2.1	List of Symbols used in Chapter 2 - Part I	50
Table 2.2	Melt Depths in Fe	60
Table 2.3	Power requirements to Maintain Weld Pool in Fe	62
Table 2.4	Various Efficiencies for Melting and Deposition Processes in Fe	63
Table 2.5	GMAW Schedule for Short-Circuiting Transfer, Single Pass Adapted from HOBART BROTHERS CO. (1980)	65
Table 2.6	GMAW Schedule for Globular Transfer, Single Pass Adapted from HOBART BROTHERS CO. (1980)	65
Table 2.7	GMAW Schedule for Spray Transfer, Single Pass Adapted from HOBART BROTHERS CO. (1980)	65
Table 2.8	Efficiencies for GMAW, Short-Circuiting Transfer, Single Pass	65
Table 2.9	Efficiencies for GMAW, Globular Transfer, Single Pass	66
Table 2.10	Efficiencies for GMAW, Spray Transfer, Single Pass	66
Table 2.11	Beam Operating Parameters for 308 Stainless Steel Deposition	66
Table 2.12	Properties of 304 Stainless Steel	67
Table 2.13	Vapor Pressures for Various Alloying Elements in 308 Stainless Steel at 2500 °C	71
Table 2.14	Heats of Vaporization for Cr, Fe, and Ni from SMITHELLS & BRANDES (1976)	71
Table 2.15	Relevant Additional Data for the Evaluation of Vaporization Power Losses	72
Table 2.16	Time - Average Surface Concentrations of Constituents in 304 Stainless	72



Table 2.17	Vaporization Fluxes for Constituents of 308 Stainless	73
Table 2.18	Power Losses due to Vaporization in 308 Stainless	73
Table 2.19	Limiting Values of Various Deposition and Melting Efficiencies	74
Table 2.20	Summary of Predicted vs. Actual Quantities for EB Deposition of 308 Stainless	74
Table 3.1	Powders Used in this Work	77
Table 3.2	Structures of Aluminides Adapted from METALS HANDBOOK - DESK EDITION (1985)	79
Table 3.3	Aluminide Intermetallic Compounds Adapted from VEDULA and STEPHENS (1987)	80
Table 3.4	Thermal Expansion Data for Iron and Nickel Aluminide Alloys Adapted from PORTER & MAZIASZ (1993)	80
Table 3.5	Mechanical Properties of Iron Aluminides Adapted from SIKKA & LIU (1994)	81
Table 3.6	Oxidation Properties of Iron Aluminides : Parabolic Rate Constants for Fe-Cr-Al Alloys in Dry Air at 800 °C Adapted from TORTORELLI & DeVAN (1992)	81
Table 3.7	Cavitating Jet Erosion Rates of Aluminides as Compared to Commercial Alloys Adapted from JOHNSON & MIKKOLA et al (1990)	82
Table 3.8	Erosion and Abrasive Wear Resistance of Ni <sub>3</sub> Al - Based Alloys Adapted from JOHNSON & MIKKOLA et al (1990)	82
Table 3.9	Erosion and Abrasive Wear Resistance of Fe <sub>3</sub> Al - Based Alloys Adapted from JOHNSON & MIKKOLA et al (1990)	83
Table 3.10	Summary of Experimental Results in EB - Assisted Reaction Synthesis of Aluminides	84
Table 3.11	Electron Microprobe Composition Analysis of Reaction - Synthesized Aluminides (Analysis performed by Neel Chatterjee, MIT)	86
Table 3.12	Fe-Al Materials in this Work and Phase Balances	88

Table 3.13	Bulk Composition of Material C Coating on Steel as Determined by Microprobe Analysis (Analysis done by Chuck Herrington, Geller Microanalytical Laboratory, Peabody, MA)	113
Table 3.14	Vickers Hardness (300g) of Material C Coating and Steel Substrate	114
Table 4.1	Weld Wires Used in Wirefeed Deposition Repair of Jet Engine Components, Adapted from WELDING JOURNAL 11/ 92 (1992)	119
Table 4.2	EB Operating Parameters and Wirefeed Rates Used in this Work ( "ipm" refers to inches per minute)	121
Table 4.3	Composition of 308 Stainless Steel, wt. % Taken from METALS HANDBOOK - DESK EDITION (1985)	122
Table 4.4	Some Possible Phases Present in Austenitic Stainless Steel Adapted from MARSHALL (1984)	126
Table 4.5	Composition of Al - Bronze and Monel	138
Table 4.6	Properties of Various Cu and Ni Alloys	138
Table 4.7	X-Ray Residual Stress Measurements 308 EB Deposit on 304L Pipe	149
Table 5.1	Taxonomic Classification of HEEB-Based Processes	153
Table 5.2	C/C Fiber Coating Strategies	156
Table 5.3	C/C Material Used in Brazing Experiments (Courtesy of Dr. Daniel L. Goodman)	168
Table 5.4	Creep Rates of Various Ceramics at 1300 °C and under an applied stress of 1800 psi Adapted from KINGERY, BOWMAN and UHLMANN (1976)	177
Table 5.5	Residual Stress Values in AD 96 and AD 998 Alumina	180
Table 5.6	Microstructural Effects of Shock Deformation	188
Table 5.7	Laser - Based Shock Processing	189
Table 5.8	Dimensionless Grüneisen Coefficients of Selected Metals Adapted from BAILEY (1992)	192

Table 5.9	Effects of Various Surface Properties on Fatigue Life	196
Table 6.1	Costs Associated with Various Deposition Processes - Capital Costs Normalized with Deposition Rates	201
Table 6.2	EB Radiation Processing of Polymers - Applications Adapted from SINGH & SILVERMAN (1992)	204
Table A.1	Values of Additional Backscattering Attenuation Factor as a Function of the Depression Aspect Ratio	227
Table A.2	Absorbtivities for Laser Processing ION, SHERCLIFF, and ASHBY (1991)	227
Table A.3	Percent of Incident Beam Lost to Bremstrahlungen Adapted from BAILEY (1992)	233
Table A.4	Number of Collisions Experienced by an Incident Electron, Adapted from BERGER (1963)	233
Table A.5	Operating Parameters of Some Very Large Pulsed Electron Beams, Adapted from MILLER (1982)	244
Table A.6	Typical Operating Parameters of Conventional EB Welders	248
Table A.7	Current Densities for Different Types of Cathodes Adapted from TURNMAN, MAZARAKIS, and NEAU (1992)	253
Table B.1	Energy Deposition Information for Aluminum adapted from SPENCER (1959)	259
Table B.2	Energy Deposition Information for Copper adapted from SPENCER (1959)	259
Table B.3	Energy Deposition Information for Iron Calculated using TIGER / ITS Codes	259
Table B.4	Energy Deposition Information for Titanium Calculated using TIGER / ITS Codes	260
Table B.5	Energy Deposition Information for 304 Stainless Steel Calculated using TIGER / ITS Codes	260
Table B.6	Energy Deposition Information for Monel Alloy 400 Calculated using TIGER / ITS Codes	260
Table B.7	Energy Deposition Information for Alloy HA-188 Calculated using TIGER / ITS Codes	261

Table B.8	Energy Deposition Information for Alloy INCONEL 718 Calculated using TIGER / ITS Codes	261
Table B.9	Energy Deposition Information for Alloy RENÉ 95 Calculated using TIGER / ITS Codes	261
Table B.10	Backscattering Information, Material Is Aluminum	262
Table B.11	Backscattering Information, Material Is Titanium	262
Table B.12	Backscattering Information, Material is 304 Stainless Steel	262
Table B.13	Backscattering Information, Material is Monel 400	263
Table C.1	Thermophysical Data	264
Table C.2	Absorbed Power (W) Needed To Initiate Surface Melt in Aluminum : 0.1 MeV	264
Table C.3	Absorbed Power (W) Needed To Initiate Surface Melt in Aluminum : 0.2 MeV	264
Table C.4	Absorbed Power (W) Needed To Initiate Surface Melt in Aluminum : 0.4 MeV	265
Table C.5	Absorbed Power (W) Needed To Initiate Surface Melt in Aluminum : 1.0 MeV	265
Table C.6	Absorbed Power (W) Needed To Initiate Surface Melt in Aluminum : 2.0 MeV	265
Table C.7	Absorbed Power (W) Needed To Initiate Surface Melt in Aluminum : 4.0 MeV	266
Table C.8	Absorbed Power (W) Needed To Initiate Surface Melt in Copper : 0.1 MeV	266
Table C.9	Absorbed Power (W) Needed To Initiate Surface Melt in Copper : 0.2 MeV	266
Table C.10	Absorbed Power (W) Needed To Initiate Surface Melt in Copper : 0.4 MeV	267
Table C.11	Absorbed Power (W) Needed To Initiate Surface Melt in Copper : 0.7 MeV	267
Table C.12	Absorbed Power (W) Needed To Initiate Surface Melt in Copper : 1.0 MeV	267

Table C.13	Absorbed Power (W) Needed To Initiate Surface Melt in Copper : 2.0 MeV	268
Table C.14	Absorbed Power (W) Needed To Initiate Surface Melt in Copper : 4.0 MeV	268
Table C.15	Absorbed Power (W) Needed To Initiate Surface Melt in Iron : 0.1 MeV	268
Table C.16	Absorbed Power (W) Needed To Initiate Surface Melt in Iron : 0.2 MeV	269
Table C.17	Absorbed Power (W) Needed To Initiate Surface Melt in Iron : 0.4 MeV	269
Table C.18	Absorbed Power (W) Needed To Initiate Surface Melt in Iron : 0.7 MeV	269
Table C.19	Absorbed Power (W) Needed To Initiate Surface Melt in Iron : 1.0 MeV	270
Table C.20	Absorbed Power (W) Needed To Initiate Surface Melt in Iron : 2.0 MeV	270
Table C.21	Absorbed Power (W) Needed To Initiate Surface Melt in Iron : 4.0 MeV	270
Table C.22	Absorbed Power (W) Needed To Initiate Surface Melt in Titanium : 0.1 MeV	271
Table C.23	Absorbed Power (W) Needed To Initiate Surface Melt in Titanium : 0.2 MeV	271
Table C.24	Absorbed Power (W) Needed To Initiate Surface Melt in Titanium : 0.4 MeV	271
Table C.25	Absorbed Power (W) Needed To Initiate Surface Melt in Titanium : 0.7 MeV	272
Table C.26	Absorbed Power (W) Needed To Initiate Surface Melt in Titanium : 1.0 MeV	272
Table C.27	Absorbed Power (W) Needed To Initiate Surface Melt in Titanium : 2.0 MeV	272
Table C.28	Absorbed Power (W) Needed To Initiate Surface Melt in Titanium : 4.0 MeV	273
Table C.29	Absorbed Power (W) Needed To Initiate Surface Melt in 304 SS : 0.1 MeV	273

<b>Table C.30</b>	<b>Absorbed Power (W) Needed To Initiate Surface Melt in 304 SS : 0.2 MeV</b>	<b>273</b>
<b>Table C.31</b>	<b>Absorbed Power (W) Needed To Initiate Surface Melt in 304 SS : 0.4 MeV</b>	<b>274</b>
<b>Table C.32</b>	<b>Absorbed Power (W) Needed To Initiate Surface Melt in 304 SS : 0.7 MeV</b>	<b>274</b>
<b>Table C.33</b>	<b>Absorbed Power (W) Needed To Initiate Surface Melt in 304 SS : 1.0 MeV</b>	<b>274</b>
<b>Table C.34</b>	<b>Absorbed Power (W) Needed To Initiate Surface Melt in 304 SS : 2.0 MeV</b>	<b>275</b>
<b>Table C.35</b>	<b>Absorbed Power (W) Needed To Initiate Surface Melt in 304 SS : 4.0 MeV</b>	<b>275</b>

This work is dedicated to my Grandparents :  
PUSHKERRAY AMBASHANKAR DAVÉ  
CHANDULAL BHUDERJEE SHUKLA  
VIDYAGAURI PUSHKERRAY DAVÉ  
PUSHPAGAURI CHANDULAL SHUKLA

# CHAPTER 1

## INTRODUCTION

### 1.1 Historical Overview

This thesis deals primarily with the application of electron beams to materials fabrication. Low energy beam technology has been extensively applied to materials processing and joining [see for example BAKISH (1962)]. Although low energy electron beam machines of very high power exist [ARATA and TOMIE (1973)], high beam voltages have been relatively rare in materials processing applications. The notable exceptions have been in the areas of polymer curing, sterilization, and lithography [POWERS (1992)], in which multi-megavolt beams have been utilized effectively. In this work, both low energy and high energy electron beams were used. High energy beams, or H.E.E.B.s, are characterized by high acceleration voltages, pulsed-mode beams, and potentially high powers through repetitive operation. Typical parameters are 1-3 MeV beam energies, pulselengths of 50 - 1000 ns, peak currents of 500 - 2000 A, and repetition rates from single shot - 1000 Hz.. This type of beam was originally developed for physics experiments and radiation damage studies [SMITH, NOLTING, and FAWLEY (1992)]. Other former uses of HEEB technology included advanced weapons applications.

Low energy beams are widely used in material joining, sputtering, and melting applications. The specific type of low energy beam used in this work was a commercial welding e-beam apparatus capable of maximum beam powers in the range 15kW - 20kW. Typical operating parameters used in practice were 120kV - 150kV acceleration voltages and 1 - 12 mA continuous beam currents, which means that the maximum beam power used was less than 2kW. Since the beam diameters used were typically very small, (0.5 -3 mm) the corresponding power density was very high.

In the early 1990's, there was an initiative in the CPB (Charged Particle Beam) Program to develop dual-use applications for HEEB technology [see SMITH, NOLTING, and FAWLEY (1992) & LUNDIN et al (1992)]. At a conference held in September of 1992, leading members of the CPB Program, various government labs, and private companies met with faculty and students from several universities to create a critical mass for the discussion of HEEB materials processing. A partial list of the ideas generated in this conference includes such topics as :

- shock processing / surface modification
- powder melting / sintering
- dynamic powder consolidation
- ceramic strengthening
- polymer matrix composite curing
- brazing of inorganic composites
- welding



It was determined that a test facility was needed to establish the viability of these processes, and a program to carry out these tests was envisioned. *This current work is in part the practical realization of this meeting in 1992, and many of the above-mentioned processes have been investigated.* As such, it represents one of the most complete assessments to date on the applicability of HEEB technology to materials processing.

There have been a few other studies in the field of HEEB processing, and the two most notable are those by LUNDIN et al (1992), and ELMER, NEWTON, and SMITH (1993). The study by Lundin et al looked at HEEB - material interaction for a variety of material systems. These studies were done on a single-shot machine with the following parameters : 2.5 - 3 MeV beam energy, 500 - 1500 ns pulselength, and 1000-2000 A peak current. This translates to roughly 1200 - 3000 Joules per pulse. The experiments of LUNDIN et al (1992) included:

- joining (brazing) of carbon - carbon composite materials
- aluminum - based MMC interaction studies
- interaction with several metallic targets
- sintering of alumina

The LUNDIN et al study was useful in that it established baseline results, but it was not able to achieve its objectives on account of the violent thermomechanical effects of pulsed irradiation. As will be discussed at length later in this work, pulsed radiation deposited volumetrically into a target over a small timescale can result in enormous pressures and shock propagation.

The study by ELMER, NEWTON, and SMITH investigated the transformation hardening of steel. This application utilizes the deep - penetration capabilities of HEEBs. HEEBs will penetrate several millimeters into most materials. Using a 6 MeV HEEB, this study was able to demonstrate subsurface hardening of steel to a depth of 2 mm without surface melting. Also, it will be later pointed out in this present work that one of the consequences of HEEB volumetric heating and the associated pressure waves is a compressive residual stress state. The study by ELMER, NEWTON, and SMITH has proven the potential for HEEB-based surface modification / heat treatment : it can result in deep subsurface hardening and potentially favorable residual stress states.

## **1.2 HEEB - Based Materials Processing**

This present work has investigated powder melting / sintering, ceramic strengthening, shock surface modification, and carbon - carbon composite joining. In each HEEB application area, demonstration experiments were carried out and interpreted. Based on these initial results, the viability of each process was assessed. Also, simple models were constructed to better elucidate the underlying physical phenomena and provide guidance in process optimization.

To better understand the potential role of HEEB processing in a manufacturing operation, it is useful to consider some of its general

characteristics. There have been many taxonomic schemes developed for the classification of unit manufacturing processes (UMPs) [see for example SCHEY (1987)]. The various HEEB processes mentioned above will now be classified according to such a scheme. The specific unit manufacturing process classes shown here are phase change processes, processes involving internal structure changes, consolidation processes, and deformation processes [EAGAR (1994)]. Phase changes refer to the change of state of the material, as is the case with casting, physical vapor deposition, etc. Internal structural changes refer to the vast array of material phase changes and transformations that are possible with various thermal and thermomechanical cycles. Consolidation processes include joining processes such as welding and brazing, and also powder consolidation methods, such as HIP, CIP, etc. Deformation processing refers to such activities as forging, rolling, drawing, etc. With respect to HEEB processing, it will also refer to surface deformation processes, like HEEB shock processing and thermal stress-induced deformation.

**TABLE 1.1**  
**Taxonomic Classification of HEEB-Based Processes**

Specific HEEB Application	Classification of Unit Manufacturing Processes			
	Phase Change (casting, vapor processing)	Internal Structure Change	Consolidation (joining and P/M included)	Deformation Processes
Shock Treatment		X		X
Surface Hardening		X		
Ceramic Strengthening		X		X (thermal stresses)
Power Melting and Sintering	X		X	
Dynamic Powder Consolidation			X	X
C/C Composite Joining			X	
Polymer Crosslinking		X		

### 1.3 EB - Based Materials Fabrication

One of the major goals of this work was to explore the feasibility of e-beam based Solid Freeform Fabrication (SFF). Low energy electron beams were applied to this aim with a high degree of success. SFF has been successfully implemented using lasers and other "3-D printing" techniques [see for example

SACHS, CIMA, and CORNIE et al (1990) and MARCUS, BEAMAN, BARLOW, and BOURELL (1990)]. The essential feature of all such schemes is that geometric computer models of parts can be converted into actual components without any intervening tooling. To date, these components have been limited to relatively small, detailed, close-tolerance parts. Also, the choice of materials used thus far has been limited by powder sintering kinetics, and the full range of structural materials of practical engineering interest has not been used. It was thought that e-beams may offer some advantages over lasers, provided that the associated tradeoffs are acceptable. These advantages and possible drawbacks are listed below.

**TABLE 1.2**  
**Comparison Between Lasers and E-Beams for SFF Applications**

PROCESS FEATURE	PROCESS	
	LASER	E-BEAM
Close Tolerances	very good	limited
Choice of Materials	limited at present - but not a <i>limiting</i> factor	potentially good
Ability to Manufacture Actual Structural Parts	limited at present	potentially good
Ability to Handle Large Parts (Beam Power)	limited	very good
Ability to Relieve Residual Stresses <i>in situ</i>	potentially good	potentially good

As can be seen from the above Table, the main application of e-beam based SFF would be for the manufacture of large structural components that would not require extremely close tolerances. Such parts could also be subject to some post-processing in the form of machining, so e-beam SFF should be classified as a Near-Net Shape process at best. Some potential applications for such a manufacturing technology are :

- Manufacture and / or repair of large parts of cylindrical geometry, such as turbine disks for steam generation turbines, continuous caster rolls, rolling mill rolls, naval drive components, etc.
- Manufacture of large parts of rectangular or irregular geometry through a process analogous to laser-based SFF.
- A new technique for the pressureless reaction synthesis of intermetallic compounds that allows control over the reaction front location and results in near full density and full extent of reaction in some systems.

Some parts which would fall into the second category would include large castings, such as aluminum bronze valve casings. The ability to make such a large casting on-demand by an SFF technique could reduce manufacturing and inventory costs for very small lot sizes and may result in faster delivery times. The envisioned advantages are :

- eliminates inventory expense for storage of large castings
- shorter lead times
- potentially better metallurgical properties, and therefore improved performance
- the ability to manufacture functionally gradient material (FGM) parts, or parts with a spatial variation of composition and properties.

For metals, there are several processes that fall under the category of "rapid prototyping," or "desktop manufacturing." One of these processes is based on lasers, and is known as Selective Laser Sintering (SLS™). This process has been commercialized by DTM Corporation of Austin, TX. The SLS process is has been successfully implemented on a range of materials including wax, polycarbonates, nylon, ABS, alumina and a few other ceramics, and some mixtures, such as Cu-Sn and Pb-Sn. The main applications of SLS are the manufacture of models, prototypes, patterns for investment casting, the investment casting mold itself, and demonstration parts. SLS™ has developed sufficiently so that parts of reasonably high dimensional accuracy (0.01 inch typical, 0.005 possible for some materials) can be produced.

Applications of SLS™ to metals of structural significance have been very limited to date. The main reason for this is that SLS relies on rapid sintering to establish partial interparticle bonding, i.e. green strength. The parts can then be sintered to achieve full density. The metal systems that have been most successful in SLS™ processing are those that have a very low melting point, or have a very large liquid fraction at the processing temperature. The large liquid fraction will allow liquid phase sintering to occur, and the timescale of this process is suitably fast for laser sintering. Materials like steels and superalloys are therefore not suitable. In fact initial experiments with these materials have produced mixed results [ZONG et al (1992)], but further development is in progress.

Another SFF scheme involves the formation of green bodies by selective spraying of binder onto layers of powders. This technique, known as Three Dimensional Printing (3DP), was developed at the MIT Ceramics Processing Laboratory [SACHS, CIMA, CORNIE et al (1990)], and is suitable for metal as well as ceramic parts. A mechanism very similar to an ink-jet printer binds selected regions of a powder bed, and the process is repeated to achieve multilayer components. The green body thus formed is then sintered to achieve full density.

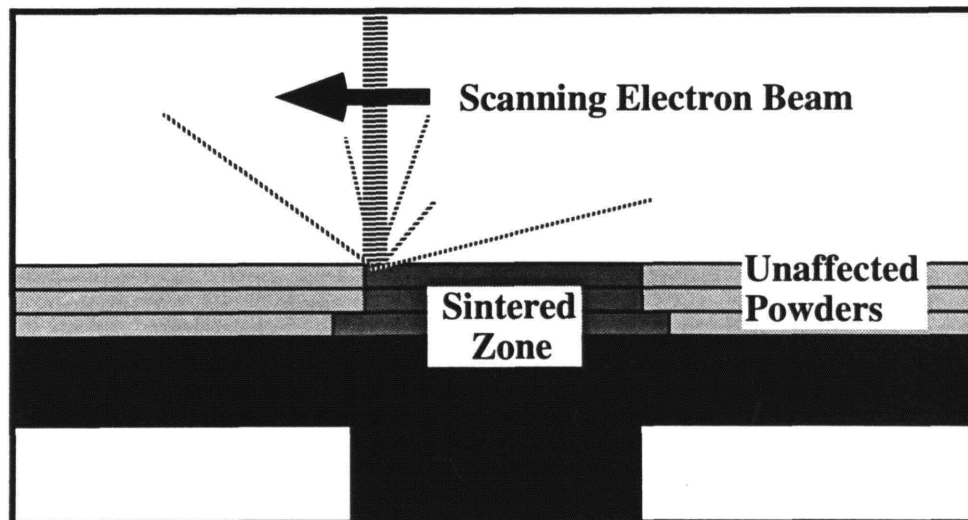
Other SFF techniques include stereolithography and Laminated Object Manufacturing. Laminated Object Manufacturing [SACHS, CIMA & CORNIE (1990)] is a process in which layers of material are cut by a computer-controlled laser, and these layers, or laminates, are then bonded together to form the desired part. Current applications of this technique include the experimental manufacture of ceramic matrix composites [ADVANCED MATERIALS & PROCESSES (1994)]. Stereolithography is the perhaps the oldest multilayer SFF technique [SACHS, CIMA, CORNIE et al (1990)]. In this method, a UV-curable liquid

polymer is selectively crosslinked by lasers or other light sources. As in other multilayer SFF techniques, this material addition is done one cross section at a time.

For electron beam - based SFF, there are three envisioned application areas : high temperature nickel or cobalt based alloys, reactive sintering of intermetallics, and conventional alloys (monel, Al - Ni - Bronze, stainless steel, etc.). The first application area deals with the production of functionally gradient materials (FGM) composed of superalloys for aerospace applications. The e-beam process could be used to make near - net shape turbine disks, or forging preforms for such disks. The ability to grade or vary the composition with position is a key objective in this application. E-beam assisted reaction sintering of intermetallics is a novel application that has been discovered during the course of this current work. The scanning electron beam acts as a localized, high energy density heat source that allows selective reaction sintering to occur. The main features of this process are :

- the ability to transform the powder precursor mix selectively, i.e. the ability to control the reaction front,
- the melted region exhibits full density and full extent of reaction on some systems (FeAl, Fe<sub>3</sub>Al)

In the rest of this work, we will be concerned with only two methods : a powder-based technique similar to selective laser sintering, and a wire feed technique similar to conventional welding. The SFF method based on powders is analogous to laser-based selective sintering, except that full melting of the compacts is achieved. In laser processing, powder layers are pressed to a moderate initial density, and then they are sintered. Typically, the layers are very thin ( 0.010" - 0.050" typical). the objective is to sinter the powders to achieve reasonable green strength. If e-beams were used, some amount of melting could also occur. The idealized process may be schematically represented by the following diagram :



(shown above)  
**FIGURE 1.1**  
**Ideal Laser or E-Beam Based SFF Process**

If the heat input to the part is kept sufficiently low, and if melting is controlled, then the ideal representation shown above can be approached in reality. Laser selective sintering has successfully commercialized such a process for small, "high resolution" parts. E-beams generally operate at higher powers than the lasers used in selective laser sintering, and melting will almost invariably occur. Furthermore, in the manufacture of a large component, melting is desirable to eliminate long cycle time firing operations required for full density. An e-beam process for large parts would require that subsequent layers be fully dense and that they adhere completely to previously deposited layers. Powders may not be the best starting materials for such operations. The powder layers will shrink considerably when a melt zone forms, and interlayer adherence is not a trivial consideration. A closer representation of the real melt profile resulting from e-beam / powder interactions is shown below.

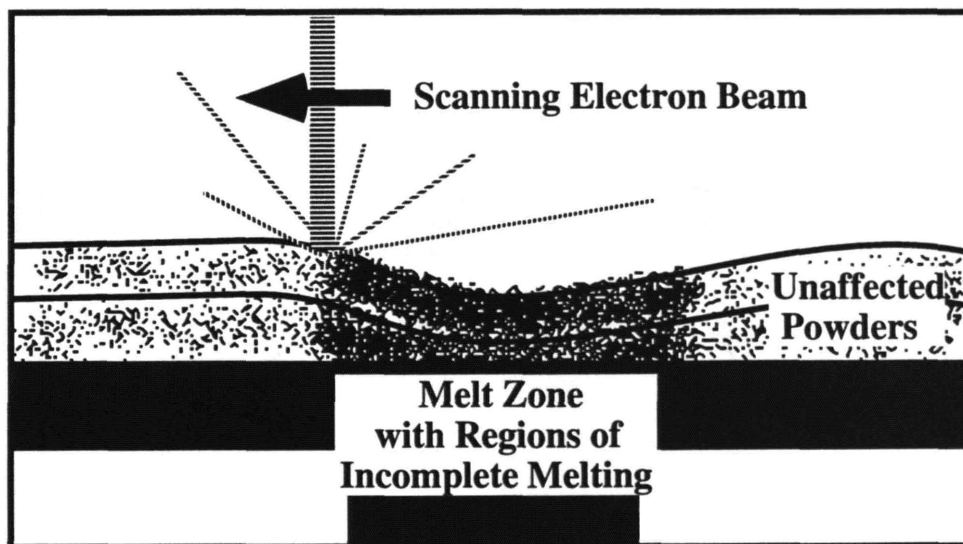


**FIGURE 1.2**  
**More Realistic Representation of E-Beam / Powder Interaction**

There are several problems associated with e-beam powder melting as an SFF technique for the processing of structural materials. Some of these issues may or may not be process limitations, and this depends on the application. The problems are :

- incomplete melting generally occurs ; it is often observed that regions of partial melting and sintering are directly below regions of full melt
- inadequate adherence between layers of powders

- if powders contain several components to be mixed, incomplete mixing is sometimes observed

The potential advantages and disadvantages will be discussed in further detail, but the essential message of this study regarding this matter is that powders are generally problematic in e-beam based SFF of materials of real engineering interest.

Another approach which is under consideration as a potential method for e-beam SFF involves the melting of wire or other feedstock. The concept is most easily implemented for parts of cylindrical symmetry, although planar geometry parts are possible. This process has been demonstrated as a viable repair technique for turbine air seals [LaFLAMME (1994)] and other components. The essential features of the process are shown below :

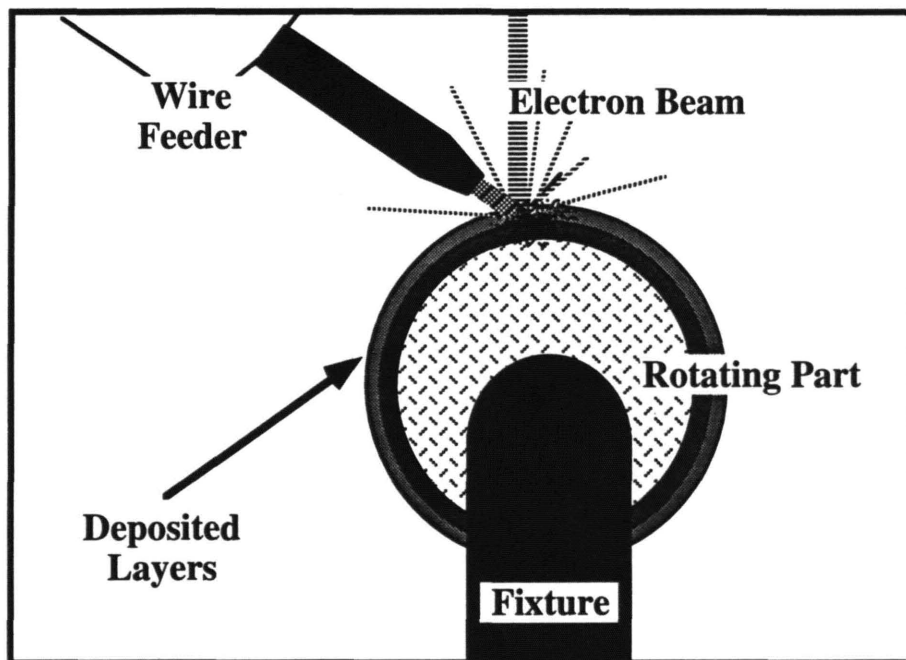


**FIGURE 1.3**  
**E-Beam SFF Using Wire Feedstock**

The wire feed technique is best-suited to parts of cylindrical geometry, and some initial trials demonstrating this method will be shown later in this chapter. The composition of the part being built-up can be varied by introducing different wire feedstocks, and a functionally-gradient material (FGM) component can be made in this way. The method of part buildup by wirefeed deposition is not new, and it has been successfully implemented by SAW (submerged arc welding) for the repair of turbomachinery [LaFAVE (1994)]. In this work, 308 stainless steel welding wire was deposited onto 304L base material. Thick deposits (greater than 1.25 cm on the radius ) were achieved without cracking problems.

## 1.4 Concise Overview of Thesis

<b>CHAPTER</b>	<b>DESCRIPTION</b>
2 - Part I	Presentation of thermal interaction model. This model describes heat effects due to moving volumetric heat sources (e-beams) and develops a framework for use in subsequent analysis.
2 - Part II	Application of thermal model. The model is used to calculate power requirements for melting, the maximum allowable power before vaporization becomes limiting, steady - state temperature profiles, and the change in these temperature profiles with increasing electron beam energy. The deposition of 308 Stainless is modeled.
3	EBSFF experiments on powders. The microstructures of EB melts in several material systems are shown. A new technique for the reaction synthesis of aluminide intermetallics is presented. A technique is demonstrated by which coatings may be melted onto steel with good adherence and microstructure.
4	EBSFF experiments using wirefeed. Experiments that deposited 308 weld wire onto 304L pipe are shown. The microstructure is analyzed. A discussion of thermal and residual stresses is presented. Residual stresses were measured using X-ray techniques.
5	HEEB materials processing applications. Several HEEB applications are shown : shock modification of weld HAZs, C/C composite brazing, and ceramic strengthening.
6	Conclusions and future work.
Appendix A	Physics background. This provides a brief introduction to the physics of electron - material interaction and the technology of electron beam accelerators.
Appendix B	Electron beam source term data. This section describes the approach used to model an electron beam as a volumetric heat source. Data for the magnitude and geometry of this source term is shown for a wide variety of materials of interest. Backscattering information is also presented.
Appendix C	Results of thermal calculations presented in Chapter 2 - Part II. This section contains the information generated by the thermal model.



**CHAPTER 2**  
**E-BEAM THERMAL**  
**INTERACTION MODEL**  
**PART I: PRESENTATION OF THEORY**

**2.1 Overview**

In this chapter, a simple analytical solution to the time-dependent heat conduction problem with the presence of volumetric heat sources ( low and high energy EBs) will be presented. The model utilizes a Green's Function approach. This technique has been widely used in previous studies [see for example TSAI (1983)]. For comparison, a solution for surface heat sources will be shown. This method of solution was selected since it represents the least complicated technique that takes into account three-dimensional heat conduction effects in the presence of a moving volumetric heat source. As such, it is the next logical step in a series of related models. ROSENTHAL (1946) and CHRISTENSEN et al. (1965) analyzed a moving point source. EAGAR and TSAI (1983) extended this treatment to the case of distributed surface heat sources. This present work develops the model for distributed *volumetric* sources. Although greater accuracy is possible through purely numerical techniques such as finite elements and finite differences. The analytical approach presented here is a good first step towards accurately capturing the relevant physical phenomena of e-beam - material thermal interactions.

**2.2 EB Irradiation**

We will start by considering the EB-irradiation of a semi-infinite solid with insulating conditions at the boundary. First a stationary beam will be considered. The geometry of the problem is illustrated below.

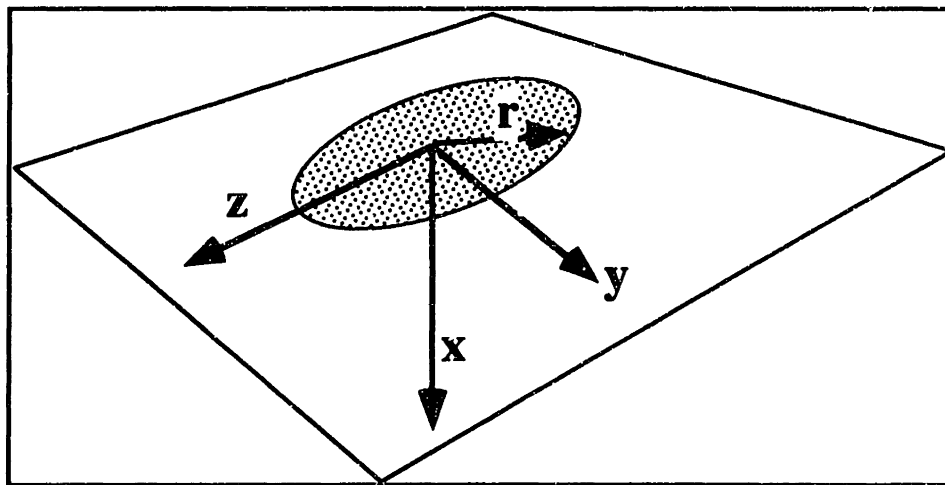


**FIGURE 2.1**  
**Coordinate System for Evaluation of Green's Functions**

The Green's function for this problem is given by [CARLSLAW & JAEGER (1959)] :

$$g = \frac{1}{8[\alpha\pi(t-t')]^{3/2}} \cdot \exp\left[\frac{-(y-y')^2 - (z-z')^2}{4\alpha(t-t')}\right] \cdot \left\{ \exp\left[\frac{-(x-x')^2}{4\alpha(t-t')}\right] + \exp\left[\frac{-(x+x')^2}{4\alpha(t-t')}\right] \right\} \quad (1)$$

This expression gives the temperature at point ( x, y, z, t ) due to a point source at ( x', y', z', t' ). X is the direction perpendicular to the free surface. For now, the temperature will only be monitored at points with coordinates ( x, 0, 0, t ).

In order to determine the temperature profile from the Green's function, the expression for the source distribution for the distributed volumetric heat source is used (see Appendix A for the derivation of this source term) :

$$\Theta(r', x') = A_0 \cdot \exp(-\lambda'^2) \text{ extending over } 0 \leq x' \leq \kappa R,$$

$$\text{where } \lambda' \equiv \frac{x'^2 + y'^2}{r_B^2}, \text{ R is the electron range,} \quad (2)$$

$r_B$  is the Gaussian Beam Radius,

$$A_0 = \frac{P_A}{\kappa\pi r_B^2 R}, \text{ and } \kappa \text{ is a constant that depends on source energy.}$$

Also, it is convenient to introduce the following additional dimensionless quantities:

$$\zeta \equiv x'/R, \quad \zeta' \equiv x'/R, \quad \gamma' \equiv y'/r_B, \quad \eta' \equiv z'/r_B, \text{ and } \mu \equiv t - t' \quad (3)$$

The expression for the temperature profile is then given by :

$$T = \iiint \int \frac{\Theta(\gamma', \eta', \zeta')}{\rho C} \cdot g \cdot dx' dy' dz' dt$$

$$= \int_0^t \int_0^\kappa \int_{-\infty}^{\infty} \int_{-\infty}^{\infty} \frac{\Theta(\gamma', \eta', \zeta')}{8\rho C [\alpha\pi\mu]^{3/2}} \cdot r_B^2 R \cdot \exp\left[\frac{-r_B^2(\gamma'^2 + \eta'^2)}{4\alpha\mu}\right] \cdot \left\{ \exp\left[\frac{-R^2(\zeta - \zeta')^2}{4\alpha\mu}\right] + \exp\left[\frac{-R^2(\zeta + \zeta')^2}{4\alpha\mu}\right] \right\} \cdot d\gamma' d\eta' d\zeta' d\mu \quad (4)$$

$$\text{where } \Theta(\gamma', \eta', \zeta') \equiv A_0 \cdot \exp[-\gamma'^2 - \eta'^2] \text{ for } 0 \leq \zeta' \leq \kappa$$

It is convenient to introduce several characteristic and dimensionless quantities :

$$\begin{aligned}
\tau &\equiv \frac{R^2}{4\alpha} = \text{characteristic time based on Range,} \\
\psi' &\equiv \frac{\mu}{\tau} = \text{dimensionless time} \left( \text{also } \psi \equiv \frac{t}{\tau} \right), \\
\phi &\equiv \frac{r_B}{R} = \text{beam aspect ratio.}
\end{aligned} \tag{5}$$

With these definitions, the temperature profile is :

$$\begin{aligned}
T &= \frac{P_A}{4\alpha\pi\rho\kappa CR} \int_0^\psi \int_0^\kappa \int_{-\infty}^\infty \int_{-\infty}^\infty \frac{1}{(\pi\psi')^{3/2}} \cdot \exp\left[-(\gamma'^2 + \eta'^2) \cdot \left(1 + \frac{\phi^2}{\psi'}\right)\right] \cdot \\
&\left\{ \exp\left[\frac{-(\zeta - \zeta')^2}{\psi'}\right] + \exp\left[\frac{-(\zeta + \zeta')^2}{\psi'}\right] \right\} \cdot d\gamma' d\eta' d\zeta' d\psi'
\end{aligned} \tag{6}$$

The larger integral can be separated into several smaller ones :

$$T = \frac{P_A}{4\alpha\pi\rho\kappa CR} \int_0^\psi \frac{Q_1 \cdot Q_2 \cdot Q_3}{(\pi\psi')^{3/2}} d\psi' \tag{7}$$

The values of the Qs are given below :

$$\begin{aligned}
Q_1 &= \int_{-\infty}^\infty \exp\left[-\gamma'^2 \left(1 + \frac{\phi^2}{\psi'}\right)\right] d\gamma' = \sqrt{\frac{\pi\psi'}{(\psi' + \phi^2)}} \\
Q_2 &= \int_{-\infty}^\infty \exp\left[-\eta'^2 \left(1 + \frac{\phi^2}{\psi'}\right)\right] d\eta' = \sqrt{\frac{\pi\psi'}{(\psi' + \phi^2)}} \\
Q_3 &= \int_0^\kappa \left\{ \exp\left[\frac{-(\zeta - \zeta')^2}{\psi'}\right] + \exp\left[\frac{-(\zeta + \zeta')^2}{\psi'}\right] \right\} d\psi' \\
&= \frac{\sqrt{\pi\psi'}}{2} \left\{ \operatorname{erf}\left[\frac{\kappa - \zeta}{\sqrt{\psi'}}\right] + \operatorname{erf}\left[\frac{\kappa + \zeta}{\sqrt{\psi'}}\right] \right\}
\end{aligned} \tag{8}$$

The final expression for the temperature profile results in an analytically intractable integral which is easily evaluated numerically :

$$T = \frac{P_A}{8\alpha\pi\rho\kappa CR} \int_0^\psi \frac{1}{\psi' + \phi^2} \left\{ \operatorname{erf}\left[\frac{\kappa - \zeta}{\sqrt{\psi'}}\right] + \operatorname{erf}\left[\frac{\kappa + \zeta}{\sqrt{\psi'}}\right] \right\} d\psi' \tag{9}$$

Moving beams will now be considered. Moving beams will in general produce lower temperature rises for a given beam power, or equivalently they will require more beam power to melt. There are several ways to analyze the moving beam problem. The equation of heat conduction in a moving coordinate system can be formulated and solved. This approach has been successfully applied to the problem of a moving distributed source under steady-state conditions [ TSAI (1983)]. The approach taken here is somewhat different. The temperature will be calculated in a coordinate system moving with the beam. This is equivalent to a stationary beam impinging on a medium which is flowing past it at some velocity  $V_0$ . It will be further assumed that the y-axis is parallel to the flow of the medium. The appropriate Green's Function in this case is :

$$g = \frac{1}{8[\alpha\pi(t-t')]^{3/2}} \cdot \exp\left\{\frac{-[y - V_0(t-t') - y']^2 - (z - z')^2}{4\alpha(t-t')}\right\} \cdot \left\{ \exp\left[\frac{-(x-x')^2}{4\alpha(t-t')}\right] + \exp\left[\frac{-(x+x')^2}{4\alpha(t-t')}\right] \right\} \quad (10)$$

Since we are interested in the temperature profile at the origin and points directly below it,  $y = z = 0$ . Rectangular coordinates will be used for this integration since they will result in an easier form for latter numerical evaluation. The Green's Function then becomes :

$$g = \frac{1}{8[\alpha\pi(t-t')]^{3/2}} \cdot \exp\left[\frac{-y'^2 - z'^2 - 2V_0(t-t')y' - V_0^2(t-t')^2}{4\alpha(t-t')}\right] \cdot \left\{ \exp\left[\frac{-(x-x')^2}{4\alpha(t-t')}\right] + \exp\left[\frac{-(x+x')^2}{4\alpha(t-t')}\right] \right\} \quad (11)$$

Non-dimensionalization can proceed as before, with the introduction of one additional dimensionless parameter :

Peclet Number  $Pe$

$$Pe \equiv \frac{2r_B V_0}{\alpha} \quad (12)$$

Although the Peclet Number usually refers to convection in fluids, the dimensionless group shown above will nevertheless be called the Peclet Number in this work. This parameter compares the convective heat transport due to the motion of the medium with the conductive transport in the medium. With the introduction of this and other dimensionless parameters, the Green's Function can be put into dimensionless form and integrated. The x-direction will be non-dimensionalized with respect to the range  $R$  as before. The y and z directions however will be non-dimensionalized with respect to the beam radius  $r_B$ . The resultant integral for evaluation of the temperature profile is :

$$T = \int_0^{\psi} \int_0^1 \int_{-\infty}^{\infty} \int_{-\infty}^{\infty} \frac{\Theta(\gamma', \eta', \zeta') \cdot r_B^2}{4\alpha\rho C(\pi\psi')^{3/2}} \exp\left[\frac{-\phi^2(\gamma'^2 + \eta'^2)}{\psi'} - \frac{Pe}{4}\gamma' - \left(\frac{Pe}{4}\right)^2 \frac{\psi'}{(2\phi)^2}\right] \cdot \left\{ \exp\left[\frac{-(\zeta - \zeta')^2}{\psi'}\right] + \exp\left[\frac{-(\zeta + \zeta')^2}{\psi'}\right] \right\} \cdot d\gamma' d\eta' d\zeta' d\psi' \quad (13)$$

$$\gamma' \equiv \frac{y'}{r_B} \quad \text{and} \quad \eta' \equiv \frac{z'}{r_B}$$

with other dimensionless quantities defined as before.

It is seen that the source term will be identical to that for the stationary beam, since the medium is considered as moving. In rectangular (dimensionless) coordinates, it is given by :

$$\Theta(\gamma', \eta', \zeta') = A_0 \cdot \exp[-\gamma'^2 - \eta'^2] \quad \text{for } 0 \leq \zeta' \leq \kappa \quad (14)$$

With the full form of the source function, the integral becomes :

$$T = \frac{P_A}{2\alpha\kappa\rho CR} \int_0^{\psi} \frac{Q_1 \cdot Q_2 \cdot Q_3}{2\pi(\pi\psi')^{3/2}} \cdot \exp\left[-\left(\frac{Pe}{4}\right)^2 \frac{\psi'}{(2\phi)^2}\right] \cdot d\psi' \quad (15)$$

The Q's are given by :

$$\begin{aligned} Q_1 &= \int_{-\infty}^{\infty} \exp\left[-\eta'^2 \left(1 + \frac{\phi^2}{\psi'}\right)\right] \cdot d\eta' \\ Q_2 &= \int_0^{\kappa} \left\{ \exp\left[\frac{-(\zeta - \zeta')^2}{\psi'}\right] + \exp\left[\frac{-(\zeta + \zeta')^2}{\psi'}\right] \right\} \cdot d\zeta' \\ Q_3 &= \int_{-\infty}^{\infty} \exp\left[-\gamma' \left(\frac{Pe}{4}\right) - \gamma'^2 \left(1 + \frac{\phi^2}{\psi'}\right)\right] \cdot d\gamma' \end{aligned} \quad (16)$$

These integrals may be readily evaluated :

$$\begin{aligned} Q_1 &= \sqrt{\frac{\pi\psi'}{(\psi' + \phi^2)}} \\ Q_2 &= \frac{\sqrt{\pi\psi'}}{2} \left\{ \operatorname{erf}\left[\frac{\kappa - \zeta}{\sqrt{\psi'}}\right] + \operatorname{erf}\left[\frac{\kappa + \zeta}{\sqrt{\psi'}}\right] \right\} \\ Q_3 &= \sqrt{\frac{\pi\psi'}{\psi' + \phi^2}} \cdot \exp\left[\left(\frac{Pe}{8}\right)^2 \frac{\psi'}{\psi' + \phi^2}\right] \end{aligned} \quad (17)$$

The Peclet Number is a convenient dimensionless quantity to use in the above equation, but it is not necessarily the most physically meaningful one. The beam interaction time may be defined as the time that the beam interacts with any given region of the target. This time is defined as :

$$t_i \equiv \frac{2r_B}{V_0} \quad (18)$$

This quantity may be related to the Peclet Number as follows :

$$\frac{Pe}{4} = \frac{\tau}{t_i} (2\phi)^2$$

$\tau$  is the characteristic  
heat conduction time

(19)

It is readily seen that when the Peclet number goes to zero, the integral expressions for the temperature profile reduce to that for the stationary beam.

### 2.3 Surface Heat Sources

The source distribution function for surface heat sources is :

$$\Theta(\lambda) = A_0 \exp(-\lambda^2)$$

$$\lambda \equiv r/r_B \text{ as before.}$$
(20)

Applying the normalization criterion (energy balance), we get :

$$\int_0^{2\pi} \int_0^{\infty} A_0 r_B^2 \cdot \exp[-\lambda^2] \lambda d\lambda d\vartheta = P_A, \text{ or}$$

$$A_0 = \frac{P_A}{\pi r_B^2}$$
(21)

If the temperature is evaluated along the line (x, 0, 0, t), The appropriate Green's function for stationary beams is :

$$g = \frac{1}{4[\alpha\pi(t-t')]^{3/2}} \cdot \exp\left[\frac{-y'^2 - z'^2}{4\alpha(t-t')}\right] \cdot \exp\left[\frac{-x^2}{4\alpha(t-t')}\right]$$
(22)

Now the following dimensionless quantities are introduced :

$$\tau \equiv \frac{r_B^2}{4\alpha}$$

$$\mu \equiv t - t', \quad \psi \equiv \frac{\mu}{\tau}, \quad \psi' \equiv \frac{\mu'}{\tau},$$

$$\zeta \equiv \frac{x}{r_B}, \quad \gamma' \equiv \frac{y'}{r_B}, \quad \eta' \equiv \frac{z'}{r_B}$$
(23)

The temperature profile is then given by :

$$T = \iiint g \cdot \frac{\Theta(\gamma', \eta')}{\rho C} \cdot d\gamma' d\eta' d\psi'$$

$$= \frac{P_A}{2\alpha\rho\pi r_B C} \int_0^\psi \int_{-\infty}^{\infty} \int_{-\infty}^{\infty} \frac{d\gamma' d\eta' d\psi'}{(\pi\psi')^{3/2}} \cdot \exp\left[\frac{-\zeta^2}{\psi'}\right] \cdot \exp\left[-(\gamma'^2 + \eta'^2) \cdot \left(1 + \frac{1}{\psi'}\right)\right]$$
(24)

As in the case of HEEB irradiation, the above expression can be considerably simplified :

$$T = \frac{P_A}{2\alpha\rho\pi r_B C} \int_0^\psi \frac{Q_1 \cdot Q_2}{(\pi\psi')^{3/2}} \cdot \exp\left[\frac{-\zeta^2}{\psi'}\right] d\psi'$$
(25)

$Q_1$  and  $Q_2$  are given by :

$$Q_1 \cdot Q_2 = \int_{-\infty}^{\infty} \exp\left[-(\gamma'^2 + \eta'^2) \cdot \left(1 + \frac{1}{\psi'}\right)\right] d\psi'$$

$$= \sqrt{\frac{\pi\psi'}{1+\psi'}} \cdot \sqrt{\frac{\pi\psi'}{1+\psi'}} = \frac{\pi\psi'}{1+\psi'}$$
(26)

The final expression for the temperature profile becomes an integral that must be numerically evaluated :

$$T = \frac{P_A}{2\alpha\rho\pi r_B C} \int_0^\psi \frac{1}{(\pi\psi')^{3/2}} \cdot \exp\left[\frac{-\zeta^2}{\psi'}\right] \cdot \frac{\pi\psi'}{1+\psi'} d\psi'$$

$$= \frac{P_A}{2\alpha\rho\pi r_B C} \int_0^\psi \frac{1}{\sqrt{\pi\psi'}} \cdot \frac{1}{1+\psi'} \cdot \exp\left[\frac{-\zeta^2}{\psi'}\right] d\psi'$$
(27)

As in the case of HEEBs, moving sources can also be included in the calculations. For a moving surface source, the temperature profile becomes :

$$T = \frac{P_A}{\alpha \rho C r_B} \int_0^{\psi} \int_{-\infty}^{\infty} \int_{-\infty}^{\infty} \frac{1}{2\pi(\pi\psi')^{3/2}} \cdot \exp[-(\gamma'^2 + \eta'^2)] \cdot \exp\left[\frac{-(\gamma'^2 + \eta'^2)}{\psi'} - \frac{Pe}{4} \gamma' - \left(\frac{Pe}{4}\right)^2 \frac{\psi'}{4}\right] \cdot \exp\left[\frac{-\zeta^2}{\psi'}\right] \cdot d\gamma' d\eta' d\psi' \quad (28)$$

All characteristic and dimensionless quantities are defined with respect to the beam radius,  $r_B$ .

As before, this expression can be reduced to an integral over time only. Carrying out the integration over all space variables, we get :

$$T = \frac{P_A}{\alpha \kappa \rho C r_B} \int_0^{\psi} \frac{Q_1 \cdot Q_2}{2\pi(\pi\psi')^{3/2}} \cdot \exp\left[\frac{-\zeta^2}{\psi'}\right] \cdot \exp\left[-\left(\frac{Pe}{4}\right)^2 \frac{\psi'}{4}\right] \cdot d\psi'$$

$$Q_1 = \int_{-\infty}^{\infty} \exp\left[-\eta'^2 \left(1 + \frac{1}{\psi'}\right)\right] \cdot d\eta'$$

$$= \sqrt{\frac{\pi\psi'}{(\psi' + 1)}}$$

$$Q_2 = \int_{-\infty}^{\infty} \exp\left[-\gamma' \left(\frac{Pe}{4}\right) - \gamma'^2 \left(1 + \frac{1}{\psi'}\right)\right] \cdot d\gamma' \quad (29)$$

$$= \sqrt{\frac{\pi\psi'}{\psi' + 1}} \cdot \exp\left[\left(\frac{Pe}{8}\right)^2 \frac{\psi'}{\psi' + 1}\right]$$

The Peclet number can again be easily related to the beam interaction time and the characteristic heat conduction time by the relation :

$$\frac{Pe}{4} = \frac{4\tau}{t_i} \quad (30)$$

## 2.4 Incorporating the Effect of Backscatter

The previous set of calculations do not take into account the effect of backscatter. The power  $P_A$  is the power *absorbed* by the workpiece. This will now be related to the actual beam power by considering the backscattering coefficients. A detailed discussion of the backscattering coefficient is given in Appendix A. Actual values for different materials are given in Appendix B. It is important to reiterate these backscattering coefficients DO NOT necessarily apply to "keyhole" melt profiles. As discussed in Appendix A, the backscattering



coefficient is a very strong function of target material and incident electron energy, and will also depend on surface geometry / surface roughness.

The relationship between beam power and absorbed power is straightforward :

backscattering correction factor :

$$S_{BACK} = \frac{P_{BEAM}}{P_A} = \frac{1}{(1 - \eta_{TOT})} \quad (31)$$

$\eta_{TOT}$  is the overall backscattering coefficient

The effect of backscattering may also be defined in terms of the beam absorption coefficient, or absorbtivity. This number will simply be the ratio of absorbed power to incident beam power. This is given by :

$$\epsilon_B \equiv \frac{P_A}{P_B} = 1 - \eta_{TOT} \quad (32)$$

## 2.5 Corrections for Thermal Radiation and Convection

So far, the Green's Function approach presented here has assumed insulating boundary conditions at the surface of the semi-infinite solid. Green's Functions cannot take into account non-linearities such as thermal (blackbody) radiation or the temperature - dependence of material properties. To take into account thermal radiation, an approximate technique will be used. It will be assumed that the entire surface region directly affected by the beam is at the melting temperature. In this case, the additional power that must be supplied is simply :

$$\Delta P_{RAD} = \pi r_B^2 e \sigma_B T_M^4 \quad \text{where} \quad (33)$$

$e$  is the emissivity of the surface ,  
 $\sigma_B$  is the Stefan - Boltzmann Constant, and  
 $T_M$  is the melting temperature of the target material

The absorbed power  $P_A$  is now interpreted as the power available to heat and melt the material, and the net power which must be absorbed will be higher to compensate for the radiation losses :

$$P_A = P_{NET} - \Delta P_{RAD}, \text{ so the radiation correction factor is :} \quad (34)$$

$$S_{RAD} = \frac{P_{NET}}{P_A} = 1 + \frac{\Delta P_{RAD}}{P_A}$$

The correction for convection is more complicated. It will not be considered in detail here, since most of the materials processing operations

discussed in this thesis are performed in vacuum. The consideration of convection effects requires a modified Green's function. This is given by [CARLSLAW & JAEGER (1959)] :

$$\begin{aligned}
 g &= g_1 - g_2 \\
 g_1 &= \frac{1}{8[\pi\alpha(t-t')]^{3/2}} \exp\left\{-\frac{(y-y')^2 + (z-z')^2}{4\alpha(t-t')}\right\} \\
 &\quad \left\{ \exp\left[\frac{-(x-x')^2}{4\alpha(t-t')}\right] + \exp\left[\frac{-(x+x')^2}{4\alpha(t-t')}\right] \right\} \\
 g_2 &= \frac{h}{4\pi\alpha(t-t')} \operatorname{erfc}\left[\frac{x+x'}{2\sqrt{\alpha(t-t')}} + h\sqrt{\alpha(t-t')}\right] \\
 &\quad \exp\left\{h(x+x') + \alpha h^2(t-t') - \frac{(y-y')^2 + (z-z')^2}{4\alpha(t-t')}\right\} \\
 \text{where } h &\equiv \frac{H}{K}, \\
 H &\text{ is the surface heat transfer coeff., } \frac{W}{m^2-\circ C} \\
 K &\text{ is the thermal conductivity, } \frac{W}{m-\circ C}
 \end{aligned} \tag{35}$$

It will be recognized that the first part of the expression above is the Green's Function for the case of insulating boundary conditions. The second portion represents the decrease in temperature due to surface convective cooling. Thus the resulting temperature profile would be the profile with insulating conditions minus the correction term. This calculation can be done, but it is not relevant to the majority of the work done in this thesis, and will therefore not be pursued further.

## 2.6 Extension of Model - Preliminary Consideration of Melt Depth

The model as presented thus far is valid only up to the point of melting. It can be used to effectively delineate the regions of material heating and melting. An extension of the model would consider the two-phase problem of solid and liquid and the geometry of the boundary between these two regions. This calculation is not possible through the use of Green's Functions, and purely numerical means must be employed [see for example OREPER, EAGAR, and SZEKELY (1983) and CHAN (1985)]. To accurately capture the geometry of the liquid-solid interface, a detailed consideration of convection effects is very

important. Use of three-dimensional finite difference or finite element codes is necessary to solve these non-linear problems with moving boundaries. Such a calculation will not be presented in this current work.

Although liquid pool convection effects are very important, it may nevertheless be useful as a very crude estimate to ignore them. Furthermore, if the difference in materials properties between liquid and solid is ignored, the model presented above can be extended to the case of a two-phase mix of liquid and solid. The main quantity of interest is the melt depth as a function of scan rate and electron beam energy. Although the severe assumptions will no doubt affect the values thus calculated, the relative magnitudes should be the same. The following calculations will therefore capture the general trends but will not have numerical accuracy.

The approach taken here will follow the technique adopted by ION, SHERCLIFF and ASHBY (1992). It is assumed that :

- no "keyhole" processes occur,
- same material properties will be used for liquid and solid,
- conduction effects dominate, and convection is ignored.

The net power absorbed by the target is now related to the beam power by the expression :

$$P_{NET} = (1 - \eta_B)P_{BEAM} - 2r_B D_M V_O \rho L_M, \text{ where}$$

$D_M$  is the melt depth, cm,

$V_O$  is the scan rate, cm / sec,

$\rho$  is the material density, g / cu.cm,

$r_B$  is the beam radius, and

$L_M$  is the latent heat of fusion, J / g

Once  $D_M$  is known, then the beam power that must (36)

be supplied under these conditions is given by :

$$P_{BEAM} = \frac{P_{NET} + 2r_B D_M V_O \rho L_M}{(1 - \eta_B)}$$

The solution of this problem now depends on the value of the melt depth. According to the assumptions made above, this value may be simply obtained from the thermal models presented earlier. The value of the net absorbed power is simply increased beyond that necessary for melt. Then, the temperature profile is calculated at the surface and below the surface. The point at which the temperature drops below the melting point will define the melt depth. This can then be related to the necessary incident beam power by the energy balance of Equation 36. Corrections for thermal radiation will be ignored for the moment. This model can be still further extended to consider what happens when feedstock is introduced into the melt pool, as would be the case in a deposition process. It

will be assumed that the feedstock material is the same as the material on which the deposit is forming. Also, the wire will be assumed to have circular cross-section with radius  $r_w$  and linear feed rate  $f_w$ . The revised version of Equation 36 is :

$$P_{NET} = (1 - \eta_{TOT})P_{BEAM} - 2r_B D_M V_O \rho L_M - \rho \pi r_w^2 f_w \cdot \{C_P T_M + L_M\}$$

$$P_{BEAM} = \frac{P_{NET} + 2r_B D_M V_O \rho L_M + \rho \pi r_w^2 f_w \cdot \{C_P T_M + L_M\}}{(1 - \eta_{TOT})} \quad (37)$$

$T_M$  is the melting point of the material,

$C_P$  is the specific heat,

$r_w$  is the wire radius, and

$f_w$  is the linear wire feed rate (cm / sec).

The extension of the model is valid only up to the point at which vaporization begins. Melt depths calculated for different beam energies and different values of net absorbed power are more readily compared when plotted against a dimensionless power number. This number will be defined as the ratio of the net absorbed power to the power needed to just initiate surface melt. This ratio is therefore the factor by which the net absorbed power exceeds the power needed to melt. Since the beam powers needed to melt for different energies are very widely scattered, this non-dimensional power ratio offers a better means of comparing the melt depths at different beam energies. Thermal radiation losses could easily be added to the numerator of Equation 37 as an additional correction term.

## 2.7 Applicability of Model to Slabs of Finite Thickness

The model presented above assumes a semi-infinite solid as the target material. This assumption will also hold for slabs of finite thickness provided that the characteristic heat conduction length is smaller than the slab thickness. The next problem is the selection of a suitable characteristic heat conduction length. Clearly the slab must be thicker than the electron range. A depth corresponding to the electron range represents the deepest volumetric heat source embedded in the target. Heat emitted from this location must not encounter a boundary within the characteristic time of interaction if the model assumptions are to hold. It is also intuitively clear that the characteristic time must incorporate the effect of heat source intensity. The transient solutions themselves can be used to find out how long it takes to reach a certain surface temperature given a certain heat flux for a given beam radius. This time can be used as a characteristic time for the problem. The corresponding characteristic heat conduction length will determine how far heat can travel during that time. When added to the electron range, this number can be used as a characteristic thickness above which the slab may be considered as semi-infinite.

This criterion may now be derived for moving / scanning EBs. The solution of the transient heat conduction problem was given by Equations 15-17, which have been consolidated into the expression shown below :

$$T = \frac{P_A}{4\pi\alpha\kappa\rho CR} \int_0^\psi \frac{\text{erf}\left[\frac{\kappa}{\sqrt{\psi'}}\right]}{(\psi' + \phi^2)} \cdot \exp\left\{\psi' \left(\frac{Pe}{8}\right)^2 \left[\frac{1}{\psi' + \phi^2} - \frac{1}{\phi^2}\right]\right\} \cdot d\psi' \quad (38)$$

The integral is a function of time and scanning velocity, and this may be schematically indicated by :

$$T(t; V_o) = \frac{P_A}{4\pi\alpha\kappa\rho CR} \cdot F\left(\frac{t}{\tau}; Pe\right) \quad (39)$$

The minimum slab thickness may now be estimated. Finite slabs that are thicker than the minimum allowable slab thickness may be treated by using the semi-infinite solid approximation.

$t^*$  is the characteristic time

$$\text{at } t = t^*, T(t^*; V_o) = \frac{P_A}{4\pi\alpha\kappa\rho CR} \cdot F\left(\frac{t^*}{\tau}; Pe\right)$$

heat conduction length corresponding to  $t^*$ :

(40)

$$\Delta x = 2\sqrt{\alpha t^*}$$

define minimum thickness as :

$$\delta_{\text{MIN}} = R + 2\sqrt{\alpha t^*}$$

## 2.8 Extension of Model to Thin Slabs

For slabs thinner than the minimum thickness shown above, a different approach must be adopted. First, we will consider the case of very thin slabs. Such a case would result if the slab thickness were significantly thinner than the characteristic thickness (slab thickness is on the order of the electron range itself). There are several ways to approach this problem. For the case of stationary beams, THOMAS (1957) has derived an expression which examines heat conduction in a thin sheet with a surface flux of  $Q$ . The terminology in this solution is shown in the figure below.

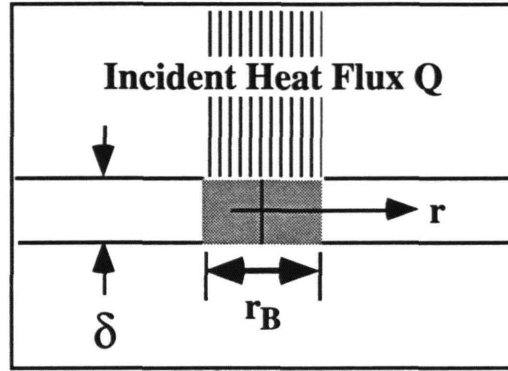


**FIGURE 2.2**  
**Terminology for Thin Slab Solution**

The transient solution at  $r = 0$  is [THOMAS (1957)]:

$$\begin{aligned} T &= \frac{Qt}{\rho C \delta} \left( 1 - \exp[-X^2] + X^2 \cdot \int_{X^2}^{\infty} \frac{e^{-U}}{U} dU \right) \\ &= \frac{Qt}{\rho C \delta} \left( 1 - \exp[-X^2] + X^2 \cdot E_1(X^2) \right) \end{aligned} \quad (41)$$

$$X = \frac{r_B}{2\sqrt{\alpha t}} \quad \text{and } E_1(x) \text{ is the exponential integral of order 1}$$

For moving beams, it is possible to derive a solution based on 2D Green's functions. The same notation will be used as for stationary beams. The 2D Green's function for an infinite sheet is given by [CARLSLAW & JAEGER (1959)]:

$$g = \frac{1}{4\alpha\pi(t-t')} \exp\left[ \frac{-(z-z')^2 - [y - V_o(t-t') - y']^2}{4\alpha(t-t')} \right] \quad (42)$$

The surface source function is the same as in the case of the semi-infinite solid :

$$\Theta(z', y') = A_o \exp\left[ \frac{-z'^2 - y'^2}{R_o^2} \right] \quad (43)$$

$$A_o = \frac{P_A}{\pi R_o^2 \delta}, \quad R_o \text{ is the Gaussian Radius}$$

The temperature profile at the center is given by :

$$T = \int_0^t \int_{-\infty}^{\infty} \int_{-\infty}^{\infty} \frac{\Theta}{4\alpha\rho C\pi\mu} \exp\left[ \frac{-z'^2 - y'^2 - 2V_o\mu y' - V_o^2\mu^2}{4\alpha\mu} \right] dz' dy' d\mu \quad (44)$$

As before, it is convenient to introduce the following dimensionless quantities :

$$Pe \equiv \frac{2R_o V_o}{\alpha}, \quad \eta' \equiv \frac{z'}{R_o}, \quad \gamma' \equiv \frac{y'}{R_o}, \quad \psi' \equiv \frac{\mu}{(R_o^2/4\alpha)} \quad (45)$$

The temperature at the center then becomes :

$$T = \frac{P_A}{4\alpha\rho C\delta\pi^2} \int_0^{\psi'} \frac{Q_1 \cdot Q_2}{\psi'} \exp\left[-\left(\frac{Pe}{8}\right)^2 \psi'\right] d\psi' \quad (46)$$

Where the Qs are defined by :

$$\begin{aligned} Q_1 &= \int_{-\infty}^{\infty} \exp\left[-\eta'^2 \left(1 + \frac{1}{\psi'}\right)\right] d\eta' = \sqrt{\frac{\pi\psi'}{1+\psi'}} \\ Q_2 &= \int_{-\infty}^{\infty} \exp\left[-\gamma'^2 \left(\frac{Pe}{4}\right) - \gamma'^2 \left(1 + \frac{1}{\psi'}\right)\right] d\gamma' \\ &= \sqrt{\frac{\pi\psi'}{1+\psi'}} \exp\left[\left(\frac{Pe}{8}\right)^2 \frac{\psi'}{1+\psi'}\right] \end{aligned} \quad (47)$$

Upon simplification, we get :

$$T = \frac{P_A}{4\pi\alpha\rho C\delta} \int_0^{\psi'} \frac{1}{1+\psi'} \exp\left[-\left(\frac{Pe}{8}\right)^2 \frac{\psi'^2}{1+\psi'}\right] d\psi' \quad (48)$$

For slabs which are thinner than the minimum slab thickness, but are significantly thicker than the range, the 2D analysis is not valid. This case involves thin slabs in which the 3D conduction effects must explicitly be taken into account. Using the Green's function approach for this case is more difficult on account of the presence of an infinite series in the Green's function expression itself. The appropriate Green's function for the temperature along the centerline of region irradiated by the beam is [CARLSLAW & JAEGER (1959)] :

$$\begin{aligned} g &= \frac{1}{4\pi\alpha\delta(t-t')} \exp\left[\frac{-z'^2 - y'^2 - 2y'V_o\mu - V_o^2(t-t')^2}{4\alpha\mu}\right] \\ &\left\{ 1 + 2 \sum_{n=1}^{\infty} \exp\left[\frac{-\alpha n^2 \pi^2 (t-t')}{\delta^2}\right] \cdot \cos\left(\frac{n\pi x}{\delta}\right) \cdot \cos\left(\frac{n\pi x'}{\delta}\right) \right\} \end{aligned} \quad (49)$$

The formal solution for the temperature at the surface and in the center of the beam will now be in the form of an infinite series. The dimensionless quantities will be the same as those used for the moving beam problem in the semi-infinite

solid case. The resulting temperature on the surface and at the center of the beam is :

$$\begin{aligned}
 T &= \frac{P_A}{4\pi\alpha\rho C\kappa\delta} \int_0^\psi \frac{Q_1 \cdot Q_2 \cdot Q_3}{\pi\psi'} \exp\left[-\left(\frac{Pe}{8}\right)^2 \frac{\psi'}{\phi^2}\right] d\psi' \\
 Q_1 &= \sqrt{\frac{\pi\psi'}{\psi' + \phi^2}} \\
 Q_2 &= \sqrt{\frac{\pi\psi'}{\psi' + \phi^2}} \exp\left[\left(\frac{Pe}{8}\right)^2 \frac{\psi'}{\psi' + \phi^2}\right] \\
 Q_3 &= \kappa + 2 \sum_{n=1}^{\infty} \exp\left[-(n\pi\beta)^2 \psi'\right] \cdot \frac{\sin(n\pi\beta\kappa)}{n\pi\beta} \quad \text{where } \beta \equiv \frac{R}{\delta}
 \end{aligned} \tag{50}$$

If the thickness is significantly larger than the range, then  $\beta$  will be small, and the series will not converge quickly. If this is the case, we may approximate the heat source as a purely surface heat source impinging on a finite slab. In practice, it will be useful to use this approximation. If the range is a significant fraction of the slab thickness, then the purely 2D approach will be more suitable. These additional approximations eliminate the case in which both volumetric penetration and 3D finite conduction effects are taken into account. For a surface source, the equation corresponding to Equation 50 is :

$$\begin{aligned}
 T &= \frac{P_A}{4\pi\alpha\rho C\delta} \int_0^\psi \frac{Q_1 \cdot Q_2 \cdot Q_3}{\pi\psi'} \exp\left[-\left(\frac{Pe}{8}\right)^2 \psi'\right] d\psi' \\
 Q_1 &= \sqrt{\frac{\pi\psi'}{\psi' + 1}} \\
 Q_2 &= \sqrt{\frac{\pi\psi'}{\psi' + 1}} \exp\left[\left(\frac{Pe}{8}\right)^2 \frac{\psi'}{\psi' + 1}\right] \\
 Q_3 &= 1 + 2 \sum_{n=1}^{\infty} \exp\left[-(n\pi\beta)^2 \psi'\right] \quad \text{where now } \beta \equiv \frac{r_B}{\delta}
 \end{aligned} \tag{51}$$

For most cases of interest,  $\beta$  will now be reasonably large, insuring quicker convergence of the series. It is now possible to specify a convergence criterion. We want a criterion that insures rapid convergence at large times without undue loss of accuracy for small times. Suppose we were to select  $n$  such that the following holds :



Select maximum value of  $n$  based on  $\psi' \approx 1$

Suppose criterion is that  $\exp\left[-(n_{MAX}\pi\beta)^2\right] = 0.01$ , (52)

Then  $n_{MAX} = \text{int}\left[\sqrt{4.605}/(\pi\beta)\right]$

$\text{int}(x)$  is the greatest integer function

This choice of the maximum  $n$  strikes a balance between fast convergence and reasonable accuracy.

## 2.9 Summary of Model Framework

The formal presentation of the mathematical framework of the beam thermal interaction model is now complete. The model presented covers the following cases :

- EB irradiation impinging on a semi-infinite solid : stationary and scanning beams,
- Surface sources impinging on a semi-infinite solid : stationary and scanning beams,
- Correction factors for backscattering and thermal radiation,
- Extension of model to include a preliminary consideration of melt depth and material deposition,
- Quantitative determination of the minimum slab thickness for the semi-infinite assumption to hold,
- Extension of model to slabs of finite thickness with consideration of both 2D and 3D conduction effects

The model will now be applied to a wide range of numerical cases that will illustrate its application to practical materials processing issues. Although the model does not incorporate such non-linearities as temperature-dependent thermal properties and a correct treatment of thermal radiation, it does offer sufficient insight into some of the thermal effects of high and low energy EBs and how these compare to surface heat sources. Part II of this chapter will explore in depth the various implications and predictions of this model. This will generate practical information that may be used to design a specific materials processing operation.

**TABLE 2.1**  
**List of Symbols used in Chapter 2 - Part I**

<b>SYMBOL</b>	<b>DEFINITION</b>
$\alpha$	thermal diffusivity, cm <sup>2</sup> /sec
$\beta$	dimensionless distance for finite slab soln., 3D conduction
C	specific heat, J / g - °C
$\delta$	slab thickness, cm
D <sub>M</sub>	melt depth, cm
$\delta_{MIN}$	minimum slab thickness for semi-infinite assumption to hold, cm
$\phi$	beam aspect ratio (dimensionless)
f <sub>w</sub>	rate of feed of wire feedstock, cm / sec
$\gamma, \gamma'$	dimensionless y coordinates
$\eta, \eta'$	dimensionless z coordinates
$\eta_{TOT}$	overall backscattering coefficient
$\kappa$	electron energy - dependent parameter in source term
L <sub>M</sub>	latent heat of fusion, J / g
P <sub>A</sub>	power absorbed by workpiece
P <sub>B</sub>	incident beam power
Pe	Peclet number
$\Theta(\psi', \eta', \zeta')$	distributed volumetric source term, W / cm <sup>3</sup>
R	electron range, cm
$\rho$	density, g / cm <sup>3</sup>
r <sub>B</sub>	Gaussian beam radius, cm
r <sub>w</sub>	radius of wire feedstock, cm
T	temperature, °C
$\tau$	characteristic heat conduction time, sec.
t <sub>i</sub>	characteristic beam interaction time, sec.
V <sub>O</sub>	beam travel velocity, cm / sec.
$\psi'$	dimensionless time coordinate
$\zeta, \zeta'$	dimensionless x coordinates

## **CHAPTER 2**

### **E-BEAM THERMAL INTERACTION MODEL**

#### **PART II : APPLICATIONS**

### **2.10 Overview**

This section is concerned with the practical application of the thermal interaction model presented in Part 1. Several numerical calculations will be carried out to illustrate how the model can be used to predict important features of materials processing applications. The first set of calculations will determine the power needed to initiate surface melt in a given material as a function of beam energy, beam radius, and travel velocity. Assuming that fluid convection effects are negligible, the power needed to raise the surface to the vaporization temperature (partial vapor pressure equals 1 atm.) will then be calculated. The range of valid power levels possible for processing must lie between the melt power and the vaporization power. These two "power envelopes" effectively define the processing space available for melting and deposition.

The melt depth model described in Part I of this chapter will then be used to find the power requirements for maintaining a melt pool at the maximum allowable power level, i.e. the vaporization power. The assumptions of the melt depth model are very limiting, but they will allow for useful comparative calculations. Finally, the effect of material deposition will be considered, as is the case for any e-beam SFF process. Wirefeeding will be looked at in particular, and the power requirements to melt and deposit material at a given rate will be calculated. The net power available for deposition will be calculated. This in turn can be used to determine the maximum deposition rate as a function of beam parameters. Of particular interest is the variation of maximum deposition rate with beam energy and the deposition efficiency. The deposition efficiency will be defined as the deposition rate achievable for a given total beam power input into the target. In this sense, it also measures the specific energy requirements of the e-beam deposition process. These performance characteristics will be compared to other processes, such as GMAW, FCAW, and SAW. For the EB process, power losses due to vaporization in vacuum processing will also be estimated.

Another set of calculations will compare the steady-state temperature profiles in different materials as a function of beam kinetic energy given that the beam radius and overall power absorbed by the sample remain fixed. These calculations will illustrate the fact that higher energy beams will produce lower surface temperatures and less sharp temperature gradients for the same absorbed power level. This can be important in applications in which evaporation of volatile constituents is a major concern. In a related set of calculations, the temperature profile will be shown below the surface when the surface is at the melting point. The effect of volumetric heating will at higher beam energies will allow deeper penetration of the thermal profile.

## 2.11 Power Requirements for Melting

The model will be applied to five materials : aluminum, copper, iron, titanium, and 304 stainless steel. Heat source data for these and other materials is tabulated in Appendix B. This section will assume the validity of the semi-infinite model. Numerical calculations for thin slabs will not be presented here, but they can be derived by using the equations developed in Part I of this chapter. The basis for these calculations is the Green's function solution for the temperature profile due to a moving EB source. The case of a stationary source is simply a degenerate case of the moving source solution. This solution was derived in Part I :

$$T = \frac{P_A}{8\pi\alpha\rho C\kappa R} \int_0^{\psi} \frac{1}{\psi' + \phi^2} \left\{ \operatorname{erf} \left[ \frac{\kappa - \zeta}{\sqrt{\psi'}} \right] + \operatorname{erf} \left[ \frac{\kappa + \zeta}{\sqrt{\psi'}} \right] \right\} \cdot \exp \left[ -\psi' \left( \frac{Pe}{8} \right)^2 \cdot \left( \frac{1}{\phi^2} - \frac{1}{\psi' + \phi^2} \right) \right] d\psi' \quad (53)$$

This equation gives the complete time-dependent solution of the problem. Increasing values of  $\zeta$ , the dimensionless depth, will give the temperature beneath the surface. For the purposes of generating a processing space, the surface temperature will be considered, so  $\zeta=0$ . This means that the temperature at the origin of the coordinate system shown in Figure 2.1 will be calculated. Furthermore, the *steady-state* solution will be considered. This power will be the power the must be *absorbed* by the material, NOT the beam power. The backscattering correction factor can be added to facilitate conversion from absorbed power to beam output power. Under these assumptions, Equation 53 becomes :

$$T_{MELT} = \frac{P_{MELT}}{4\alpha\pi\rho\kappa CR} \cdot I_{1\infty} \quad \text{where}$$

$$I_{1\infty} = \lim_{\psi \rightarrow \infty} \int_0^{\psi} \frac{1}{\psi' + \phi^2} \cdot \operatorname{erf} \left[ \frac{\kappa}{\sqrt{\psi'}} \right] \cdot \exp \left[ -\psi' \left( \frac{Pe}{8} \right)^2 \cdot \left( \frac{1}{\phi^2} - \frac{1}{\psi' + \phi^2} \right) \right] d\psi' \quad (54)$$

The limiting case for moving surface sources can be derived from Equation 29 :

$$T_{MELT} = \frac{P_{MELT}}{2\alpha\pi\rho C r_B} \cdot I_{2\infty} \quad \text{where}$$

$$I_{2\infty} = \lim_{\psi \rightarrow \infty} \int_0^{\psi} \frac{1}{\sqrt{\pi\psi'}} \cdot \frac{1}{1 + \psi'} \cdot \exp \left[ -\psi' \left( \frac{Pe}{8} \right)^2 \cdot \left( 1 - \frac{1}{1 + \psi'} \right) \right] d\psi' \quad (55)$$

The results of these calculations are shown in the tables of Appendix C. Also in this Appendix are the assumed thermal properties for the various materials.

The determination of the vaporization power is done using the same Equations 54 and 55 with the exception that  $T_{MELT}$  is replaced by  $T_{VAPORIZATION}$ . The range of powers between the vaporization and melt powers defines the processing space. An actual representation of this space in its most general form is difficult since there are several variables (radius, travel velocity, and beam energy), and hence multiple "dimensions." 2-D cross-sections of this space are very useful, however. Several examples of these are shown below. The material under consideration in these diagrams is iron. In all of the charts shown below, the assumed electron beam energy is 0.1 MeV. The effect of increasing the beam energy will be shown later.

First consider the power needed to initiate surface melting.

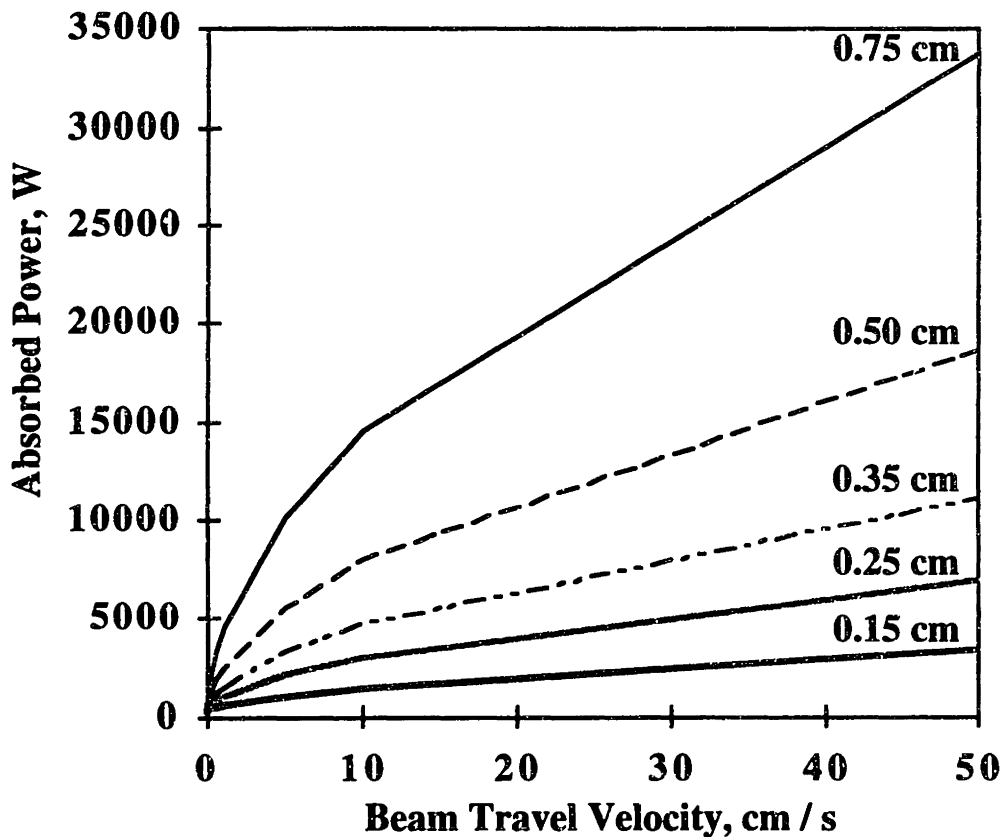


**FIGURE 2.3**  
**Power Needed to Initiate Surface Melt in Fe**  
**as a Function of Beam Travel Velocity and Beam Radius,**  
**Beam Energy is 0.1 MeV.**

The calculation of the incident power needed to vaporize the surface depends on several assumptions. Firstly, it is assumed that the limiting power is reached when the surface temperature reaches the boiling point, i.e. the temperature at which the metal's vapor pressure is equal to 1 atm. In vacuum processing, vaporization losses may become limiting at lower partial pressures, and it may not be possible in practice to reach the boiling point. Secondly, it is assumed that liquid and solid have essentially the same thermal properties. Within the framework of both of these assumptions, the vaporization power can be simply obtained from Equations 54 and 55. It turns out that the model predictions are not too far off from reality, as will be demonstrated by comparison to actual data. The vaporization power for iron is shown below.

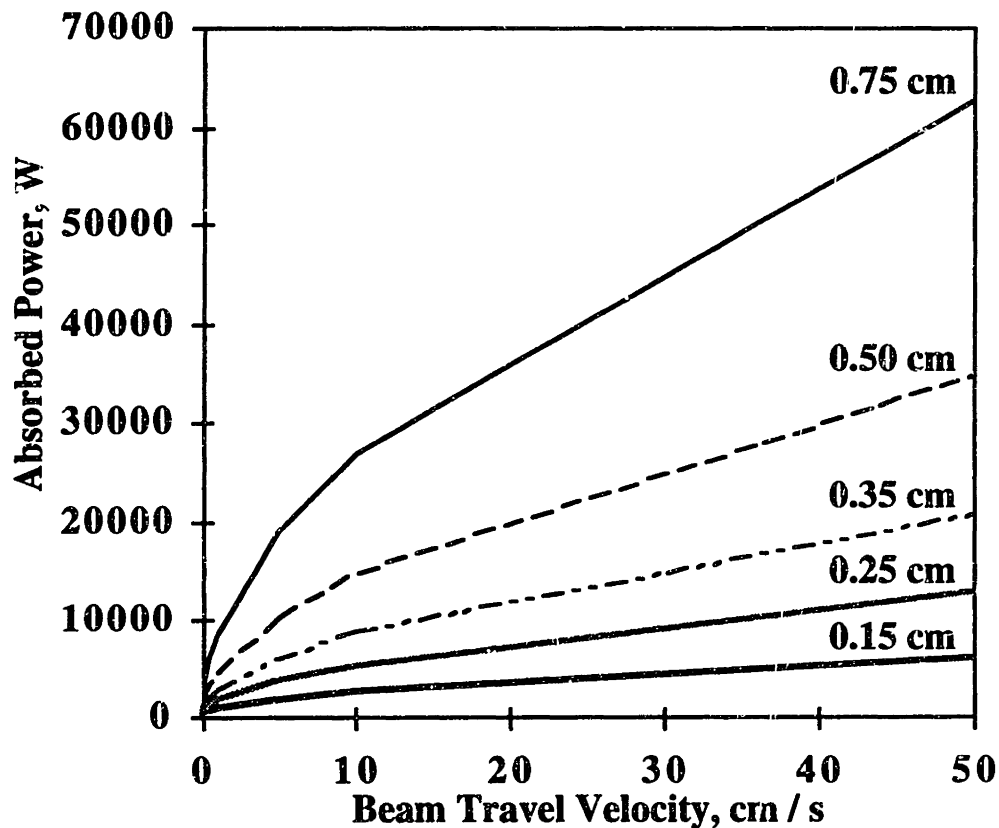


**FIGURE 2.4**  
**Power Needed to Vaporize Surface of Fe**  
**as a Function of Beam Travel Velocity and Beam Radius,**  
**Beam Energy is 0.1 MeV.**

The difference between the vaporization limit and the melt limit defines the range of powers available for processing. The difference between these two power levels defines the maximum fraction of beam power available for deposition and melting. Part of this power will be used to sustain a melt pool on the surface of the target, and the rest of this power can be used to melt and deposit material. This maximum power is shown below.

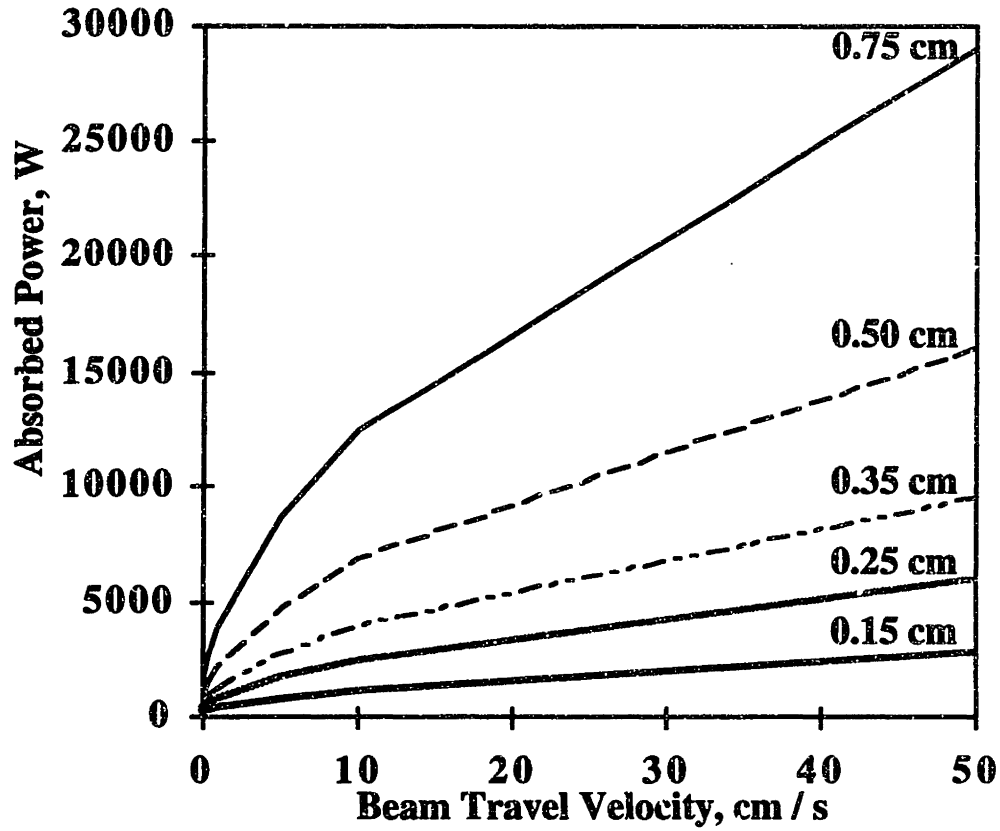


**FIGURE 2.5**  
**Maximum Power Available for Melting and Deposition of Fe**  
**as a Function of Beam Travel Velocity and Beam Radius,**  
**Beam Energy is 0.1 MeV.**

If a specific beam radius is chosen, say 0.35 cm, then the "processing space" is more clearly visualized :

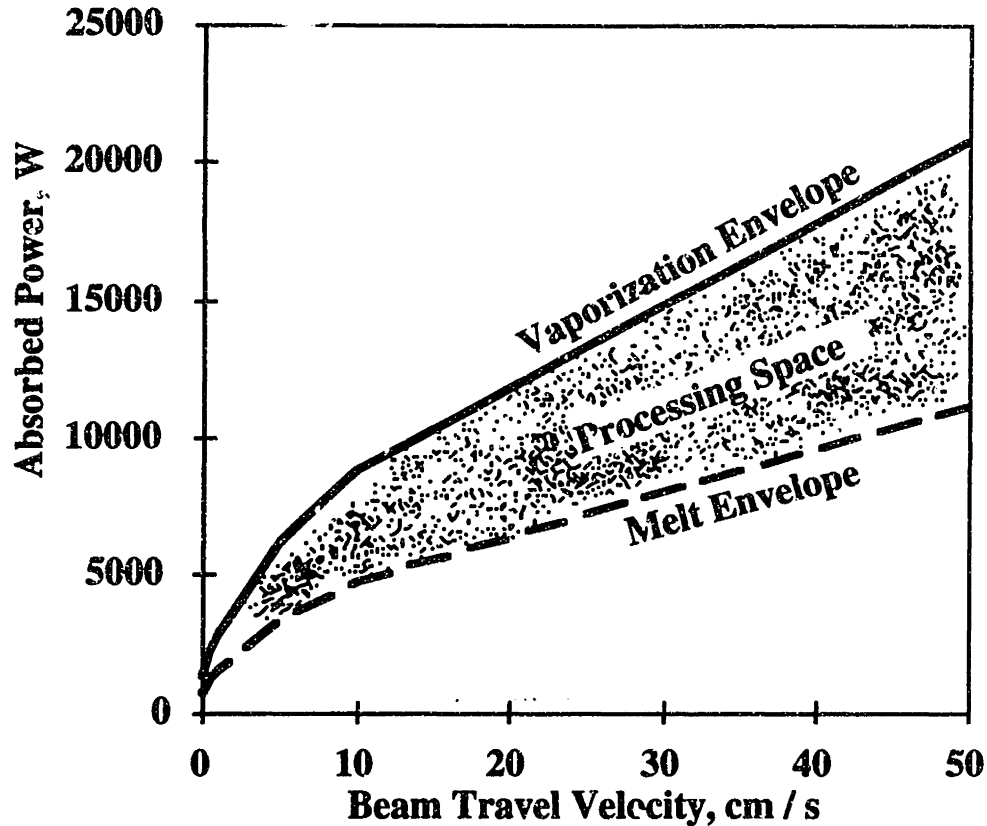


**FIGURE 2.6**  
**Processing Space for Fe,**  
**Beam Energy is 0.1 MeV, Beam Radius is 0.35 cm.**

### 2.12 High Energy Beam Effects

The effect of increasing the beam energy will be to shift all these curves upwards. Higher energy beams will require greater power levels to achieve surface melting or vaporization, but they will also allow for greater deposition and melting rates. To make the representation easier to visualize, a specific beam radius and beam travel velocity are chosen. The beam energy is varied to show the increased power available for deposition.



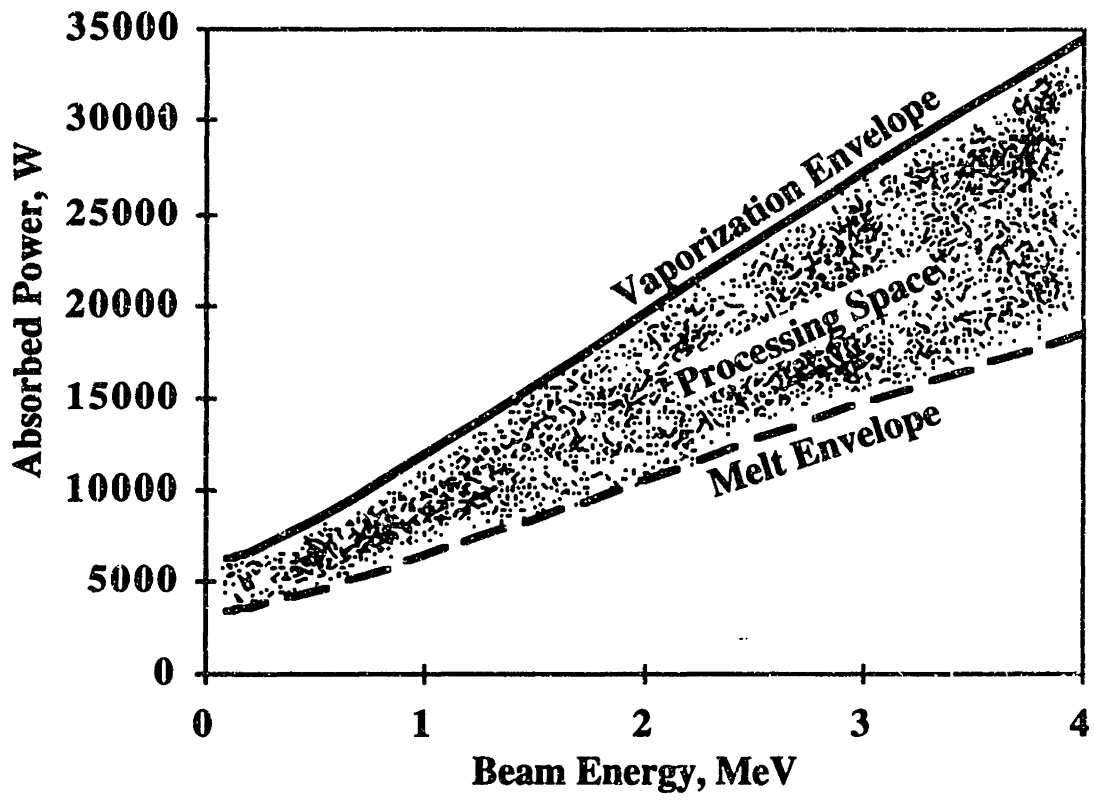


**FIGURE 2.7**  
**Range of Allowable Processing Powers for Fe (Processing Space),**  
**Beam Radius is 0.35 cm, Beam Travel Velocity is 5 cm / s.**

Looking at 304 stainless steel as another model material, it is possible to represent the effect of increasing beam energy in a slightly different way. Suppose that the beam radius and scan rate are fixed, and that the beam energy is increased. Two additional sets of calculations can be performed that illustrate the power requirements for melting as well as the surface temperature for a fixed absorbed power level as the beam energy goes up. First, the power needed to initiate surface melt is found as beam energy increases. Secondly, for a fixed beam power, the surface temperature is evaluated for increasing beam energies. The results of these two calculations are shown in the figures below.

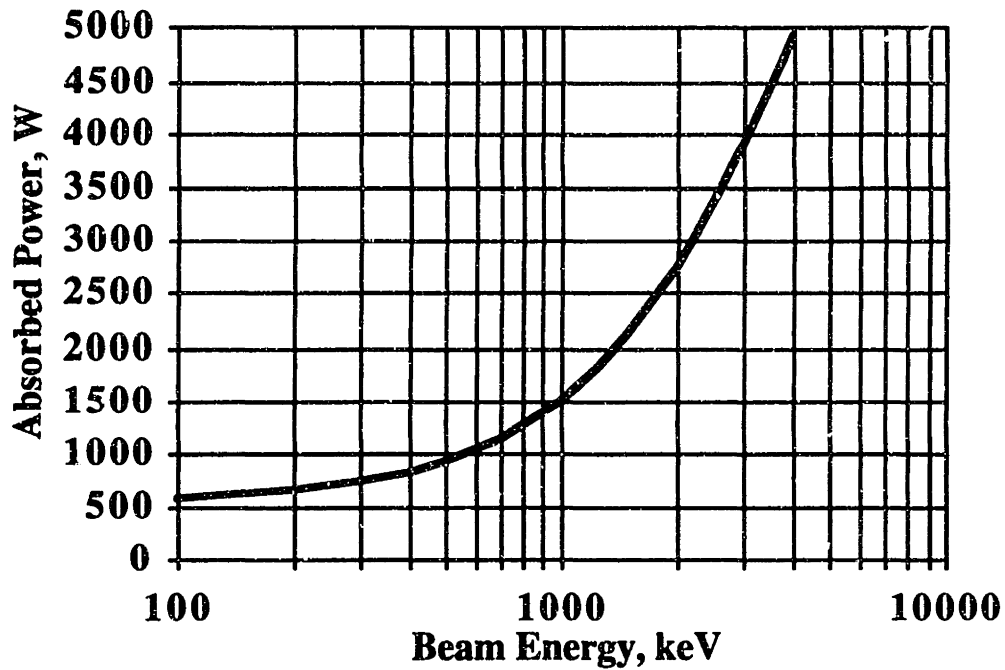


**FIGURE 2.8**  
**Absorbed Power Needed to Initiate Surface Melt in 304 Stainless,**  
**Beam Radius is 0.15 cm, Beam Travel Velocity is 5 cm / s.**

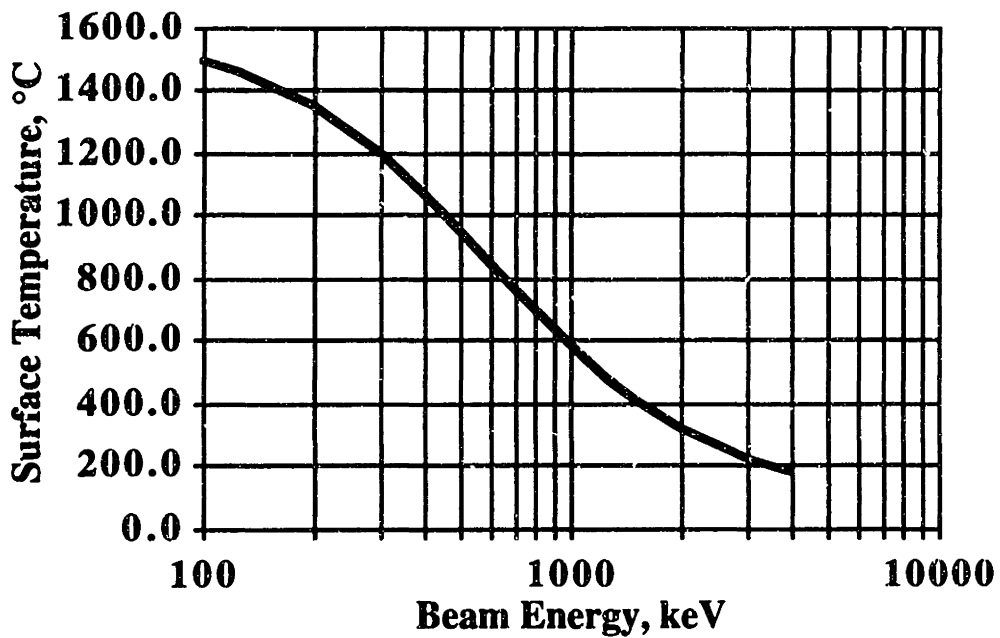


**FIGURE 2.9**  
**Surface Temperature of 304 Stainless, Absorbed Power is 600W,**  
**Beam Radius is 0.15 cm, and Beam Travel Velocity is 5 cm / s.**

Yet another way of looking at the effect of increasing the beam energy is to examine temperature profiles as a function of depth below the surface for increasing beam energies. Two calculations will be presented for 304 stainless steel as the model material. The beam radius and travel velocity will be held fixed. In the first calculation, the temperature profiles beneath the surface will be shown when the surface is at the melting temperature. The second calculation will assume an absorbed power level such that at 100 kV, the surface is at the melting point. This same power level will be applied to higher energies, and the temperature beneath the surface will be evaluated. The results of these two calculations are shown below.

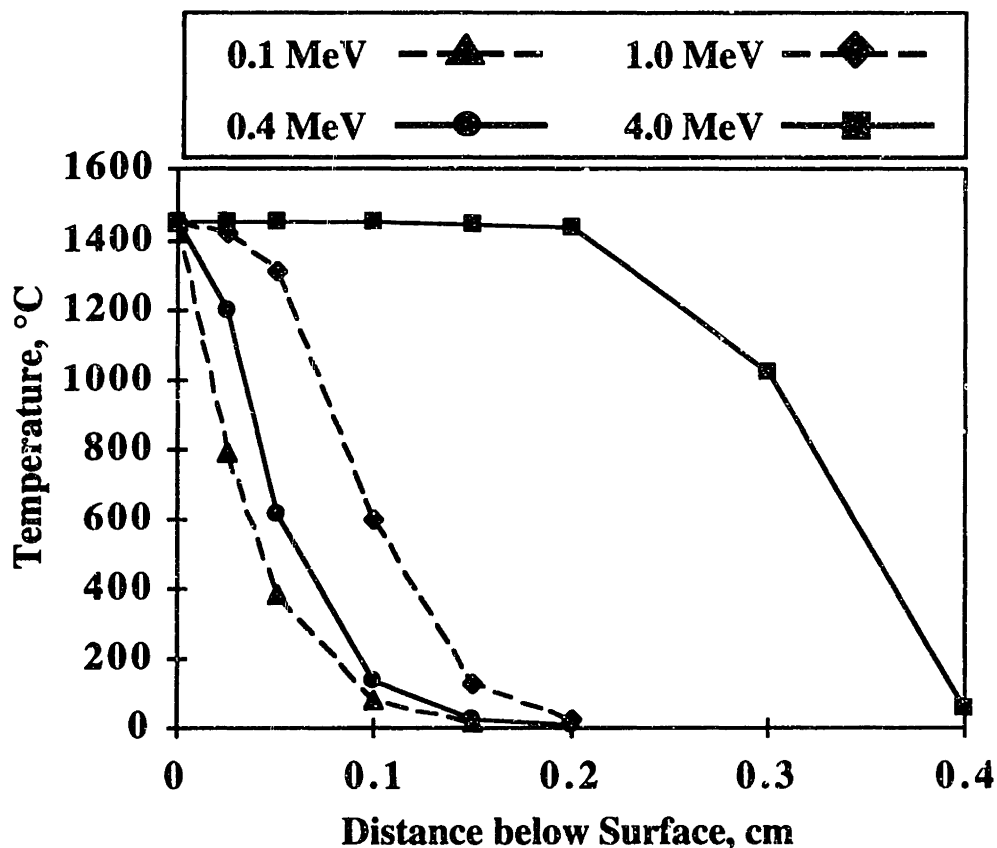


**FIGURE 2.10**  
**Temperature Profiles in 304SS when Surface is at Melting Point,**  
**Beam Radius is 0.15 cm, Beam Travel Velocity is 5 cm / s**

Clearly the higher the beam energy, the further into the material the temperature profile extends. At 4.0 MeV, the melt temperature extends more than 2mm below the surface, which also means that a melt pool under these conditions is at least 2mm deep. In order to melt the surface at 100 kV, 582 W must be absorbed. If this power is now applied to the higher energy cases, it is expected that the surface temperature will drop. This is illustrated below.

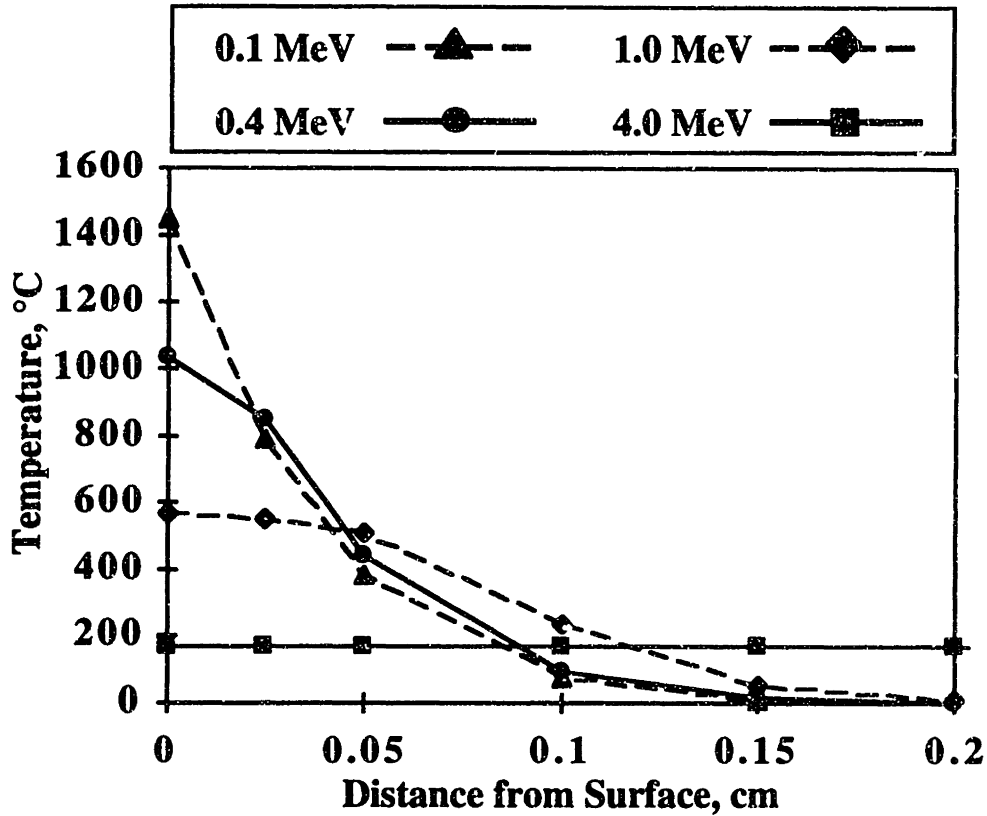


**FIGURE 2.11**  
**Temperature Profiles in 304 Stainless**  
**Assuming Absorbed Power of 582W,**  
**Beam Radius is 0.15 cm, Beam Travel Velocity is 5 cm / s.**

### 2.13 Melt Pools and the Efficiency of EB Deposition Processes

The melt depth model can now be used to estimate the melt depths for various conditions. The incident power was assumed to be the vaporization limit. The full set of these calculations is shown in Appendix B, but a few cases are excerpted in the table below. The melt depth was calculated by finding the depth at which the temperature just drops below the melting point, assuming no convection.

**TABLE 2.2**  
**Melt Depths in Fe**

Beam Energy, MeV	Radius, cm	Travel Speed, cm / s	Melt Depth, cm
0.1	0.15	5	0.028
0.1	0.15	50	0.011
0.1	0.75	5	0.059
0.1	0.75	50	0.02

TABLE 2. 2 Continued

Beam Energy, MeV	Radius, cm	Travel Speed, cm / s	Melt Depth, cm
1.0	0.15	5	0.093
1.0	0.15	50	0.092
1.0	0.75	5	0.111
1.0	0.75	50	0.092

These melt depths are most likely *underestimates* since convection is being ignored. Based on these melt depths, the cross-sectional area of the melt pool can be estimated. This is an important number, since some of the power available for melting and deposition must be used for the maintenance of the melt pool. Two possible shapes will be assumed for the melt pool cross section : circular and rectangular. The circular shape is actually a segment of a circle, and the rectangular cross-section is self-explanatory. These two shapes are shown below.

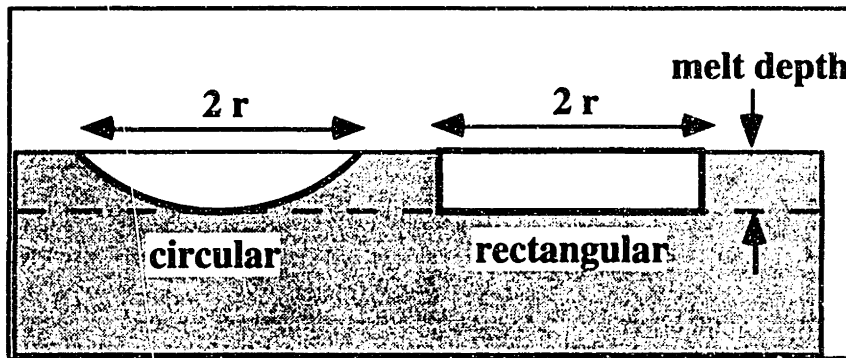


FIGURE 2.12

Schematic Representation of Melt Depth Cross - Section

The rectangular melt pool cross-section has been used in other works, such as ION, SHERCLIFF, & ASHBY (1992). Based on these profiles, the travel velocity of the beam, the calculated melt depth, and the thermal properties of the solid, the power needed to sustain the melt pool can be found. This power is given by Equation 36 of Part I :

In the case of a rectangular pool :

$$P_{POOL} = 2r_B D_M V_O \rho L_M , \text{ where}$$

$D_M$  is the melt depth, cm,

$V_O$  is the scan rate, cm / sec, (56)

$\rho$  is the material density, g / cu.cm,

$r_B$  is the beam radius, and

$L_M$  is the latent heat of fusion, J / g

The power requirements for maintaining a melt pool in iron are shown for the same processing conditions listed in Table 2.2. These power values are given in the table below.

**TABLE 2.3**  
**Power requirements to Maintain Weld Pool in Fe**

Beam Energy, MeV	Radius, cm	Beam Travel Velocity, cm/s	Melt Pool Power, W	Total Power of Deposition, W
0.1	0.15	5	91	829
0.1	0.15	50	356	2858
0.1	0.75	5	954	8781
0.1	0.75	50	3235	29075
1.0	0.15	5	301	2097
1.0	0.15	50	2976	19547
1.0	0.75	5	1795	13837
1.0	0.75	50	14879	98913

As can be seen from the numbers, the power needed to maintain the melt pool is about 10% - 15% of the total power available for melting and deposition. This total power of deposition is the difference between the vaporization and melt power envelopes. This number remains fairly constant over the range of beam energies from 0.1 MeV to 1.0 MeV.

Another important figure of merit describing the EBSFF deposition process is the deposition efficiency. For the purposes of this work, the deposition efficiency will be defined as follows :

Definition of Deposition Efficiency :

$$D.E. = \frac{\dot{m}_{MAX}}{P_{TOTAL}}, \text{ where} \quad (57)$$

$\dot{m}_{MAX}$  is the maximum deposition rate (lbs./hr.) and

$P_{TOTAL}$  is the total power input to the workpiece (kW)

Two other efficiencies will also be defined :

Definition of Deposition Melting Efficiency :

$$D.M.E. \equiv \frac{P_{DEPO}}{P_{TOTAL}} \quad (58)$$

Definition of Overall Melting Efficiency :

$$O.M.E. \equiv \frac{P_{DEPO.NET}}{P_{TOTAL}}$$

The power values appearing in the above expression are defined below.

- $P_{DEPO}$  is the power used for deposition ONLY (excluding power needed to maintain melt pool),
- $P_{DEPO,NET}$  is the total power available for both melting and deposition, and
- $P_{TOTAL}$  is the total power input to the workpiece.

(59)

These efficiencies are now tabulated for the cases shown previously.

**TABLE 2.4**  
**Various Efficiencies for Melting and Deposition Processes in Fe**

Beam Energy, MeV	Beam Radius, cm	Travel Velocity, cm / s	Deposition Efficiency, D.E., lbs/hr/kW	Deposition Melting Efficiency, D.M.E.	Overall Melting Efficiency, O.M.E.
0.1	0.15	5	2.29	0.41	0.46
0.1	0.15	50	2.25	0.41	0.46
0.1	0.75	5	2.38	0.41	0.46
0.1	0.75	50	2.29	0.41	0.46
1.0	0.15	5	2.20	0.40	0.46
1.0	0.15	50	2.18	0.39	0.46
1.0	0.75	5	2.24	0.40	0.46
1.0	0.75	50	2.18	0.39	0.46

It is interesting to note that the value of the overall melting efficiency is consistent with other predictions for laser and e-beam welding [e.g. SWIFT-HOOK & GICK (1973)]. There seems to be an asymptotic limit to the welding efficiency, and in this case, this number is 46%. It is largely independent of beam energy.

## 2.14 EB Deposition Process vs. Conventional Welding Processes

It is possible to compare the melting and deposition efficiencies of the EB deposition process with those of a conventional welding process, such as GMAW (gas metal arc welding). The efficiencies of GMAW will most likely be higher than FCAW (flux - cored arc welding) and SAW (submerged arc welding) since these other processes involve flux that must be heated and melted. The power requirements for heating and melting the flux represent power that is not available for metal deposition.

Shown below are typical GMAW welding schedules for steel. This data was taken from HOBART BROTHERS CO. (1980). The tables show data for three different modes of GMAW : short-circuiting transfer, globular transfer, and spray transfer. Without entering into the details of arc welding, the essential physical characteristics of these different modes may be understood with the aid of the diagram shown below.

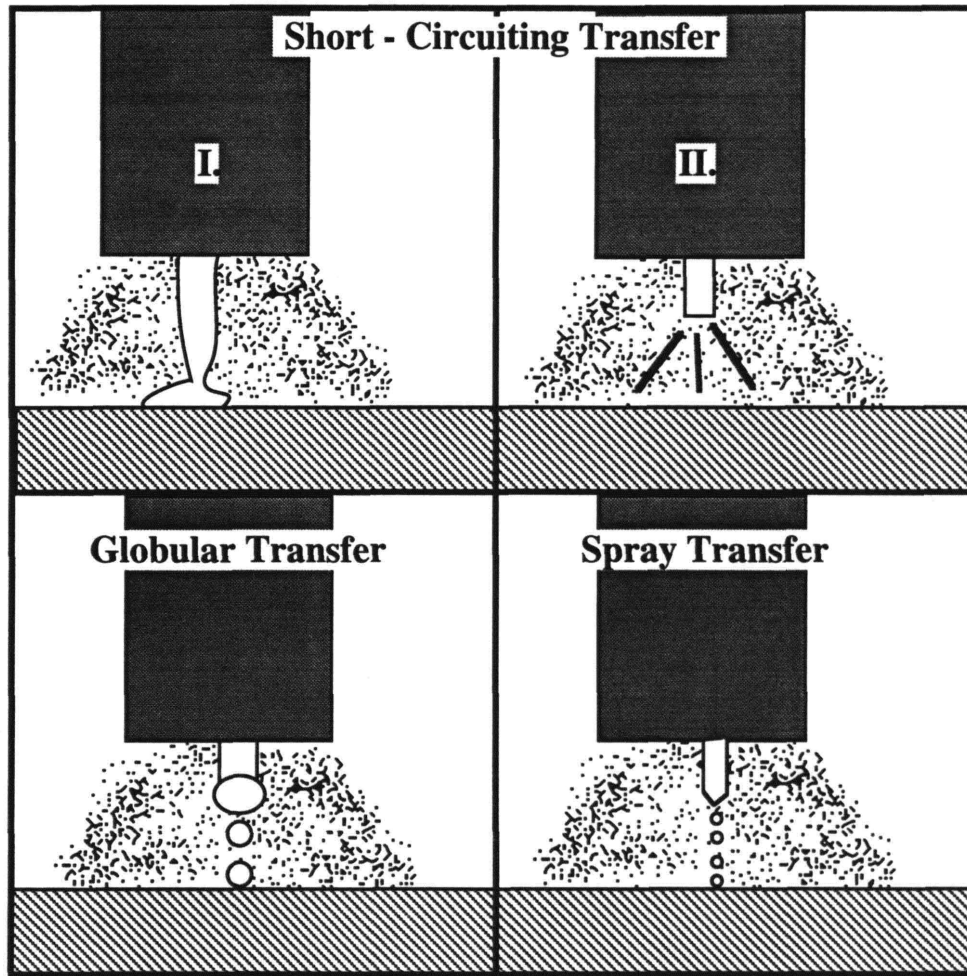


**FIGURE 2.13**  
**GMAW Mass Transfer Modes**  
 Adapted from HOBART BROTHERS CO. (1980)

In short - circuiting transfer, the molten metal actually makes contact with the weldpiece, resulting in a short circuit. As the material from the metal electrode is deposited, the electrode "melts back" and the arc is re-ignited. In globular transfer, the drops grow until they fall off due to gravitational forces or are intentionally shaken off [JONES (1994)]. Spray transfer occurs when the drops are electromagnetically pinched off. The electrode thus becomes tapered and "sprays" off a large number of fine droplets. Some typical welding schedules for these droplet detachment modes are shown in the tables below. The power ratings were derived from the arc current and voltage settings. It was assumed that the overall equivalent electrical circuit (including the arc) is mainly resistive in nature, so that the power is simply the product of the voltage and current. This is a reasonable assumption for most GMAW processes [JONES (1994)]. For subsequent calculations and for the determination of the deposition rate, it will be assumed that the steel wires have a density of  $7.85 \text{ g / cm}^3$ , a mean specific heat of  $0.75 \text{ J / g - }^\circ\text{c}$ , and a heat of fusion of  $275 \text{ J / g}$ .



**TABLE 2.5**  
**GMAW Schedule for Short-Circuiting Transfer, Single Pass**  
**Adapted from HOBART BROTHERS CO. (1980)**

Fillet Size, cm	Total Power, W	Electrode Dia., cm	Wire Feed Rate, cm / s	Deposition Rate, g / s
0.09	1200	0.09	4.6	0.23
0.12	1620	0.09	6.2	0.31
0.24	2280	0.09	9.1	0.46
0.64	3000	0.09	12.7	0.64

**TABLE 2.6**  
**GMAW Schedule for Globular Transfer, Single Pass**  
**Adapted from HOBART BROTHERS CO. (1980)**

Fillet Size, cm	Total Power, W	Electrode Dia., cm	Wire Feed Rate, cm / s	Deposition Rate, g / s
0.12	6875	0.11	14.8	1.10
0.32	10150	0.11	21.2	1.58
0.64	15200	0.16	16.5	2.60
1.27	22500	0.24	6.9	2.45

**TABLE 2.7**  
**GMAW Schedule for Spray Transfer, Single Pass**  
**Adapted from HOBART BROTHERS CO. (1980)**

Fillet Size, cm	Total Power, W	Electrode Dia., cm	Wire Feed Rate, cm / s	Deposition Rate, g / s
0.32	7200	0.16	7.0	1.10
0.48	8750	0.16	10.0	1.57
0.64	8750	0.16	10.0	1.57
0.95	11687	0.24	4.6	1.63

From the tables above and the previously mentioned thermophysical data, it is possible to estimate the deposition efficiency and the deposition melting efficiency for various processes. These results are shown below. In calculating the deposition power, it was assumed that the wire feedstock experienced a temperature excursion of 1534 °C.

**TABLE 2.8**  
**Efficiencies for GMAW, Short-Circuiting Transfer, Single Pass**

Total Power, W	Deposition Rate, g / s	Deposition Power, W	D.E., lbs/hr/kW	D.M.E.
1200	0.23	328	1.52	0.27
1620	0.31	442	1.52	0.27
2280	0.46	656	1.60	0.29
3000	0.64	913	1.69	0.30

**TABLE 2.9**  
**Efficiencies for GMAW, Globular Transfer, Single Pass**

Total Power, W	Deposition Rate, g/s	Deposition Power, W	D.E., lbs/hr/kW	D.M.E.
6875	1.10	1569	1.27	0.23
10150	1.58	2253	1.23	0.22
15200	2.60	3708	1.35	0.24
22500	2.45	3494	0.86	0.16

**TABLE 2.10**  
**Efficiencies for GMAW, Spray Transfer, Single Pass**

Total Power, W	Deposition Rate, g/s	Deposition Power, W	D.E., lbs/hr/kW	D.M.E.
7200	1.10	1569	1.21	0.22
8750	1.57	2239	1.42	0.26
11687	1.63	2324	1.10	0.20

It is seen that EB deposition is approximately twice as productive as GMAW and also has twice the deposition melting efficiency (D.M.E.). In terms of the overall melting efficiency (O.M.E.), this cannot be calculated from the data shown above. The melt pool dimensions must also be taken into account. The O.M.E. has been measured experimentally for a variety of arc welding processes by several workers. In the case of PAW (plasma arc welding) and GTAW (gas tungsten arc welding) for example, FUERSCHBACH & KNOROVSKY (1991) report an asymptotic O.M.E. of a little over 40%.

### 2.15 Modeling of 308 Stainless Steel Wirefeed Deposition Process

To investigate the predictive capabilities of the model, the model will be compared to actual beam parameters used in the deposition of 308 stainless steel. The operating parameters for a typical run were :

**TABLE 2.11**  
**Beam Operating Parameters for 308 Stainless Steel Deposition**

Quantity	Value
Beam Voltage	120 kV
Beam Current	10.5 mA
Beam Power	1260 W
Spot Size (radius)	0.15 cm
Surface Speed of Target	3.8 cm / s
Wire Feed Rate	6.4 cm / s
Wire Diameter	0.089 cm (0.035 ")
Material Deposition Rate	1.15 kg / hr. (2.53 lbs./hr.)
Mean Melt Depth	0.0762 cm

Also needed for this computation are the properties of 308 stainless. It will be assumed that these are identical to 304 stainless. The relevant properties are listed below.

**TABLE 2.12**  
**Properties of 304 Stainless Steel**

Quantity	Value
Density	8 g / cc
Melting Range	1400°C - 1450°C
Mean Specific Heat	0.5 J / g - °C
Heat of Fusion	250 J / g

The model will now be used to attempt to predict the power needed to achieve the deposition rates reported in Table 2.11. For 304 stainless, a beam radius of 0.15 cm, and a scan rate of 3.8 cm / s, an incident power of 520 W is needed to induce surface melt. This is the absolute minimum power needed for processing. Next, the power requirements for melting the substrate and the feed wire need to be evaluated. The estimate for the surface melting power requirements will be made using the *measured* melt depth to determine the amount of the surface that must be melted. After a total incident power is determined via this calculation, an additional check of the model can then be easily implemented by using the incident power thus determined to predict a melt depth which can be compared to the measured value. Now the power needed to maintain the melt pool assuming a rectangular approximation will be calculated.

$$\begin{aligned}
 \text{Melt Depth} &= 0.0762 \text{ cm} \\
 \text{Radius} &= 0.15 \text{ cm} \\
 \text{Melt Pool Cross - Section} &= 0.02286 \text{ cm}^2 \\
 P_{\text{POOL}} &= V_o \rho A_c L_M = 174 \text{ W}
 \end{aligned} \tag{60}$$

Next, the power needed to heat and melt the wire will be found.

$$\begin{aligned}
 P_{\text{WIRE}} &= f A_c \rho (C \cdot \Delta T + L_M) \\
 f &\text{ is the wire feed rate (6.4 cm / s)} \\
 A_c &\text{ is the cross - sectional area of the wire (0.00622 cm}^2\text{)} \\
 \text{Assume } \Delta T &\text{ is 1450 }^\circ\text{C, then} \\
 P_{\text{WIRE}} &= 312 \text{ W}
 \end{aligned} \tag{61}$$

It is now possible to calculate the total absorbed power needed to deposit the material. This will simply be the sum of the separate contributions found thus far:

Minimum Melt Power	520 W	
Melt Pool Power	174 W	
Wire Heating / Melting	312 W	
<b>Total Absorbed Power</b>	<b>1006 W</b>	<b>(62)</b>

To complete the analysis, it is necessary to find the total beam power and compare it with the experimental value. For this purpose, the overall backscattering coefficient is needed. From Appendix B, we find that for 304 stainless and for 0.125 MeV incident electrons, the absorption coefficient for perfectly flat surfaces is 0.8354. Assuming this to be the correct coefficient, we can easily find the total beam power :

$$P_{BEAM} = P_{ABSORB} / \eta_{TOT} \quad (63)$$

$$P_{BEAM} = 1006 / 0.8354 = 1204 \text{ W}$$

The actual beam power used under these conditions was 1260W, so the model did a reasonable job in predicting the correct value. For the 308 stainless deposition, a large copper heat sink was placed inside of a stainless pipe, which was then used as the workpiece for material deposition. The assumption of semi-infinite solids works well in that case. Also, convection effects can play a large role in determining the power requirements. The more prominent the convection effects, the more power will be needed to both sustain the melt pool and to keep the melting process going. This is because the effective conductivity of the liquid can be considerably enhanced by convection effects, thus increasing overall power requirements to keep the liquid within the range of desired processing temperatures. ELMER (1988) discusses regimes of operation for e-beam surface melting and delineates regions where convection is and is not important. For a regime where convection is important (high weld pool Peclet Number), the model will most likely not work so well. Temperature dependence of thermal properties could also be a factor. As another check of the model performance, the total calculated power for processing, i.e. 1204 W, will be used as an input to the heat conduction model, and the melt pool depth can be found. The resulting calculated weld pool depth is 0.041 cm. This is not too close to the measured depth (mean value of 0.0762cm), and this may be explained by the fact that the model ignores convection.

## 2.16 Estimation of Power Losses due to Vaporization

In addition to convection processes, evaporation losses will also increase processing power requirements. This is especially true for vacuum processing, where partial pressures of metal vapor far below 1 atm can still result in sizable energy losses due to evaporation. The power lost from vaporization will not be absorbed by the material. The power losses due to vaporization may be crudely estimated as follows. The vaporization of alloy constituents from a melt can be described by their respective partial pressures [GEIGER & POIRIER (1973)]:

$$P_A = \gamma_A X_A P_A^o \quad \text{where}$$

$P_A$  is the partial pressure of constituent A,  
 $\gamma_A$  is the activity coefficient for A, (64)  
 $X_A$  is the concentration of A at the surface, and  
 $P_A^o$  is the vapor pressure of pure A at the same temperature.

A detailed model of vaporization effects will not be developed here. There are several such studies, including a recent one by MUNDRA & DEBROY (1993) and CHOO & SZEKELY (1992). The essence of such investigations involves a fluid flow model, a thermal model, and a detailed consideration of vaporization kinetics. A much simpler but reasonably realistic consideration of alloy constituent vaporization involves at least two steps [GEIGER & POIRIER (1973)]:

- mass transport from the bulk to the surface
- evaporation from the surface

The first part of a vaporization model involves determining the relation between bulk and surface concentrations of any given constituent. This relation will in general depend on the details of the fluid flow within the melt pool. The relation can be generically written in the form [GEIGER & POIRIER (1973)]:

$$j_A = k_{M,l}(C_{A\infty} - C_A^s), \quad \text{where}$$

$j_A$  is the flux in mol[A] / cm<sup>2</sup> - sec,  
 $k_{M,l}$  is the mass transfer coefficient in cm / sec, (65)  
 $C_{A\infty}$  is the bulk concentration of A in mol[A] / cm<sup>3</sup>, and  
 $C_A^s$  is the surface concentration of A in mol[A] / cm<sup>3</sup>

The second part of such a model is the expression for the surface evaporation flux:

$$j_A = \frac{\gamma_A P_A^o C_A^s}{\rho_{MA} \sqrt{2\pi MRT}}$$

$\rho_{MA}$  is the molar density of the alloy in mol / cm<sup>3</sup>,  
M is the molar mass in g / mol, (66)  
R is the gas constant in g - cm<sup>2</sup> / sec<sup>2</sup> - °K - mol, and  
T is the temperature in °K.  
All other quantities are as previously defined.

The assumptions of the thermal conduction model are that convection effects are negligible. Under these circumstances, the relationship between the surface concentration of a given species is simply related to the bulk concentration

by a diffusion relation with evaporative boundary conditions at the free surface. The solution to this equation is given by [GEIGER & POIRIER (1973)] :

$$C_A^s/C_A^o = \exp[Y^2 Dt] \cdot \operatorname{erfc}[Y\sqrt{Dt}] , \text{ where}$$

$$Y \equiv \frac{\gamma_A P_A^o}{D\rho_{MA}\sqrt{2\pi MRT}} , \quad (67)$$

$D$  is the diffusivity of A in the melt,  
and  $t$  is the time spent at temperature  $T$ .

The characteristic beam interaction time will be taken as the time in Equation 67. Furthermore, a value of  $5.0 \times 10^{-5} \text{ cm}^2/\text{sec}$  will be chosen as the diffusivity. This will be taken as the diffusivity of Ni and Cr in molten 308 stainless as well as the self-diffusivity of Fe in stainless steel. Since most liquid metal diffusivities are between  $10^{-5} \text{ cm}^2/\text{sec}$  and  $10^{-4} \text{ cm}^2/\text{sec}$ , this is a reasonable assumption. The surface concentration in Equation 67 will drop off as it is depleted by the vaporization. For the purposes of estimating the vaporization flux, the average surface concentration during the time interval of interaction (i.e. the characteristic beam interaction time) must be calculated. This is given by the relation below.

$$\frac{\overline{C_A^s}}{C_A^o} = \frac{1}{t_i} \int_0^{t_i} \frac{C_A^s(t)}{C_A^o} dt =$$

$$= \frac{1}{t_i} \left[ \frac{2\sqrt{Dt_i}}{DY\sqrt{\pi}} + \frac{\exp(Y^2 Dt_i) \cdot \operatorname{erfc}(Y\sqrt{Dt_i})}{Y^2 D} - \frac{1}{Y^2 D} \right] \quad (68)$$

$$t_i \equiv \frac{2r_B}{V_o} \equiv \text{characteristic beam interaction time}$$

The remaining quantities to be determined are the thermodynamic properties of the alloy system in question and the temperature of the surface. The surface temperature is the hardest piece of information to accurately determine. As pointed out by BLOCK-BOLTEN & EAGAR (1984), the surface temperature distribution is difficult to predict or measure. CHCO & SZEKELY (1992) have also indicated the importance of thermocapillary flows in determining this temperature distribution. The approach taken here will be consistent with the assumption of no convection, i.e. the surface temperature will be taken as that predicted by the model. This approach is not strictly correct since the evaporation rate will have a cooling effect on the surface. Within the assumptions of the model however, there is internal consistency in the sense that the surface temperature will be calculated on the basis on the *absorbed* power only, and vaporization is a *loss* term. Applying 1006 W to the surface under the given beam parameters gives a surface temperature of approximately 2500 °C.

The thermodynamic properties will be determined in the same manner as was done by BLOCK-BOLTEN & EAGAR (1984). For stainless steel, the partial pressure of Fe, Cr, and Ni will be calculated. It will be assumed that ternary and higher order mixing effects are negligible so that binary alloy data can be used. Thermodynamic data will be used from the tabulations of HULTGREN ET AL. (1973). BLOCK-BOLTEN and EAGAR (1986) have created processing diagrams from the data in HULTGREN ET AL (1973). These diagrams give the vapor pressure of various alloying elements in iron as a function of temperature and concentration. Using this data together with the estimated surface temperature, the following partial pressures are estimated :

**TABLE 2.13**  
**Vapor Pressures for Various Alloying Elements**  
**in 308 Stainless Steel at 2500 °C**

ELEMENT	NOMINAL WEIGHT %	VAPOR PRESSURE AT 2500 °C, atm
Fe	67	0.021
Cr	21	0.018
Ni	12	0.001

In the prediction of the partial pressure of iron, it was assumed that the activity coefficient of iron in stainless steel is close to 1. Following BLOCK-BOLTEN & EAGAR (1984), the power loss due to evaporation is :

$$P_A^{VAP} = j_A \cdot (L_A^{VAP} - \overline{\Delta H_A}), \text{ where} \quad (69)$$

$P_A^{VAP}$  is the power loss due to vaporization, W / cm<sup>2</sup>,  
 $j_A$  is the molar evaporation flux,  
 $L_A^{VAP}$  is the molar latent heat of vaporization of pure A, and  
 $\overline{\Delta H_A}$  is the partial molar heat of mixing of A in the alloy.

The partial molar heat of mixing will be ignored in comparison to the latent heat term. The heats of vaporization for Fe, Ni, and Cr are given in the table below.

**TABLE 2.14**  
**Heats of Vaporization for Cr, Fe, and Ni**  
**from SMITHELLS & BRANDES (1976)**

ELEMENT	HEAT OF VAPORIZATION, kJ / mol [kJ / g]
Cr	342 [6.58]
Fe	340 [6.09]
Ni	374 [6.37]

It is now possible to compute the power loss due to vaporization. The steps are :

- find the volumetric concentrations of Cr, Fe, and Ni in the bulk from the corresponding atomic fractions
- apply Equation 68 using appropriate data to get the time - average surface concentrations of the constituent elements
- apply Equation 66 to get the fluxes of each constituent, and multiply by the beam spot area to get the vaporization rates
- use Equation 69 to find the power loss for each constituent and sum to get the overall power loss due to vaporization

Data needed to this perform the calculation is tabulated below.

**TABLE 2.15**  
**Relevant Additional Data**  
**for the Evaluation of Vaporization Power Losses**

QUANTITY	CONSTITUENT		
	Fe	Cr	Ni
Weight Percent	0.67	0.21	0.12
Atomic Percent	0.667	0.222	0.111
Bulk Concentrations, mol / cm <sup>3</sup>	0.096	0.032	0.016
Partial Pressures, atm	0.021	0.018	0.001
Partial Pressures, g / cm - sec <sup>2</sup>	21264	18226	1012
Alloy Density, g / cm <sup>3</sup>	8.0		
Alloy Density, mol / cm <sup>3</sup>	0.144		
Beam Interaction Time, sec.	0.08		

The results of applying Equation 68 for the determination of the time - average surface concentrations of the constituent elements are shown in the table below. These values may be used to evaluate the vaporization fluxes.

**TABLE 2.16**  
**Time - Average Surface Concentrations of**  
**Constituents in 304 Stainless**

Element	Bulk Concentration, mol / cm <sup>3</sup>	Time - Average Surface Conc., mol / cm <sup>3</sup>	Ratio of Surface to Bulk Concentrations
Fe	0.096	0.062	0.647
Cr	0.032	0.022	0.674
Ni	0.016	0.0156	0.976



Using these surface concentrations, the vaporization fluxes are calculated next. These values are shown below.

**TABLE 2.17**  
**Vaporization Fluxes for Constituents of 308 Stainless**

Element	Vaporization Flux, mol / cm <sup>2</sup> - sec.	Vaporization Flux, g / cm <sup>2</sup> - sec.
Fe	0.00102	0.057
Cr	0.000315	0.0164
Ni	0.000012	0.0007

The vaporization power loss is easily calculated from these fluxes. The separate and total power losses are tabulated below. The total power loss assumes a spot radius of 0.15 cm.

**TABLE 2.18**  
**Power Losses due to Vaporization**  
**in 308 Stainless**

Quantity	Constituent		
	Fe	Cr	Ni
Power Losses, W / cm <sup>2</sup>	375	100	4
Total Power Loss, W / cm <sup>2</sup>	479		
Total Power Loss, W, (0.15 cm rad.)	34		

The total power loss due to vaporization is therefore 34 W for the beam conditions under consideration. This number must also be corrected by the backscattering coefficient, since this power is absorbed and then lost, and is therefore subject to backscattering. This means that the total predicted incident beam power including the effect of vaporization is 1238 W. Since the actual beam power was 1260 W, this updated prediction is very close. *More important than the actual numbers is the methodology that was developed to predict vaporization losses in EB deposition.*

## 2.17 Summary of Model Applications

This section developed several applications of the EB thermal interaction model developed in Part I of Chapter 2. The model was used in a variety of predictive and analytical roles that provide important information for EB deposition processing. Some of the more important conclusions derived from these calculations are listed below.

- The model is able to determine the EB processing space. This space is the range of allowable incident beam powers that lie between the melt envelope and the vaporization envelope. Below the melt envelope, sample heating without melting will occur. Above the vaporization envelope, there is a very good chance that deep penetration effects may develop. The model predicts the processing space as a function of beam radius, beam travel velocity, and incident beam energy.
- For deposition processes, the model is able to predict the deposition efficiency, the deposition melting efficiency, and the overall melting efficiency. This is done by introducing the model extension discussed in Part I dealing with melt pools. The limiting values of these efficiencies are :

**TABLE 2.19**  
**Limiting Values of Various Deposition and Melting Efficiencies**

Quantity	Limiting Value
D.E.	2.2 - 2.3 lbs / hr / kW
D.M.E.	0.39 - 0.41
O.M.E.	0.46

These numbers are consistent with other studies of a similar nature.

- The corresponding D.E. and D.M.E. for arc welding processes were calculated. The D.E. for EB processing is about twice as large as that for GMAW, and the D.M.E. is also bigger by approximately the same factor. Both these facts reiterate the greater efficiency of the EB process as compared to conventional welding processes.
- The model is able to predict the power necessary for the EB deposition of 308 Stainless wire within 5% of the actual beam power. The table below summarizes model performance.

**TABLE 2.20**  
**Summary of Predicted vs. Actual Quantities for EB Deposition of 308 Stainless**

Actual Power Needed to Deposit Material	1260 W
Calculated Power <i>Using the Measured Melt Depth</i>	1204 W
Calculated Power <i>Including the Effect of Vaporization Losses</i>	1238 W
Measured Melt Depth	0.076 cm
Predicted Melt Depth Based on Beam Power of 1204 W	0.041 cm

- The assumption of negligible convection leads to the difference between the predicted melt depth and the measured melt depth. Convection effects will result in a deeper and/or wider melt pool.

## **CHAPTER 3**

### **E-BEAM BASED POWDER MELTING / SINTERING**

#### **3.1 Overview**

This chapter deals with several experiments in EB powder processing. One of the possible SFF techniques mentioned in the introduction is analogous to the laser-based SLS™ process for making powder green bodies. As discussed in the introduction, on account of several processing and metallurgical limitations, alloys of practical engineering importance have not been extensively used in the SLS™ process. The first series of experiments characterized EB - powder interactions for the following materials : commercially pure Al, Al + TiC MMC, Al - Cu alloys, Monel, Al - Ni - Bronze, HY-100 steel, and 304L stainless steel. Based on these preliminary experiments, several problems with EBSFF using powders were identified.

The second series of experiments resulted in the independent discovery of a technique for the reaction synthesis of coatings of aluminide intermetallics. The following intermetallic and intermetallic matrix composite (IMC's) systems were investigated: FeAl, Fe<sub>3</sub>Al, NiAl, Ni<sub>3</sub>Al, TiAl, FeAl + TiC, Fe<sub>3</sub>Al + TiC, NiAl + TiC, Ni<sub>3</sub>Al + TiC, and TiAl + TiC. The most promising application identified was the application of iron aluminide - based coatings on other metallic substrates (carbon steels and stainless steels). The EB process for these materials results in a fully adherent coating with full density. The position of the reaction front is also easily controlled with the beam. The EB technique combines all these features into a potentially viable coating process.

#### **3.2 E-Beam Sintering and Melting of Powders**

One of the original ideas which motivated this work was the potential use of e-beams as part of an SFF system which utilized powder feed materials. To study the effects of electron beams on powders, a series of experiments were conducted on alloys of engineering significance. No special modifications were made to the powder blends to enhance sintering properties. As discussed in the introduction, such modifications are common in laser sintering. The objective of these trials was to test the EBSFF concept on powder systems of practical interest.

As in any powder-based SFF process (excluding spray casting or plasma spray), there are several recurrent problems which must be solved in processing. Firstly, loosely to moderately packed powder beds must be able to melt or sinter in a uniform way which produces a surface which is smooth and contiguous. Secondly, there must be some means of introducing the second layer in such a way that it will fuse together well with the layer below it when exposed to the beam. Furthermore, the sintering / melting process must be predictable and repeatable, and residual stresses should be reasonably small so as not to exceed the strength of the green body or partially melted compact. Lastly, post-

processing such as furnace sintering or HIPing should not introduce excessive distortion, or at least such distortions should be uniform and predictable. It is clear from initial experiments that the e-beam process as applied to real engineering materials may not be practical. There are several problems, which were enumerated in the introduction. they are repeated below :

- incomplete melting generally occurs ; it is often observed that regions of partial melting and sintering are directly below regions of full melt
- inadequate adherence between layers of powders
- if powders contain several components to be mixed, incomplete mixing is sometimes observed

The following material systems were investigated : commercially pure Al, Al + TiC, Al - Cu alloys, Monel, Al - Ni - Bronze, and HY - 100 steel. Powder samples were usually pressed into compacts which typically had a diameter of 1.25 - 1.33 inches. Typical compaction pressures were in the range 10 - 12 ksi applied uniaxially in a closed die. The compacts were then exposed to a variety of beam conditions. A commercial EB welder with a peak acceleration voltage of 150kV was used for these experiments. Typical beam powers were in the range 250 - 1000 W, and the beam size was usually 0.1 - 0.125 inches diameter. Typical beam travel velocities were 30" / min - 50" / min, or 1.3 cm / s - 2.1 cm / s. The actual beam had an annular shape formed by scanning a "pencil point" beam (0.020" diameter) in a larger circular pattern. This pattern could then be scanned across the powders, effectively producing a larger beam size. Also, a "line scan" was tried on some samples. Both of these scan patterns are discussed in Appendix A. These patterns are shown again below.

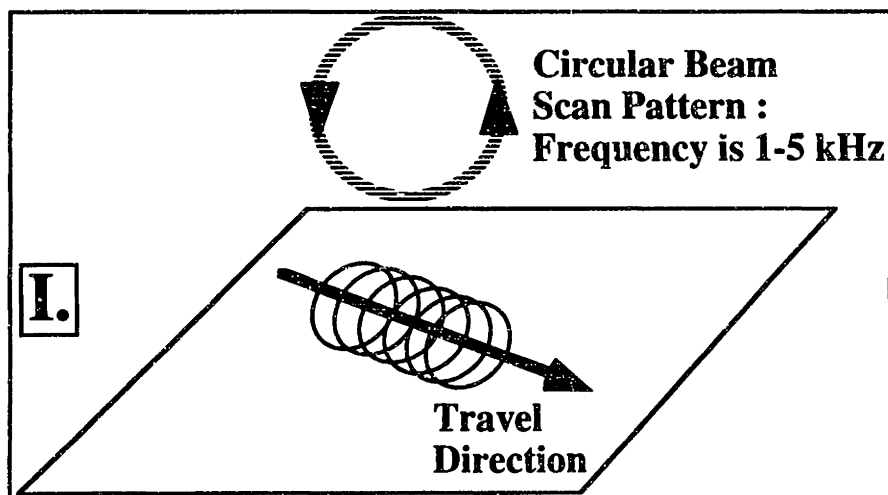


**FIGURE 3.1**  
**Circular Scan Pattern for**  
**Commercial EB Welder - PTR Machine**

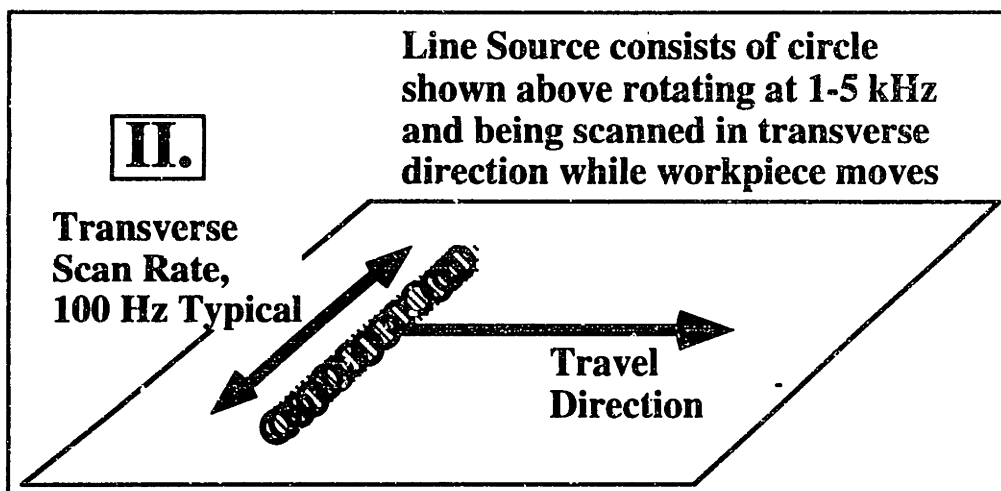


**FIGURE 3.2**  
**"Line Source" Consisting of Scanning Circular Source**  
**Commercial EB Welder - PTR Machine**

The table below shows the particle size, manufacturer, and brief description of morphology for all the powder materials used in this work.

**TABLE 3.1**  
**Powders Used in this Work**

Material	Manufacturer	Particle Size	Comments
Al	Alcan-Toyo	-100 mesh	irregular particles
Cu	Johnson Matthey	-325 mesh	spherical particles
Fe : MH-100	Hoeganaes	-100 mesh	irregular particles
Fe	Johnson Matthey	-200 mesh	spherical particles
Ni	INCO / Novamet	7 $\mu\text{m}$ average dia.	irregular particles
Ti	Johnson Matthey	-325 mesh	irregular particles
TiC	CERAC	-325 mesh	irregular particles
HY-100	unknown	-100 mesh	irregular particles

The powder systems described above will not be further discussed. Some of the microstructures were interesting, as in the case of HY-100 (high yield 100, i.e. Y.S. = 100 ksi) steel, in which very fine grain sizes resulted from EB re-melting. This is to be expected, however, and is entirely consistent with the rapid cooling rates associated with energy beam processing. The microstructure of the HY-100 power melt is shown in the pictures below. The primary melt looks very much like a weld solidification structure, but the regions that were re-melted and rapidly solidified exhibit a much finer grain size. This observation is related to the thermal conductivity of the powder bed. The thermal conductivity of the powders will determine the cooling rate of the melt, and hence the scale of the microstructure. The thermal conductivity of a porous, unsintered powder bed in vacuum can be 100 - 1000 times less than that of the corresponding fully dense solid material [MASAMUNE & SMITH (1963)]. The re-melt occurs in regions that have already been melted and hence have a higher thermal conductivity. This accounts for the rapid quench and finer structure.

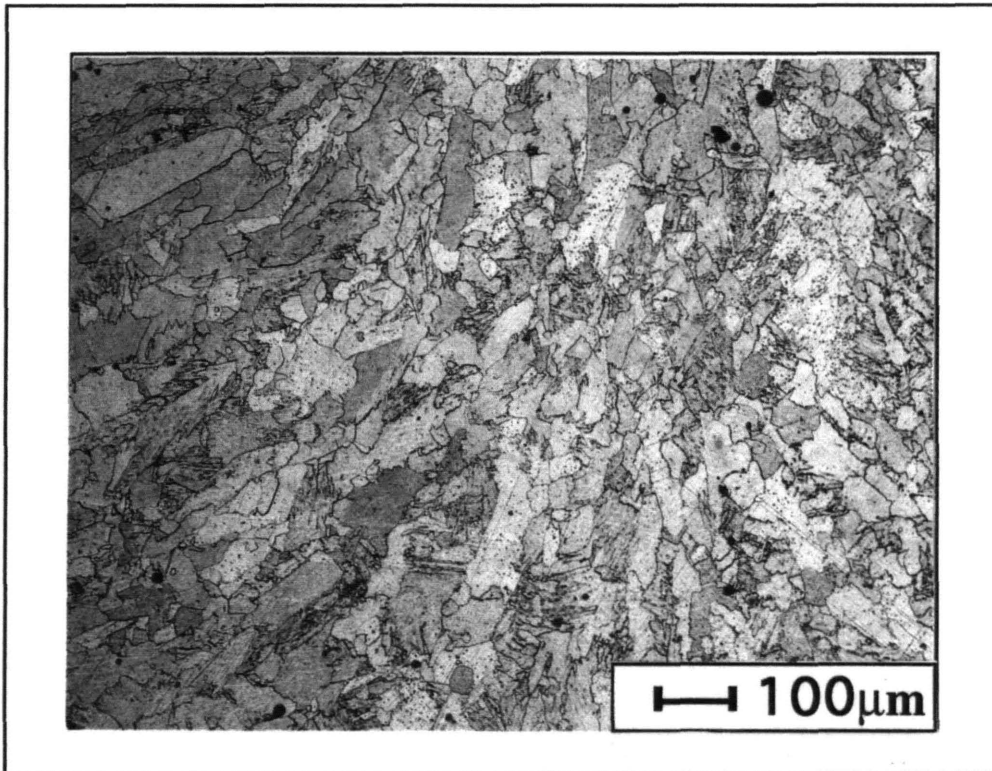


**FIGURE 3.3**  
**Microstructure of Primary Melt in HY-100 Steel, 100X**  
**EB Melting of HY-100 Powder Compact**

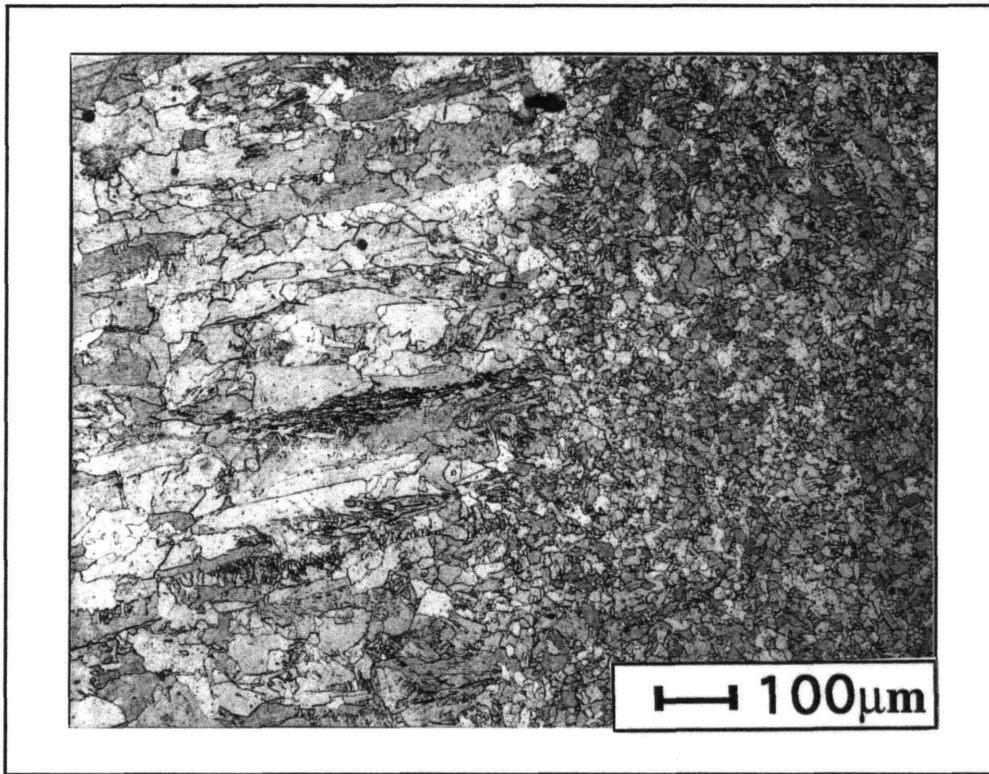


**FIGURE 3.4**  
**Microstructure of Re-melt Region in HY-100 Steel, 100X**  
**EB Melting of HY-100 Powder Compact**

### 3.3 Properties of Selected Aluminides

The structures of several common aluminides are summarized below.

**TABLE 3.2**  
**Structures of Aluminides**  
**Adapted from METALS HANDBOOK - DESK EDITION (1985)**

Material	Strukturbericht Notation	Structural Prototype
FeAl	B2 (ordered bcc)	CsCl
Fe <sub>3</sub> Al	D0 <sub>3</sub> (ordered bcc) OR B2 (ordered bcc)	BiF <sub>3</sub> OR CsCl
NiAl	B2 (ordered bcc)	CsCl
Ni <sub>3</sub> Al	L1 <sub>2</sub> (ordered fcc)	AuCu <sub>3</sub>
TiAl	L1 <sub>0</sub> (ordered tetragonal)	AuCu
Ti <sub>3</sub> Al	D0 <sub>19</sub> (ordered hcp)	Ni <sub>3</sub> Sn
TiAl <sub>3</sub>	D0 <sub>22</sub> (ordered tetragonal)	Al <sub>3</sub> Ti

It is possible to form a range of solid solution alloys in several aluminide systems while maintaining LRO (long range order). For example, in Ni<sub>3</sub>Al, Cu and Co will substitute Ni, whereas Ti and V will substitute for Al. Fe and Cr can be on either sublattice [see OHIAI, OYA, & SUZUKI (1984)]. In Fe<sub>3</sub>Al, Ti, Mo, and Si are the most effective as solid solution strengthening agents [DIEHM & MIKKOLA (1987)]. Cr is often added to iron aluminides to provide additional corrosion protection [SIKKA & LIU (1994)]. Microalloying with boron has shown to be effective in improving ductility for NiAl and Ni<sub>3</sub>Al, as well as for the iron aluminides. In iron aluminides, there is a transformation from the D0<sub>3</sub> structure to the B2 structure. The temperature associated with this transition is approx. 540 °C for alloys with 20 at. % - 28 at. % Al [ ALLEN & CAHN (1975)]. Addition of more than 32 at. % Al results in stable B2 at room temperature. The temperature of this transition can be increased by as much as 250 °C by alloying additions of Si, Ti, and Mo [FORTNUM & MIKKOLA (1987)].

The aluminide intermetallic compounds have potential use as high temperature structural materials in a wide range of applications [ SIKKA & LIU (1994) and GERMAN, BOSE, & STOLOFF (1989)]. In this present work, five compounds were synthesized, and all of these were also tested as matrix materials for intermetallic matrix composites (IMCs). The complete set of aluminide - based systems that were investigated is : FeAl, Fe<sub>3</sub>Al, NiAl, Ni<sub>3</sub>Al, FeAl + TiC, Fe<sub>3</sub>Al + TiC, NiAl + TiC, Ni<sub>3</sub>Al + TiC, and TiAl + TiC. Some of the basic properties of the aluminides are given in the tables below. Emphasis will be placed on iron and nickel aluminides.

**TABLE 3.3**  
**Aluminide Intermetallic Compounds**  
**Adapted from VEDULA and STEPHENS (1987)**

Material	Crystal Structure	Melting Point, °C	Density, g / cc
TiAl	L10	1460	3.9
Ti <sub>3</sub> Al	DO <sub>19</sub>	1600	4.2
FeAl	B <sub>2</sub>	1330	5.6
Fe <sub>3</sub> Al	DO <sub>3</sub>	1540	6.7
NiAl	B <sub>2</sub>	1640	5.9
Ni <sub>3</sub> Al	L1 <sub>2</sub>	1390	7.5

**TABLE 3.4**  
**Thermal Expansion Data for Iron and Nickel Aluminide Alloys**  
**Adapted from PORTER & MAZIASZ (1993)**

Alloy and Composition, atomic %	Thermal Expansion in ppm / °C		
	at 100 °C	at 500 °C	at 1000 °C
Fe <sub>3</sub> Al nominal, 28% Al, 5% Cr	15.4	19.2	23.4
FeAl nominal, 35.8% Al	18.3	20.6	23.8
Ni <sub>3</sub> Al nominal, 15.9% Al, 8% Cr	12.8	14.0	16.6



The thermal expansion of 304 stainless for comparison is 17.2 ppm/°C at 100°C and 18.4 ppm/°C at 538°C. It is therefore seen that iron aluminides have similar thermal expansion properties as those of 304 stainless (and most 300 series steels for that matter). Some room-temperature mechanical properties are listed below.

**TABLE 3.5**  
**Mechanical Properties of Iron Aluminides**  
 Adapted from SIKKA & LIU (1994)

Alloy and Test Environment	Elongation, %	Yield Strength, MPa (ksi)	Ultimate Tensile Strength, MPa (ksi)
<b>Fe<sub>3</sub>Al, annealed 1 h @ 850°C and 5 d @ 500°C</b>			
tested in air	3.7	279 (40.5)	514 (74.5)
tested in vacuum, 10 <sup>-4</sup> Pa	12.4	316 (45.8)	813 (117.9)
tested in water vapor	2.1	322 (46.7)	439 (63.7)
<b>FeAl</b>			
tested in air	2.2	360 (52.2)	412 (59.7)
tested in vacuum, 10 <sup>-4</sup> Pa	5.4	352 (51.1)	501 (72.7)
tested in water vapor	2.4	368 (53.4)	430 (62.4)

**TABLE 3.6**  
**Oxidation Properties of Iron Aluminides :**  
**Parabolic Rate Constants for Fe-Cr-Al Alloys in Dry Air at 800 °C**  
 Adapted from TORTORELLI & DeVAN (1992)

Alloy Composition, atomic %, bal. is Fe	Parabolic Rate Constant, mg <sup>2</sup> • cm <sup>-4</sup> • h <sup>-1</sup>
28% Al	(2.3±1.1) X 10 <sup>-5</sup>
28% Al, 2% Cr	1.3 X 10 <sup>-5</sup>
28% Al, 4% Cr	(1.8±0.7) X 10 <sup>-4</sup>
28% Al, 10% Cr	2.0 X 10 <sup>-4</sup>
20% Cr, 12% Al	1.5 X 10 <sup>-5</sup>

The parabolic rate constant of course assumes parabolic oxidation kinetics, in which case the change in weight (gain) per unit area is given by :

$$\left(\frac{\Delta W}{A}\right)^2 = K_{parabolic} \cdot t \quad (3.1)$$

$$(\text{weight change per unit area})^2 = (\text{rate const.}) \cdot (\text{exposure time})$$

For coating applications, the wear characteristics are just as important as the oxidation resistance. JOHNSON & MIKKOLA et al (1990) has measured the resistance of various aluminides to both cavitation erosion and abrasive wear.

These tests were done in accordance with ASTM Standard G 32 - 85 (1985) for cavitation erosion and ASTM Standards G 65 - 80 (1980) and B 611 - 76 (1976) for abrasive wear. Cavitation erosion is an important consideration in hydrodynamic and marine applications. Abrasive wear can be a factor in many applications, especially those in mining, petrochemicals, excavation, etc. The results of this study are summarized below.

**TABLE 3.7**  
**Cavitating Jet Erosion Rates of Aluminides**  
**as Compared to Commercial Alloys**  
**Adapted from JOHNSON & MIKKOLA et al (1990)**

Alloy	Cavitation Erosion Rate, mg / hr.
Stellite 21 (weld overlay)	7.3
308 Stainless (weld overlay)	31.6
Nitronic 60	12.8
EPRI / AMAX NOREM B4	4.4
nickel aluminide (87.5 wt. % Ni, 12.0 wt. % Al, 0.5 wt. % Hf) - P/M cold-worked alloy	1.4
nickel aluminide, same alloy as above, but plasma spray deposited	7.0
iron aluminide (pure Fe <sub>3</sub> Al, weld overlay)	11.6

For various nickel aluminide - based alloys, the abrasive wear and erosion properties are given below :

**TABLE 3.8**  
**Erosion and Abrasive Wear Resistance of Ni<sub>3</sub>Al - Based Alloys**  
**Adapted from JOHNSON & MIKKOLA et al (1990)**

Alloy	Abrasive Wear Rate, g / hr.	Erosion Rate, mg / hr.
12.7 wt. % Al, P/M processed	6.72	0.92
10.1 wt. % Al, 8.5 wt. % Cr, P/M processed	7.45	1.00
9.0 wt. % Al, 11.3 wt. % Fe, &.0 Wt. % Cr, P/M processed	7.58	1.49

For iron aluminide, similar data is shown below.

**TABLE 3.9**  
**Erosion and Abrasive Wear Resistance of Fe<sub>3</sub>Al - Based Alloys**  
 Adapted from JOHNSON & MIKKOLA et al (1990)

Alloy	Abrasive Wear Rate, g / hr.	Erosion Rate, mg / hr.
15.8 wt. % Al, 0.1 wt. % Ti, P/M processed	4.37	2.38
15.5 wt. % Al, 0.5 wt. % Mo, 4.7 wt. % Ti, P/M processed	3.25	0.99
20.9 wt. % Al, 0.54 wt. % Hf, 3.7 wt. % Mo, 3.8 wt. % Ti, P/M processed	2.75	0.42

The study by JOHNSON & MIKKOLA et al (1990) has several important conclusions that are significant for aluminide coating applications. Firstly, in both iron and nickel aluminides, fine-grained P/M materials have the best wear properties. Secondly, alloying additions that increase the temperature of the D0<sub>3</sub> to B<sub>2</sub> transition have a favorable effect on the wear and erosion properties. This is significant in that it can serve as a guideline for alloy design for wear applications.

### 3.4 Reactive Synthesis of Aluminides

Processing conditions will dramatically affect the mechanical properties of intermetallics in general. For example, finer grains result in stronger materials for the B<sub>2</sub> aluminides (FeAl, NiAl) at temperatures as high as 70% of melt temperature [VEDULA ET AL (1985)]. In iron aluminides, recent studies [LIU (1993)] have demonstrated that environmental embrittlement (water vapor reacts with Al to release hydrogen, which then embrittles material) is the major cause of ductility loss at room temperature for FeAl and Fe<sub>3</sub>Al. FeAl with greater than 38 at. pct. Al is *intrinsically* brittle, however [LIU (1993)]. Processing strategies to alleviate ductility limitations include [LIU (1993)]:

- chromium additions to form protective oxide layers
- thermomechanical grain refinement
- refinement of grain structure by second phase particle additions (dispersoids / particulates)
- grain boundary strengthening by boron microalloying
- reduce hydrogen solubility / diffusivity by alloying additions

Reaction sintering has several attractive features which may address the issues listed above. As compared to casting processes or HIPing, the processing temperatures are potentially lower and the thermal gradients during processing can be steeper. Both of these factors can contribute to the formation of a fine microstructure. Some of the potential disadvantages of reaction synthesis are [DUNAND (1994)] :

- porosity
- incomplete mixing and extent of reaction
- geometry control
- ability to control the location of the reaction front

The e-beam method proposed in this current work overcomes some of these problems. The e-beam allows control over the reaction front while maintaining a low overall sample temperature. The reacted zone is in contact with a relatively cold unreacted region thus allowing for rapid cooling and a fine microstructure. Heating and convection within the affected region is sufficient to fully mix and react the elemental powders (at least in the case of iron aluminides). Secondary phase particles were successfully introduced, and these additions did result in grain refinement. Lastly, full density was achieved within the melt regions in the FeAl and Fe<sub>3</sub>Al systems. This was not the case in some of the other systems tested. For iron aluminides, the e-beam technique seems to be a very good method for obtaining full density, full extent of reaction, control over the location of reaction, and a low average processing temperature. The EB reaction synthesis process as applied to a variety of aluminides is summarized below.

**TABLE 3.10**  
**Summary of Experimental Results in**  
**EB - Assisted Reaction Synthesis of Aluminides**

Material System	Comments
FeAl	Control over reaction front, full density, and full extent of reaction were achieved, but cracking was observed. This is consistent with the intrinsic brittleness of FeAl with more than 38 at. % Al.
FeAl + TiC	Control over reaction front position, full density, and full extent of reaction were achieved. Microstructure exhibited grain refinement. Cracking was reduced, but not eliminated.

**TABLE 3.10 Continued**

Fe <sub>3</sub> Al	Single pass : columnar grains with well-developed substructure. Multipass : some large recrystallized grains (200 μm +) with well-developed substructure. No trouble with cracking.
Fe <sub>3</sub> Al + TiC	Grains did show some refinement, but substructure network is extensive and very complex. Substructure dimension is about 5 μm and less.
NiAl	System was too exothermic ; SHS ensued under all beam operating conditions tested. Still too exothermic even when unreacted powders were mixed with up to 50% pre-reacted powders.
Ni <sub>3</sub> Al	Under low beam fluences, a complete scan across 2 cm wide sample was possible, but with scan rates slower than 1.25 cm / s and 1kW, system was too exothermic. Scan rates that did work did not produce fully density. Also secondary Al-rich phases were present.
TiAl	Selective reaction synthesis was possible. Further optimization could result in fully reacted and mixed coating.

The EB-based reaction synthesis technique discussed here constitutes one of the more significant contributions of this work. This process was independently discovered during the course of this work, and it has recently come to the author's attention that there have been other similar experiments done in the past. ABOUD & WEST (1990) and HIROSE, UEDA & KOBAYASHI (1993) have all investigated the formation of a reaction - synthesized titanium aluminide layer through surface alloying of titanium samples with aluminum powders. These microstructures were not single phase, but did exhibit improved wear and corrosion resistance as compared to the uncoated substrates [HIROSE, UEDA, & KOBAYASHI (1993)]. As mentioned in the table above, titanium aluminides are a very good candidate for the electron beam selective reaction sintering process. ABOUD & WEST (1990) and HIROSE, UEDA, & KOBAYASHI (1993) have had success with these aluminides, and it is certainly possible to reproduce these results with e-beams.

Through electron microprobe analysis, the compositions of the EB - processed melts were determined. The results of the compositional analysis are shown below. These measurements were made at the MIT Geology and Earth Sciences Dept. using a JEOL Superprobe 733. The atomic fractions have been rounded off to the nearest tenth of one percent. The cumulative estimated error from all sources is  $\pm 1.5$  atomic percent. This error is due to oxide layers, excluded trace elements, counting errors, and is also related to the assumed form of the empirical-coefficient analysis equation which is chosen [for a more detailed discussion of quantitative X-Ray analysis, see CULLITY (1978)].

**TABLE 3.11**  
**Electron Microprobe Composition Analysis of**  
**Reaction - Synthesized Aluminides**  
**(Analysis performed by Neel Chatterjee, MIT)**

Compound (nominal comp.)	Atomic Percentages		
	Al	Fe	Ni
FeAl	49.7	50.3	---
FeAl	49.5	50.5	---
FeAl	48.9	51.1	---
FeAl	48.3	51.7	---
FeAl	51.7	48.3	---
<b>Mean FeAl</b>	<b>50.4</b>	<b>49.6</b>	---
Fe <sub>3</sub> Al	23.9	76.1	---
Fe <sub>3</sub> Al	23.7	76.3	---
Fe <sub>3</sub> Al	24.1	75.9	---
<b>Mean Fe<sub>3</sub>Al</b>	<b>23.9</b>	<b>76.1</b>	---
NiAl	48.7	---	51.3
NiAl	49.4	---	50.6
NiAl	49.4	---	50.6
NiAl	49.9	---	50.1
NiAl	48.9	---	51.1
NiAl	50.7	---	49.3
<b>Mean NiAl</b>	<b>49.5</b>	---	<b>50.5</b>
Ni <sub>3</sub> Al	24.2	---	75.8
Ni <sub>3</sub> Al	24.4	---	75.6
Ni <sub>3</sub> Al	24.5	---	75.5
<b>Mean Ni<sub>3</sub>Al</b>	<b>24.4</b>	---	<b>75.6</b>

The phase diagram for the Fe - Al system is shown below.

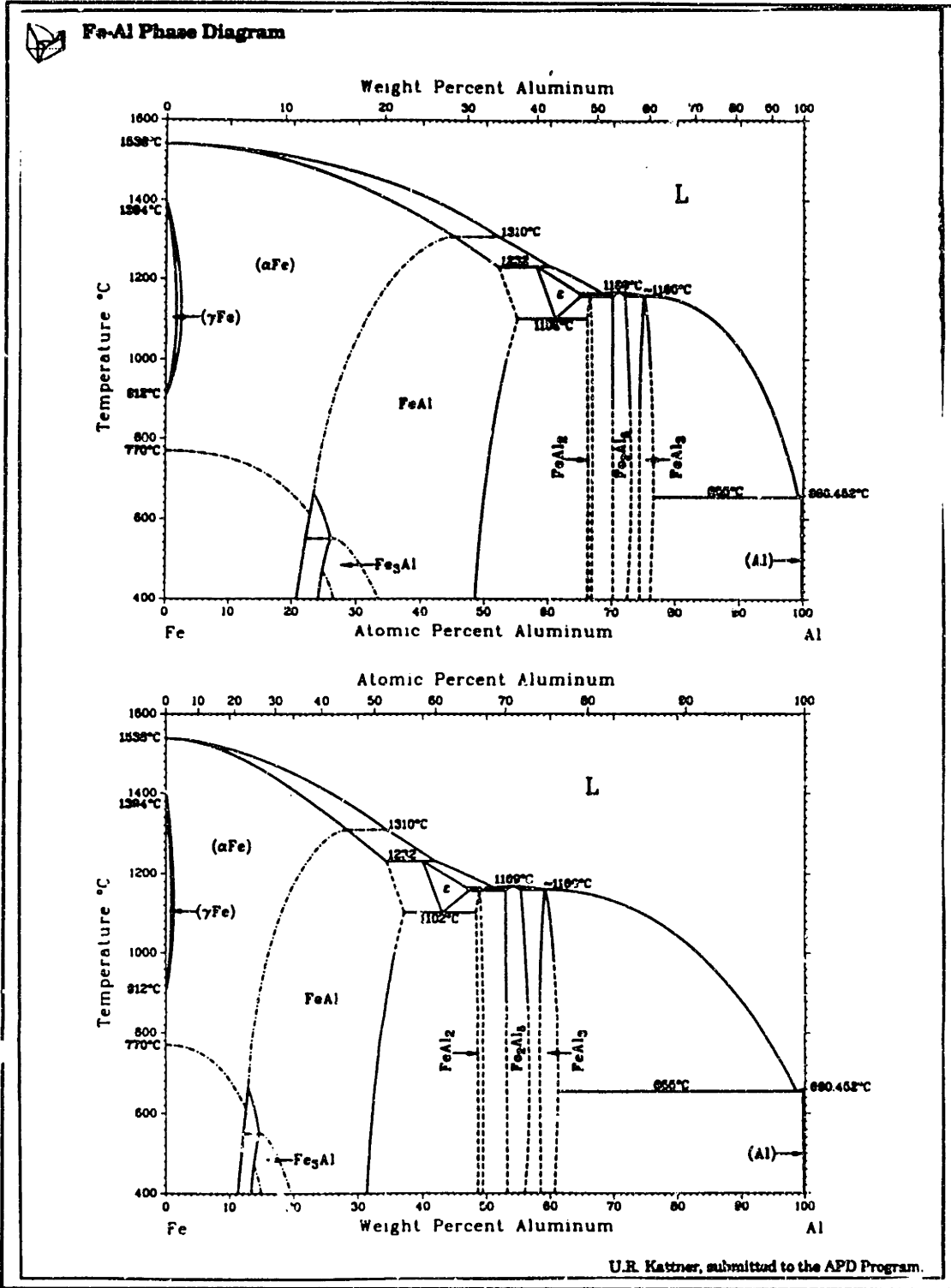


**FIGURE 3.5**  
**Fe - Al Phase Diagram**  
 Reprinted with Permission from  
 MASSALSKI (1990)

The focus in this thesis will be on iron aluminides. By looking at the composition analysis shown above and comparing it the Al-Fe phase diagram shown above, it is clear that the Fe<sub>3</sub>Al material is actually in the dual - phase region  $\alpha$ Fe + Fe<sub>3</sub>Al. Similarly, the FeAl synthesized lies just at the boundary of two phase fields : FeAl and FeAl + FeAl<sub>2</sub>. This is consistent with the observation that the FeAl material is slightly Al-rich (although the error bars associated with the microprobe measurements are greater than the difference between the Fe and Al atomic percentages). The coating application started initially as 25 at. % Al and 75 at. % Fe in powder form. Since the coating was applied to steel, additional iron was dissolved, and the resulting coating was entirely within the  $\alpha$ Fe phase field. This is also shown by microprobe composition analysis, which is presented below in a later section. To get iron aluminides, perhaps pure Al on to steel would result in a mix of phases, some of which would include FeAl and Fe<sub>3</sub>Al. The three Fe - Al materials synthesized in this work are listed in the table below, together with their predicted phase equilibria. X-ray phase identification did confirm the presence of the phases listed below. A more precise quantitative X-ray analysis was not undertaken.

**TABLE 3.12**  
**Fe-Al Materials in this Work and Phase Balances**

Starting Materials	Phase Balance as per Phase Diagram	Designation for latter Discussion
Pure Fe and Al powders, 25 at. % Al	final average composition is 23.9 ( $\pm$ 1.0) at. % Al : lies within $\alpha$ Fe + Fe <sub>3</sub> Al Dual Phase Region	Material A
Pure Fe and Al powders, 50 at. % Al	final average composition is 50.4 ( $\pm$ 1.0 ) at. % Al : lies within FeAl + FeAl <sub>2</sub> Dual Phase Region	Material B
Pure Fe and Al powders on steel sheet, powders initially had 25 at. % Al	final average composition is 19.8 at. % Al : lies within $\alpha$ Fe Region	Material C

The microstructures of Materials A and B are shown in the following series of pictures. Material C will be discussed in the next section. These pictures also show the grain refinement effect resulting from TiC additions. The macrostructure of a single - pass melt in material A is shown in Figure 3.6. It is seen that the melt region is characterized by columnar grains that are a maximum of 0.125 cm in length. At higher magnifications, these columnar grains are seen to contain a well - developed substructure. This is illustrated in Figure 3.7 - 3.9. In samples that were subjected to multipass melting / sintering, the columnar structure was replaced by an equiaxed structure in the regions of overlap between successive passes. This is illustrated in Figures 3.10 and 3.11. Figure 3.10



shows the boundary between passes and the transition to equiaxed grains in the interpass remelt region. It is seen that these equiaxed grains also possess a substructure. This is shown in Figure 3.11. Figure 3.12 shows the melt centerline and the two impinging solidification fronts. There are cracks and grain boundaries visible in this picture. Figure 3.13 shows another region near the melt centerline at higher magnification. Figure 3.14 shows a crack in the surface of Material A near the edge of the melt. The residual stresses from solidification are expected to be the greatest near the edges, and thus the likelihood of such cracking is enhanced.

Figure 3.15 shows the grain size distribution in a multipass specimen of Material B. As was the case with Material A, there are columnar grains in the original primary melt structure, and equiaxed grains in the remelt regions. In Material B, there was no observed substructure. Figure 3.16 shows the remelt grains at higher magnification. Material B was much more susceptible to cracking and centerline porosity. Figures 3.17 and 3.18 are nearly at the same magnification, and they show centerline porosity in the remelt region (finer equiaxed grains). Figure 3.17 shows the surface of the melt whereas 3.18 is a section below the surface.

Both Materials A and B showed grain refinement upon addition of TiC. Figure 3.19 shows the microstructure of Material A upon addition of TiC. Extensive solidification substructure in the form of dendrites is visible in this figure. Comparing the size of these dendrites to those in the single - pass melt, it is seen that the solidification microstructure is approximately 100 times finer. Figure 3.20 shows a similar picture for Material B. In Material B with TiC additions, the grains are clearly discernible, and the grain size refinement is a factor of 5 to 10. In both Material A and B with TiC additions, there was no apparent cracking in the as-solidified structures. Figure 3.21 shows a TiC particle at high magnification protruding from the surface of Material A. Wetting of the TiC by the melt in Material A and B was excellent, as evidenced by Figure 3.21.

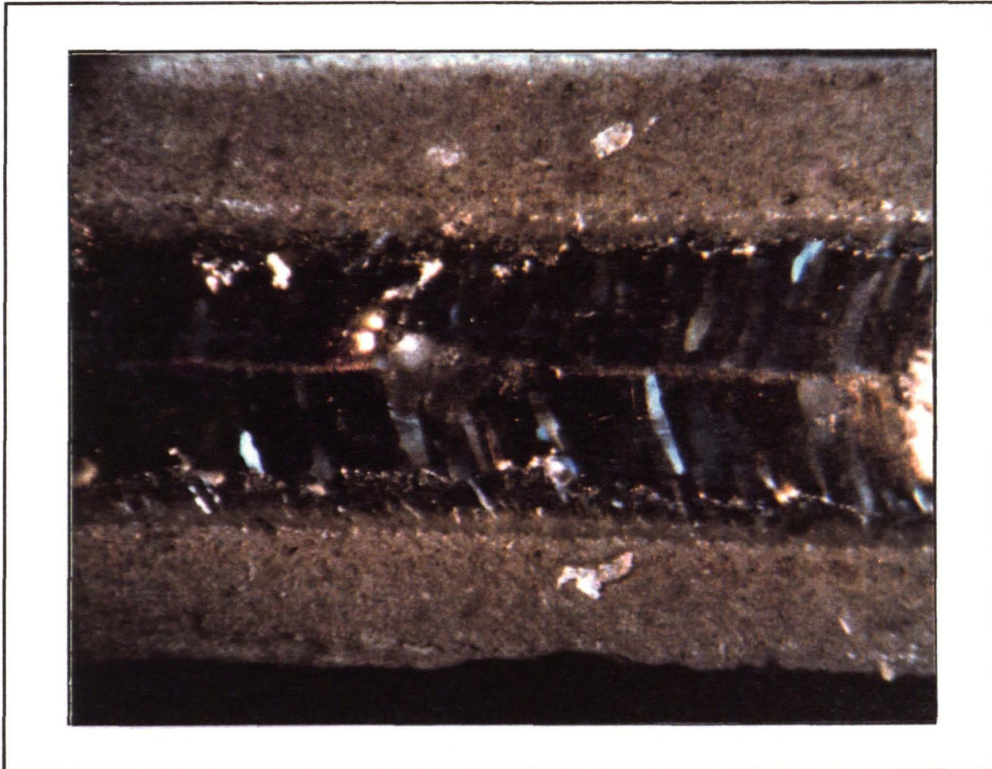


**FIGURE 3.6**  
**Macrostructure of Material A, 16X**  
**EB - Assisted Reaction Synthesis**

Although this melt pattern appears similar to an epitaxial growth pattern, it cannot be strictly classified as such since the columnar grains shown border unreacted elemental powders. The growth pattern is predominantly dictated by the heat flow and the shape of the melt pool generated by the traveling e-beam.

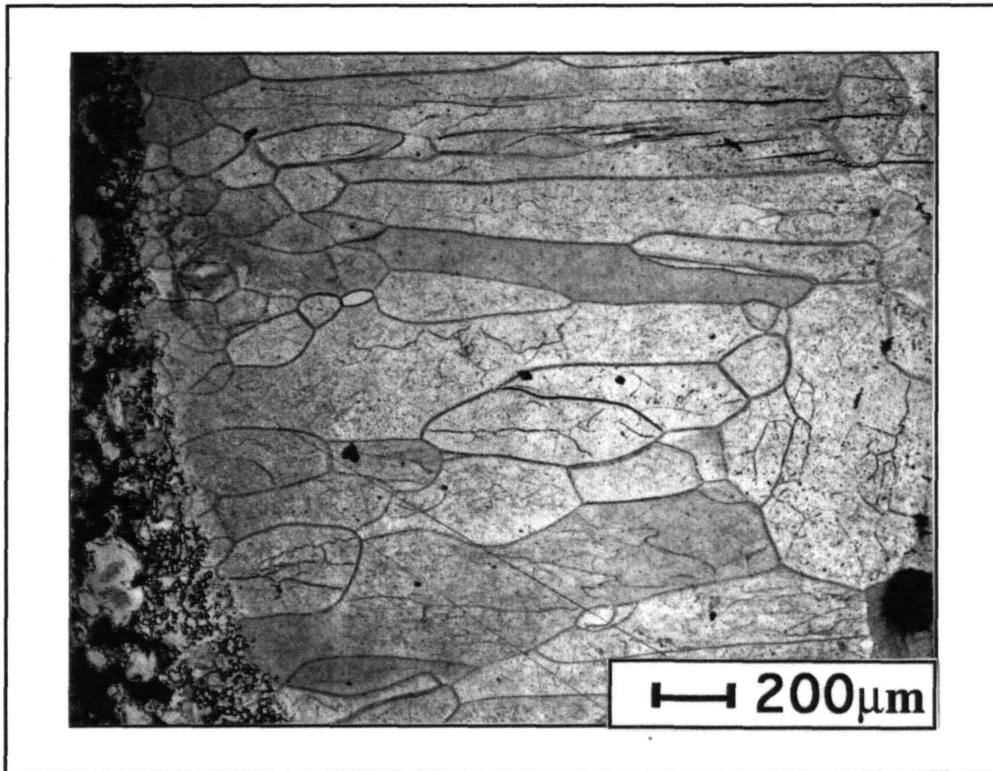


**FIGURE 3.7**  
**Microstructure of Material A, 50X**  
**Single-Pass Melt,**  
**EB - Assisted Reaction Synthesis**

This figure shows more clearly the interface between the columnar grains and the powder precursor in this single-pass melt in Material A. In some regions, there does appear to be a chill zone, whereas in other parts the columnar grains extend directly back to the interface with the powder material. The well-developed substructure is seen in this figure and the next two as well.

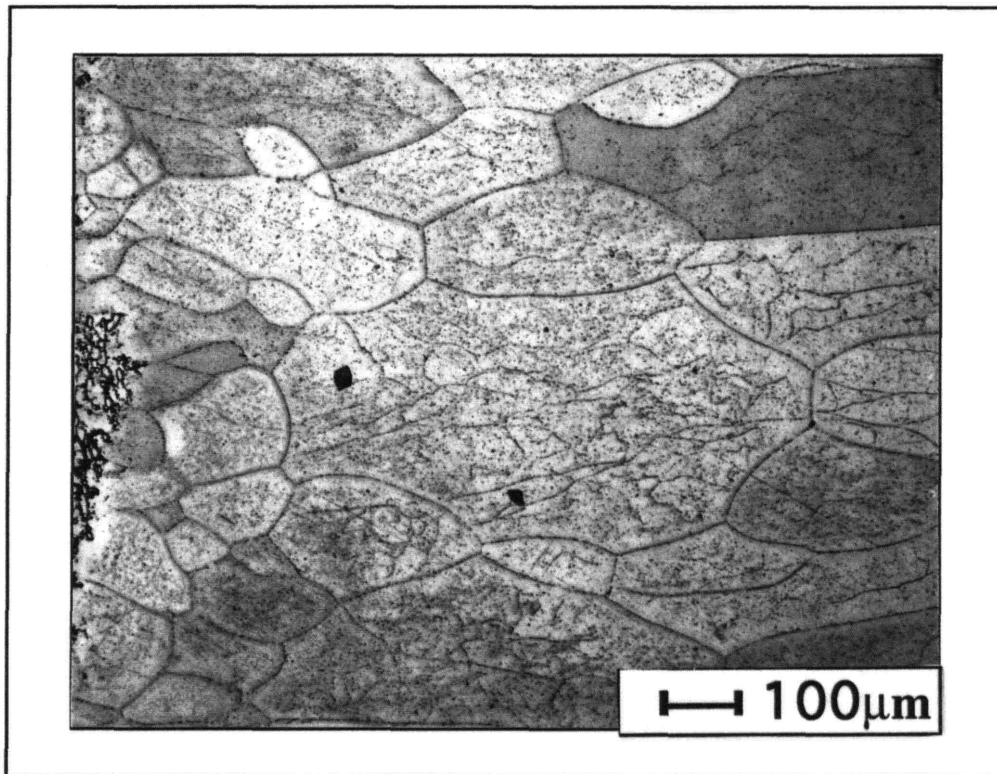


**FIGURE 3.8**  
**Microstructure of Material A, 100X**  
**Single -Pass Melt,**  
**EB - Assisted Reaction Synthesis**

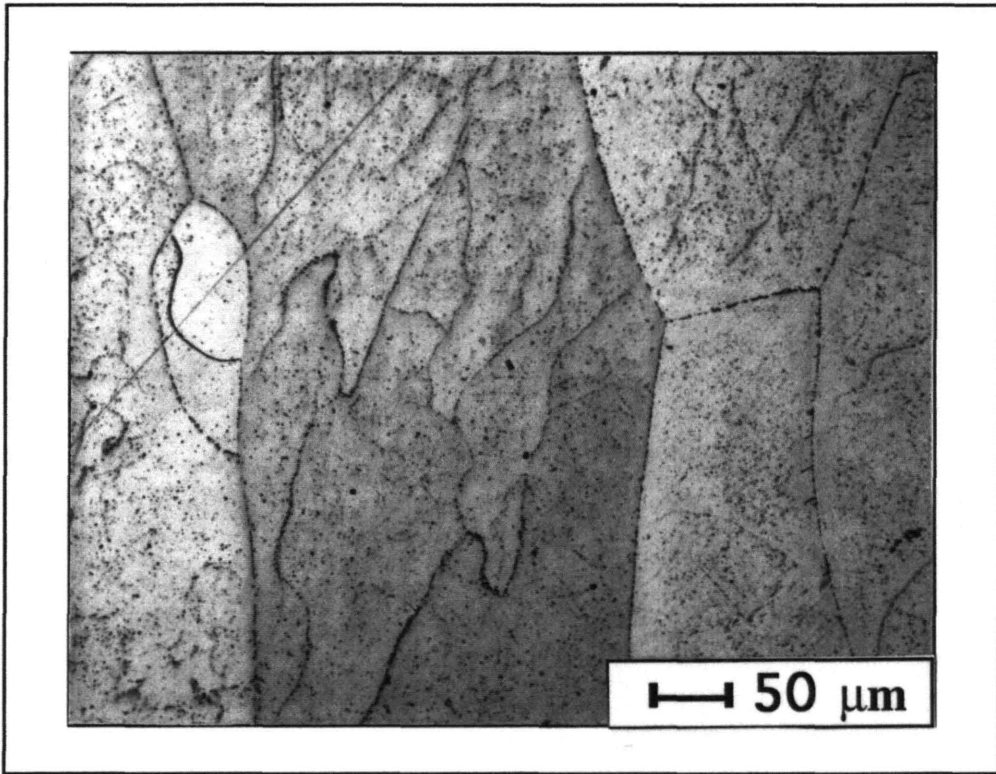


**FIGURE 3.9**  
**Microstructure of Material A, 200X**  
**Single-Pass Melt,**  
**EB - Assisted Reaction Synthesis**

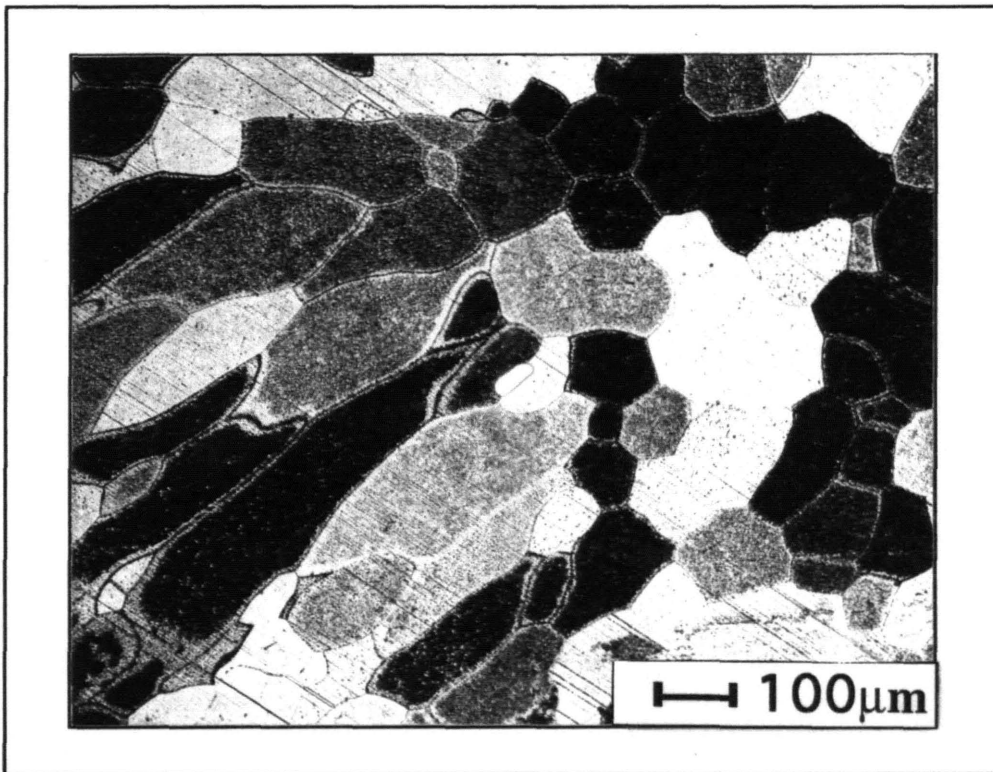


**FIGURE 3.10**  
**Microstructure of Material A, 100 X**  
**Multi-Pass Melt,**  
**EB Assisted Reaction Synthesis**

In this figure, the transition from a columnar grain structure to an equiaxed one is shown. This occurred in the remelt regions between overlapping passes. The remelt grains also exhibited a solidification substructure, as shown in the next figure.

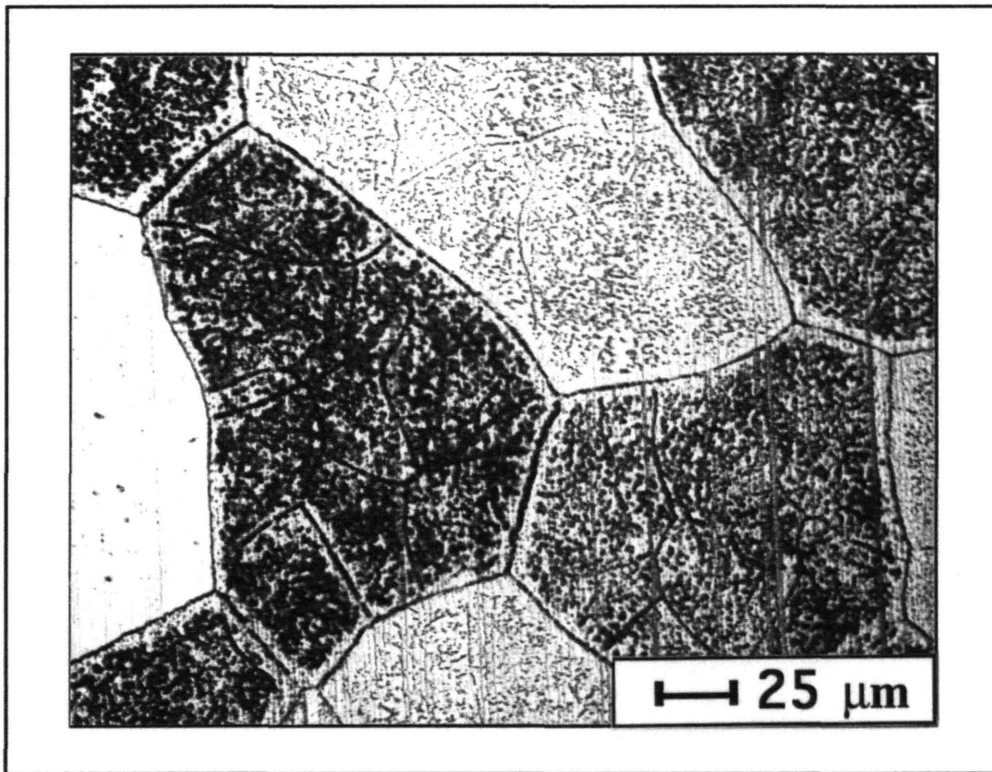


**FIGURE 3.11**  
**Microstructure of Material A, 400X**  
**Multi-Pass Melt,**  
**EB Assisted Reaction Synthesis**

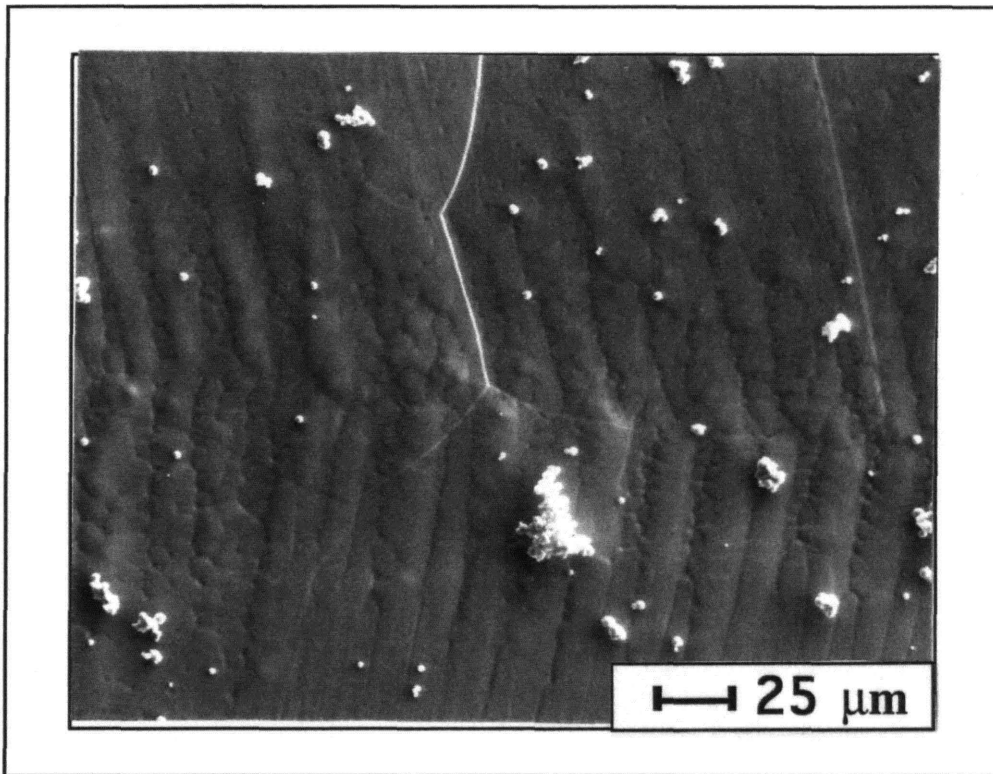


**FIGURE 3.12**  
**Surface Melt Features of Material A, 400X**  
**Single-Pass Melt,**  
**EB Assisted Reaction Synthesis**

This figure shows the centerline of a single-pass melt in Material A. The two solidification fronts are seen to impinge. Also, several grain boundaries are visible in this picture. The grains are long, narrow, and columnar as shown in Figure 3.6.



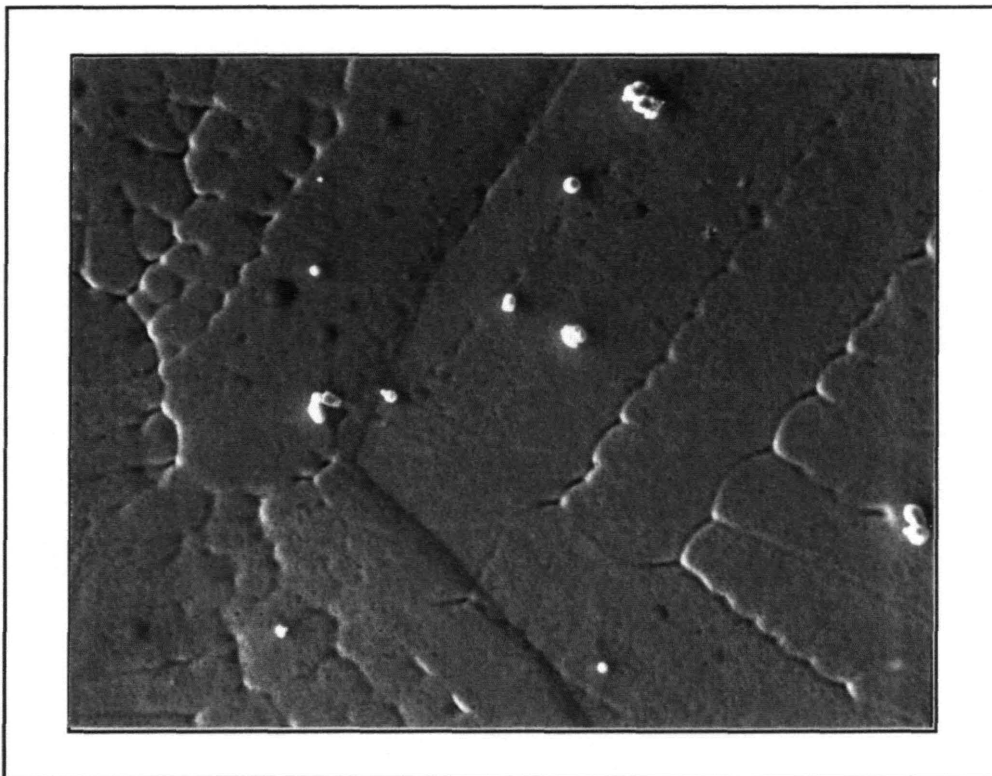


**FIGURE 3.13**  
**Surface Solidification features of Material A, 750X**  
**Single-Pass Melt,**  
**EB Assisted Reaction Synthesis**

This picture shows a close-up of one of the grain boundaries shown in the previous picture.

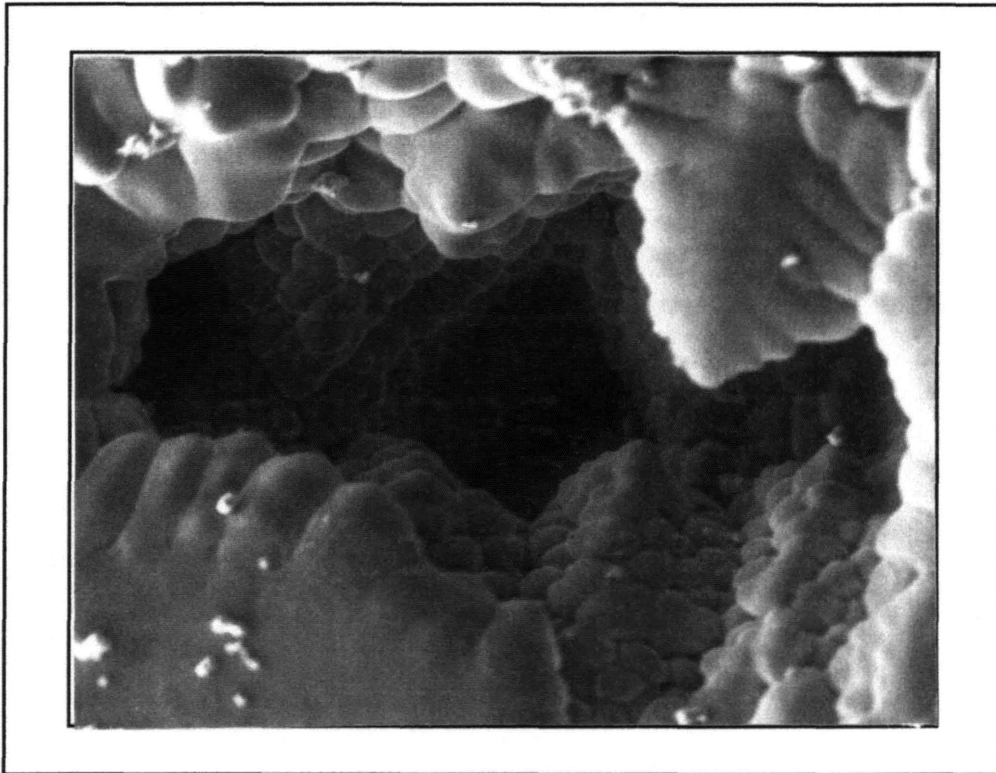


**FIGURE 3.14**  
**Surface Crack in Material A, 660X**  
**Single-Pass Melt,**  
**EB Assisted Reaction Synthesis**

Near the edges of the melt in Material A in the single-pass melt, there were some centerline cracks like the one shown above. This is to be expected, since the residual stresses will be tensile along the centerline and will be further accentuated near the edges. Also, the powder material surrounding the melt is far from fully dense, and it will experience greater thermal expansions / contractions than the corresponding solid material. This will make the residual stress issue worse.

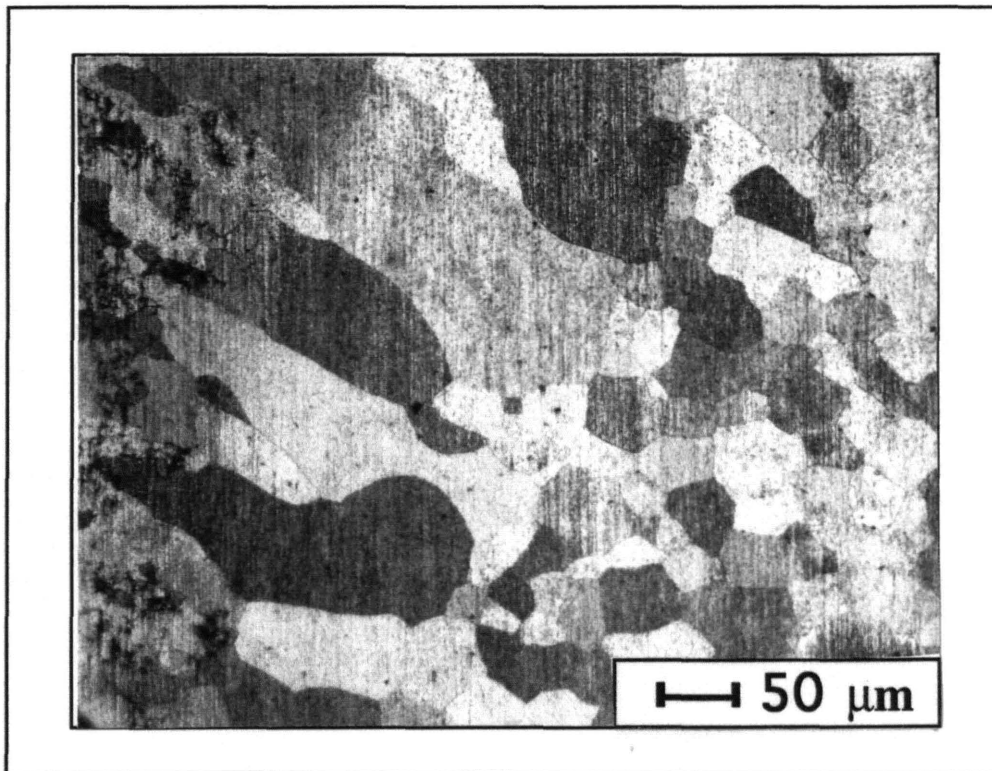


**FIGURE 3.15**  
**Microstructure of Material B, 200X**  
**Multi-Pass Melt,**  
**EB Assisted Reaction Synthesis**

Material B also exhibited a columnar primary melt structure. The remelt regions in multi-pass melts were equiaxed. Unlike Material A, Material B exhibited no solidification substructure. Also, Material B was much more susceptible to cracking, as is shown in the next few figures. This is consistent with the fact presented earlier that FeAl materials with more than 38 at. % Al are intrinsically brittle.

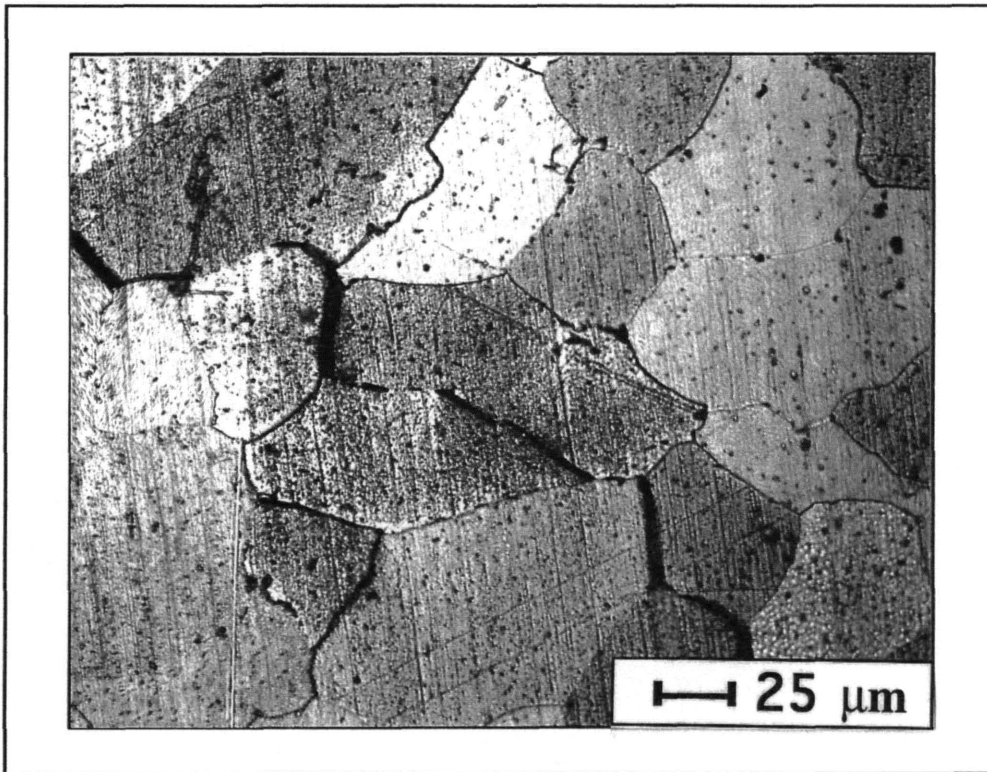


**FIGURE 3.16**  
**Microstructure of Material B, 400X**  
**Multi-Pass Melt,**  
**EB Assisted Reaction Synthesis**

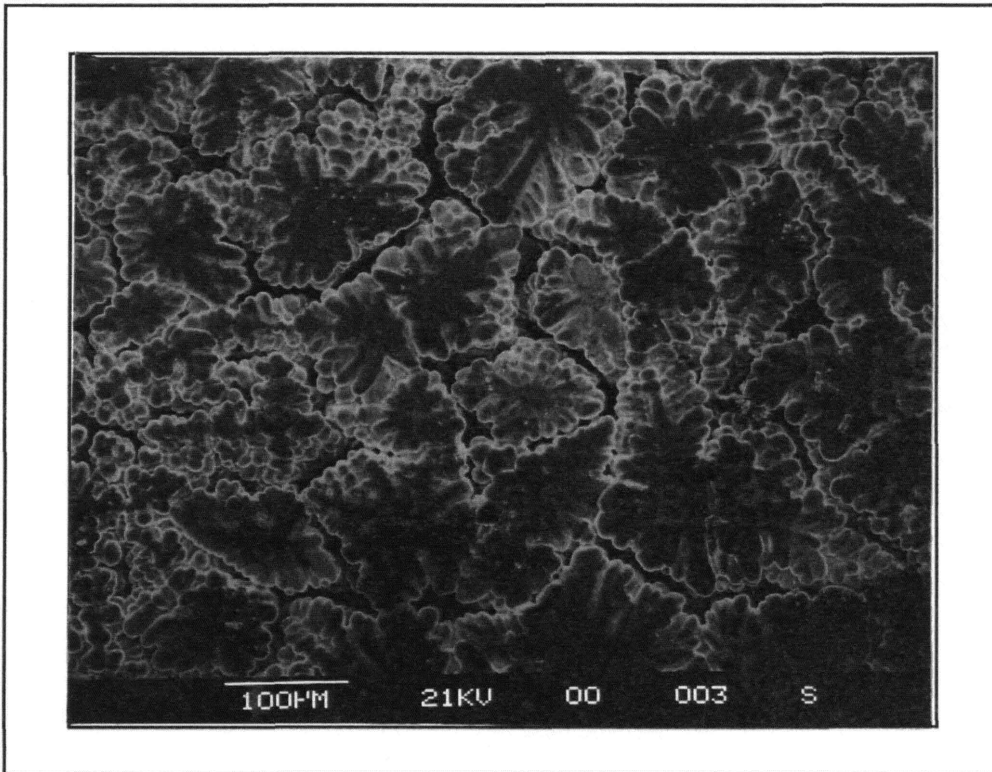


**FIGURE 3.17**  
**Surface Solidification Features in Material B, 150X**  
**Multi-Pass Melt,**  
**EB Assisted Reaction Synthesis**

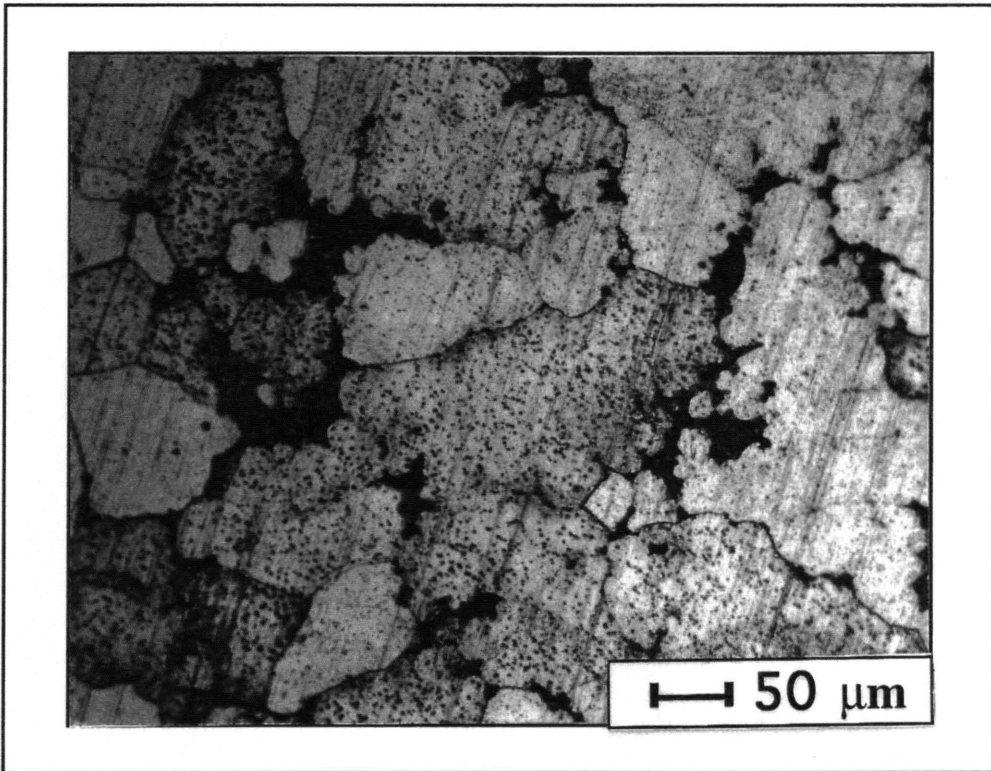


**FIGURE 3.18**  
**Centerline Porosity in Material B, 200X**  
**Multi-Pass Melt,**  
**EB Assisted Reaction Synthesis**

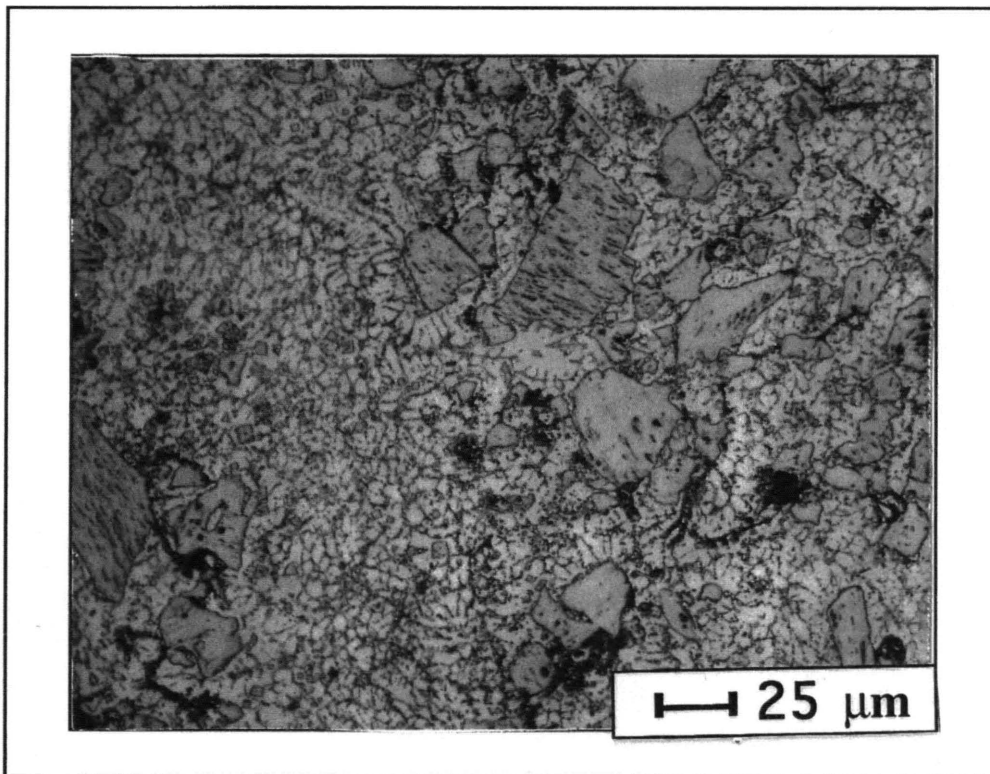


**FIGURE 3.19**  
**Microstructure of Material A + TiC, 400X**  
**Multi-Pass Melt,**  
**EB Assisted Reaction Synthesis**

This figure shows the grain refinement effect resulting from the addition of TiC to Material A. It is also interesting to note that there were no discernible variations in microstructure across the multi-pass melt. This suggests that TiC additions are a very effective nucleating agent, and this is seen in the figure above. The TiC particles have an average size of 10-30 microns, and the dendrites visible in the picture are also of that typical dimension. This is a reduction in dendrite size of about 100 as compared to the case of Material A without TiC.

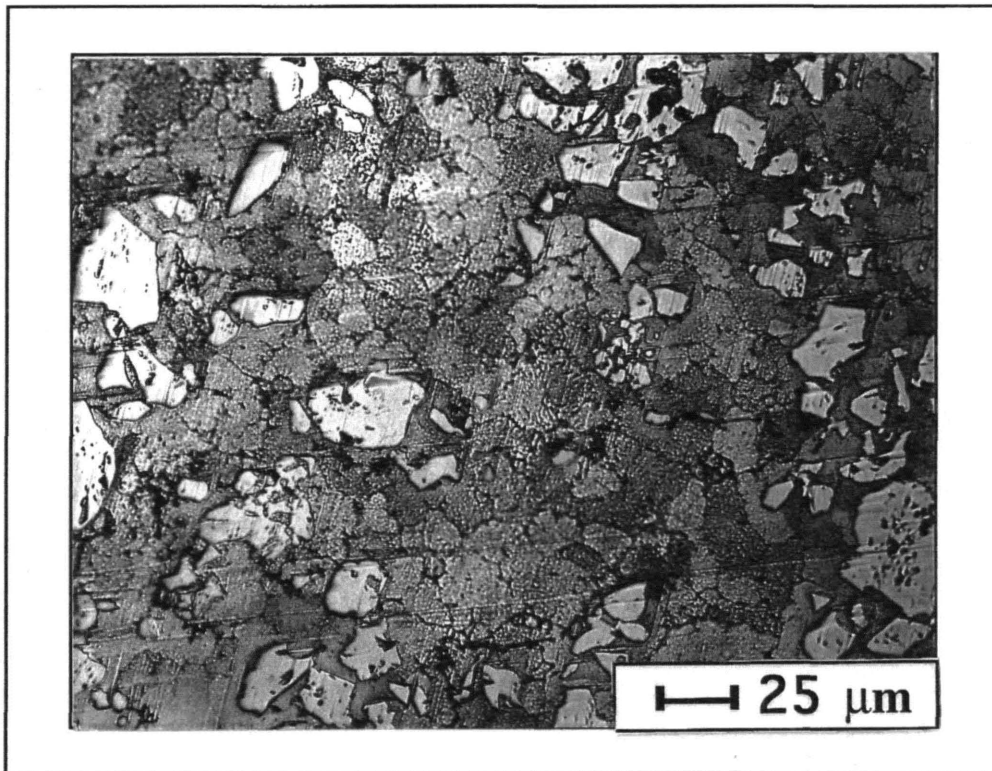


**FIGURE 3.20**  
**Microstructure of Material B + TiC, 400X**  
**Multi-Pass Melt,**  
**EB Assisted Reaction Synthesis**

As was the case with Material A + TiC, Material B + TiC exhibits a grain refinement effect with a reduction in grain size of a factor of 5 - 10. The TiC is also a very effective nucleating agent for Material B, since there are no structural variations from pass to pass or in the interpass regions. Also, the tendency of Material B to crack was dramatically reduced by TiC additions. There were no detectable cracks or centerline porosity in the Material B + TiC melts.



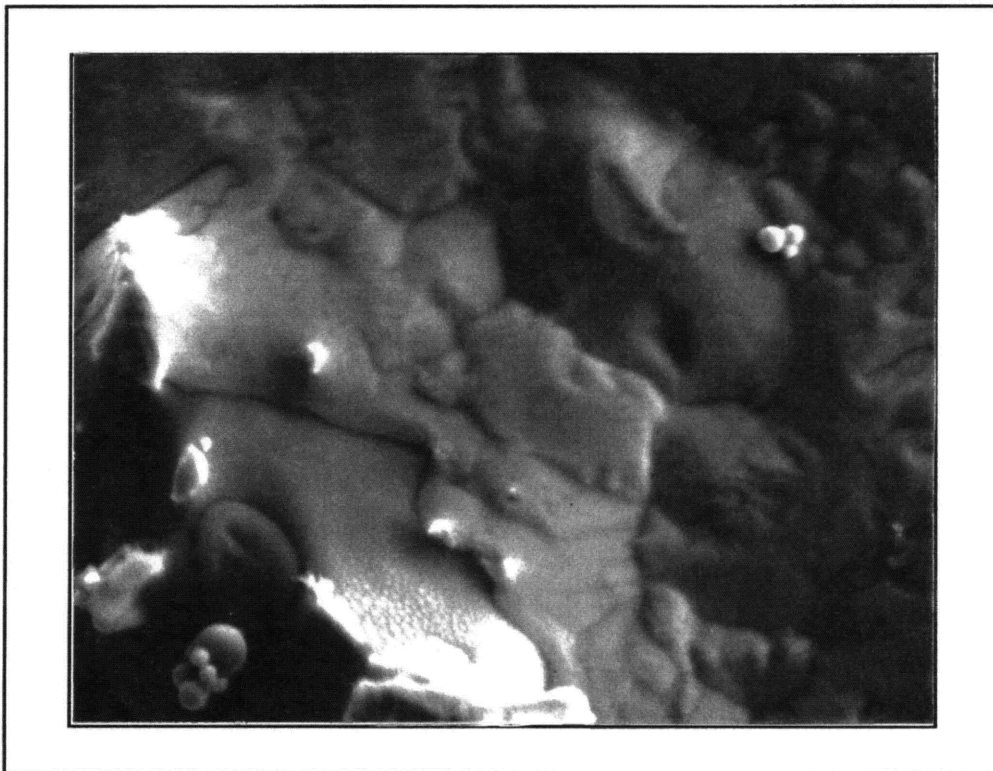


**FIGURE 3.21**  
**TiC Particle Protruding from Surface of Material A, 1800X**  
**Multi-Pass Melt,**  
**EB Assisted Reaction Synthesis**

TiC was easily wetted by the powder precursors in both Material A and B. These precursors consisted of elemental Fe and Al, both of which can wet TiC. This figure shows a single TiC particle at the surface of a melt in Material A + TiC. The particle is in the lower left of the figure, and the interface between the melt and the TiC particle can be clearly seen.

### 3.5 Aluminide Coating Applications

One potential area of application for the reaction synthesis technique developed in this work is the application of aluminide coatings. Such coatings on steel would have excellent corrosion resistance and could withstand moderate to high temperature exposure (no more than 700°C for iron aluminides, higher for the others). There exists the possibility of applying any one of the aluminides, but FeAl and Fe<sub>3</sub>Al will be examined here. Nickel aluminides are extremely exothermic. This makes control over the reaction front very difficult. Also, if self-propagating high temperature synthesis does occur (SHS), the resulting microstructure is porous without the application of some external pressure or post-processing to achieve full density. Titanium aluminides have potential mixing problems, and during these preliminary studies, it was difficult to control the extent of reaction. More development is needed in both nickel and titanium aluminide systems to make them feasible as practical coating systems. The potential range of applications of these coatings is very large, and includes marine, aerospace, petrochemical, power generation, and automotive applications. For example, Ti<sub>3</sub>Al on cast iron is being considered for use in diesel engines [TIBBETTS (1994)].

A two - step coating process was developed for iron aluminides. The first step consisted of applying pre-mixed elemental powders to steel plate by use of spot welding. Although there was some reaction between the powders in the center of the spot weld, a large fraction of the powders were unaffected. This is due to the rapid thermal cycle (1 second at most) during the spot welding process. The powders did develop sufficient adherence to stick to the steel sheets. After this application process, the powders were subjected to electron beam melting and reaction synthesis in vacuum. The operating parameters were identical to those quoted earlier for the other powder experiments. The resulting coatings were about 500 μm thick and were fully dense and fully adherent. The deposits were homogeneous in structure with no evidence of a second phase in the bulk or at the grain boundaries. The next series of pictures shows the microstructure of these deposits and shows the process of application. The material generated is not actually Fe<sub>3</sub>Al but rather α-Fe. The initial powder precursor contained 25 at. % Fe, but the final Al content in the deposit was about 19% at. A significant amount of Fe was dissolved from the base material. Starting with a higher Al - content precursor will result in aluminide formation.



**FIGURE 3.22**  
**Unreacted powders Spot-Welded onto Steel Sheet, 12 X**  
**Material C Precursor,**  
**Single EB Melt Pattern is Visible,**  
**EB Assisted Reaction Synthesis**

This picture shows the powder precursors in the unreacted state. Also shown is a single EB melt track. This illustrates the excellent control over extent of reaction that is possible with the EB reaction synthesis technique. It is possible to selectively react powders, and by superimposing EB melt tracks, larger areas can be covered. There is also the possibility of carrying out an EBSFF process for building aluminide parts layer - by - layer. This potential application was not investigated during the current work.

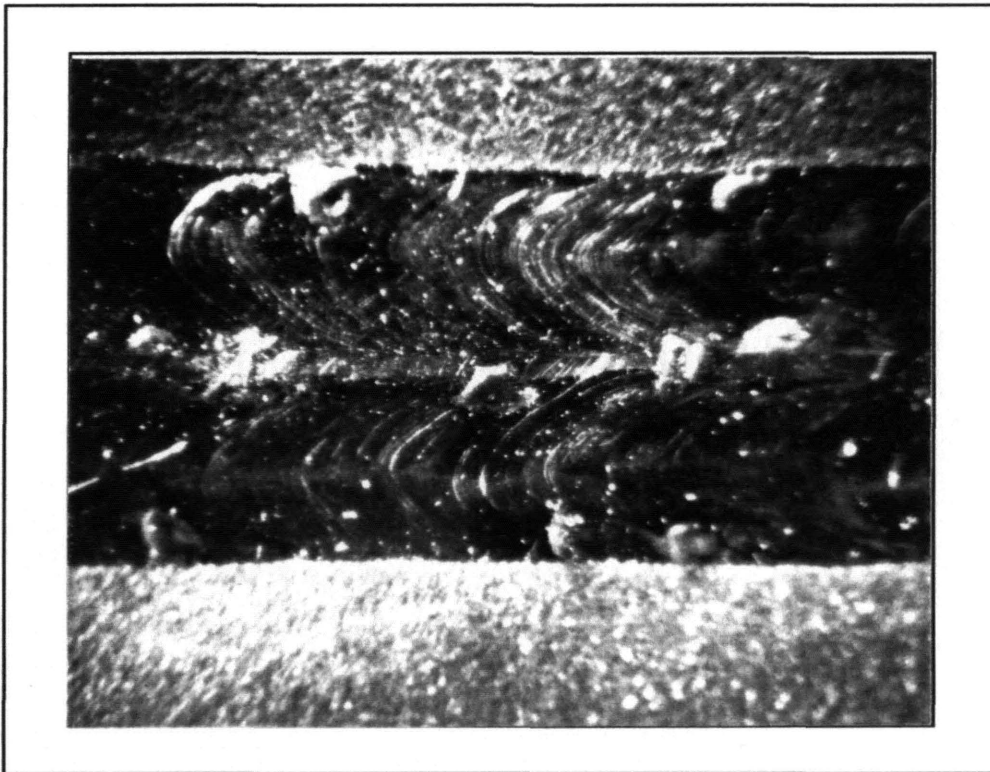


**FIGURE 3.23**  
**Deposited and Fully Melted Fe<sub>3</sub>Al Tracks on Steel, 12 X**  
**EB Assisted Reaction Synthesis**

This shows the powder precursor deposits after EB processing. The powders have formed fully adherent, fully reacted, and fully dense coatings that are 500  $\mu\text{m}$  thick in the center of the deposit. Larger spots can cover larger areas during a single pass, allowing more efficient coverage of large parts.

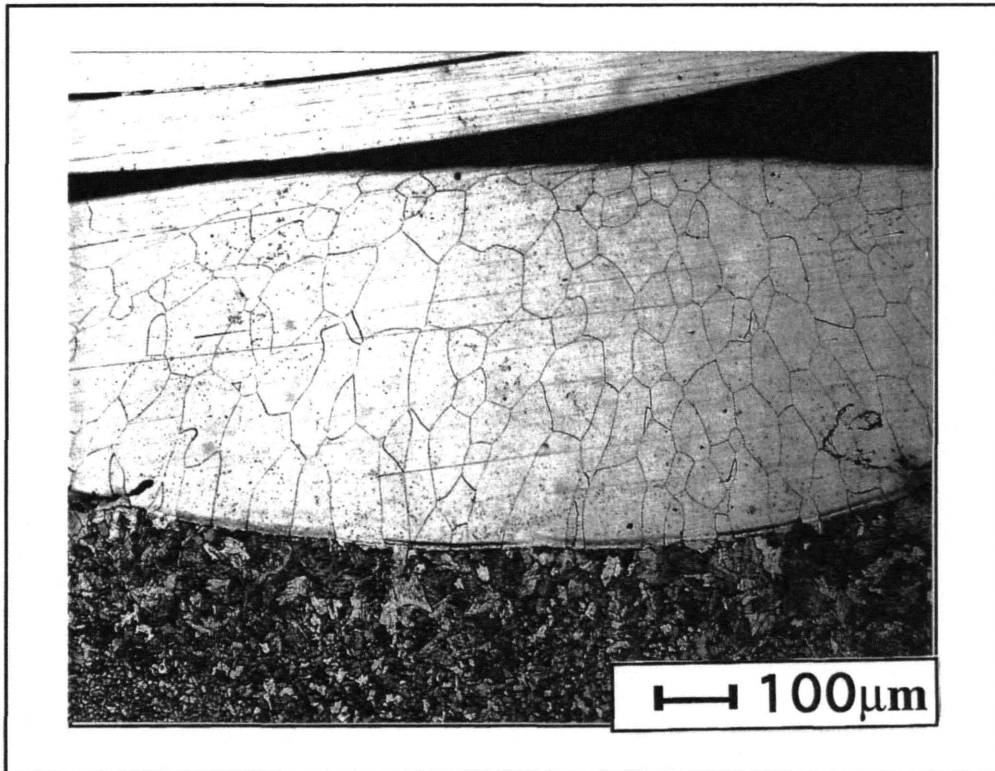


**FIGURE 3.24**  
**Microstructure of Material C on Steel, 100 X**  
**Through Thickness of Melt, Multi-Pass Melt,**  
**EB Assisted Reaction Synthesis**

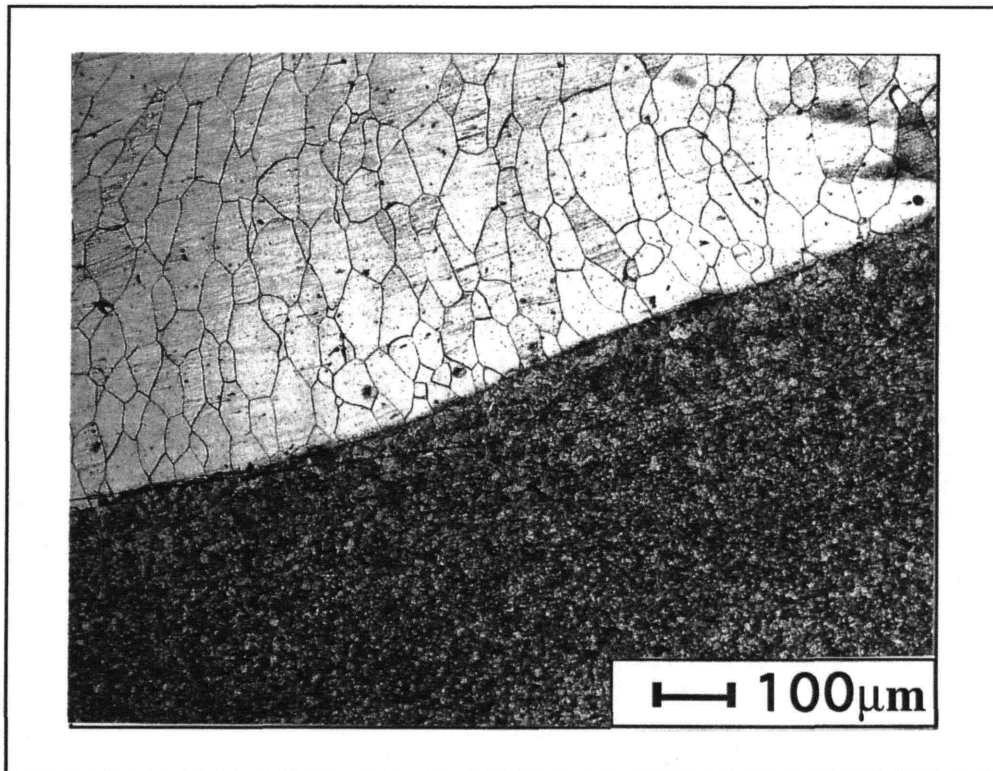


**FIGURE 3.25**  
**Microstructure of Material C Deposit on Steel, 100X**  
**Edge of Melt, Multi-Pass Melt,**  
**EB Assisted Reaction Synthesis**

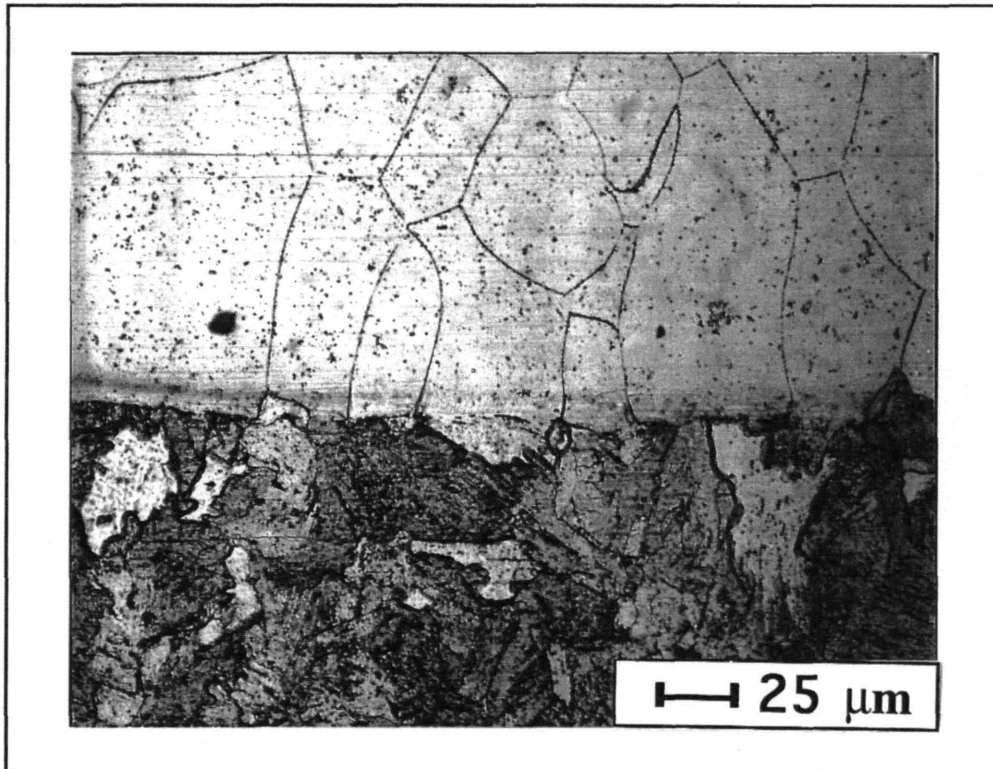


**FIGURE 3.26**  
**Interface between Material C and Steel Substrate, 400 X**  
**EB Assisted Reaction Synthesis**

Figures 3.24 and 3.25 show deposits of Material C on a steel plate. Figure 3.24 shows the bottom of the deposit, and Figure 3.25 shows the edge. The locations of these figures with respect to the deposit are schematically shown below.

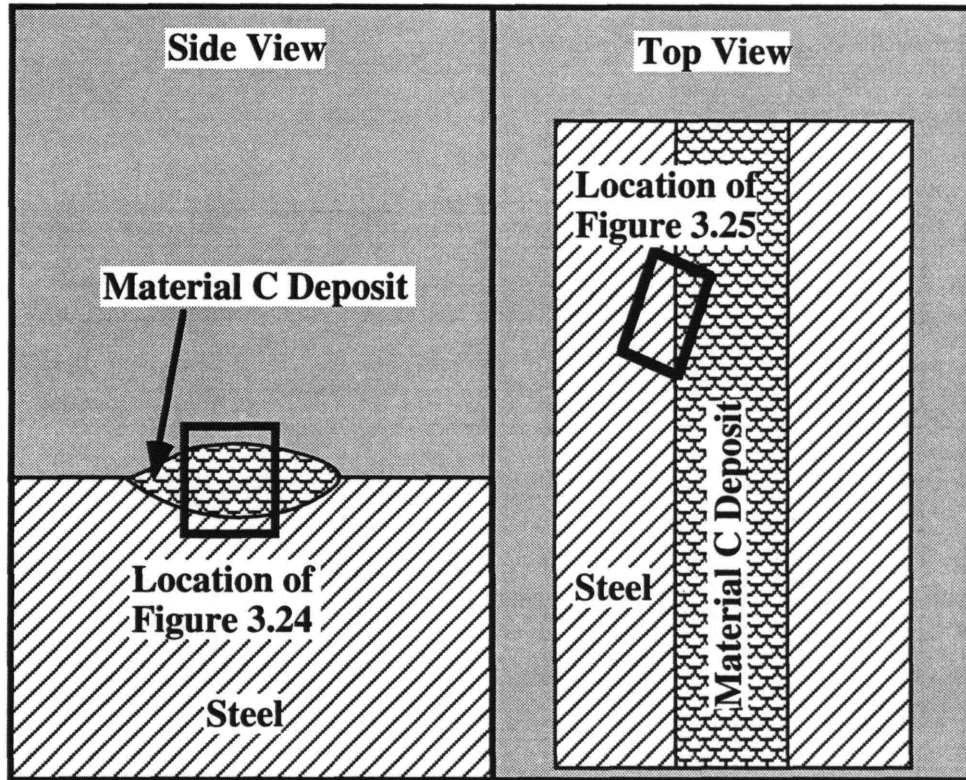


**FIGURE 3.27**  
**Schematic of Material C Deposit on Steel,**  
**Location of Figures 3.24 and 3.25**

The interfaces between the cladding deposit and the steel substrate were exceptionally well - defined with no intermediate regions. There were few cracks or delaminations between the deposit and the substrate. What cracks there were occurred in regions that were not fully melted by the beam. There were no detectable secondary phases in the bulk of the deposit or in the steel directly below the deposit. Also, the grain boundaries of the cladding layer did not exhibit any secondary phases. All of these facts support the contention that the deposits are single phase  $\alpha\text{Fe}$ , fully mixed and fully adherent.

The bulk composition and the change in composition at the interface were studied by electron microprobe analysis. This analysis was done at Geller Micro Analytical Laboratory in Peabody, MA. A JEOL Superprobe 733 was used. As discussed earlier, the estimated error in the atomic percentages is about  $\pm 1.5\%$ . The measured values for the bulk composition of the coating were based on measurements taken at several locations in the coating. The composition across the interface was measured in  $5\ \mu\text{m}$  intervals.



**TABLE 3.13**  
**Bulk Composition of Material C Coating on Steel**  
**as Determined by Microprobe Analysis**  
**(Analysis done by Chuck Herrington,**  
**Geller Microanalytical Laboratory, Peabody, MA)**

Reading No.	Fe Atomic %	Al Atomic %
1	80.5	19.5
2	79.8	20.2
3	79.8	20.2
4	79.9	20.1
5	80.5	19.5
6	80.5	19.5
7	80.4	19.6
<b>MEAN</b>	<b>80.2</b>	<b>19.8</b>

The compositional variations across the interface are shown in the figure below.

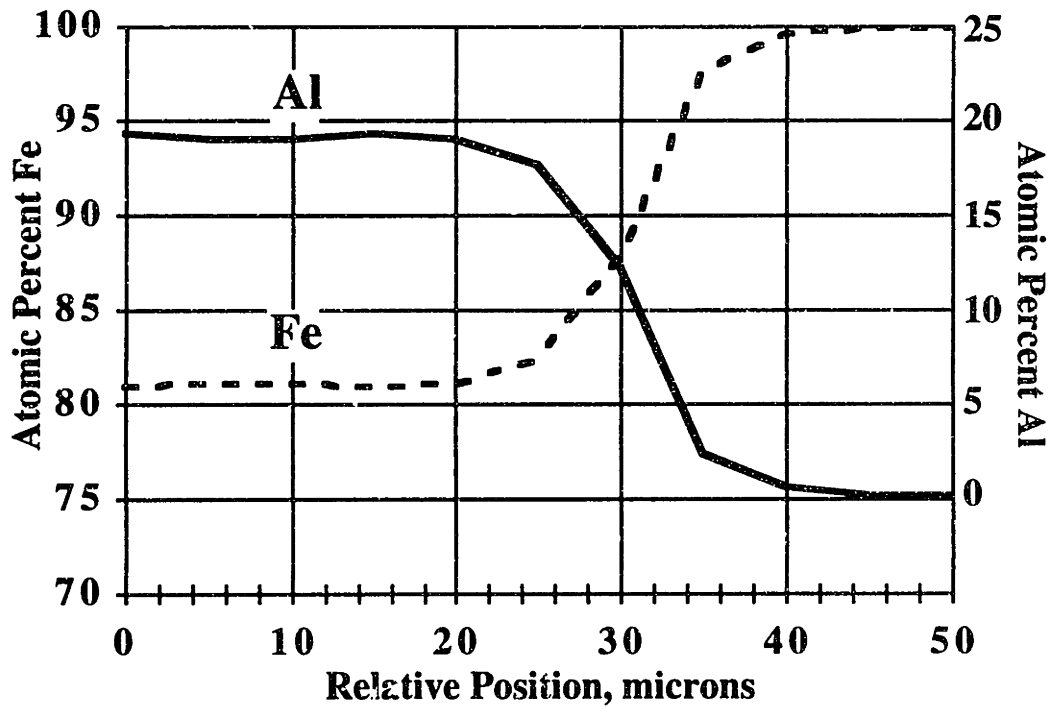


**FIGURE 3.28**  
**Composition Variation Across Interface,**  
**Material C Coating on Steel**

The above compositional scan ignores other trace elements, such as Si and C (and possibly S) that will be present in the steel.

### 3.6 Hardness of Material C ( $\alpha$ Fe) Coating

The hardness of the Material C coatings was measured using a Clark Instruments microhardness tester. The Vickers hardness was evaluated based on a load of 300 g. The results of these hardness tests on both the steel substrate and the coating are shown in the table below.

**TABLE 3.14**  
**Vickers Hardness (300g) of Material C Coating and Steel Substrate**

<b>Hardness of Coating</b>		
<b>d1, microns</b>	<b>d2, microns</b>	<b>Vickers Hardness</b>
50.6	49.4	222.5
51.3	50.5	214.7
50.2	49.9	222.1
51.0	50.2	217.3
50.0	47.4	234.6
<b>Mean Values for Coating</b>		
50.6	49.5	222.2
<b>Hardness of Steel Substrate</b>		
64.9	67.1	127.7
66.3	67.3	124.7
67.3	66.1	125.0
66.3	66.1	126.9
65.8	66.3	127.5
<b>Mean Values for Steel Substrate</b>		
66.1	66.6	126.4

The absolute values of the hardness are not very high as compared to other hardfacing materials, but there is a substantial difference between the hardness of the steel and that of the coating.

### 3.7 Summary of EB Powder Processing

One of the more significant contributions of this thesis was the independent development of pressureless EB - assisted reaction synthesis. This coating technique was developed for lasers by several workers mentioned earlier, and the higher power capabilities of e-beams may offer some advantages in the coverage of large pieces in addition to higher deposition rates. The essential features of this technique are reiterated below .

- E-beam reaction synthesis allows control over position of reaction front : selective reaction synthesis is possible, and the potential exists for a reaction synthesis version of EBSFF for the freeform manufacture of intermetallic components.
- This technique applied to the iron aluminide system results in complete mixing and complete extent of reaction. The traveling e-beam creates a superheated region with sufficient convection to mix the precursor powders and sufficient heat input to produce a homogeneous, fully reacted liquid phase. The rapid thermal cycles associated with EB processing result in a solidification structure with grain sizes that are comparable to those achievable by other processing routes.
- The potential for coating applications is high. Application of coatings via a P/M approach coupled with the very high cooling rates possible in e-beam processing can result in hard, wear resistant aluminides with acceptable mechanical properties and excellent corrosion resistance. Further development is needed to implement coatings for titanium aluminides, and alternate powder precursor application schemes can also be pursued. The process may also have applicability to other reaction synthesis applications, such as SiC coatings, IMC (intermetallic matrix composite) coatings, and others.

## CHAPTER 4

### EB Material Deposition Utilizing Wirefeed

#### 4.1 Overview

As discussed in Chapter 2, EB material deposition is roughly twice as efficient as conventional welding processes both in terms of deposition rate and melting efficiency. One of the objectives of this work was to investigate the feasibility of EBSFF, or Electron Beam Solid Freeform Fabrication. In Chapter 3, the difficulties with powder systems were outlined. Powders can be successfully used for coatings, however. In this section, a different approach to EBSFF will be described. This method utilizes wirefeed to melt and deposit material. This process is completely analogous to conventional welding processes that are currently used for repair and part build-up. E-beam wirefeed buildup is schematically illustrated below. This figure shows the process for parts of cylindrical geometry. In principle, it is not significantly more difficult to adapt the process to other geometries.

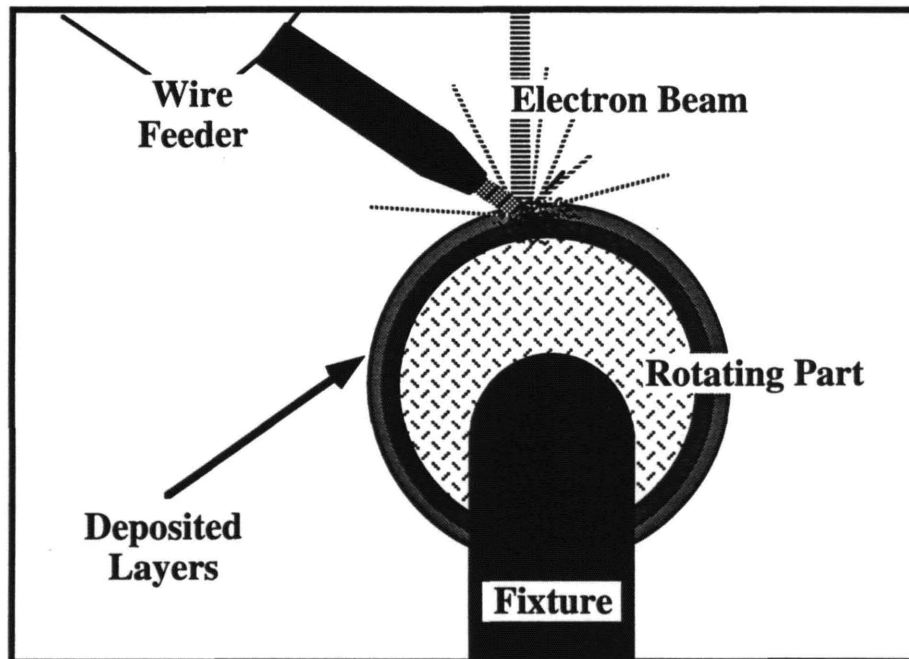


**FIGURE 4.1**  
**Schematic of EB Wirefeed Deposition Process**

Two specific material systems will be discussed : stainless steel and Al - bronze. These two systems have applications in marine structural components such as propellers, shafts, bearings, flanges, overlay coatings, etc. EB deposition is characterized by high deposition rates and millimeter-scale dimensional

resolution : both of these factors are well-suited to the repair or manufacture large parts. Post processing in the form of machining or grinding will be necessary. As an example of such a process, consider the repair of a turbine disk for a steam-driven electrical power generation turbine. Such repair processes are commonly done with conventional welding processes [see LaFAVE and WIEGAND (1994)]. The material being deposited here would be a Cr-Mo-V rotor steel.

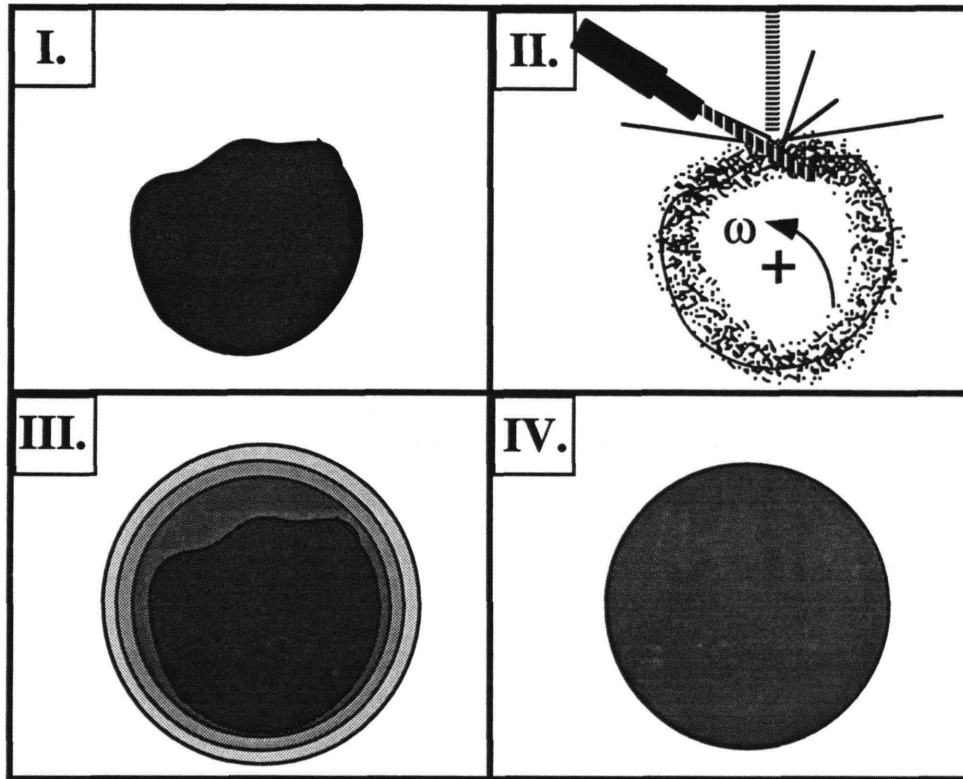


**FIGURE 4.2**  
**Schematic Representation of Disk Repair**

Step I. shows the disk in the "as-received" condition. The second step consists of EB wirefeed deposition, which results in an oversized part, step III. The final disk shape is obtained by machining or grinding, and perhaps the appropriate heat treatment. This method may also be applied to the manufacture of a spare part. Such a process could be economical for large parts for ships. It is estimated that the typical dry dock expenses for a large commercial or military vessel are approximately \$ 200,000.00 - \$ 250,000.00 per day [STEFANSSON (1995)]. In addition to this expense, there is the cost of lost productivity. Depending on the type of vessel, it is within the realm of possibility that the total economic consequences of ship down time can be as high as \$ 500, 000.00 per day. Given this statistic, the additional expense of EB processing is thoroughly justifiable if it can save even one day of down time. EB deposition could build up a 100 - 1000 lb part in one-half the time required to process the same component by conventional welding. When compared to casting or forging

processes, the time savings could be even greater, since the lead time associated with such large castings is significant, on the order of weeks at best.

There may also be applications in the repair of aerospace components. Some typical components that could be repaired include air seals and blades. Shown below is schematic of a repair made to a turbine blade using a wirefeed deposition process. EB deposition in particular is very well-suited to such applications, and has in fact been applied to them already. Other processes used include GTAW (gas tungsten arc welding) and LBW (laser beam welding). The main advantages of EB deposition for aerospace applications are :

- highly localized application of heat can alleviate distortion problems on delicate components,
- vacuum environment of EB processing ensures cleanliness of operation and minimizes oxidation / contamination, and
- e-beams (and lasers) can focus very finely, allowing precision repairs that are difficult at best with conventional welding techniques.

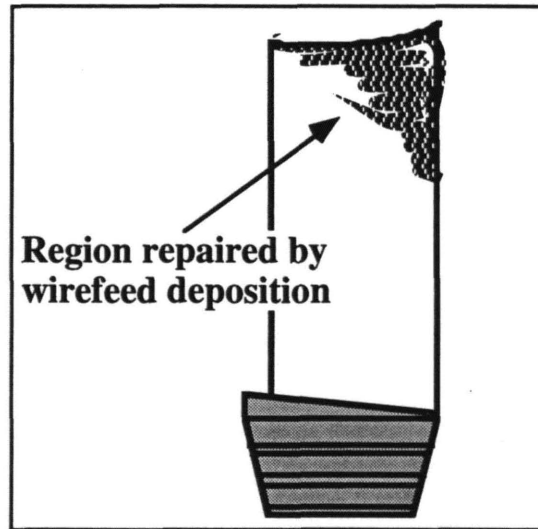


**FIGURE 4.3**  
**Schematic of Turbine Blade Repair by**  
**Wirefeed Deposition Process,**  
**Adapted from WELDING JOURNAL 11 / 92 (1992)**

Such repairs have been done on Waspalloy air seals from Pratt & Whitney TF30 / P100 engines, for example. The materials used for these repairs are very carefully controlled in terms of composition and trace contaminants. The list below shows the AMS (Aerospace Materials Specification) numbers for several wire stock materials that are processed by VIM / VAR (vacuum induction melting / vacuum arc remelting ) before wire drawing. These alloys are not necessarily used in blade repair, but are used in engine applications in general.

**TABLE 4.1**  
**Weld Wires Used in Wirefeed Deposition Repair of**  
**Jet Engine Components,**  
**Adapted from WELDING JOURNAL 11/ 92 (1992)**

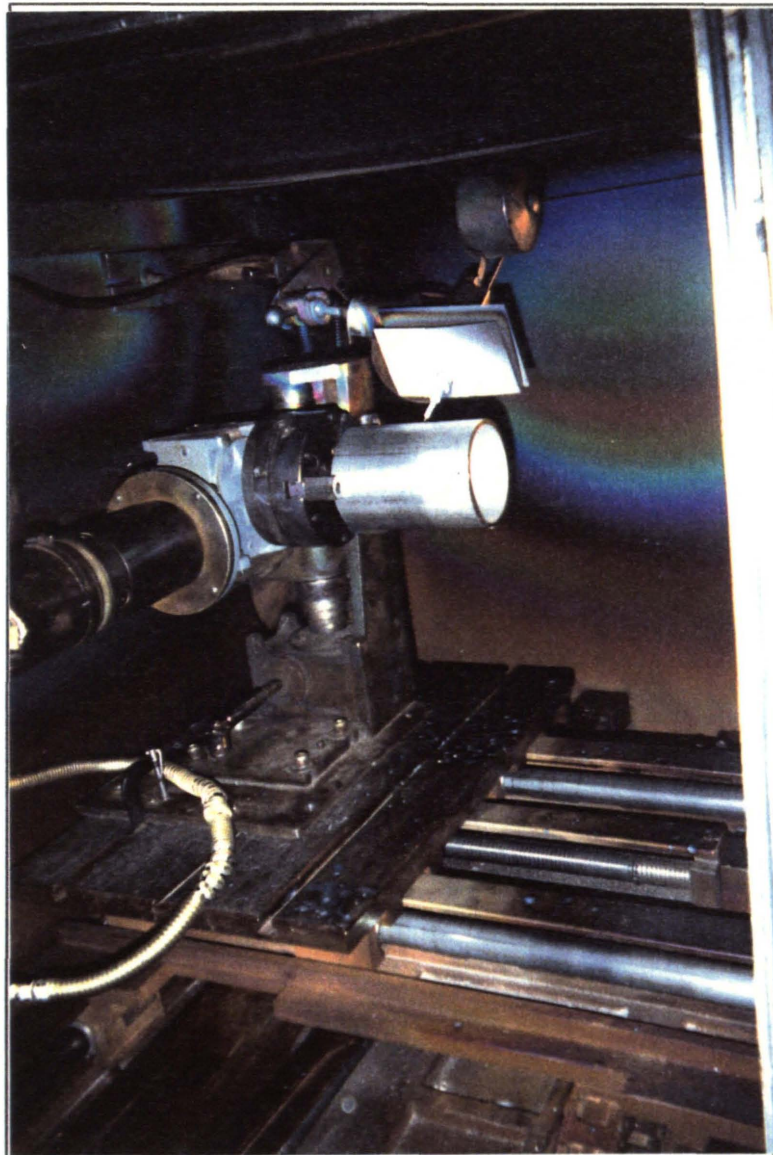
AMS Designation	Common Designation
5828	Waspaloy
5832	Inconel 718
5830	Incoloy 901

#### 4.2 Low Energy EB Deposition Apparatus



(shown above)  
**FIGURE 4.4**  
**150kV EB Commercial Welder Located at**  
**PTR - Precision Technologies, Enfield, CT.**

On the previous page is a picture of the commercial e-beam apparatus used in this work. The wire deposition equipment is shown below. The position controls available on this machine were x, y, and rotation. This meant that there was no way of automatically indexing the height of the wirefeeder with respect to the surface of the part. As a result, after about 5 - 6 layers of deposition, the height of the wirefeeder had to be manually adjusted. A more complete system with fully articulated wire position was not implemented.





(shown above)  
**FIGURE 4.5**  
**Wirefeed Mechanism and XY - Motion Table,**  
**PTR - Precision Technologies, Enfield, CT.**

The typical beam and wirefeed operating parameters used in this work are specified below.

**TABLE 4.2**  
**EB Operating Parameters and Wirefeed Rates**  
**Used in this Work**  
 ("ipm" refers to inches per minute)

Quantity	Value
Beam Voltage	120 kV - 150 kV
Beam Current	7 mA - 14 mA
Beam Power	850 W - 2000 W
Beam Spot Size	0.125 cm - 0.150 cm
Surface Speed of Target	90 ipm ( 3.8 cm / s)
Wire Feed Rate	130 ipm - 150 ipm ( 5.5 cm / s - 6.4 cm / s)
Axial Feed Rate	0.05" / rev. (0.125 cm / rev.)

The axial feed rate refers to the "pitch" of the spiral in the deposition pattern. As one layer was deposited, the part was moved so that upon commencement of the next revolution, the tip of the wire was indexed axially by the amount specified by the axial feed rate.

**4.3 EB Wirefeed Deposition of 308 Stainless Steel :**  
**Experimental Assembly**

To test the feasibility of multipass, thick section buildup using EB wirefeed deposition, the deposition of 308 weld wire onto 304L pipe was investigated. The target piece had dimensions shown below :

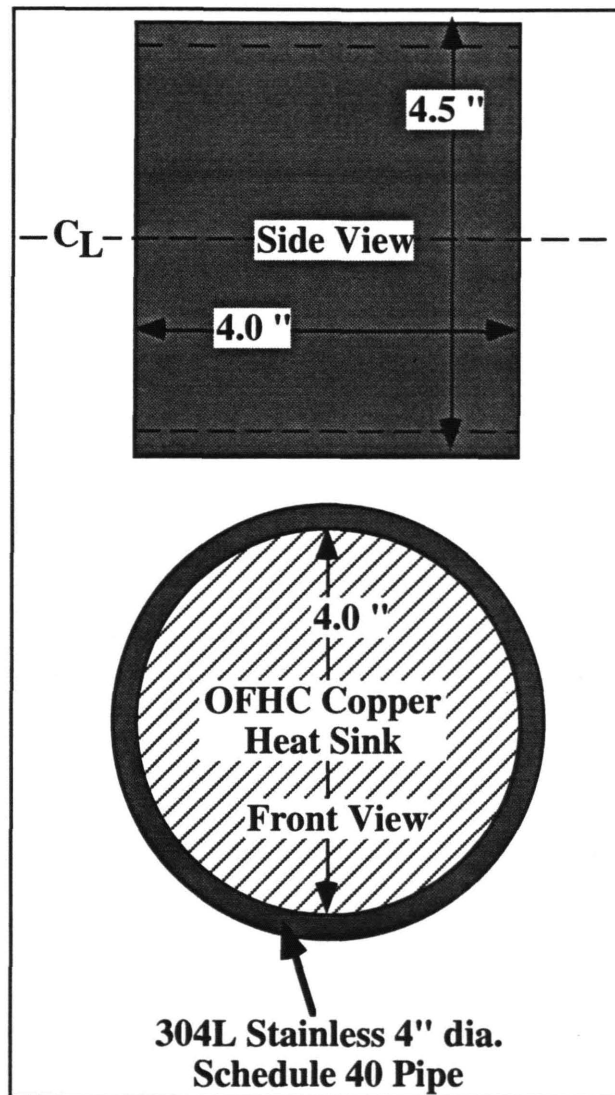


**FIGURE 4.6**  
**Geometry of Stainless Target,**  
**Drawn to 1 / 2 Scale**

The weld wire used was 308 stainless. The composition of this wire is :

**TABLE 4.3**  
**Composition of 308 Stainless Steel, wt. %**  
**Taken from METALS HANDBOOK - DESK EDITION (1985)**

<b>C</b>	<b>Mn</b>	<b>Si</b>	<b>Cr</b>	<b>Ni</b>	<b>P</b>	<b>S</b>
0.08	2.00	1.00	19.0-21.0	10.0-12.0	0.045	0.03

#### 4.4 Concise Review of the Metallurgy of 304 and 308 Stainless Steel

This section will provide a brief overview of the metallurgy of 304 and 308 stainless steels. These grades are primarily Austenitic at room temperature with variable levels of residual ferrite found in weld metal. For 304 (and 308) stainless, the solidification structure will initially be Ferritic, and will later convert to primarily Austenitic upon further cooling. The appropriate section of the Fe-Cr-Ni phase diagram that includes the composition of 308 stainless steel is shown below.

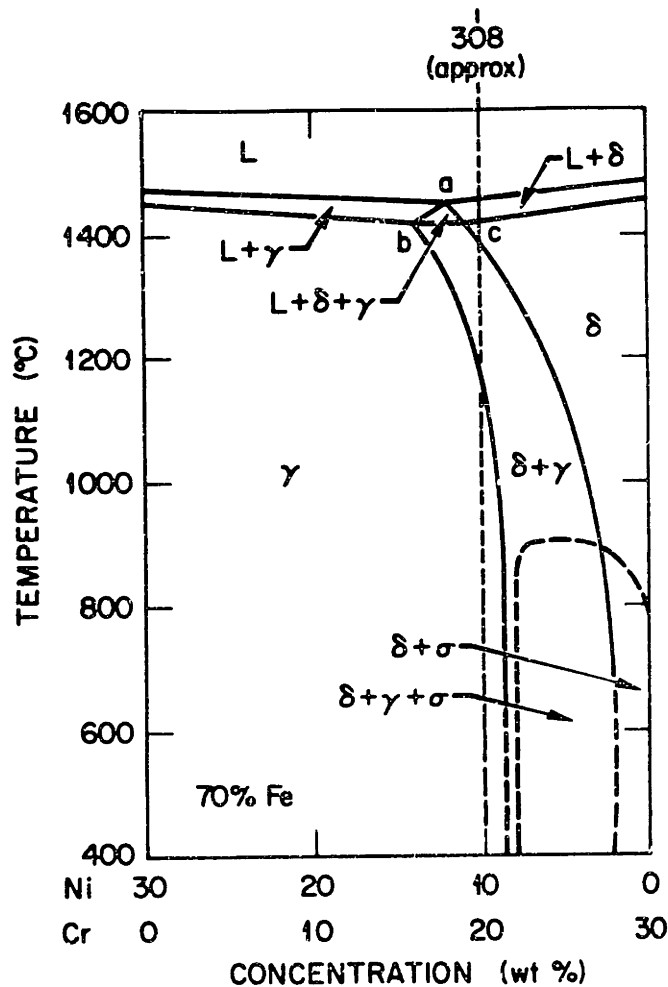


**FIGURE 4.7**  
Section of Fe-Cr-Ni Phase Diagram at 70 wt. % Fe  
Reprinted with Permission from VITEK et al (1992)

From the phase diagram, it is seen that Ferrite is not an equilibrium phase at temperatures below 1100 °C. There are several elements that are "Ferrite-forming," and these include Ti, Si, Nb, and Mo [MARSHALL (1984)]. The amount of Ferrite in a weld deposit is primarily a function of the weld material composition, but also depends on cooling rate [ELMER (1988)]. One of the earliest attempts to predict the amount of Ferrite in a weld was by SCHAEFFLER (1949). Schaeffler's Diagram predicts the amount of Ferrite as a function of the so-called nickel and chromium equivalents. These equivalents are the weight percentages of Ni and Cr plus weighted sums of other alloying elements. Figure 4.9 shows a Schaeffler diagram modified to include the effect of cooling rate [DAVID, VITEK & HEBBLE (1987)]. The nature of residual Ferrite in welds is schematically illustrated below.

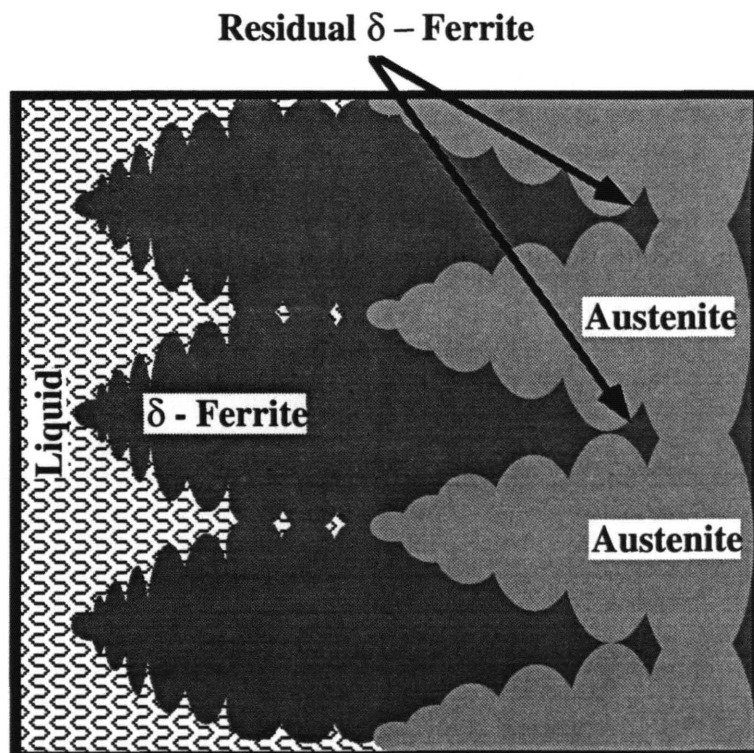


**FIGURE 4.8**  
**Solidification of 304 (308 also) Stainless Steel**  
**Adapted from MATSUDA & LEE (1990)**

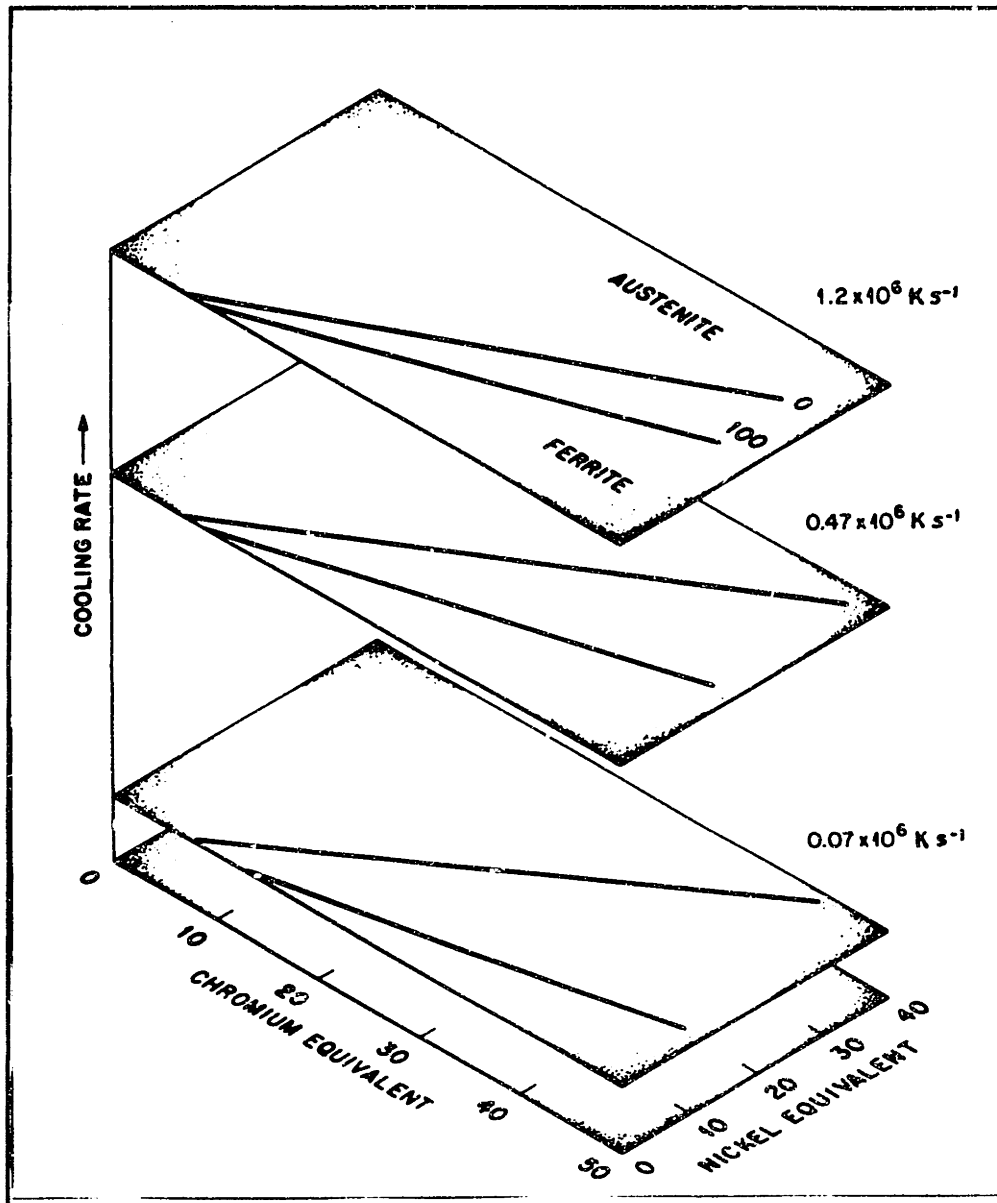


**FIGURE 4.9**  
**Schaeffler Diagram Modified to Include Cooling Rate Effect**  
 Copied with Permission from DAVID, VITEK & HEEBLE (1987)

In addition to Austenite and Ferrite, there are several other phases which are observed in Austenitic stainless steels. A partial list of these phases is given in the table below.

**TABLE 4.4**  
**Some Possible Phases Present in Austenitic Stainless Steel**  
**Adapted from MARSHALL (1984)**

Phase	Structure	Possible Compositions
Austenite	fcc	FeCrMo
Ferrite	bcc	FeCrMo
Carbide ; $M_7C_3$	pseudo hexagonal	$Cr_7C_3$ , $(FeCr)_7C_3$
Carbide ; $M_{23}C_6$	fcc	$(FeCr)_{23}C_6$
Sigma, $\sigma$	bcc tetragonal	$(FeNi)_x(CrMo)_yFeCr$ , $(FeNi)_x(CrMo)_y$
Laves, $\eta$	hexagonal	$Fe_2Mo$ , $Fe_2Ti$

The carbides and Sigma phases will be in the form of fine precipitates in the interdendritic regions between the Austenite dendrites. Sigma phase will also grow out of the Ferrite phase upon long exposure to moderate temperatures (600 °C - 700 °C). This transformation will have a deleterious effect on mechanical properties, resulting primarily from cracking at the Sigma phase interfaces. For multipass welds, the heat affected zones of the subsequent welds will affect the microstructure of the previous deposits below them. At reheat temperatures above 950 °C, most of the Ferrite will be converted to Austenite. Also, carbides will precipitate in the Ferrite or at the Ferrite / Austenite boundaries. For long term exposures at elevated temperatures ( $10^3$  -  $10^4$  hours at 600 °C), the carbide precipitates can form a continuous, interconnected network which is actually free-standing when removed from the steel [EVANS (1980)].

#### 4.5 Microstructure of EB - Deposited 308 Stainless Steel

Electron beams are capable of producing melts with a wide range of cooling rates. Several authors have considered the effect of increasing cooling rate on the solidification structure of stainless steel [ELMER (1988) and DAVID, VITEK, and HEBBLE (1987)]. The solidification structures that resulted from the EB deposition process implemented in this work are typical of lower cooling rates. The final structure is predominantly Austenitic with interdendritic Ferrite. Figures 4.10 and 4.11 show the part illustrated schematically in Figure 4.6. The 304L stainless pipe is filled with a copper heat sink, and the EB deposit is shown on the circumference. Figure 4.11 shows the deposit edge - on. The thickness of the deposit is 0.50" on the average, or close to 1.25 cm.

Figures 4.12 and 4.13 show regions of smooth and disturbed deposit respectively. The surface features of a smooth deposit are shown in greater detail in Figures 4.14 and 4.15. The rough deposit resulted from small "glitches" due to wire misfeed. The mechanism by which these positive defects were formed is schematically shown in Figure 4.16. Due to stray vibration and lack of straightness in the wire, the wire would occasionally exit the region of the material being heated and melted by the beam. Upon reentry and exit from this region, globules of the filler metal were left on the surface of the deposit. These

bumps were further accentuated with each passing layer, and the result was the occurrence of defects that spanned many layers of deposit. A cross - section through such a defect is shown in Figure 4.17.

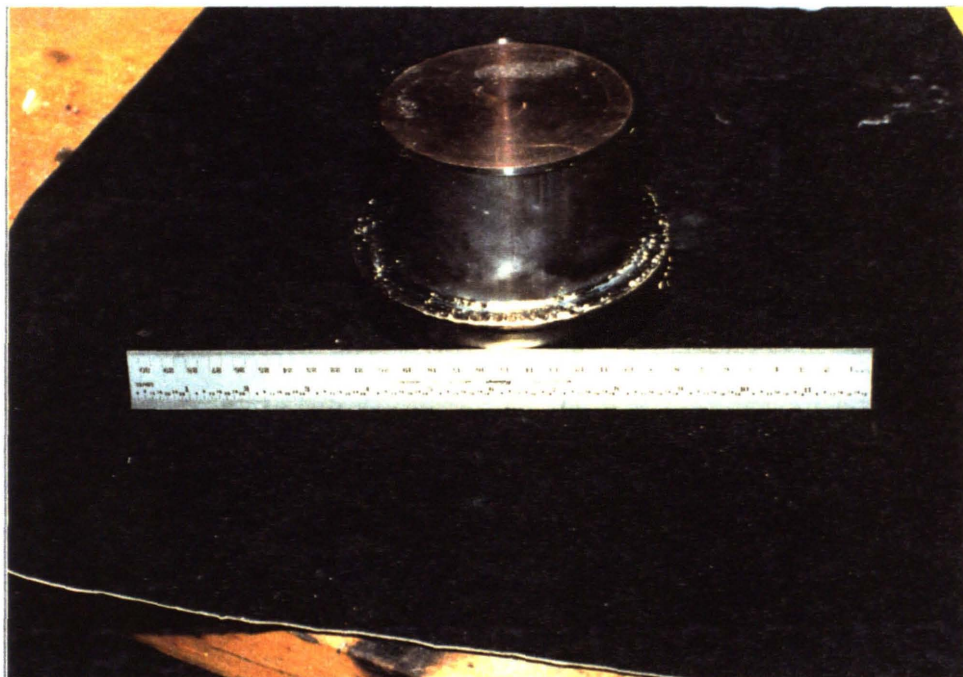
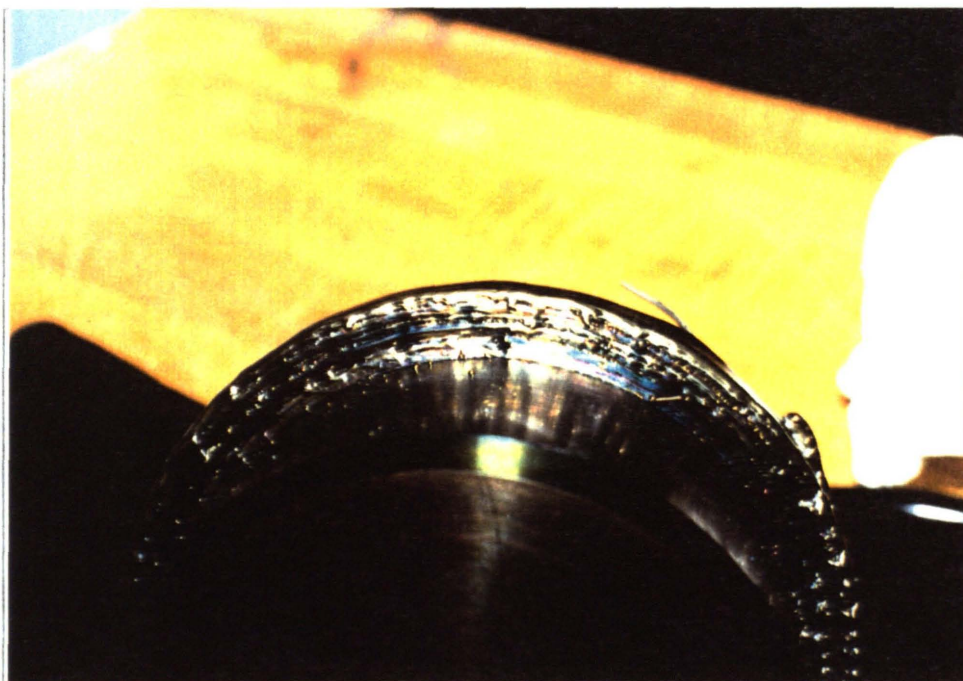


**FIGURE 4.10**  
EB Deposit of 308 SS Wire on 304L SS Pipe



(shown above)  
**FIGURE 4.11**  
Side View of 308 SS EB Deposit

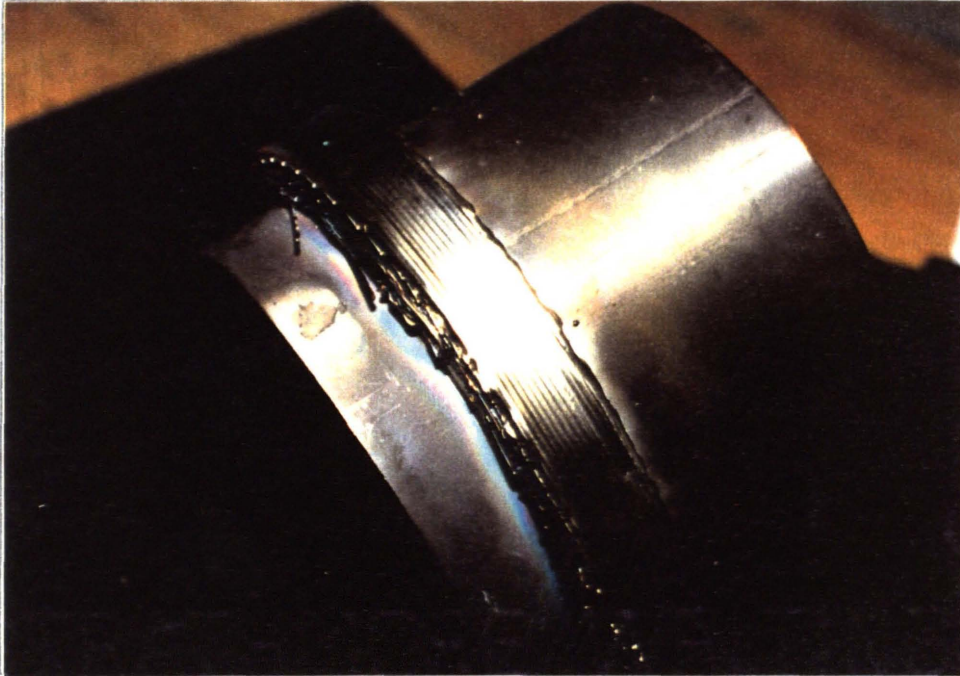
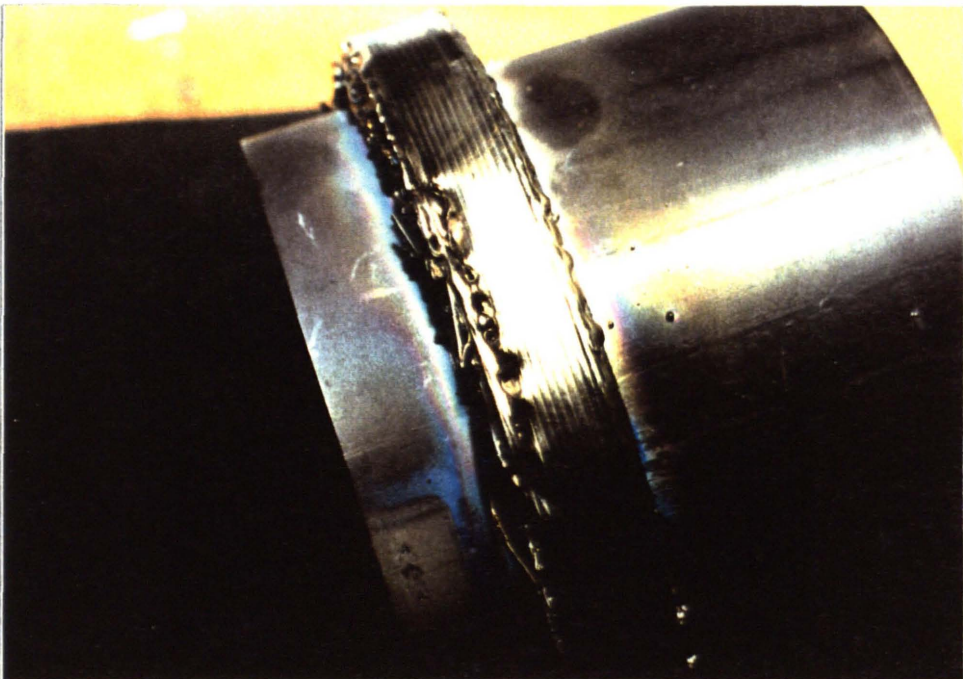


**FIGURE 4.12**  
Smooth Section of 308 SS EB Deposit





(shown above)  
**FIGURE 4.13**  
**Disturbed Region on 308 SS EB Deposit**

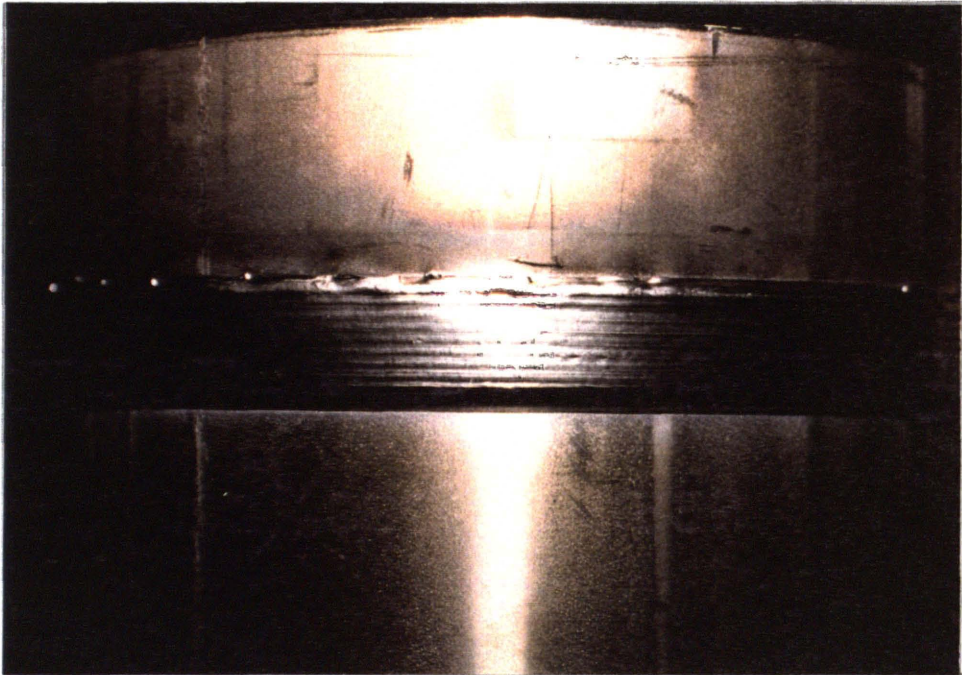


**FIGURE 4.14**  
**Smooth 308 EB Deposit**

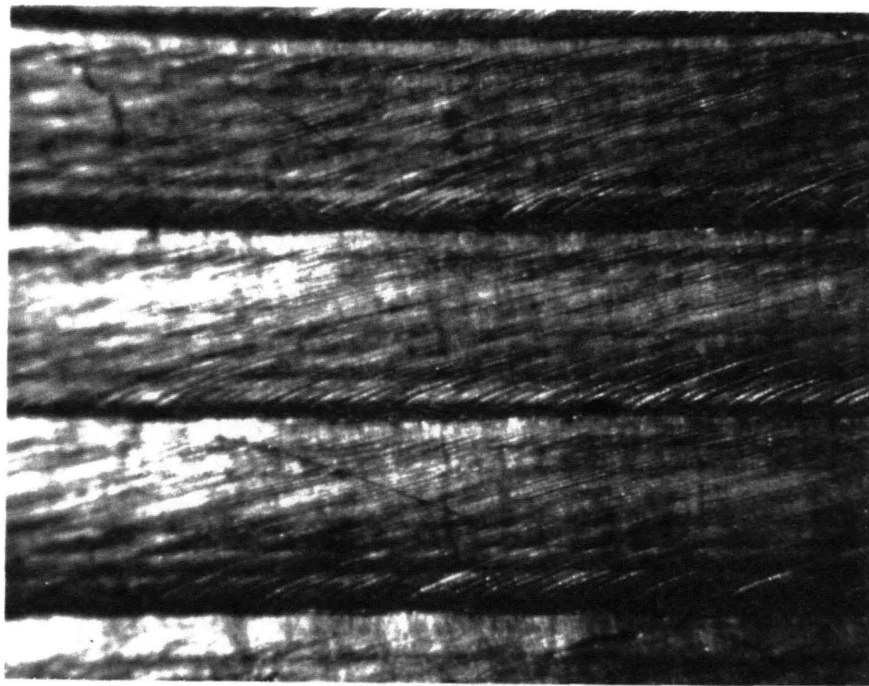


**FIGURE 4.15**  
**Macro Close-up of Surface of Smooth Deposit, 25X**  
**308 SS EB Deposit**

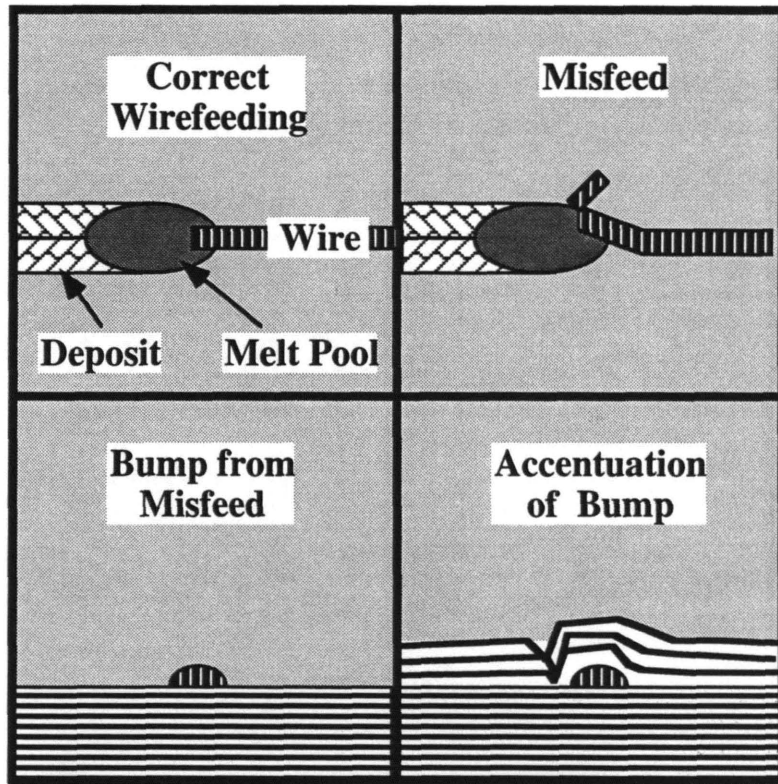


**FIGURE 4.16**  
**Schematic of Defect Formation in**  
**EB Wirefeed Deposition**



**FIGURE 4.17**  
**Multilayer Defect in 308 SS EB Deposit, 10X**

The microstructure of the 308 Stainless deposit is typical of arc weld deposits in this material. The solidification microstructure is characterized by a complex interlocking dendritic microstructure with interdendritic Ferrite. The combination of this interlocking structure together with some amount of residual Ferrite results in a crack - free, relatively ductile weld deposit. There will most likely be fine carbide precipitates at the Austenite - Ferrite boundaries, but they are not visible in optical micrographs. Figures 4.18 and 4.19 show the weld microstructure at the top and bottom of the 0.5" thick deposit respectively. Figure 4.20 shows the boundary between two successive weld passes at high magnification. Figure 4.21 and 4.22 show the multi - pass nature of the deposits.

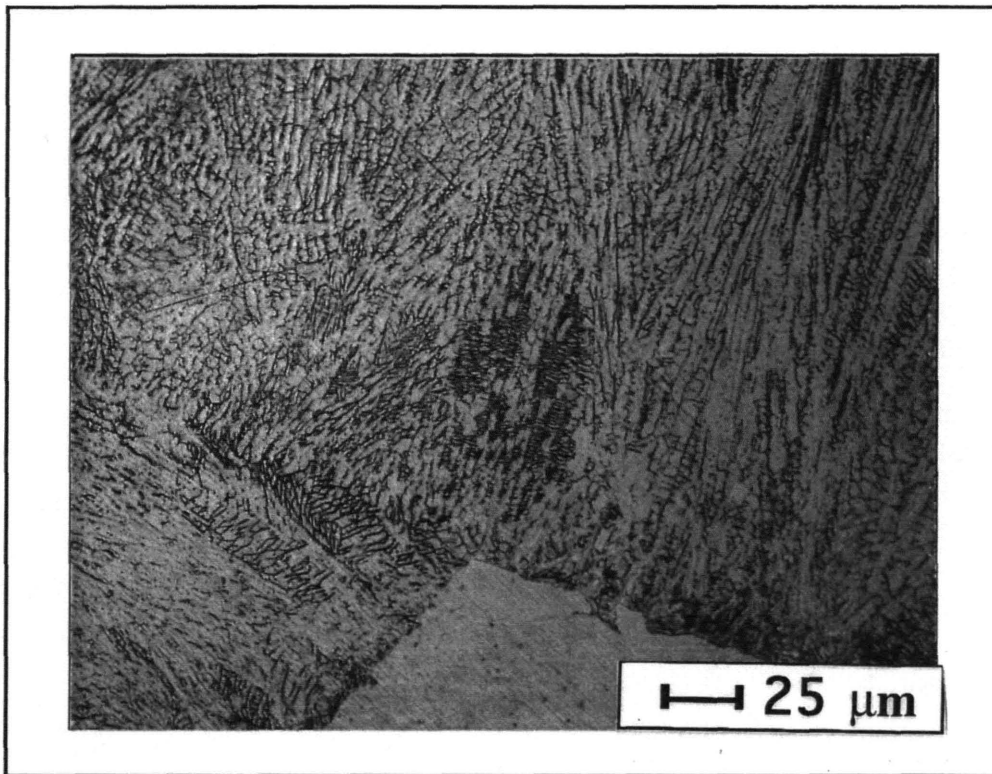


**FIGURE 4.18**  
**Bottom of 1.25 cm thick 308 SS EB Deposit, 400X**

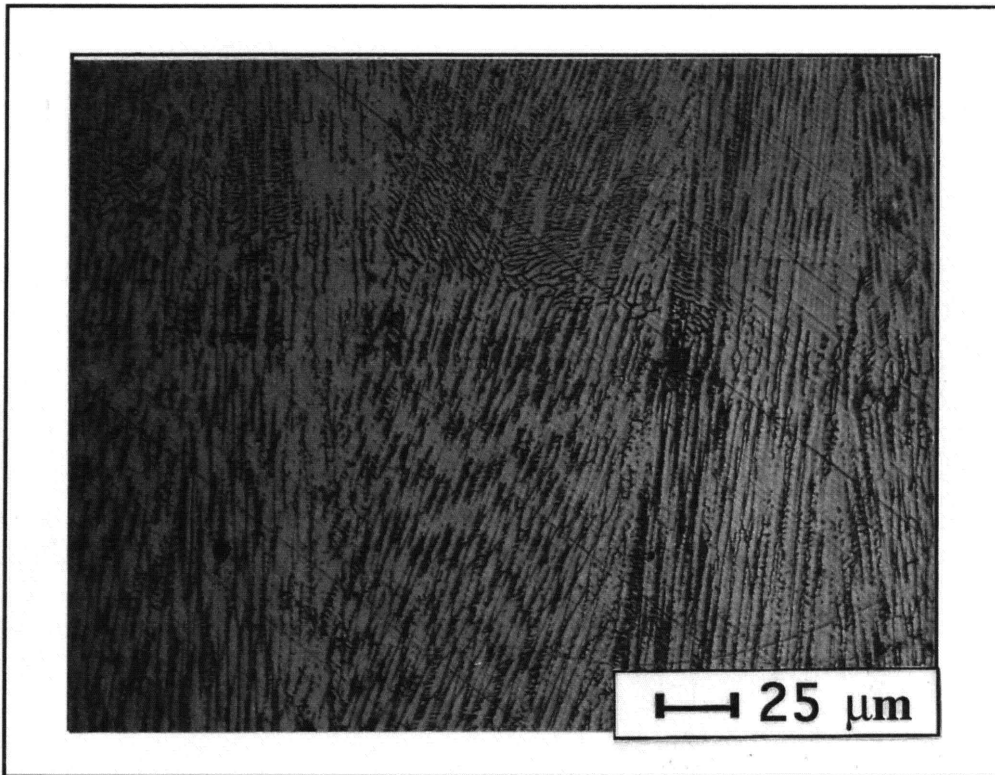


**FIGURE 4.19**  
**Top of 1.25 cm thick 308 SS EB Deposit, 400 X**

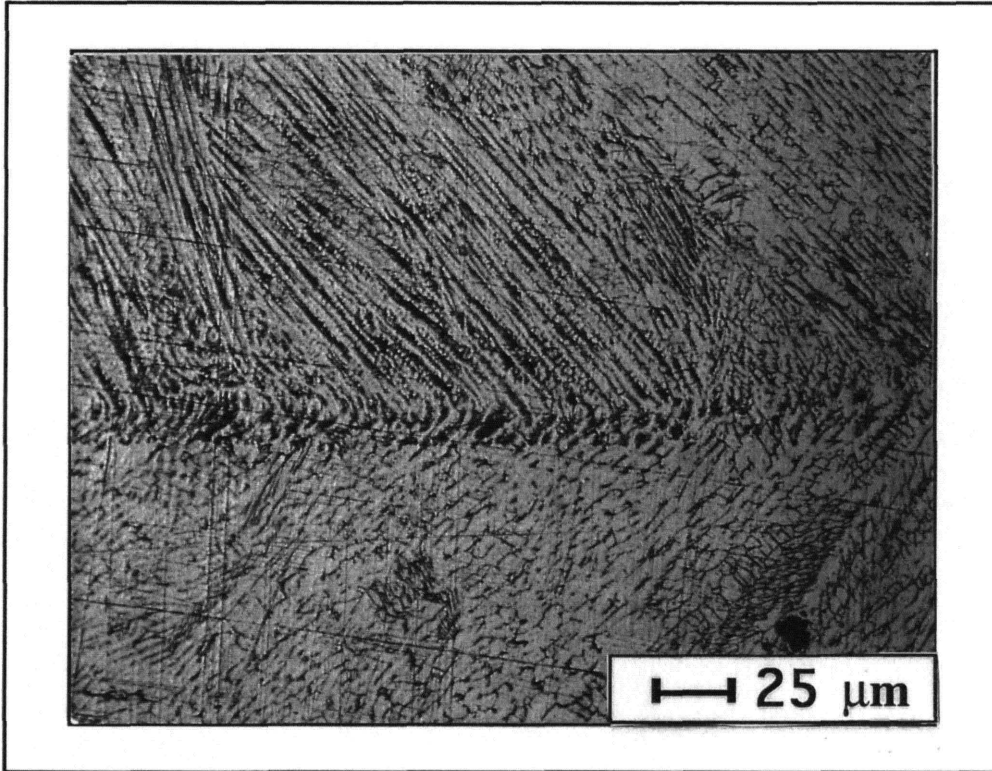


**FIGURE 4.20**  
**Interface Between Two Successive Weld Deposits,**  
**308 SS EB Deposit, 400 X**

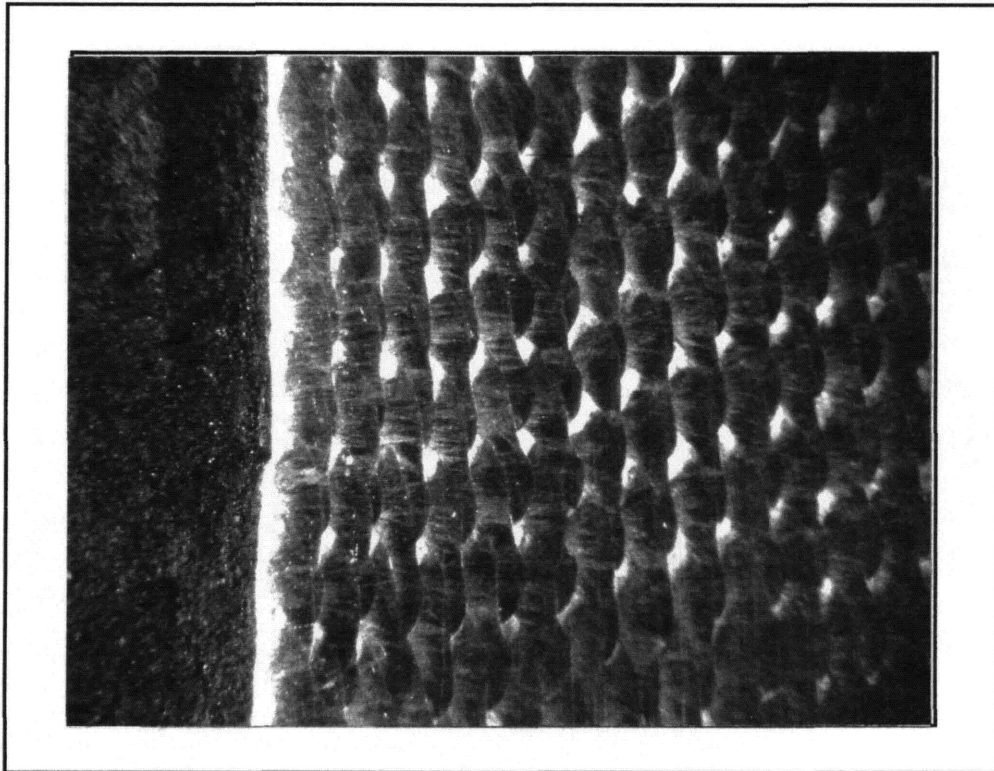


**FIGURE 4.21**  
**308 SS EB Deposit, Multipass Nature of Deposits, 12X**



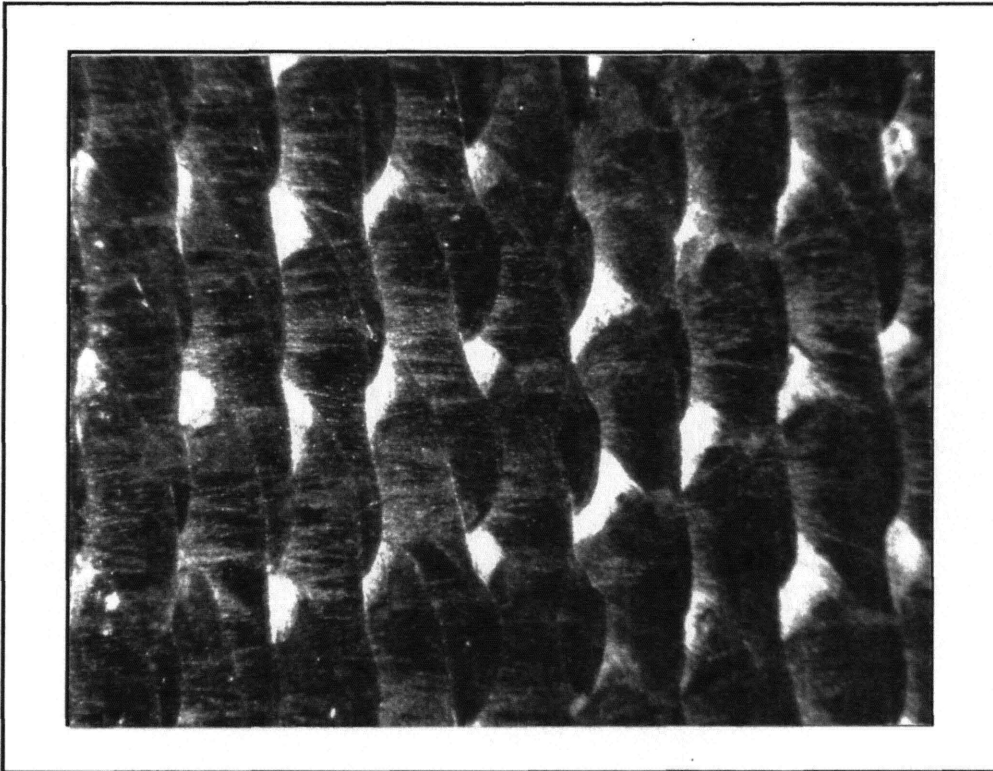


**FIGURE 4.22**  
**308 SS EB Deposit, Multipass Nature of Deposit, 25 X**

#### 4.6 Al - Bronze EB Deposit on Monel

Another system that was investigated using wirefeed EB deposition was Al - Bronze on Monel. Al - Bronze is an alloy commonly used in naval applications on account of its excellent corrosion resistance and lower cost as compared to Monel. The specific grade of Al - Bronze used was an ERCuAl-A2 filler material (AWS 5.7). The compositions of the filler material and the Monel base metal are shown below.

**TABLE 4.5**  
**Composition of Al - Bronze and Monel**

Alloy	Composition, wt. %			
	Al	Fe	Ni	Cu
Monel 400	---	2.5	at least 63.0	28.0 - 34.0
ERCuAl-A2	9.0 - 11.0	1.5	---	balance

This coating is an example of a graded coating where there is a substantial difference in thermal expansion properties. A more gradual transition from the Monel to the Al - Bronze could involve the use of a Constantan transition layer. The thermal expansion coefficients and melting points of these alloys are shown below.

**TABLE 4.6**  
**Properties of Various Cu and Ni Alloys**

Material	Density, g / cm <sup>3</sup>	Melting Range, °C	CTE, 10 <sup>-6</sup> / °C
Monel 400	8.8	1300 - 1350	13.9
Constantan (45% Ni, 55% Cu)	8.9	1220 - 1280	14.9
Al-Ni-Bronze	7.58	1035 - 1055	16.2

The more gradual transition on thermal expansion could avoid the excessive residual stresses that would otherwise develop. The direct application of Al - Bronze onto Monel did produce an adherent layer, but one which exhibits microcracks near the interface.

Figure 4.23 shows a low magnification picture of the Al - Bronze deposit and the interface between the Monel and the deposit. At higher magnifications, Figures 4.24 and 4.25 show a complex mixing region characterized by a very intricate dendritic network. This structure exhibits extensive hot tearing, as shown in Figures 4.26 and 4.27. This type of tearing and cracking is typical of welds in Monel and some of the other Cu - Ni and Cu alloys. The microstructure of the pure Al - Bronze portion of the deposit is shown in Figure 4.28. This portion of the deposit is characterized by a fine dendritic network and is crack - free.

Despite microcrack defects, the overall Al - Bronze deposit does have very good adherence. This is in part due to the excellent ductility of both Monel and Al - Bronze. If the coating is not required to be a load - bearing surface, it could

adequately perform in a corrosion protection capacity. For naval drive components, there is substantial interest in coating steels with thick overlay coatings of Al - Bronze. There are also components of Al - Bronze and Monel such as bearings, hubs, and propellers which could be repaired by an EB deposition technique. Although conventional welding is considerably cheaper, EB deposition offers higher deposition rates and more localized heating. This can result in faster repairs and repairs to components that are susceptible to heat - related distortion, such as propeller blades. The cost savings due to minimization of downtime and the ability to repair thin section parts may make EB deposition an economically viable alternative.



**FIGURE 4.23**  
**Al - Bronze Deposit on Monel, 16 X**

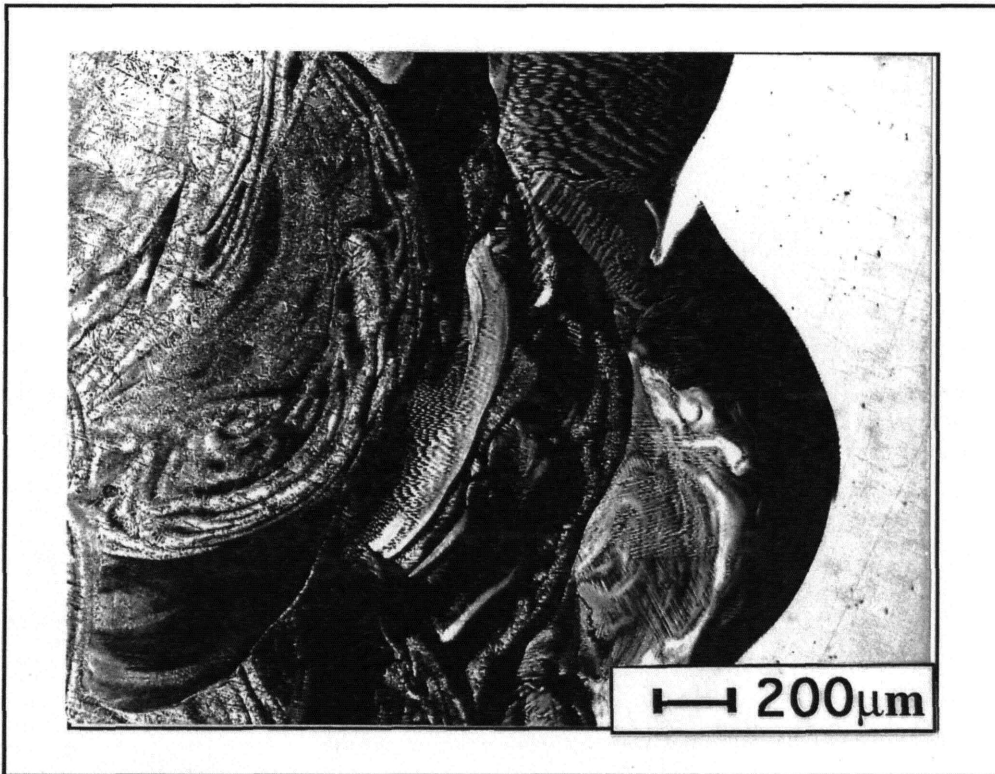


**FIGURE 4.24**  
**Mixing Region Between Al - Bronze and Monel, 50 X**

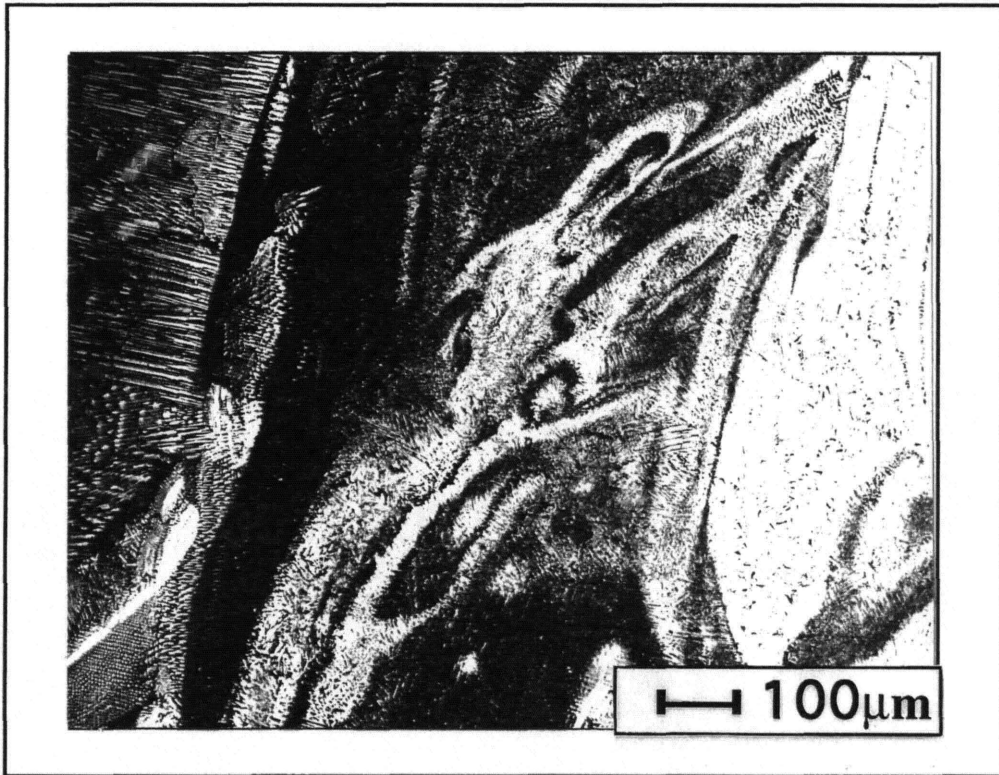


**FIGURE 4.25**  
**Region of Mixing Between Al - Bronze and Monel, 100 X**

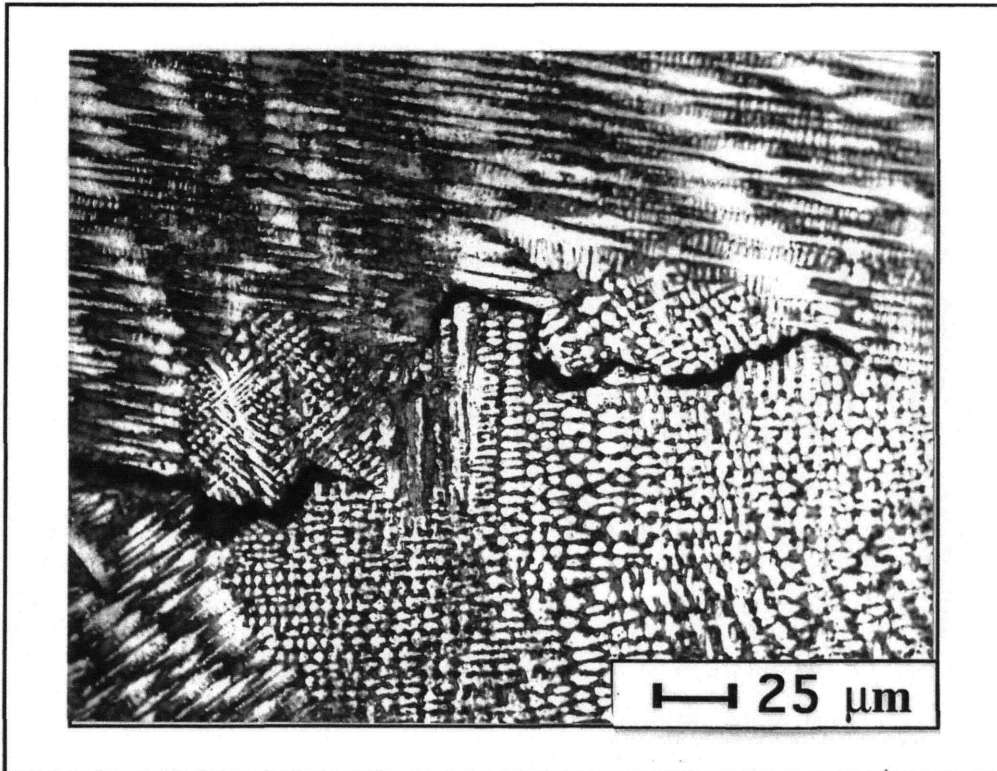


**FIGURE 4.26**  
**Hot Tear Near Bottom of Mixing Region, 400 X**

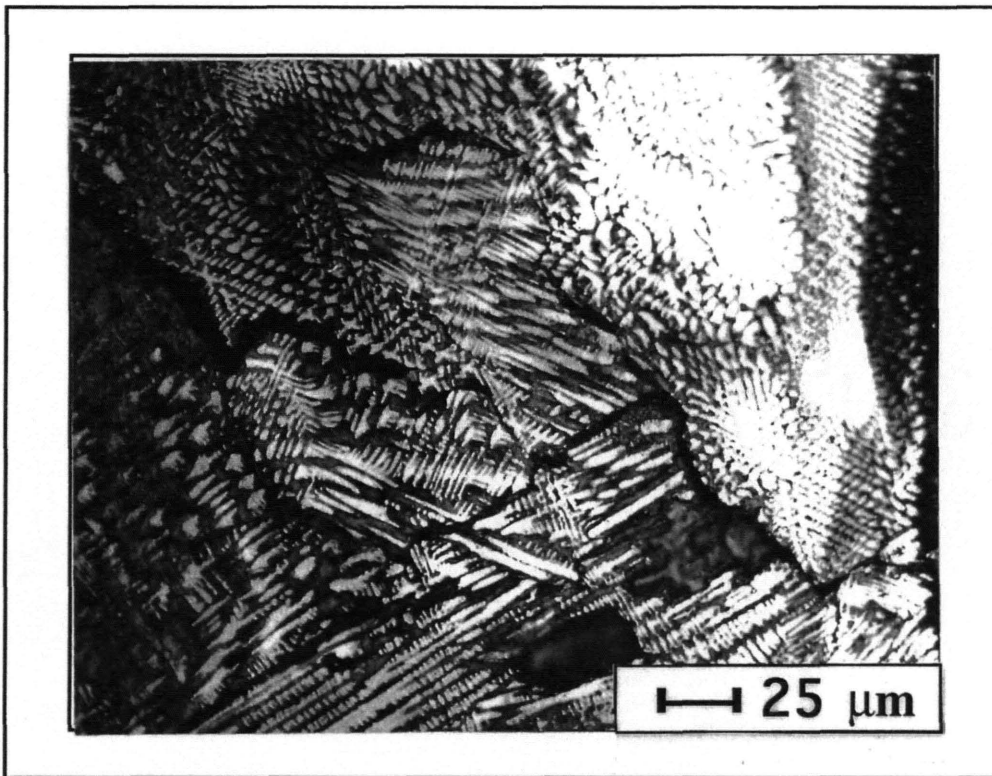


**FIGURE 4.27**  
**Hot Tear Near Bottom of Mixing Region, 400 X**

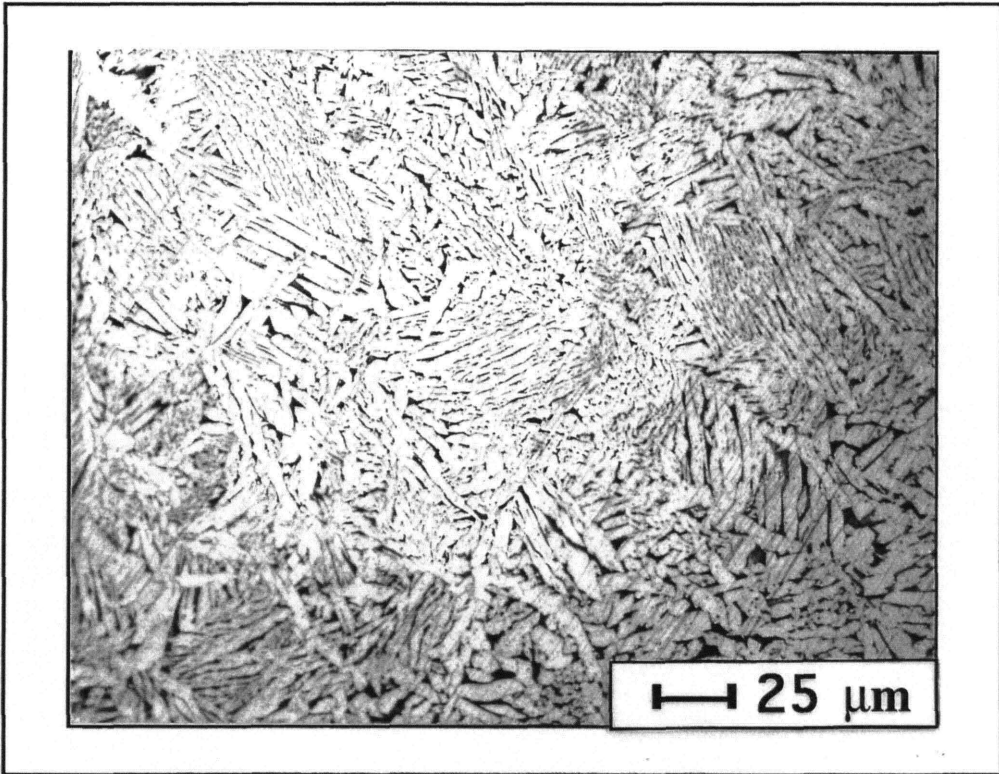


**FIGURE 4.28**  
**Microstructure of Al - Bronze EB Deposit, 400 X**



## 4.7 Residual Stresses

Residual stresses will be present in the EB deposited material as a result of non-uniform thermal profiles and the thermomechanical properties of the deposited material. As the deposited material cools, non-uniform temperature gradients (non-linear) will result in thermal stresses. The material will deform under the influence of these stresses, and upon final cooling, residual stresses will be "locked in" the deposited layer. A newly deposited layer will alter this residual stresses state in the penultimate layer below it, and thus the overall residual stress profile will evolve as the deposit becomes thicker layer by layer.

If a single layer is considered, the residual stresses can be estimated by using an approximate analytical technique. There have been many such analytical solutions proposed, and one of the first was due to WEINER & BOLEY (1963). Of primary concern here will not be the specifics of the calculation but the essential results. Qualitatively, the final residual stress will be compressive near the chill zone and tensile at the free surface. The residual stresses are schematically indicated in the figures below.

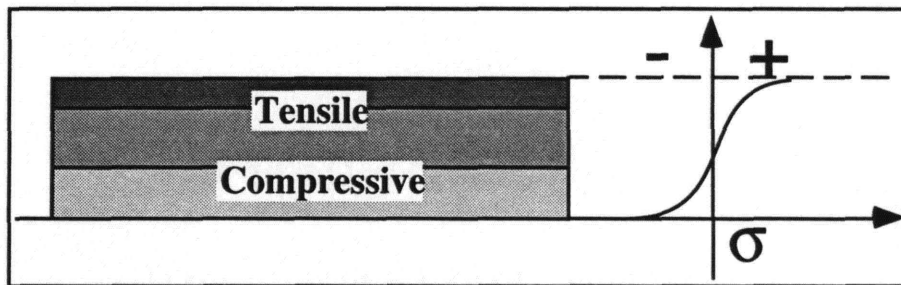


**FIGURE 4.29**  
Schematic Representation of Residual Stresses  
for a Single Layer EB Deposit

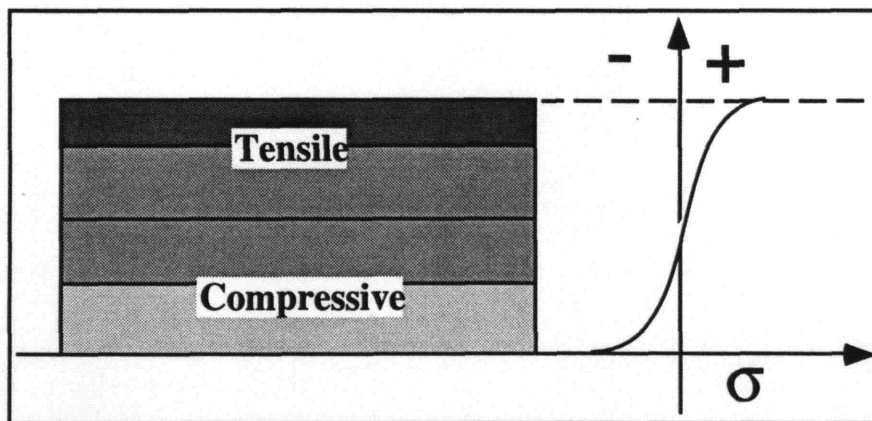
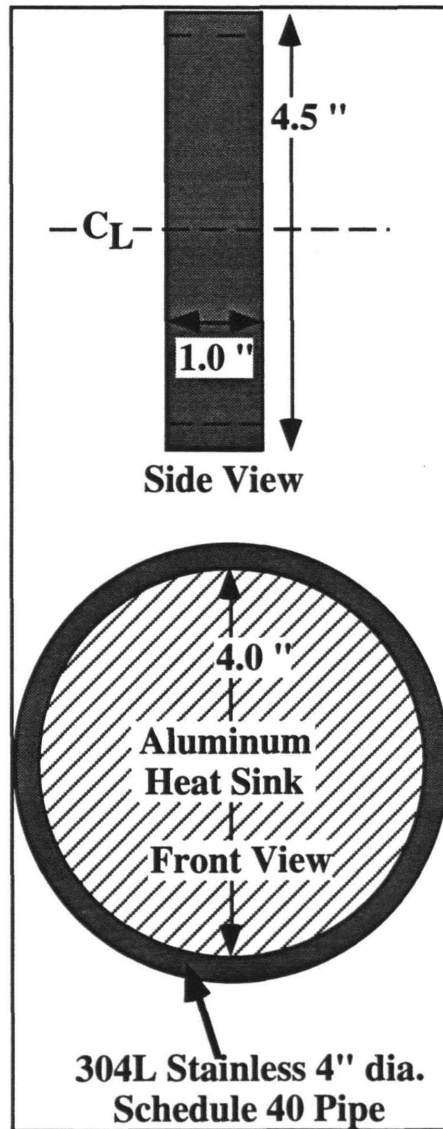


**FIGURE 4.30**  
Schematic of Residual Stresses in a  
Multilayer EB Deposit

In multilayer deposits, the successive layers disrupt the residual stresses in the layers below, and the resultant stress profile is shown in Figure 4.30. An important qualification must be made to the stress profile shown in figure 4.30. This figure shows the stresses that would occur from a consideration of solidification stresses ONLY. This implies that all temperature gradients have more or less subsided before the next layer is deposited. If this is not the case, then the effect of thermal stresses over many layers must be considered. This will intensify the stress profiles, increasing the values of the tensile and compressive stresses and the free surface and chill wall respectively.

Residual stresses in 308 SS EB deposits were measured using the X-Ray diffraction technique. Measurements were made on a single layer deposit and on a deposit that had four layers. The latter measurement was disturbed slightly due to non-uniform yielding of the embedded aluminum heat sink that was placed in the sample. A schematic of the samples used in the residual stress evaluation is shown below.



(shown above)  
**FIGURE 4.31**  
**Schematic of Targets used for**  
**Residual Stress Evaluation, Shown 1/2 Scale**

Residual stress evaluation is based on the fact that X-ray diffraction peaks are shifted by uniform macrostrains imposed on the sample. In X-ray stress measurements, the lattice spacings serve as the "strain gages" by which the stress state may be inferred [for detailed discussion, see CULLITY (1978)]. It is important to keep in mind that residual stresses are clearly *elastic only*. These elastic stresses affect the lattice spacings in the crystalline material being measured, thus making X-ray residual stress measurement possible.

The most commonly used X-Ray diffractometer-based residual stress measurement technique assumes that a state of plane stress exists in the sample. The following brief description of this measurement is adapted from CULLITY (1978). The figure below shows such a state of stress and shows the principal stresses. Although there is no out-of-plane stress, there is a strain component perpendicular to the surface.

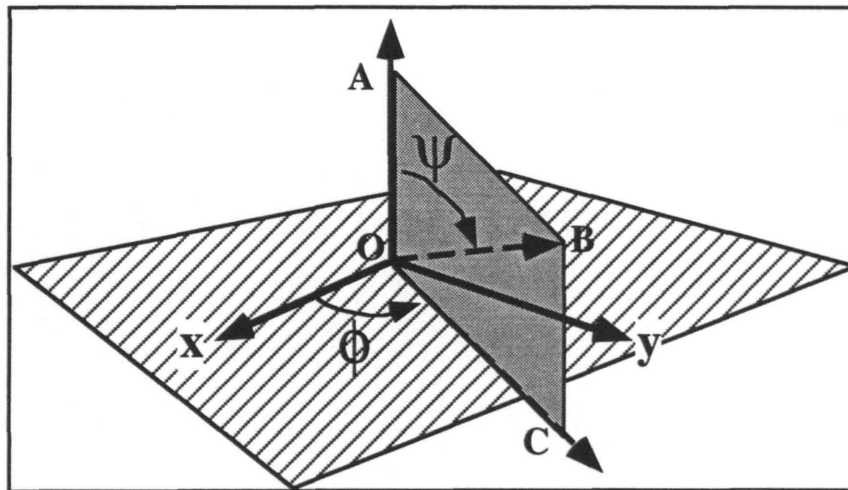


**FIGURE 4.32**  
**Coordinate System for Residual Stress Measurement**  
**Adapted from CULLITY (1978)**

The strain normal to the surface will be designated  $\epsilon_n$ , and the strain along the direction OB will be labeled  $\epsilon_i$ . The corresponding atomic plane spacings will be designated  $d_n$  and  $d_i$  respectively. The expression for the strain along the direction OB in response to the in-plane stresses can be expressed in terms of the stresses along the principal axes x and y and in terms of the stress along the axis OC. This latter stress is the stress to be measured by the X-ray diffraction technique. The expression for the strain along OB is :

$$\varepsilon_i = \frac{1}{E} \left[ \sigma_{oc} (1 + \nu) \sin^2 \psi - \nu (\sigma_x + \sigma_y) \right] \quad (1)$$

The strain along the normal direction is simply given by :

$$\varepsilon_n = -\frac{\nu}{E} (\sigma_x + \sigma_y) \quad (2)$$

The difference between these two strains will eliminate the stresses in the x and y directions leaving only the stress to be measured in the resulting equation.

$$\varepsilon_i - \varepsilon_n = \frac{\sigma_{oc}}{E} (1 + \nu) \sin^2 \psi \quad (3)$$

If the non-stressed plane spacing is designated  $d_o$ , then the strains may be written in terms of the difference between the plane spacings :

$$\varepsilon_i - \varepsilon_n = \frac{d_i - d_o}{d_o} - \frac{d_n - d_o}{d_o} = \frac{d_i - d_n}{d_o} \quad (4)$$

Since the lattice spacings are all very close to one another, the difference of any two spacings is very small when compared to any of the spacings. This means that the above expression may be approximated by an expression that does not contain the stress-free plane spacing :

$$\sigma_{oc} = \frac{E}{(1 + \nu) \sin^2 \psi} \cdot \frac{d_i - d_n}{d_o} \cong \frac{E}{(1 + \nu) \sin^2 \psi} \cdot \frac{d_i - d_n}{d_n} \quad (5)$$

This last equation is the basis for X-ray residual stress measurement, and it expresses the stress to be measured in terms of two plane spacings : normal to the surface and at some other orientation (usually 45°). This means that two X-ray measurements are needed to determine the residual stress in the desired direction.

The actual measurements on the 308 stainless deposits were made for two different samples : one with a single deposit and the other with four layers of deposit. The deposition conditions were as described in Table 4.2. The residual stress was measured in the "hoop" direction, or the circumferential principal stress. There were two measurements per sample, and they were located at sites 180° degrees apart on the circumference in the center of the deposit. The irradiated region had dimensions 0.2 in. X 0.2 in. and the incident beam divergence was 1.0 deg. The detector was set for 90% acceptance of the manganese K- $\alpha$  radiation used. The table below shows the results of the stress measurements.

**TABLE 4.7**  
**X-Ray Residual Stress Measurements**  
**308 EB Deposit on 304L Pipe**

Sample	1st Measurement, ksi	2nd Measurement, ksi
Single Layer Deposit	32.9 ± 2.8 tensile	29.5 ± 2.2 tensile
Four Layer Deposit	21.9 ± 4.3 tensile	36.0 ± 5.7 tensile

The measurements on the single layer were fairly consistent, but the measurements on the multiple layer deposit showed some variation. Although a full series of measurements around the circumference was not taken, the discrepancies between the two measurements in the second case could have been caused by the fact that in the four layer deposit, the aluminum heat sink expanded and yielded under the influence of thermal stress. This did slightly distort the stainless ring, and hence the deposit. This distortion is also expected to affect the residual stress state in the deposit, making it non-uniform around the circumference.

The main message from these limited residual stress measurements is that the stress values do not significantly increase with layer thickness at least out to four layers thick. Measurements on thicker pieces would be needed to verify this trend, but there are several factors that could contribute to the relatively flat or sluggish growth of the residual stresses with thickness. Each subsequent layer deposited serves as a "stress relief" for the layer below it. If there are no temperature gradients extending over many layers during the deposition, there will not be an excessive buildup of tensile residual stresses with thickness. The reasons for this are qualitatively elucidated below.

There are at least three main sources of residual stress inherent to the EB deposition process : stresses associated with solidification, stresses due to differing thermophysical properties between the base metal and the deposit, and the influence of temperature gradients extending over many layers during cooling. Assuming that there is no mismatch of material properties for the deposition of 308 stainless onto 304L stainless, the remaining sources of stress are solidification and thermal gradients.

If the deposition process is sufficiently slow, the influence of stresses due to severe temperature gradients will be minimal. Sufficiently slow in this case means that all temperature transients must die down in the deposited material before the next layer is deposited. In this manner, the solidification and cooling stresses will be essentially isolated to the deposited layer and perhaps the layer directly below it. If the part is not actively cooled, there will not be any other temperature gradients that can have an effect on the residual stress state. There will of course be additional residual stresses after processing as the entire part cools to room temperature, but these can be mitigated by avoiding a rapid quench and using a stress-relief anneal.

Schematically, the residual stress profiles expected in the EB deposition profile are shown in Figures 4.29 and 4.30. These figures show the expected variation in hoop stress as a function of thickness through the deposit. The annealing effect of successive layers is schematically indicated by showing

accentuated stresses at the top and bottom of the layer, with much smaller values in the interior.

An indirect indicator of residual stresses can be gleaned from microhardness measurements. These measurements will be affected by residual stresses in two ways. Firstly, the diagonals of the indent will be distorted by the residual stresses, and this will increase or decrease the apparent hardness. It is expected that compressive residual stresses will result in a higher apparent hardness, whereas tensile stresses will result in a lower one. This is because at least one diagonal will be shortened or lengthened, depending on the orientation of the indent with respect to the orientation of the stresses. Another way in which hardness measurements can correlate to regions of higher residual stress within the deposit is related to actual material work hardening through plastic deformation. Under the influence of thermal stresses, the material in the deposit will plastically flow. This effect is expected to be the greatest near the interface between the base metal and the deposit. As successive layers are deposited, the material near the center and bottom of the deposit acquires a higher dislocation density than more "freshly" deposited material. This will increase the measured microhardness. These regions are also expected to be the regions of highest residual stress. Corners in particular will exhibit the maximum effect due to geometric stress concentration.

To verify the above conjectures, microhardness measurements were carried out on a 0.5" (1.25 cm) thick 308 stainless EB deposit. The Vickers microhardness indenter was used with a load of 300 g. A typical microhardness trace is shown below.

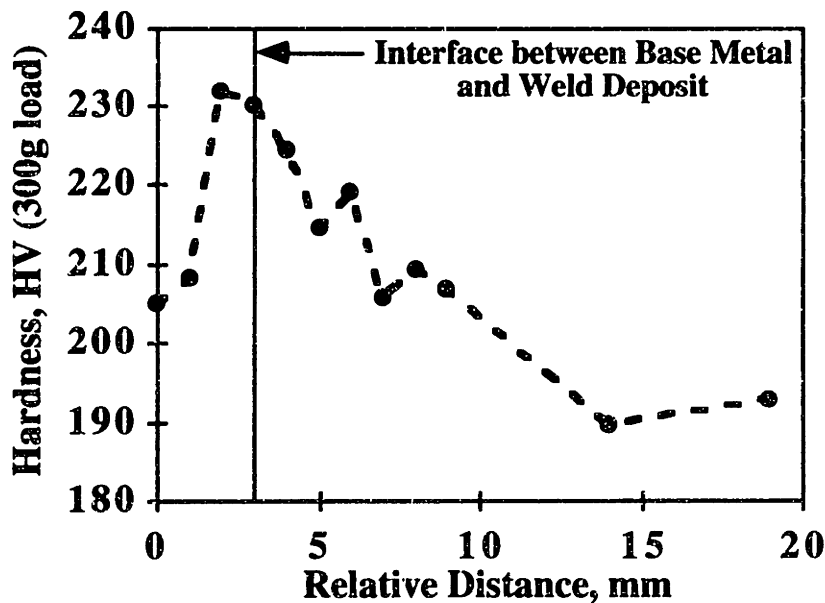


**FIGURE 4.33**  
**Microhardness Profile in 308 EB Deposit**

The hardness peaks at the interface between the base metal and the deposit and gradually decreases towards the top of the deposit. This profile is a qualitative indicator of the combined effects of residual stress and actual hardness increase due to increased dislocation density. The precise correlation of hardness data to residual stress state is not legitimate, although these measurements do illustrate the trends discussed above.

Previous investigators [SETTY et al. (1957)] have also noted this effect, and it may be qualitatively understood through the following analysis. Both the Vickers and Brinell hardness measures are defined as the indent load divided by the indent area. If the flow under an indenter is analyzed under the assumptions of plane - strain compression, then the geometrical constraint factor is given by [DIETER (1986)]:

$$\frac{\sigma_M}{\sigma_Y} = 1 + \frac{\pi}{2} \approx 2.57$$

$\sigma_Y$  is the yield stress, and (6)  
 $\sigma_M$  is the mean pressure required to cause yield under the indenter.

When residual stresses are present, the magnitudes of the principal stresses change, and the above constraint factor will also change. This will in turn directly affect the hardness, since by definition the hardness is proportional to the mean pressure required to cause yield under the indent. There will of course be correction factors for strain hardening, but to a first approximation, this explanation is satisfactory.

#### 4.8 Conclusions

The potential of EB wirefeed deposition as a freeform fabrication technique has been successfully demonstrated in 308 SS and Al-Bronze. There are several applications of this technique that are potentially promising :

- repair of naval drive components
- rapid prototyping of large (100 - 1000 lbs) parts
- thick overlay coatings for naval components
- overlay and hardfacing applications in the steel and petrochemical industries (rollers, valves, wear surfaces, etc.)
- applications to the power generation industry ( rebuilding of steam turbines, shafts, flanges, etc.)

- potential for high power (20kW) atmospheric applications with commercially available equipment (although no atmospheric tests have been conducted)

Under the proper control conditions, the deposits are defect-free, fully dense, and exhibit a microstructure typical of that found in multipass welds. The effect of residual stress has not been a limiting factor at least out to deposit thicknesses of 1.25 cm. It is expected that residual stresses will become more of an issue at higher deposition rates. To avoid problems with cracking at higher deposition rates, in - situ stress relief may be necessary. The alternative to such stress relief is preheating and slow cooling. The advantage of in-situ stress relief is that the residual stress profile may be precisely altered as the component is built up. Pulsed lasers or pulsed e-beams may be used in this capacity.

EB deposition is at best a near net-shape process. It is not intended to give a high degree of dimensional accuracy, and post-processing will be necessary. This is not necessarily a limitation, however. As was discussed earlier in this Chapter, arc welding processes are currently used in precisely the same capacity, and post processing in the form of machining, grinding, and heat treatment is not a process limitation.

The EB deposition technique has inherent limitations that must be clearly recognized. It is a very specialized technique with niche applications. The technique is expensive. Capital costs are at least \$ 1 - \$ 2 million. E-beam systems must therefore have a high utilization factor to be economical in operation. Any potential application should meet several criteria :

- need for very high deposition rates, i.e. large parts
- need for very fast turn around time
- low volume and custom production parts work best

Ship components, steel mill rollers, and steam turbine parts all meet these criteria. In each case, the economic penalty for adding even one additional day to the processing time is very severe (as high as \$ 500, 000.00 / day). These parts are very large and would require large deposition rates to process them in a reasonable amount of time. They are also very low production volume parts, with only one or two parts being processed at a time. For the right applications, the EB deposition technique could make substantial contributions without the need for extensive development of new equipment or processes. Currently available commercial e-beam welding equipment is very suitable for deposition applications. Further studies are needed to determine fabrication procedures and strategies for specific components.



## CHAPTER 5

### High Energy Electron Beam (HEEB) Materials Processing Applications

#### 5.1 Overview

As mentioned in the introduction, this thesis is one of the most complete experimental studies of the applicability of HEEBs for materials processing applications. The taxonomic classification of HEEB processes is a useful starting point for the presentation in this chapter, and Table 1.1 is shown again below.

**TABLE 5.1**  
**Taxonomic Classification of HEEB-Based Processes**

Specific HEEB Application	Classification of Unit Manufacturing Processes			
	Phase Change (casting, vapor processing)	Internal Structure Change	Consolidation (joining and P/M included)	Deformation Processes
Shock Treatment		X		X
Surface Hardening		X		
Ceramic Strengthening		X		X (thermal stresses)
Powder Melting and Sintering	X		X	
Dynamic Powder Consolidation			X	X
C/C Composite Joining			X	
Polymer Crosslinking		X		

In this work, the following processes were considered : shock strengthening, C /C composite brazing, ceramic strengthening, and a preliminary consideration of powder sintering / melting. For each of these applications, preliminary results will be shown, and an assessment will be made as to the feasibility and practicality of the process. One of the most promising applications for HEEB processing is for polymer crosslinking and the production of PMCs (polymer matrix composites). These applications will not be discussed in detail.

## **5.2 C / C Composite Joining**

### **5.2.1 Introduction**

Carbon - carbon (C/C) composites are a class of inorganic composites that utilize carbon for reinforcement and matrix materials. They are extremely lightweight and have excellent high temperature strength. These materials were originally developed for use in thermal protection systems for space planes, beginning with the Dyna Soar program and culminating with the Space Shuttle [BUCKLEY(1992)]. Current applications of these materials also include the following areas [RUBIN (1992)] :

- F-100 jet engine afterburner nozzle
- nose caps and leading edges on Space Shuttle
- nose caps for missiles
- non-wetting crucibles for molten metal processing
- racing car disk brakes
- potential applications for high speed turbine wheels
- rocket motor nozzles
- RF parabolic reflector dishes
- experimental motorcycle engine pistons

The main feature which makes C/C materials attractive is their relative strength at high temperatures. The following schematic illustrates this point [adapted from BUCKLEY (1992)] :

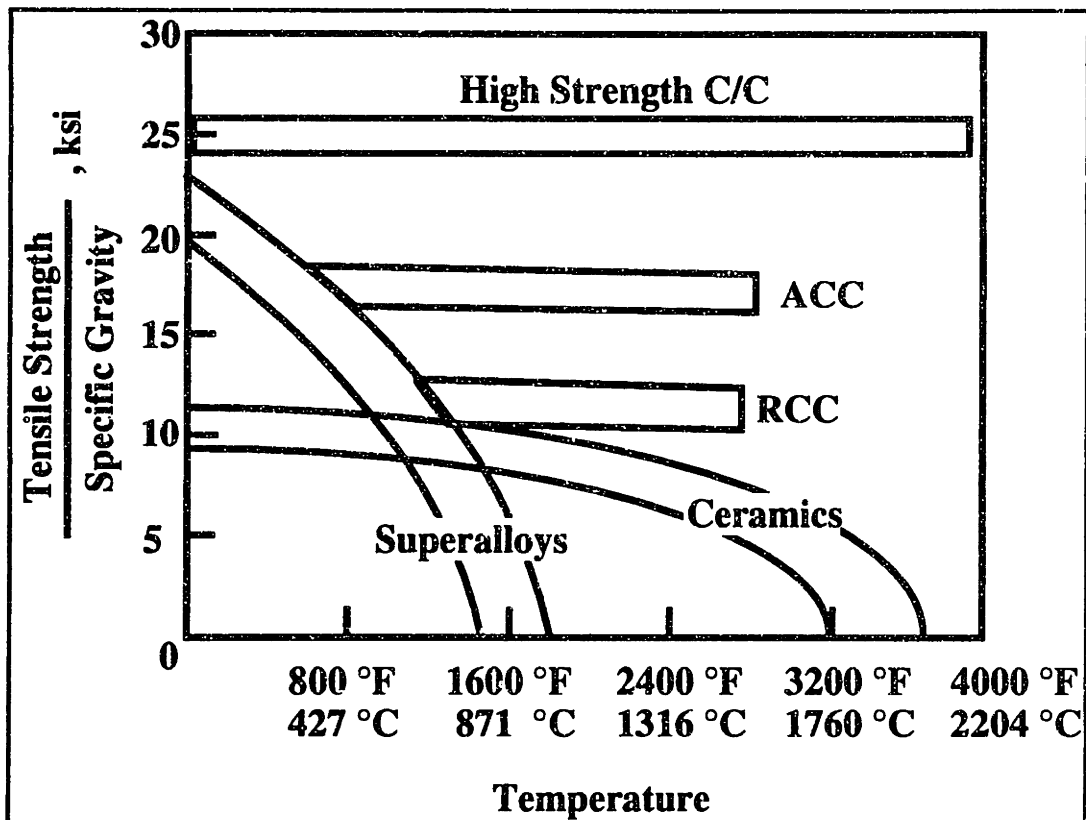


**FIGURE 5.1**  
**Relative Strength of C/C Materials**

In the graph above, RCC stands for Reusable Carbon - Carbon. This is the type of material originally used on the Space Shuttle. ACC stands for Advanced Carbon - Carbon, which represents the next generation of C/C materials currently in application (including the Space Shuttle). The high strength material represents the current state of the art. In addition to favorable high strength properties, the thermal expansion coefficient of most C/C materials is also very low. A typical value for the linear expansion coefficient is approximately  $0.5 \times 10^{-6}$  cm/cm/°C [BUCKLEY (1992)].

The major drawbacks of C/C materials are high cost and poor oxidation resistance. The list of applications above shows that the majority of the current and future uses of C/C are limited to low volume aerospace and defense applications where the high cost is justified by gains in performance. Oxidation resistance is perhaps an even more serious issue, since it places an effective limit on the maximum use temperature which is far below the potential temperature capabilities of the material. Generally speaking, unprotected C/C materials cannot be used at temperatures higher than 450 °C [SHEEHAN (1992)]. A successful protection scheme must protect fibers and provide a coating on the outer surface of the composite part. Many techniques have been applied to the problem of coating fibers, and they include [SHEEHAN (1992)] :

**TABLE 5.2**  
**C/C Fiber Coating Strategies**

COATING METHOD	COATING MATERIAL(S)
CVD	TiB, TiC, TiN, SiC, BN, Si, Ta, C
Sputtering	SiC
Ion Plating	Al
Electroplating	Ni, Co, Cu
Liquid Precursor	SiO <sub>2</sub>

Coatings on the composite parts themselves have utilized some of the same processing techniques. One of the first attempts was the coating of the RCC material for use on the Space Shuttle. The liquid precursor in this case was TEOS, or tetraethoxysilane, which when activated by an acid will produce a silica sol/gel [ILER (1955)]. Other coatings include the CVD application of SiC. Current coating concepts are multilayer coatings that somewhat resemble Thermal Barrier Coatings (TBCs) used in the protection of superalloys.

The performance limit of present silica-based coatings is approximately several hours at temperatures in the range 1000 °C to 1400 °C [SHEEHAN (1992)]. SiC and Si<sub>3</sub>N<sub>4</sub> have also been used as external coatings at temperatures up to 1700 °C. These temperature limits are below the temperature capabilities of the coating materials, and the limiting factors that disrupt coating performance are [SHEEHAN (1992)] :

- CTE mismatch - cracks
- CTE mismatch - spalls
- ability of coating to accommodate differential strains, i.e.  
flow characteristics of coating
- volatilization of coating
- chemical and thermal stability of coatings

This list of problems is formidable, and any realistic coating design is a tradeoff between these factors. The state of the art is that C/C can be protected for hundreds of hours up to 700 - 1000 °C, and for limited time exposures to temperatures as high as 1700 - 1800 °C.

### **5.2.2 HEEB-Based Joining of Carbon-Carbon Materials : Theory**

Joining of C/C materials to date has been very application-specific. Mechanical fasteners have been made from C/C materials [ADVANCED MATERIALS AND PROCESSES (1994)], and brazing has been done to a limited extent [McMANUS (1994)]. It was the aim of this current investigation

to examine brazing techniques for C/C materials to metallic substrates, and to examine the mechanical and metallurgical integrity of these joints.

The basis of the HEEB-based approach to C/C joining was first discussed in 1992 by Danko, Lundin, and Nolting [LUNDIN ET AL (1992)]. High energy electrons will penetrate a considerable distance into carbon. If the C/C layer to be joined is range thick or thinner, then the potential exists for depositing energy directly into the braze interlayer. This approach is very non-isothermal, and it was originally thought that HEEB brazing may thus be able to partially alleviate thermal residual stresses. The range of electrons in carbon is shown below [SPENCER (1959)].

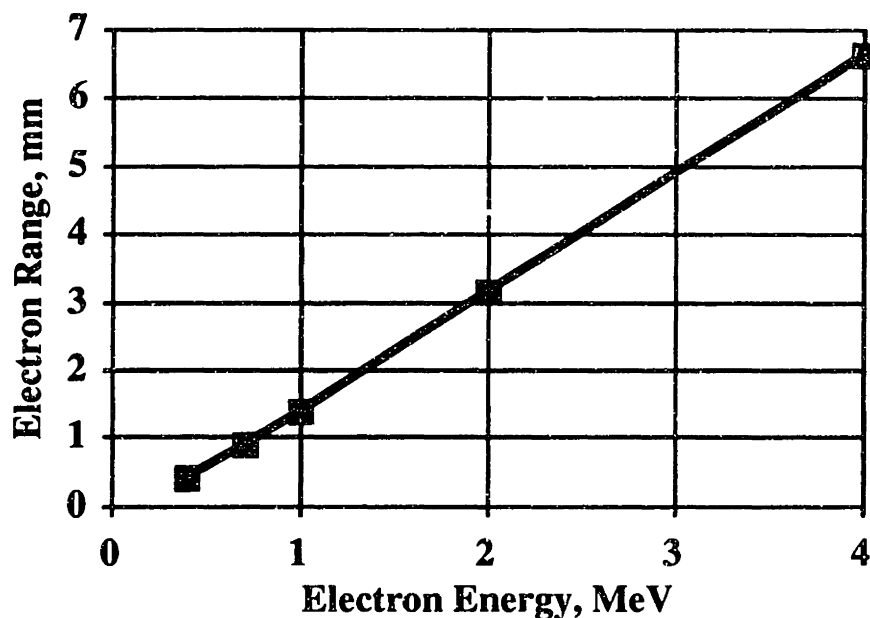


**FIGURE 5.2**  
**Electron Range in Carbon**

The primary motivation behind using an HEEB process is the opportunity to directly heat the braze interlayer. In ordinary vacuum furnace brazing, both parts of the joint are elevated to a high temperature and then cooled. C/C components would most likely be joined in vacuum due to oxidation and contamination considerations. In such conditions, it is likely that all portions of the joint will experience the same maximum temperature in an isothermal brazing process. This is shown in the figure below.

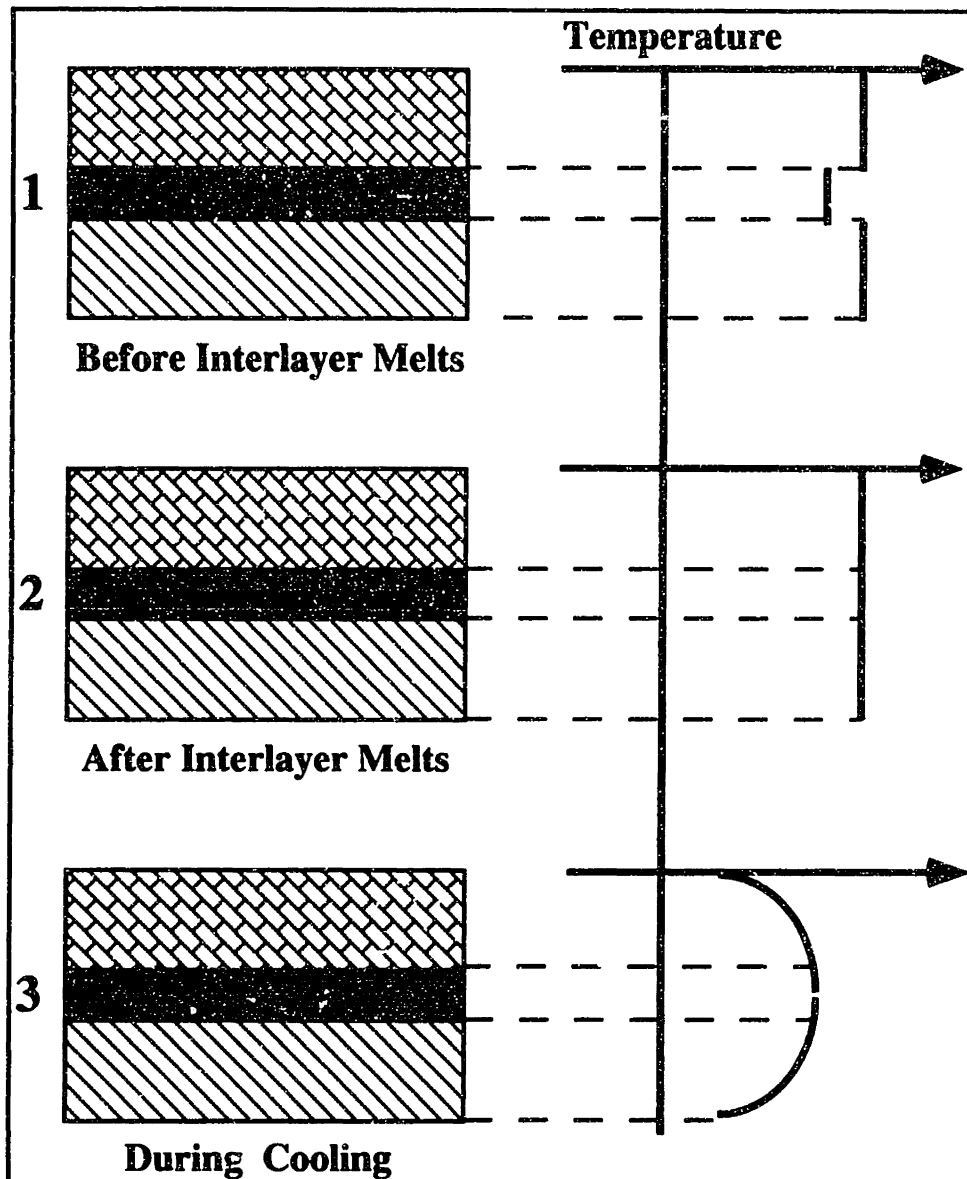


**FIGURE 5.3**  
**Isothermal Brazing**

Suppose now that a concentrated surface heat source is applied to one of the surfaces. The heat transfer through the joint would be poor until the braze interlayer material melts, at which point the heat transfer will be very good. This is true because contact resistances in a vacuum are extremely high [HOLMAN (1986)]. The braze interlayer will melt and form a bond, and only the outer regions of the base material will experience a large thermal cycle. Conventional e-beam and laser brazing could accomplish such a process. The schematic thermal cycle for this process is shown below.

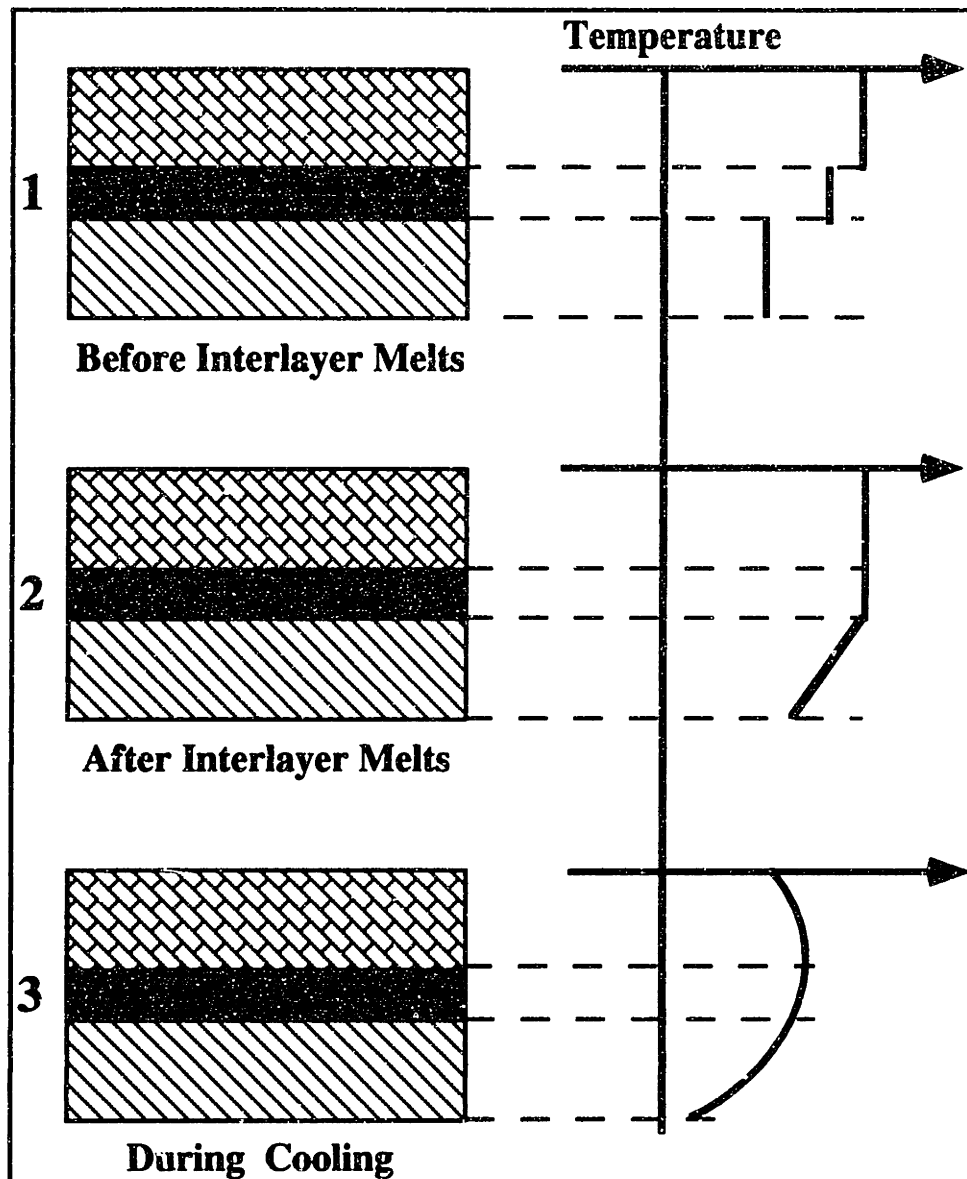


**FIGURE 5.4**  
**Laser / Conventional E-Beam Brazing**

HEEB joining goes one step further in that it localizes the heat to the braze interlayer. Now the top and bottom parts of the joint will be cooler than the braze interlayer until it melts. In this way, very little heat goes into heating the two materials being joined, and most of the heat goes into the formation of the braze itself. This process does have some limitations in that some heating of both adherends is necessary to promote good wetting and flow of the braze filler. The difference in resulting thermal cycle is shown below. Now the interlayer is actually warmer than either adherend up to the point of melting.

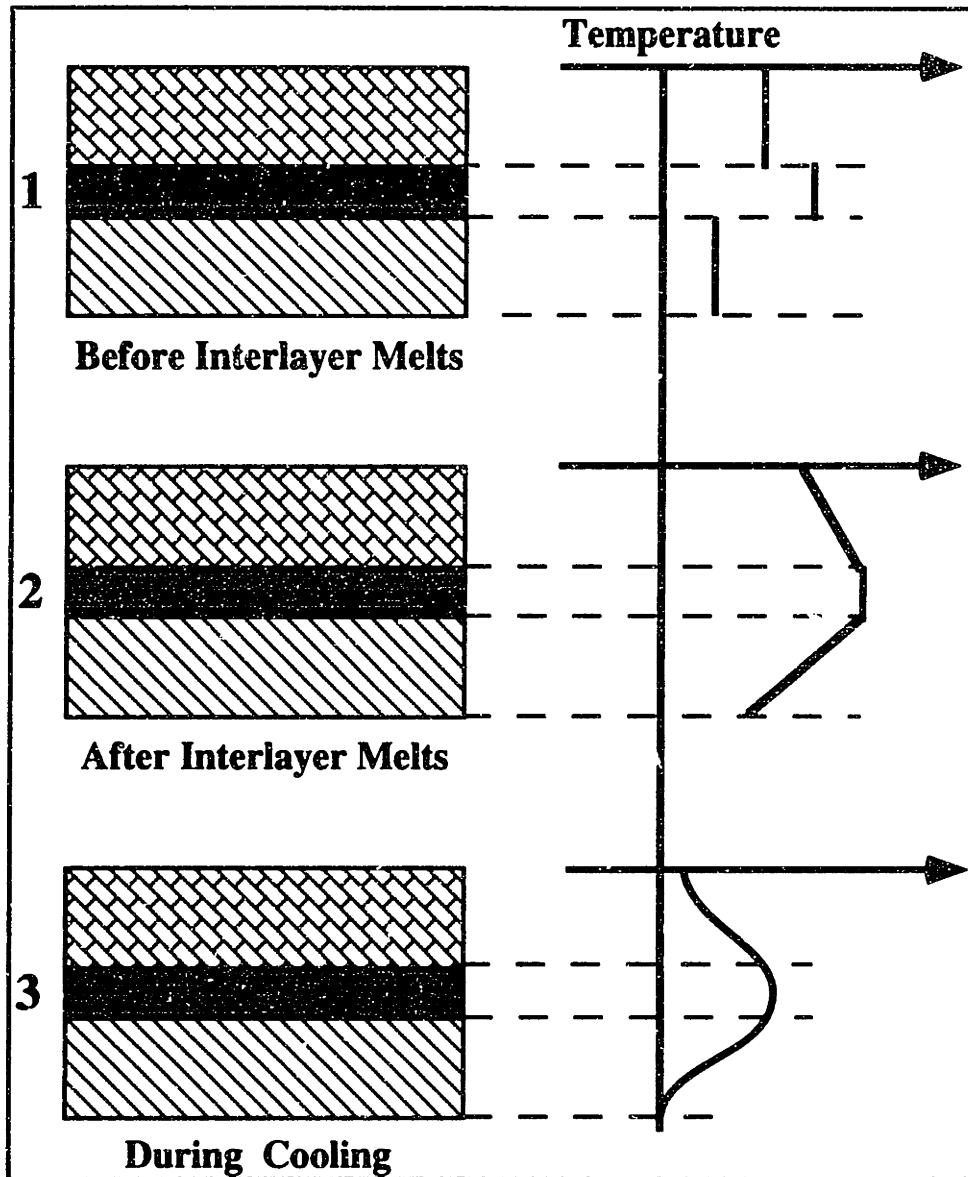


**FIGURE 5.5**  
**HEEB Brazing**

### 5.2.3 Thermally Induced Residual Stresses

In order to understand the differences between the various brazing techniques in more quantitative terms, consider the dimensional changes upon cooling experienced by the adherends in all three cases. More specifically, the free expansion / contraction of the adherends will be considered, i.e. the dimensional change that they would experience if totally isolated from all other bodies and not acted upon by any surface tractions. It will be seen later that this quantity can be incorporated into a crude estimate of the residual shear and



normal stresses experienced in the joint due to thermal mismatch. The coordinate system for these calculations is shown below.

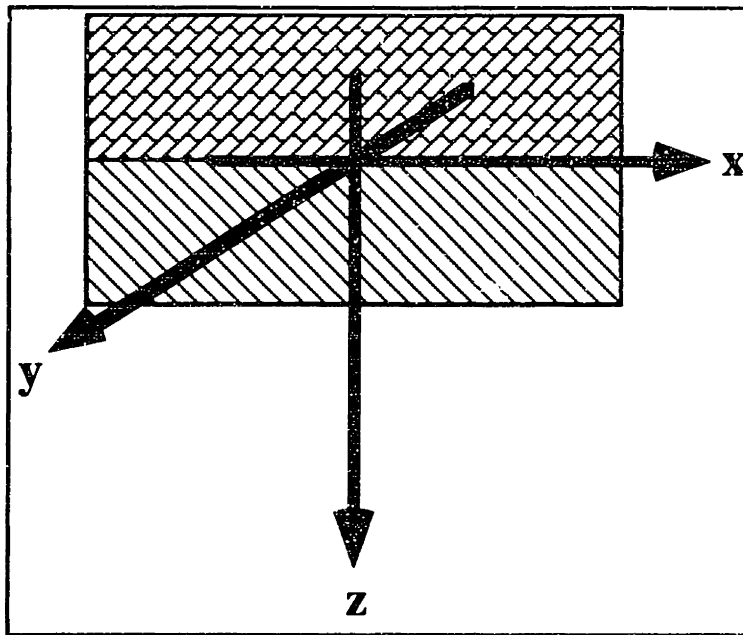


**FIGURE 5.6**  
**Coordinate System used for Calculation**  
**of Unconstrained Thermal Mismatch Strain**

For the purposes of this calculation, ignore the properties of the interlayer and consider the joint to be a bimetallic strip. First, consider the case of isothermal brazing. Both parts of the joint reach the melting temperature of the braze throughout their full extent. Suppose that the materials started at a temperature  $T_0$ . Consider the free expansion of the two halves, taking them to be isolated bodies with no imposed surface tractions. The solution of the thermoelastic problem for a free plate with temperature variations only through its thickness is given below. Suppose that the adherends are plates of thickness  $2h$ , and that the origin of the coordinate system is in the center of the plate. This means that one of the surfaces will be at  $z=-h$ , and the other will be at  $z=+h$ . Then the solution is given by [BOLEY and WEINER (1960)]:

Stresses are given by:

$$\begin{aligned} \sigma_{zz} = \sigma_{xz} = \sigma_{xy} = \sigma_{yz} &= 0 \\ \sigma_{xx} = \sigma_{yy} &= \frac{\alpha E}{1-\nu} \left\{ -T(z) + \frac{1}{2h} \int_{-h}^h T(z) dz + \right. \\ &\quad \left. + \frac{3z}{2h^3} \int_{-h}^h z \cdot T(z) dz \right\} \end{aligned} \quad (1)$$

Strains are given by:

$$\begin{aligned}\epsilon_{XY} &= \epsilon_{XZ} = \epsilon_{YZ} = 0 \\ \epsilon_{XX} &= \epsilon_{YY} = \frac{1}{E} \left\{ \frac{1}{2h} N_T + \frac{3z}{2h^3} M_T \right\} \\ \epsilon_{ZZ} &= -\frac{2\nu}{(1-\nu)E} \left\{ \frac{1}{2h} N_T + \frac{3z}{2h^3} M_T \right\} + \left( \frac{1+\nu}{1-\nu} \right) \alpha T(z)\end{aligned}\quad (2)$$

where

$$N_T \equiv \alpha E \int_{-h}^h T(z) dz, \quad \text{and} \quad M_T \equiv \alpha E \int_{-h}^h z \cdot T(z) dz$$

The Displacement Field is given by:

$$\begin{aligned}U &= \frac{x}{E} \left\{ \frac{1}{2h} N_T + \frac{3z}{2h^3} M_T \right\} \quad (\text{x-dir.}) \\ V &= \frac{y}{E} \left\{ \frac{1}{2h} N_T + \frac{3z}{2h^3} M_T \right\} \quad (\text{y-dir.}) \\ W &= -\frac{3M_T}{4h^3 E} (x^2 + y^2) + \frac{1}{(1-\nu)E} \left\{ (1+\nu) \alpha E \int_0^z T(z) dz - \right. \\ &\quad \left. -\frac{\nu z}{h} N_T - \frac{3\nu z^2}{2h^3} M_T \right\} \quad (\text{z-dir.})\end{aligned}\quad (3)$$

The symbols used are :

- $\alpha$  is the thermal expansion coefficient,
- $E$  is Young's Modulus,
- $\nu$  is Poisson's Ratio, and
- $h$  is the half - thickness of the plate.

For use in later analyses, we will be only concerned with the x-component of the strain and the displacement field. For the case of constant temperature throughout, these are :

Suppose plate held at  $T_M$ , then :

$$\begin{aligned}\epsilon_{XX} &= \alpha T_M \\ U &= \alpha T_M x\end{aligned}\quad (5)$$

In the case of a plate which is being cooled at one end, the temperature will depend on  $z$ . Suppose that an amount of heat  $Q$  is being removed from one surface of the plate, and that the other end is held at some temperature  $T_M$ . Then the temperature profile through the thickness of the block is given below. This

assumes the same coordinate system as above, i.e. that the origin is at the center of the block.

$$\text{Suppose } T(-h) = T_M \text{ and } -k \left. \frac{dT}{dz} \right|_{z=h} = Q \text{ in } \frac{\text{W}}{\text{cm}^2}$$

then the temperature profile is :

$$T(z) = T_M - \frac{Q}{k}(h+z), \text{ where} \quad (6)$$

$k$  is the thermal conductivity.

With this temperature profile, the strain and displacement in the  $x$ -direction are :

$$\begin{aligned} \varepsilon_{xx} &= \alpha \left( T_M - \frac{Q}{k}(h+z) \right) \\ U &= \alpha x \left( T_M - \frac{Q}{k}(h+z) \right) \end{aligned} \quad (7)$$

We see that the  $x$ -displacement is now a function of  $z$  also. One way of removing the  $z$ -dependence is to calculate an average value of  $U$ , one which is averaged over  $z$  as follows :

$$\bar{U}(x) \equiv \frac{1}{2h} \int_{-h}^h U(x,z) dz \quad (8)$$

When this is done for the displacement calculated earlier, we get :

$$\bar{U} = \alpha x \left( T_M - \frac{Q}{k}h \right) \quad (9)$$

Comparing this to the case of a plate at uniform temperature  $T_M$ , we note that the average displacement is smaller in the case of the plate being cooled on one side. The lowest practical value of average displacement is reached when  $Q$  is such that the temperature at  $z = +h$  is zero. Then,  $Q$  is given by :

$$Q = \frac{T_M k}{2h} \quad (10)$$

The displacement is then :

$$\bar{U} = \frac{\alpha T_M x}{2} \quad (11)$$

This displacement is one-half that of the plate at uniform temperature. The importance of this result will now be discussed in the context of residual interfacial stresses in a bimetallic strip. The following analysis will be based on beam theory and is purely elastic. Although this is a gross simplification, it will nevertheless shed some light on the effect of various temperature profiles during brazing and how they determine the final thermal residual stress state.

The bimetallic strip has received much attention as a model for dissimilar materials bonding. There is a very large body of literature addressing this problem through both analytic and numeric approaches. The basic model is one of two strips welded together in a stress free state, and then subjected to a temperature excursion. Due to the differing thermoelastic properties of the two dissimilar adherends, residual interfacial stresses will develop. The two most important stresses are the interfacial shear stress and the peeling stress. The interfacial shear stress lies in the plane of the joint. The peeling stress acts normal to this plane, and assumes its maximum value at the edge of the joint. These two stresses are shown schematically below :

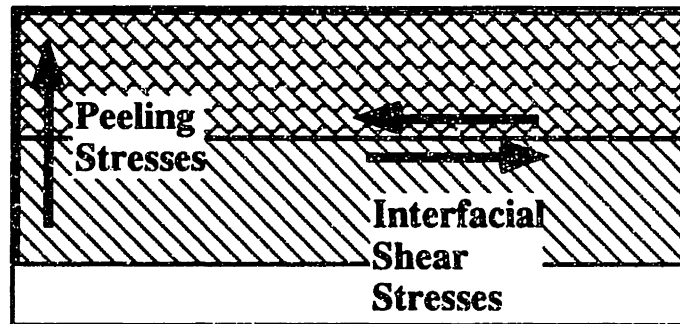


**FIGURE 5.7**  
**Interfacial Shear and Peeling Stresses**

The specific model used in this evaluation is due to SUHIR (1989). A recent study due to SWEENEY (1992) compared this solution to others, including numerical (FEM) calculations. Although there were discrepancies between the Suhir model and more realistic formulations, it does correctly show the general trends. For our purposes, it will be sufficient in that it will allow for a quantitative comparison of the effect of different heating profiles during brazing.

The solution for the interfacial shear and peeling stresses in the Suhir model are given by :

$$\begin{aligned} \tau(x) &= C_1 \sinh(\beta_1 x) + C_3 \cosh(\gamma_1 x) \sin(\gamma_2 x) + C_5 \sinh(\gamma_1 x) \cos(\gamma_2 x) \\ p(x) &= C_2 \cosh(\beta_1 x) + C_4 \cosh(\gamma_1 x) \cos(\gamma_2 x) + C_6 \sinh(\gamma_1 x) \sin(\gamma_2 x) \end{aligned} \quad (12)$$

The C's,  $\gamma$ 's, and  $\beta$ 's are constants that incorporate materials properties and geometry. The expressions for these are algebraically complex. The factor  $\Delta\alpha\Delta T$  enters into the evaluation of these constants. This quantity is the difference in the free expansion strains of the two materials being joined for a

temperature excursion of  $\Delta T$ . It is also the difference in thermal expansion strains in the x-direction. In order to compare different thermal profiles during brazing, this quantity will be replaced by the difference of the *average* thermal strains, with the average strain as defined according to the averaging procedure presented earlier. The Suhir model will now be used to perform several comparative analyses.

Even without fully evaluating the numerical expressions, it is possible to see the effect of various temperature profiles. Only the C - constants in equation() depend on  $\Delta\alpha\Delta T$ . It turns out that All the C's are directly proportional to  $\Delta\alpha\Delta T$ . This means that any reduction in the mismatch of thermal strain will have a proportional effect on both the peeling and interfacial shear stresses. For a C/C to metal joint, the physical quantities relevant to the problem will be defined as :

- $\alpha_{CC}$  thermal expansion coefficient of the C / C material
- $\alpha_{MT}$  thermal expansion coefficient of the metal
- $T_M$  maximum temperature reached at the interface (13)
- $\Delta_T$  difference in free expansion thermal strains,  
(this will take the place of  $\Delta\alpha\Delta T$ )

The reference temperature used to calculate the temperature excursion will be taken as zero.

For the case of isothermal brazing, the difference in strains is given by :

$$\Delta_T = (\alpha_{MT} - \alpha_{CC})T_M \quad (14)$$

Now consider the case of laser brazing, and suppose that the carbon surface is exposed to the laser beam. Suppose that the entire extent of the carbon piece reaches the maximum joint temperature, whereas the metal piece is being cooled from its rear surface. Then the corresponding difference in *average* thermal strains is given by :

for the C / C :  $\epsilon_{XX} = \alpha_{CC}T_M$

for the metal :  $\bar{\epsilon}_{XX} = \alpha_{MT} \left( T_M - \frac{Q}{k_M} h_M \right)$

where  $h_M$  is the half - thickness of the metal plate, and (15)

$k_M$  is the thermal conductivity of the metal.

$$\therefore \Delta_T = (\alpha_{MT} - \alpha_{CC})T_M - \frac{\alpha_{MT} Q h_M}{k_M}$$

Suppose now that the HEEB brazing method is used. In practice, the front surface of a thin piece of C/C material will not be substantially cooler than the maximum temperature reached in the joint. The advantage of HEEB lies mainly in that it deposits energy directly into the interlayer and does not rely on conduction through the C/C material. This means that less "overheat" of the C/C material is needed. The same profile will be used for HEEB as in the case of laser brazing.

If we take the ratio of the strain differences in the two cases shown above, the result is :

$$R = 1 - \frac{\alpha_{MT}}{\alpha_{MT} - \alpha_{CC}} \cdot \frac{Qh_M}{k_M T_M}$$

since  $\alpha_{MT} \gg \alpha_{CC}$ ,

$$R \approx 1 - \frac{Qh_M}{k_M T_M} \tag{16}$$

This ratio will also describe the ratio of the peak shear and peak peeling stresses that would occur in the joint under the two different thermal brazing profiles :

$\rho_{ISO}$  peak peeling stress in isothermal braze  
 $\rho_{NON}$  peak peeling stress when metal is cooled  
 $\tau_{ISO}$  peak interfacial shear stress in isothermal braze  
 $\tau_{NON}$  peak interfacial shear stress when metal is cooled

$$R = \frac{\rho_{NON}}{\rho_{ISO}} = \frac{\tau_{NON}}{\tau_{ISO}} \equiv 1 - \frac{Qh_M}{k_M T_M} \tag{17}$$

Q is the heat removed from the metal in  $\frac{W}{cm^2}$

It is thus seen that substantial reductions in both peeling and shear residual stresses may be achieved through cooling of the metallic substrate. This is a general result that applies to brazes other than C/C - metal. The limitation on cooling is that the temperature must be high enough to allow for wetting and joint formation. Localization of heating and rapid heating (as in the case of EB brazing) will in general help reduce residual brazing stresses, as the above equation shows.

The effect of using different metals may also be assessed in this analysis. Consider two different samples of a C/C - metal joint with different materials used in each case. Consider two brazing thermal histories : one in which both samples are brazed isothermally, and the other in which both samples are cooled by removing the same amount of heat Q from each metal side. We can define another ration similar to R, but in this case, it represents the ratio of the stresses in each separate sample. The relevant physical properties of the two metallic pieces are :

$$\begin{aligned}
\alpha_1 & \text{ thermal expansion coefficient of metal 1,} \\
\alpha_2 & \text{ thermal expansion coefficient of metal 2,} \\
k_1 & \text{ thermal conductivity of metal 1, and} \\
k_2 & \text{ thermal conductivity of metal 2.}
\end{aligned}
\tag{18}$$

Consider also the following stresses :

$$\begin{aligned}
\rho_1 & \text{ the peak peeling stress in the sample with metal 1,} \\
\rho_2 & \text{ the peak peeling stress in the sample with metal 2,} \\
\tau_1 & \text{ the peak interfacial shear stress in the sample with metal 1, and} \\
\tau_2 & \text{ the peak interfacial shear stress in the sample with metal 2.}
\end{aligned}
\tag{19}$$

Then, the ratio of these stresses may be defined as before :

$$R_{12} \equiv \frac{\rho_1}{\rho_2} = \frac{\tau_1}{\tau_2} \tag{20}$$

This ratio can now be related to the strain mismatch. For the case of isothermal brazing, this ratio is given by:

$$R_{12} \equiv \frac{\rho_1}{\rho_2} = \frac{\tau_1}{\tau_2} = \frac{\alpha_1}{\alpha_2} \tag{21}$$

If heat is removed from both samples at the same rate  $Q$ , and if the metal halves of both samples have the same thickness  $h$ , then the ratio becomes :

$$R_{12} \equiv \frac{\rho_1}{\rho_2} = \frac{\tau_1}{\tau_2} = \frac{\alpha_1}{\alpha_2} \cdot \frac{k_2}{k_1} \cdot \frac{(k_1 T_M - Qh)}{(k_2 T_M - Qh)} \tag{22}$$

In both cases, it was assumed that the C/C material has a negligible thermal expansion coefficient compared to the mating metal.

The arguments above show that EB brazing and intense surface source brazing have the potential for substantially reducing thermal residual stresses. This applies to the joining of materials other than C/C, and the penetration characteristics of HEEBs are not essential in achieving the stress reductions. The stress reductions will result from *any* process in which the higher thermal expansion material is heated only as much as is needed to achieve the braze joint. Lasers, low energy EBs, and HEEBs all offer a convenient way to provide an intense heat flux in a very small and localized region, thereby meeting the criterion of limiting the heat effect in the braze joint.

### 5.2.4 Experimental Program

A limited experimental program was performed in order to assess the effectiveness of HEEB-based brazing of C/C materials. There were several C/C materials used, and they are summarized in the table below :

**TABLE 5.3**  
**C/C Material Used in Brazing Experiments**  
**(Courtesy of Dr. Daniel L. Goodman)**

MATERIAL	DESCRIPTION
ACC4 C/C Advanced Technologies, Ft. Worth, TX	Eight harness satin weave 2-D material, T-300 fibers, Woven Prepreg, phenolic resin based matrix
HDFG Fiber Materials, Inc. Biddeford, ME	"4-D" Composite 3 in-plane 1mm dia. fibers at 60° Large 2mm perpendicular fibers
P120 Martin Marietta Denver, CO	P120/P120 1:1 Balanced Composite CVD infiltrated matrix
RICC-14 Rohr, Inc. Chula Vista, CA	T-300 Fibers, Bordens SC-1008 Phenolic resin based matrix Fiber Vol. 48%

There were two metallic substrate materials used : Mo-47%Re and HA-188. Two so-called "active" braze alloys were used : CUSIL ABA (Lucas Milhaupt Alloy 721) and TICUNI (Wesgo, Inc.). CUSIL is basically a Cu-Ag eutectic with a 5% wt. pct. addition of Ti. The Ti is in the form of a thin surface coating on one side of the braze foil. The TICUNI is mostly Ti, with a composition of Ti-15%Cu-15%Ni. The melting range of CUSIL ABA is 829 °C - 849 °C, and for TICUNI the range is 910 °C - 960 °C. The braze alloys were in the form of foils in one of two thicknesses; 0.0025" or 0.005". In order to further promote wetting to the C/C materials, it was necessary to sublimate a thin coating of Ti onto the surface of the C/C samples.

Front surface temperature was monitored with an infrared measurement system (Williamson Inc., Concord, MA). This sensor simultaneously uses two different IR wavelengths to get a more accurate temperature measurement. The calibrated range of the sensor is 550 °C - 1500°C. The C/C - metal samples were mounted on a water-cooled copper target holder, and they were moved in a reciprocating fashion in front of the beam at a frequency of approximately 2 Hz.. A constant pressure was applied to the braze sandwich by means of a spring-loaded plate. The brazing was done in moderately low vacuum, approx 10<sup>-5</sup> - 10<sup>-4</sup> Torr. The beam power used was in the range from 500 - 1000 W. The samples were all 1" squares. Approximate processing time was no more than 4 minutes per sample. The front surface temperature was held in the range 1200°C - 1400 °C for various soak times to allow sufficient time at temperature to promote wetting.



Three types of joints were made : C/C to itself, C/C - MoRe, and C/C - HA-188. There were three main techniques used in the analysis of the C/C joints : infrared non-destructive imaging to determine the area bonded, metallographic sectioning, and shear testing to determine joint strength. The infrared imaging was performed using a Hughes PROBEYE™ Thermal Imaging System (courtesy of Prof. John Hansman, MIT Aeronautical Engineering Dept.) This system is essentially identical to the FLIR imaging systems found in most military strike aircraft ; the main component is an argon-cooled IR camera. The braze samples were mounted on a hot-plate with the C/C side facing up, and convective cooling on the top surface was provided by fans. The thermal imaging system was then able to discern the area bonded by the difference in the heat conducted through bonded and non-bonded regions. Subsequent comparison of the IR pictures with the samples after mechanical testing showed a close correlation between the IR images and the actual area bonded, indicating the effectiveness of this NDE technique. Some sample IR images are shown at the end of this section.

Shear tests were performed by Mass Materials Research, Inc., in West Boylston, MA. Since most of the braze samples were 1" squares, pull tabs had to be mounted in order to allow the samples to be tested in a vertical tensile testing machine. Fiberglass pull tabs were mounted with heat-cured epoxy at the MIT TELAC Composites Lab (Courtesy of Mr. Al Supple). The single lap joint shear test specimens were then tested at Mass Materials Research using an Instron Servohydraulic testing machine.

The large thermal expansion mismatch between C/C and HA-188 resulted in very poor joints that often failed on handling. The only C/C material that was successfully joined to HA-188 was the HDFG material. The samples of HDFG thus joined were perhaps not representative of the bulk material, since they were machined from a much larger block. It is thought that this process of machining the C/C disrupted its weave structure, and the samples thus had far greater compliance than the corresponding bulk material. This is also supported by metallographic analysis of the joints, which showed large gaps in the fiber structure into which braze interlayer material had flowed. This "wicking" action is believed to be the reason why the HDFG samples were able to bond to the HA-188.

ACC4 was joined to itself using a TICUNI interlayer, and P120 was also joined to itself using CUSIL ABA. Both of these joints showed almost complete wetting and bonding over the braze area. The P120 samples were metallographically examined, and revealed good wetting and some mechanical interlocking. ACC4 was also successfully joined to MoRe.

The joint shear strengths were rather low, but they were consistent with observed shear strengths in other C/C brazes [McMANUS (1994)]. ACC4 joined to itself with TICUNI exhibited a typical shear strength of 360 psi for a 1" square sample. ACC4 joined to MoRe with CUSIL ABA showed a strength of only 150 psi over a 1" bonded area. The ACC4 material has an interlamellar shear strength of about 600 psi, so the ACC4 joint to itself has a strength of 60% of the maximum shear strength possible with this material. Perhaps further process optimization could increase this strength value. Within the limited scope of the short experimental program in this work, such additional testing was not possible.

### **5.2.5 Summary of Brazing Results**

A limited experimental program in HEEB-based C/C brazing was executed. The following joints were made : C/C to itself, C/C to HA-188, and C/C to Mo-47%Re (MoRe). The samples were analyzed by IR imaging, metallographic sectioning, and shear testing. The C/C - C/C and C/C - MoRe joints exhibited good area bonded, good wetting, and good mechanical interlocking at the C/C - braze interlayer surface. Joints to HA-188 failed upon cooling and handling due to the very large CTE mismatch. The mechanical properties of the joints were very low, but they were consistent with previous experimental studies (C/C - Mo joints). Due to the limited nature of this experimental program, further process optimization was not possible. Further improvements in joint properties may be possible through further experimentation with braze interlayer materials, wetting strategies, and greater control over heating and cooling rates through beam rastering and improved heat-sinking on the metal side of the joint.

It was also shown that the essential premise of the EB-based brazing approach is the opportunity to reduce residual thermal stresses by controlling the amount of heat input to the metal side of the joint. This heat input should be kept to the absolute minimum : just enough to promote wetting and braze interlayer flow. This observation is completely general and extends beyond C/C - metal joints. The combination of a localized heat source (laser, IR, low energy EB, HEEB) and proper thermal management can result in residual stress reductions in a variety of dissimilar material joining applications.

### **5.2.6 NDE Analysis Via Thermal Imaging**

The two photographs illustrate the non-destructive inspection of C/C joints using thermal imaging. The thermal images of two different joints are shown. These are joints between ACC4 and MoRe. The next picture shows these same two joints after shear testing. The correlation between the thermal images and the actual bonded area is seen by comparing these two pictures. It is seen that this thermal imaging technique is a viable means of NDI evaluation of such joints.

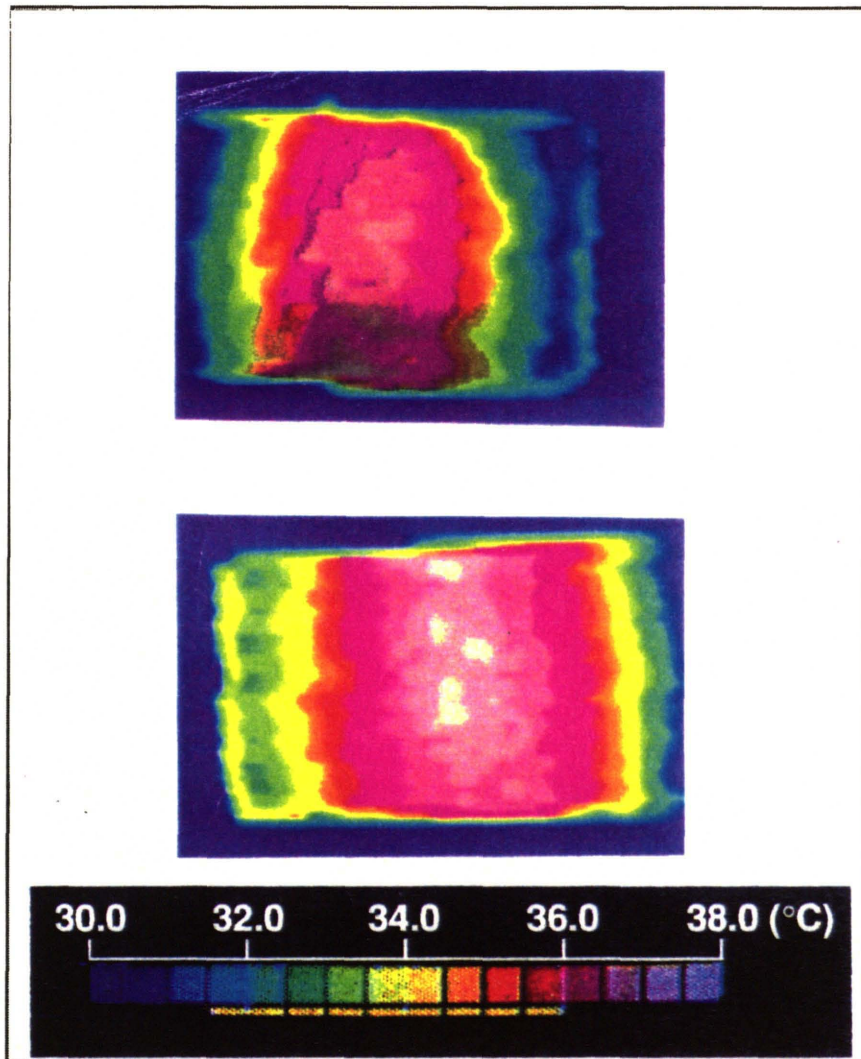


**FIGURE 5.8**  
**Thermal Images of ACC4 - to - MoRe Braze Joints**

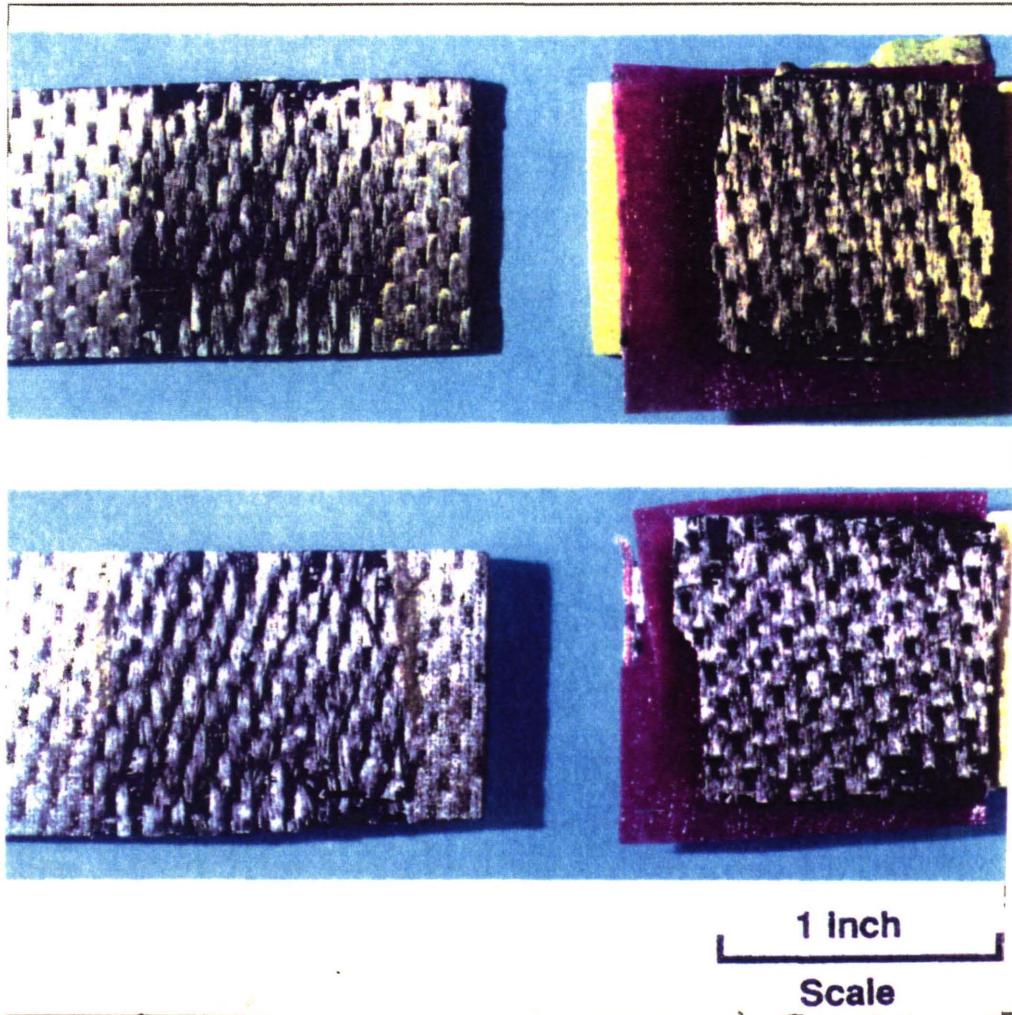


**FIGURE 5.9**  
**Bonded Area of ACC4 - to - MoRe Braze Joints**  
**Revealed After Shear Testing**

## **5.3 HEEB - Based Ceramic Strengthening**

### **5.3.1 Introduction**

Structural applications of ceramics have been severely limited due to poor mechanical properties. There have been many attempts to strengthen ceramics and to decrease their sensitivity to surface flaws. Some of these techniques include [KIRCHNER (1979)] :

- annealing
- compressive residual stresses at surface
- dispersion strengthening
- fiber reinforcement
- solid solution strengthening
- unidirectional solidification

The most commonly applied technique involves the introduction of compressive residual stresses near the surface by a variety of techniques. Some of the techniques commonly applied to achieve these stresses include [KIRCHNER (1979)] :

- glazing
- quenching
- ion exchange at surface
- formation of low (or high) expansion solid solution layers at surface
- formation of surface layers that are accompanied by an increase in volume

The current set of experiments sought to introduce a new heat-and-quench scheme which would utilize electron beams as the heat source and radiative or convective cooling as the means of quenching. Samples of 96% and 99.8% alumina were subjected to various HEEB irradiation schedules and were allowed to quench primarily by radiative cooling. Since this work was done in a vacuum, there was no convective cooling.

### 5.3.2 Thermally - Induced Residual Stresses : Mechanisms of Formation

Consider a plate that is unconstrained. If a thermal gradient is introduced such that the temperature varies through the thickness of the plate, there will be thermal stresses only if this temperature profile is not linear. The geometry of the plate is shown in the figure below.

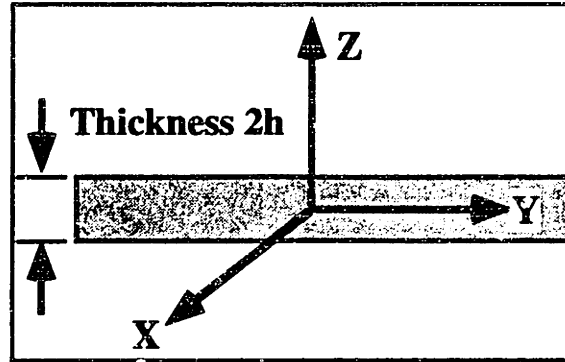


**FIGURE 5.10**  
Schematic of Coordinate System Used  
to Evaluate Thermal Stresses

If the temperature profile is given by  $T(z)$ , then the stress state is [BOLEY and WEINER (1960)] :

$$\begin{aligned} \sigma_{zz} = \sigma_{xz} = \sigma_{xy} = \sigma_{yz} &= 0 \\ \sigma_{xx} = \sigma_{yy} &= \frac{\alpha E}{1-\nu} \left\{ -T(z) + \frac{1}{2h} \int_{-h}^h T(z) dz + \right. \\ &\quad \left. + \frac{3z}{2h^3} \int_{-h}^h z \cdot T(z) dz \right\} \end{aligned} \quad (23)$$

Furthermore, the strain and displacement fields are specified by [BOLEY and WEINER (1960)] :

Strains are given by:

$$\begin{aligned}\epsilon_{xy} &= \epsilon_{xz} = \epsilon_{yz} = 0 \\ \epsilon_{xx} &= \epsilon_{yy} = \frac{1}{E} \left\{ \frac{1}{2h} N_T + \frac{3z}{2h^3} M_T \right\} \\ \epsilon_{zz} &= -\frac{2\nu}{(1-\nu)E} \left\{ \frac{1}{2h} N_T + \frac{3z}{2h^3} M_T \right\} + \left( \frac{1+\nu}{1-\nu} \right) \alpha T(z)\end{aligned}\quad (24)$$

where

$$N_T \equiv \alpha E \int_{-h}^h T(z) dz, \quad \text{and} \quad M_T \equiv \alpha E \int_{-h}^h z \cdot T(z) dz$$

The Displacement Field is given by:

$$\begin{aligned}U &= \frac{x}{E} \left\{ \frac{1}{2h} N_T + \frac{3z}{2h^3} M_T \right\} \quad (x\text{-dir.}) \\ V &= \frac{y}{E} \left\{ \frac{1}{2h} N_T + \frac{3z}{2h^3} M_T \right\} \quad (y\text{-dir.}) \\ W &= -\frac{3M_T}{4h^3 E} (x^2 + y^2) + \frac{1}{(1-\nu)E} \left\{ (1+\nu)\alpha E \int_0^z T(z) dz - \right. \\ &\quad \left. -\frac{\nu z}{h} N_T - \frac{3\nu z^2}{2h^3} M_T \right\} \quad (z\text{-dir.})\end{aligned}\quad (25)$$

The above equations apply to elastic stresses and strains only. If the material in question can be modeled as a perfectly elastic solid, then heating followed by quenching would produce no residual stresses. Initially, the surface of the plate would be in tension as it cools faster than the center. Later, the center would cool faster than the exterior, so that the final result upon reaching temperature equilibrium is that no net residual stress is impressed.

Now consider the case of a material that can deform through viscous deformation or by creep. Assume also that this phenomenon is strongly temperature-dependent. Glasses and ceramics fall into this category. Glass is a thermoviscoelastic material, and ceramics can deform by a variety of creep mechanisms. At high temperatures, all stress distributions can be relieved through deformation. As the temperature get lower, however, the ability of the material to deform under thermal stress becomes markedly reduced, and stresses can become "locked in." In this manner, residual stresses can be impressed.

For the case of thermal tempering of glass or ceramics, the outer regions of the sample are cooler immediately following a quench. This means that the exterior will initially be in tension. The center of the part will be hotter than the exterior at this point, and thermal stresses will be relieved in the center. After a certain point, thermal stresses will not relax in the center either, and this portion will then have a rapid cooling rate as compared to the exterior. The exterior will

then heat and expand, while the center will cool and contract. As a result, the residual stresses in the center will eventually become tensile, whereas those at the edges will be compressive. In this manner, near-surface compressive residual stresses can be impressed in glass or ceramics. There are many mathematical analyses of this process [for glass tempering, see for example NARAYANASWAMY and GARDON (1969), and for quenching of alumina, see BUESSEM and GRUVER (1972)].

In the case of crystalline ceramic materials, thermally activated creep is the mechanism of stress relief at high temperatures. There are several creep mechanisms that could determine the overall creep rate. Diffusional creep is one such commonly occurring mode in ceramic bodies. Diffusional creep occurs when the material deforms by diffusional flow from regions of compressive stress to regions of tensile stress. Solid state bulk diffusion typically occurs by vacancy motion, and vacancies tend to segregate to regions of tensile stress within a grain. This motion is schematically shown in the figure below.

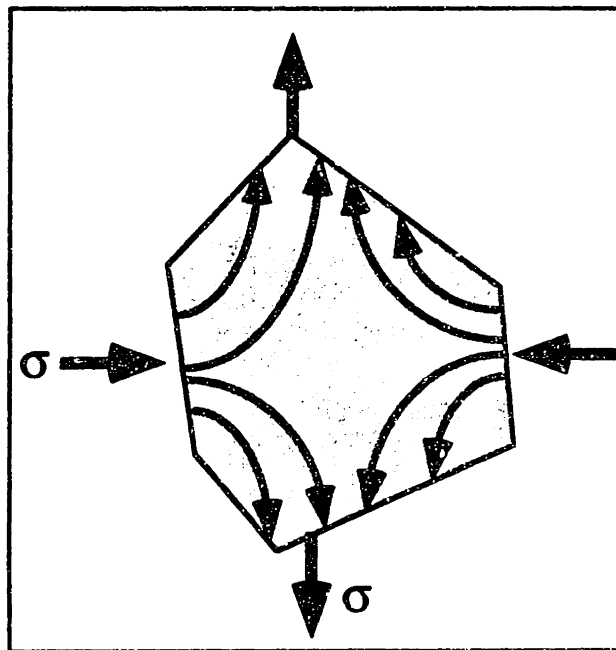


**FIGURE 5.11**  
**Schematic of Flow in Diffusional Creep**  
Adapted from KINGERY, BOWMAN and UHLMANN (1976)

If the diffusion is dominated by vacancy diffusion through the bulk of the grain, then the Nabarro-Herring equation describes the creep rate [NABARRO (1947) and HERRING (1950)] :



$$\dot{\epsilon} = \frac{13.3\Omega D\sigma}{kTd^2}$$

$\dot{\epsilon}$  is the creep rate,  
 $\sigma$  is the applied stress,  
 $\Omega$  is the volume of a vacancy (nominally the atomic volume)  
 $D$  is the bulk diffusivity, (26)  
 $k$  is Boltzmann's Constant,  
 $T$  is the temperature, and  
 $d$  is the grain size.

If grain boundary diffusion is dominant, then Coble's relation gives the creep rate [COBLE (1963)]:

$$\dot{\epsilon} = \frac{47\Omega\delta D_b\sigma}{kTd^3}$$

$\delta$  is the grain boundary width, and (27)  
 $D_b$  is the diffusion coefficient for grain boundary diffusion.

The relations above are somewhat of a simplification in light of the complex diffusion processes that occur in oxides. Since oxides are ionic solids, there must be overall charge neutrality. Vacancies will in general have charge associated with them, as will interstitial atoms. In general cationic and anionic species will have different diffusion rates. The influence of dopants and other impurities must also be accounted for [see for example KRÖGER and VINK (1956) or KOFSTAD (1972)]. If there are other structural changes, such as grain growth, the kinetics of these processes must also be considered. The table below shows typical creep rates for a specific loading condition and temperature.

**TABLE 5.4**  
**Creep Rates of Various Ceramics at 1300 °C**  
**and under an applied stress of 1800 psi**  
**Adapted from KINGERY, BOWMAN and UHLMANN (1976)**

Material	Creep Rate, in. / in. / hr.
polycrystalline alumina	0.13 X 10 <sup>-5</sup>
polycrystalline Thoria	100 X 10 <sup>-5</sup>
polycrystalline stabilized zirconia	3 X 10 <sup>-5</sup>
quartz glass	20,000 X 10 <sup>-5</sup>

It is clear from the above discussion that both the thermal cycle and the thermorheological properties of the ceramic will determine the magnitude of the impressed residual stresses. Assuming that diffusional creep processes are dominant in materials like polycrystalline alumina, it is useful to examine the temperature dependence of the creep rate. If the creep rate is given by either the

Nabarro-Herring relation or the Coble relation, the following proportionality holds true :

$$\dot{\epsilon} \propto \frac{D}{T} \quad (28)$$

$D$  is the appropriate diffusivity

If we assume for the moment that no grain growth occurs and that the temperature dependence of the vacancy volume is negligible, then the temperature dependence of the creep rate is determined by the temperature dependence of the above ratio. The diffusivity typically has a temperature dependence that is incorporated in a thermal activation term. This is usually represented by the following empirical relation :

$$D = D_0 \exp\left[\frac{-Q}{RT}\right] \quad (29)$$

$Q$  is an activation energy

This means that the overall temperature dependence of the creep rate due to diffusion controlled creep is given by :

$$\dot{\epsilon} \propto \frac{1}{T} \cdot \exp\left[\frac{-Q}{RT}\right] \quad (30)$$

The temperature dependence of the creep rate is an important consideration in the development of an optimum heat treatment strategy to achieve maximum residual stress. Ideally, if the creep rate were to fall to zero below some "freezing temperature," then the strategy for maximum residual stress would be to maximize the temperature difference between the exterior and interior of the part being processed. This is actually not the case, and as the interior cools, there is further stress relaxation. This relaxation of the interior will lower the residual stress that is developed.

In the processing of ceramic parts, there are several tradeoffs and compromises that must be made in the development of an optimum heat treatment. The premise behind the HEEB-based approach is that HEEB treatment will produce a sharp temperature gradient due to volumetric energy deposition. The region below the surface can be heated to a temperature at which creep rates are high enough to relieve thermal stresses. The part is then quenched in the usual manner through radiative cooling or the use of a quenching media.

For the HEEB process to be most effective, rapid thermal cycles are desirable. The thermal conductivity of alumina and most other ceramic materials is very low. As a result, energy that is deposited volumetrically will heat the interior faster than conduction effects can cool it. The ability to "beat thermal conduction" is therefore one of the main justifications of the HEEB-based approach. For the HEEB-approach to have maximum effectiveness, the heat must be deposited in a time faster than the time needed to conduct it away.

Furthermore, the relaxation time of the material must be short enough (creep rate must be fast enough) to allow for stress relief while the sharp temperature gradient is maintained. Then if the beam is quickly shut off, thermal conduction will cool the interior and compressive residual stresses will develop near the surfaces.

In practice, the efficacy of the HEEB process is marginal. Quenching by radiation is ineffectual as compared to quenching in a fluid media. Quenching in liquids will result in a heat transfer coefficient that is larger by a factor of 100 - 1000. Furthermore, HEEB heating must be uniformly distributed over the entire surface to be treated to avoid cracking. Whatever potential benefits that can accrue from volumetric penetration and more precise control over surface temperature gradients are nullified by the lack of adequate quenching and difficulty of process control.

### 5.3.3 Experimental Program

A limited experimental program was established to test the feasibility of HEEB - based ceramic strengthening. AD96 and AD998 alumina were subjected to HEEB heating with radiative cooling. AD96 has approx. 4% silica impurities, whereas AD998 has 0.2% magnesia. The samples were procured from LSP Ceramics (Lambertville, NJ). Specimen geometry was cylindrical with a diameter of 1.59 cm and a thickness of 0.394 cm. The samples were polished before HEEB treatment to a 1  $\mu\text{m}$  RMS finish with diamond paste. This was done since post-process grinding and polishing would have influenced the near-surface residual stress state.

The samples were carbon-coated to ensure uniform surface emissivity. Also, the carbon served as a means for charge to leave the ceramic surface and drain onto the grounding leads. For samples in which electrical contact was broken, fracture invariably occurred, and the ceramic was discolored due to formation of color centers. Samples that were properly grounded did not crack due to charge build-up (although most samples did have thermal cracks). The pulse repetition rate of the HEEB was slowly varied from 2 - 35 Hz, which resulted in an incident power flux that ranged from 0 to 50 W / cm<sup>2</sup>. After processing times of about 15 - 20 minutes, the front surface temperature as measured by optical pyrometry was typically 1500 °C and above. At this point, the beam was either turned off, resulting in a "fast" quench ( approx. 10 seconds), or was more gradually ramped down over a time interval of a few minutes.

Residual stresses were measured using a controlled indent technique. These tests were performed by Professor John Ritter, University of Massachusetts, Amherst, MA. This method is predicated on the assumption that the residual stress state can be correlated to the material hardness and the fracture toughness. In practice, the method consists of introducing a flaw by using an indenter under a specified load. Then, the hardness is calculated from the indent load and the length of the indent diagonal. The indent will have cracks extending from its corners into the material surrounding the indent. The total crack length thus formed is measured through optical microscopy, and the fracture toughness is

deduced. Finally, a correlation between the residual stress state, the hardness, the crack length, and the fracture toughness is used. The specific relations used are given below :

$$H = \frac{P}{2a^2},$$

$$K_C = 0.016 \sqrt{\frac{E}{H}} \cdot \frac{P}{C^{3/2}}, \text{ where}$$

E is the Young's Modulus,  
H is the material Hardness,  
C is the total crack length, (31)  
P is the indent load,  
a is the indent half - diagonal, and  
K<sub>C</sub> is the fracture toughness.

First, the indents are performed on untreated samples, and the fracture toughness is calculated. Then, assuming that the fracture toughness is the same for the treated and untreated samples, the residual stress may be found from the measured crack length in the treated sample using the relation :

$$\sigma_R = \frac{\sqrt{\pi}}{2\sqrt{C}} \cdot \left[ K_C - 0.016 \sqrt{\frac{E}{H}} \cdot \frac{P}{C^{3/2}} \right] \quad (32)$$

P and C now refer to the *treated* sample. The controlled indent technique assumes that crack length can be accurately measured. This is often not the case, since the measurement of crack length depends on microscopic examination of the cracks around the indent. This measurement is very sensitive to the quality of the polished surface. Surface roughness or other polishing defects such as missing grains (grain "pull-out") will result in measurement uncertainties. Furthermore, this technique assumes that stresses are uniform in the area being sampled. Some typical values of the residual stresses measured using the controlled indent technique are shown below.

TABLE 5.5  
Residual Stress Values in AD 96 and AD 998 Alumina

SAMPLE	a (µm)	C (µm)	H (GPa)	σ <sub>R</sub> (MPa)
AD96	130 (±1.9)	381 (±18)	11.8 (±0.3)	-57.4 (±12.7)
AD998	63 (±3.5)	135 (±12)	12.6 (±1.3)	-58 (N/A)

### **5.3.4 Summary of HEEB Ceramic Strengthening**

HEEB ceramic strengthening was briefly investigated in this study, and the experiments performed to date do not indicate that the HEEB process offers significant advantages over conventional heating and quenching operations. The values of the residual stresses achieved in the test samples are not as high as those possible with a liquid quench. A purely radiative quench does not provide a fast enough cooling rate to generate large residual stresses. HEEBs may offer the ability to rapidly heat samples without the need for high temperature furnaces, and that could be a potential advantage when processing at temperatures approaching 1500 °C. Care must be taken to uniformly distribute the HEEB dose however to avoid excessive cracking problems. Further work is needed to evaluate the potential of HEEBs in tailoring the thermal profiles in ceramic parts to achieve higher degrees of strengthening. From a processing point of view however, such efforts are not justifiable considering the ease and economy of conventional processing and the superior results obtained from existing processes.

## **5.4 HEEB - Based Shock Processing**

### **5.4.1 Introduction**

The deposition of radiation into metals on very short timescales results in large pressure rises. These pressure rises can be many times in excess of the yield strength of the metal, and can also result in surface spallation and vaporization. X-rays, lasers, and electron beams are all capable of generating such pressure waves. In this section, attention will be focused on materials processing applications which utilized HEEB - generated shock waves to modify material properties. Pressure and shock waves can induce substantial subsurface deformation and can relieve adverse residual stresses. One application of these effects will be shown, namely the shock hardening of weld regions in 5000 series aluminum. Other applications of HEEB shock processing include non-contact "shot-peening" for impressing a compressive residual stress (to improve fatigue properties) and a combined mechanical / thermal heat treatment that uses the deformation structure induced by shocks to enhance precipitation reactions.

### **5.4.2 Mechanics and Thermodynamics of Shocks**

A brief overview of shock wave mechanics and thermodynamics will now be presented. This discussion is an abridged version of similar discussions found in many books on hydrodynamics, for example COURANT & FRIEDERICHS (1948). Ideally, a shock wave is a discontinuous transition in stress, density, velocity, and internal energy. The idealized shock is a sharp transition between the undisturbed material ahead of the shock and the region in the wake of the shock. The relationships that connect the states of these two regions are called the jump conditions. These jump conditions are nothing more than expressions

of the law of conservation of mass and energy and the momentum equation. The figure below schematically illustrates the variables associated with an ideal shock.

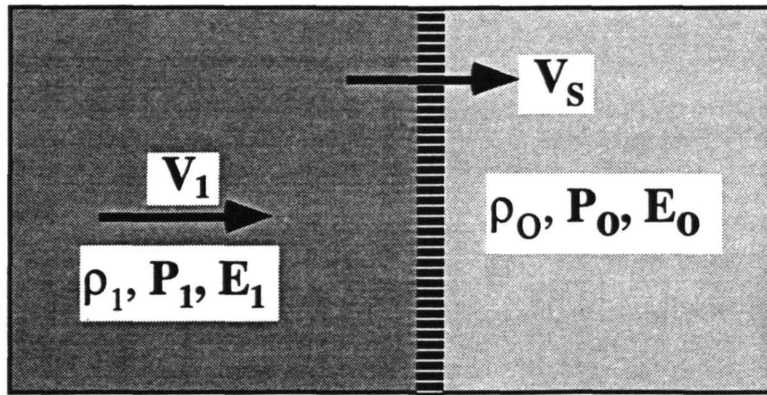


**FIGURE 5.12**  
**Definition of Variables Used in Jump Conditions**

In terms of the variables shown above, the jump conditions are given below. It is assumed that for the geometry shown above, there is unit cross-sectional area.

Conservation of Mass :

$$\rho_0 V_s = \rho_1 (V_s - V_1)$$

Conservation of Energy :

$$P_1 V_1 = \frac{1}{2} \rho_0 V_s V_1^2 + \rho_0 (E_1 - E_0) \quad (33)$$

Momentum Equation :

$$P_0 - P_1 = \rho_0 V_s V_1$$

The jump conditions may be derived from the application of elementary mechanics to the geometry shown in Figure 5. . The jump conditions can be combined to form the Rankine - Hugoniot relation :

$$E_1 - E_0 = \frac{1}{2} (v_0 - v_1) \cdot (P_1 + P_0), \text{ where} \quad (34)$$

the  $v$ 's are specific volumes.

Material passing through the shock front will have an increased internal (and kinetic) energy with respect to the unaffected material. There is an overall entropy rise associated with the passage of a shock front since the work done on the material going through the front is irreversible in nature. By differentiating the Rankine - Hugoniot relation and combining with the Second Law of Thermodynamics, it is possible to show that the rise in entropy is given by :

$$\begin{aligned}
T_1 dS_1 &= dE_1 + P_1 dV_1 \\
&= \frac{1}{2}(v_o - v_1) \left[ 1 - \left( \frac{V_s - V_1}{C_1} \right)^2 \right] \text{ where} \quad (35) \\
C_1 &\equiv v_1^2 \frac{dP_1}{dv_1}
\end{aligned}$$

The Rankine - Hugoniot relation is the locus of all final values of pressures and specific volume that can be reached via a shock transition. It represents the trajectory in P - v space of material that passes through the shock, and it is neither isothermal nor adiabatic. This curve is shown together with the associated adiabatic compression curve and the so-called Rayleigh line in the figure below. It is clear that if an isothermal shock path were shown in pressure - specific volume space, it would lie between the adiabat and the Rankine - Hugoniot curve.

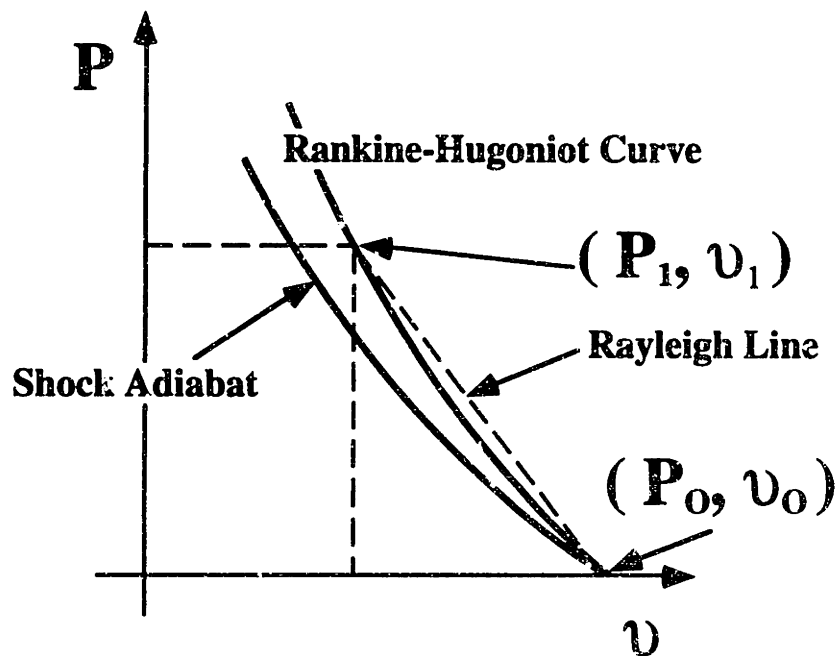


**FIGURE 5.13**  
**Rankine - Hugoniot Curve**  
**in Comparison to Shock Adiabate**

The Rankine - Hugoniot relation indicates the pressure and specific volume changes due to the passage of a shock. Electron beam and laser generated shocks are due to a rise in the internal energy of a near-surface region of the material. To interrelate the pressure, specific volume, and energy, an equation of state is needed. One often-assumed form of this equation (for single phase materials) is the Mie - Grüneisen equation of state, given by :

$$P(v) = P_{ref.}(v) + \frac{\Gamma(E - E_{ref.})}{v}, \text{ where} \quad (36)$$

$P_{ref.}$  and  $E_{ref.}$  are reference values, either along the adiabat or the isotherm, and  $\Gamma$  is the Grüneisen ratio, which is a function of density.

Thus the R-H relation provides information about the compressibility of the material, whereas the M-G equation is the thermodynamic equation of state.

For shocks due to electron beam irradiation, the shock intensity will also depend on the geometry of the irradiated zone and the pulselength of the deposition transient. Also, there will in general be rarefaction and compression waves associated with an e-beam pulse. This is shown schematically below.

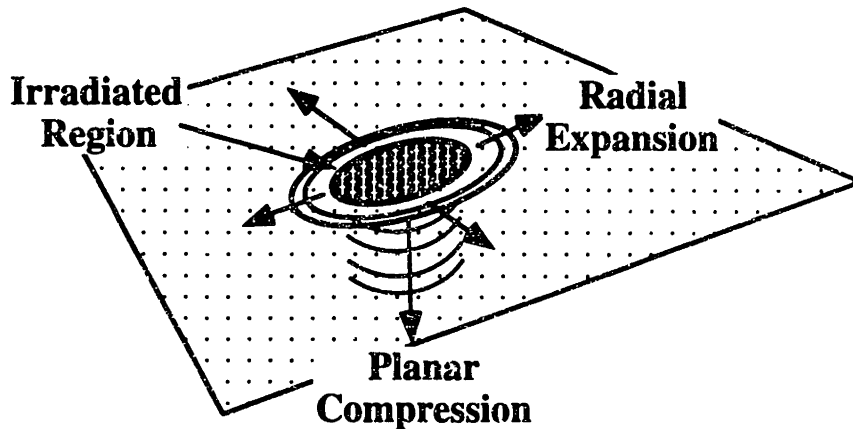


**FIGURE 5.14**  
**Pressure / Shock Waves Resulting from**  
**Pulsed E-Beam Irradiation**

The longer the pulselength, the less severe the pressure wave generated since relaxation waves (radial expansion and planar compression) carry energy away from the irradiated region. If the energy were deposited "instantaneously," then the maximum pressure developed would be directly related to the Grüneisen ratio. This expression is given by [ BAILEY (1994) ] :

$$\sigma_m = \frac{1}{2} \rho \Gamma E \quad (37)$$

This equation gives the maximum compressive stress assuming instantaneous energy deposition and a 1-dimensional planar shock front. Also, compressibility effects (R-H relation) will be ignored for the moment.

For finite pulselengths, the energy deposited in the material will be carried away by pressure / shock waves *during* the deposition process itself. There are two distinct regimes of interaction, and they are delineated by the electron range



as compared to the distance traveled by waves during the pulselength. The two regimes are [BAILEY (1994)] :

Case 1 :  $0 \leq c\tau \leq R$

$$\sigma_m = \frac{\rho\Gamma E}{2} \left( 1 - \frac{1}{2} \cdot \frac{c\tau}{R} \right)$$

Case 2 :  $c\tau > R$

$$\sigma_m = \frac{\rho\Gamma E}{2} \cdot \frac{1}{2} \cdot \frac{1}{(c\tau/R)} \quad (38)$$

$c$  is the wave propagation speed,

$\tau$  is the pulselength, and

$R$  is the electron range.

It has been assumed in the above discussion that shocks in metals are purely hydrodynamic phenomenon. This is of course not true, and a more realistic assessment of shocks in real materials must carefully consider material constitutive behavior and plastic deformation. A detailed discussion of this subject is beyond the scope of the present work, but a few brief calculations will be shown with a graphical interpretation using the R-H curve. The following comments are based on a more detailed discussion by DUVALL & FOWLES (1963).

Assuming that the surface of the material in question is subjected to a pressure  $P_x$ , a pressure wave will propagate under conditions of uniaxial strain. The state of stress will be triaxial, however, and it is possible to represent  $P_x$  in terms of the hydrostatic and shear stresses. By straightforward manipulation, we get :

Given that :

$$\bar{P} \equiv \frac{1}{3}(P_x + P_y + P_z) \text{ and}$$

maximum resolved shear stress is

$$\tau \equiv \frac{1}{2}(P_x - P_y), \quad (39)$$

the linear compressive stress  $P_x$  is

$$P_x = \bar{P} + \frac{4}{3}\tau$$

As long as the material is elastic, the pressure  $P_x$  may be directly related to the shear by invoking the stress-strain relations associated with elasticity :

Uniaxial strain means  $\epsilon_y = \epsilon_x = 0$

From the elastic constitutive relations :

$$P_y = P_z = \frac{\nu}{1-\nu} P_x, \text{ where } \nu \text{ is Poisson's Ratio.} \quad (40)$$

Therefore :

$$\tau = \frac{1-2\nu}{2(1-\nu)} P_x$$

For an elastic - perfectly plastic material, the relation above will no longer hold at yield. Assuming that the uniaxial yield strength is  $Y$ , then according to the von Mises' yield criterion, the shear stress at yield is :

$$\tau = \frac{Y}{2} \quad (41)$$

Assuming that the yield is sharp and that there is no work-hardening, the linear compressive stress  $P_x$  will offset from the hydrostatic stress  $\bar{P}$  by an amount equal to  $2Y/3$ . This may be schematically represented on the R-H curve :

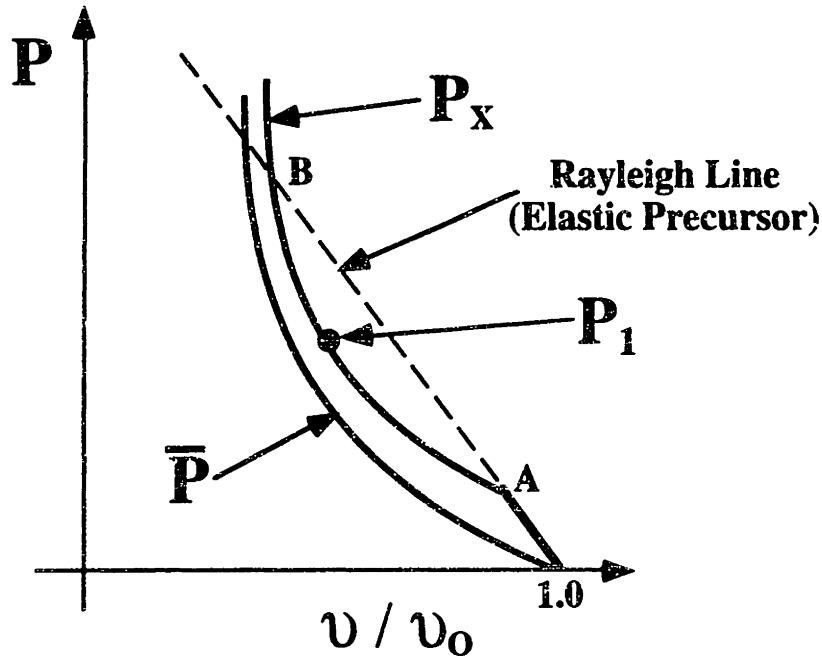


**FIGURE 5.15**  
**Shock Wave in an Elastic - Perfectly Plastic Material**

If the final shock pressure lies above point B on the above figure, then there will be only one shock front. If the pressure lies between A and B, there will be an elastic precursor with peak pressure  $P_A$  and a slower plastic wave with pressure  $P_1$ . If the final pressure lies below the elastic limit indicated by A, then the wave is purely elastic (Rayleigh Waves). For the intermediate case shown in the figure above, the corresponding shock front profile is shown below.

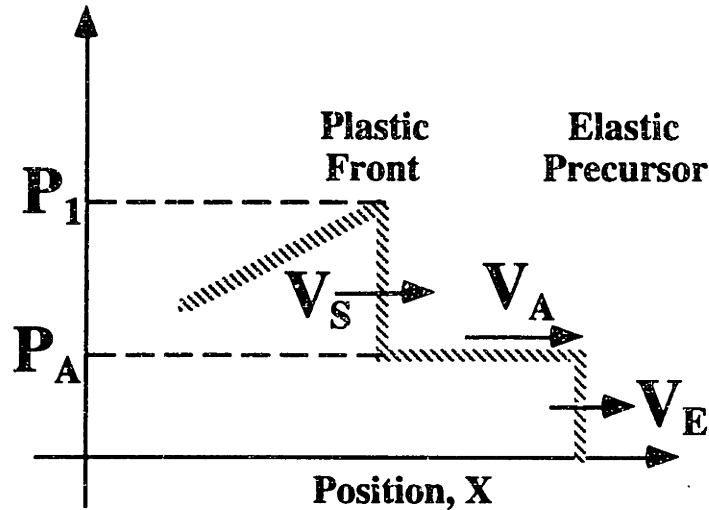


**FIGURE 5.16**  
**Elastic and Plastic Wave Fronts in an**  
**Elastic - Perfectly Plastic Material**

The effect of work-hardening and rate-dependence will add extra complexity to this simplified picture, and the elastic precursor may not be so sharply defined. To properly capture these effects would require a detailed consideration of the constitutive response of the material, and would most likely require a numerical scheme to actually solve the resulting equations.

### 5.4.3 Metallurgical Considerations of Shock Deformation

Shock deformation produces unique microstructures that may be effectively used in a wide variety of materials processing applications. As compared to slower rate cold working, shock deformation structures are characterized by greater dislocation densities, correspondingly higher hardness, and greater stored work of deformation for a given plastic strain. Also, there is very little grain distortion in shock-loaded materials (away from any impact craters!) which would suggest that large numbers of closely-spaced defects may be introduced. In fact, such homogeneous nucleation is expected to play a role, since the stresses needed to achieve it are on the order of  $G / 30$  [COTTRELL (1953)]. This corresponds to stresses on the order of  $10^5 - 10^6$  psi, which are achievable in shock loading.

The following table is adapted from LESLIE (1973). It describes the microstructures observed in a variety of shock loaded materials. All the materials in this table were loaded in uniaxial compression, but some of the results could be similar for electron beam and laser beam generated shocks.

**TABLE 5.6**  
**Microstructural Effects of Shock Deformation**

<b>Material</b>	<b>Microstructural Observations</b>
pure copper, polycrystalline	Hardness, dislocation density, stored deformation energy, yield stress, and UTS all increase with increasing shock pressure, and then reach a maximum. Cellular dislocation structure.
pure nickel, polycrystalline	Very similar to copper. At pressures above 1000 kbar (14500 ksi), no cellular structure is observed, but dislocation densities are very high.
pure aluminum	No dislocation cell structures formed up to pressures of 150 kbar (2175 ksi), although it was expected. Structure consists of randomly distributed, heavily jogged dislocations, high point defect concentration, and many dislocation loops.
FCC alloys	As stacking fault energy goes down due to alloying additions, cellular structure gives way to planar dislocation arrays, stacking faults, and twins.
Austenitic stainless steels (302, 304, 316, & A286)	Arrays of dislocations, stacking faults and twins were predominantly observed. One point of dispute : observation of $\alpha$ martensite in 302 and 304. <i>Also, it has been recognized already that the high density of defects generated in Austenite by shock loading will act as nucleation sites for precipitation of carbides &amp; intermetallics. This is one example of a combined mechanical / thermal treatment.</i>
Austenitic Hadfield Mn steel	One of the few commercial application of shock loading. Mechanism of high hardening rate may be the interaction between the Mn-C complexes in solid solution in the Austenite.
pure iron	At pressures less than 130 kbar (1885 ksi), uniform dislocation distributions accompanied by twins. Twinning can be suppressed by pre-existing dislocation structure.
Ferritic steels	Steels containing free ferrite are more susceptible to hardening. Embrittlement is also observed.

#### 5.4.4 Laser-Based Shock Processing

Before discussing e-beam applications, it is useful to consider laser-based processes. Laser shock processing has been used for hole drilling, superficial compaction of powders, shock hardening, altering of magnetic domain structure in Si - iron transformer steel, and as part of combined mechanical / thermal heat treatments. The table below briefly reviews these applications. Laser hole drilling will not be discussed, since it is more closely categorized as a laser-based machining process.

**TABLE 5.7**  
**Laser - Based Shock Processing**

<b>Reference</b>	<b>Relevant Findings</b>
FAIRLAND et al (1972)	Examined shock hardening in 7075 aluminum. Tests were conducted on material which was solution treated & water quenched, treated to T73, to T6, and an interrupted T6 condition with intermediate laser shocking. Solution treated and quenched and T73 conditions showed a 25% increase in yield strength with only slight decreases in elongation. UTS went up 14%. Dense, tangled dislocation structures observed. T6 largely unaffected.
CLAUER, FAIRLAND, & WILCOX (1977)	Treated weld zones in wrought 5086 and 6061 with pulsed laser irradiation. Yield strength of weld region in 5086 can be restored to that of parent material, and in 6061, yield reaches midway between as-welded strength and parent material strength. 11% increase in hardness values. Shock loading was able to influence hardness profiles at least 3mm below surface.
INAL & MURR (1978)	This study compared explosive shock - generated microstructures and compared them to ones produced by laser shock. A high degree of similarity was found.
IUCHI et al (1982)	Pulsed lasers were applied to grain - oriented Si - transformer steel to refine magnetic domains and thereby reduce core losses. The process was developed and patented by Nippon Steel and licensed to Armco Steel.
BOITSOV et al (1988)	Russian study which demonstrated feasibility of shock hardening followed by subsequent aging. Study demonstrated shock strengthening followed by artificial aging increased strength by 20% over similar aging without prior shock loading.

**TABLE 5.7 Continued**

BANAS et al (1990)	Shock hardening of welds in 18 Ni (250) maraging steel. This study demonstrated ability of pulsed laser to impart compressive residual stresses and thus increase fatigue resistance.
DUBRUJEAUD (1992)	This work examined superficial laser shock densification of P/M steel alloy for automotive applications. Partially sintered steel parts were irradiated to achieve near full density to a depth of several hundred microns. The wear properties of samples thus treated were improved.

#### **5.4.5 HEEB-Based Shock Processing - Experimental Studies**

There is very limited work on the use of HEEBs for shock processing. This current work probably is the only study of the use of HEEBs for the treatment of weld zones in aluminum. The work was limited in scope, and did not address such issues as residual stresses and fatigue resistance. The effect on hardness profiles across the weld was clear and detectable, and the surface of the aluminum was not at all damaged by the e-beam pulses. A concise description of the experimental details follows.

A welded piece with a fusion zone width of 0.2 inches was prepared from 0.375 inch thick 5086 plate with 5356 filler wire using a manual TIG welding process. The weld bead was machined so that it was flush with the parent material. Hardness profiles were made across the width of the weld using the Rockwell F scale. Hardness profiles were recorded as a function of the number of e-beam pulses delivered to various samples. The parent metal hardness was 70 HRF, and the as-welded hardness along the weld centerline was 62 HRF. By subjecting the welded region to pulsed e-beam irradiation, the hardness was restored to the base metal value. The beam used was a 0.5 MeV pulsed beam operating at 10 Hz with a spot size of no larger than 3mm diameter and an energy of 10 J / pulse.

One interesting observation involved the number of pulses delivered to a given location along the weld centerline. The maximum value of hardness was attained at approx. 200 - 250 pulses, and further pulses actually lowered the measured hardness. This is shown in the figure below. This observation is perhaps related to alterations in the residual stress state of the surface with increasing pulses. Annealing is perhaps another possible explanation for this phenomenon, although the typical temperature rise due to the pulsed beam at 10Hz is not expected to be greater than 100 °C.

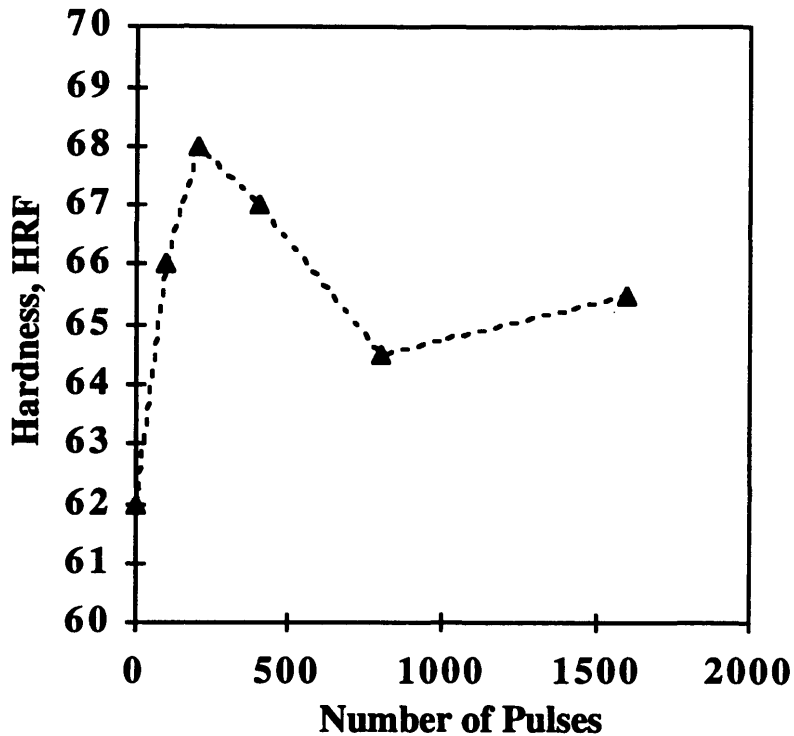


**FIGURE 5.17**  
**Hardness at Irradiated Spots**  
**as a Function of Number of Pulses,**  
**Weld Centerline in 5086 Aluminum**

#### 5.4.6 Estimate of HEEB - Generated Pressure

For the experimental conditions discussed above, it is possible to estimate the pressure resulting from HEEB irradiation. In this calculation, the radial expansion waves will be ignored. In reality, these could have a very significant effect on the maximum pressure developed. The estimate developed here is therefore an upper bound. According to Equation 38, the maximum pressure developed will depend on the Grüneisen coefficient, the specific energy deposition, the pulselength, the pressure wave speed, and the electron range. From other calculations, [GOODMAN, BIRX, & DAVÉ (1992)], maximum specific energy (radiation dosage) resulting from a single pulse of the SRL 0.5 MeV SNOMAD IV accelerator is 400 J / g in aluminum. This figure was calculated through Monte Carlo simulations of electron transport (see Appendix A). It will be assumed that the wave speed is approximately 1000 m / s. The pulselength is 50nS, and the Grüneisen coefficient of Al and other metals is given in the table below.

**TABLE 5.8**  
**Dimensionless Grüneisen Coefficients of Selected Metals**  
**Adapted from BAILEY (1992)**

Material	Density, g / cm <sup>3</sup>	Grüneisen Coeff. $\Gamma \equiv \frac{1}{\rho} \frac{\partial P}{\partial E} _p$
Al	2.7	2.13
Fe	7.87	1.46
Ti	4.5	1.1

The electron range at 0.5 MeV in Al is approximately 0.07 cm. The distance traveled by the pressure wave during the pulselength is 0.005 cm. Therefore, the appropriate equation for the maximum pressure is :

Case 1 :  $0 \leq c\tau \leq R$

$$\sigma_m = \frac{\rho \Gamma E}{2} \left( 1 - \frac{1}{2} \cdot \frac{c\tau}{R} \right) \quad (42)$$

The resulting pressure is 1109 MPa, which is 160 ksi. This is a rather large pressure, and it is interesting to note that there was NO surface damage as a consequence of HEEB pulsed irradiation. In reality, this number could be up to 30% smaller, since the average radiation dosage will be less than 400 J / g, and the radial expansion waves will further attenuate the maximum pressure developed. It is seen however that pulsed e-beams offer a very plausible means of generating reasonably large pressures without surface damage.

#### 5.4.7 HEEB Shock Generation vs. Surface Sources

It is useful to compare the shock generation efficiency of HEEBs vs. surface sources by considering the total amount of energy deliverable by various energy sources without causing surface damage. Actually, the specific energy deposition will be considered, since this parameter will enter into equation for shock pressure shown in the previous sections. The volume of material affected by the pulsed energy input will be assumed to be cylindrical in shape. The radius will be taken as the Gaussian radius, and the height of the cylinder will be the electron range. For surface sources, the height of the cylinder will correspond to the characteristic heat conduction length for a time equal to the pulselength. Actually, one-half of the conventionally defined heat conduction length will be taken, since we want to focus on the material that is heated the most and therefore produces the largest pressure rise. For most pulses, the pulselengths are extremely small, and to a good approximation, the energy input from the pulse may be taken as instantaneous. For example, in aluminum, the characteristic heat conduction length corresponding to a 50ns pulse is shown below.



$$x = \sqrt{\alpha t}$$

$$\alpha \text{ for aluminum is } 0.84 \text{ cm}^2/\text{s}, \text{ so} \quad (43)$$

$$x \approx 0.0002 \text{ cm.}$$

This is significantly smaller than the electron range at all energies of interest. The range at 0.1 MeV is 0.007 cm, for example. In the sample calculation that follows, aluminum will be taken as the target material. The total specific energy deposition will be calculated assuming that this value will cause the surface to just reach 100 °C. From these maximum energy deposition values, the pressures generated for each case can be calculated using the appropriate form of Equation 38.

In order to evaluate the energy deposition for HEEBs and surface sources, the Green's Function solutions presented in Chapter 2 will be utilized. These relations will require a slight modification since the source term will now be considered as an instantaneous source. Equation 9, Chapter 2 gives the form of the solution for continuous sources :

$$T = \frac{P_A}{8\alpha\pi\rho\kappa CR} \int_0^\psi \frac{1}{\psi' + \phi^2} \left\{ \operatorname{erf} \left[ \frac{\kappa - \zeta}{\sqrt{\psi'}} \right] + \operatorname{erf} \left[ \frac{\kappa + \zeta}{\sqrt{\psi'}} \right] \right\} d\psi'$$

$$\tau \equiv \frac{R^2}{4\alpha} = \text{characteristic time based on Range,} \quad (44)$$

$$\psi \equiv \frac{t}{\tau} = \text{dimensionless time, and}$$

$$\phi \equiv \frac{r_B}{R} = \text{beam aspect ratio.}$$

For instantaneous sources, the solution becomes :

$$T = \frac{E}{\tau} \cdot \frac{1}{8\alpha\pi\rho\kappa CR} \cdot \frac{1}{\psi + \phi^2} \cdot \left\{ \operatorname{erf} \left[ \frac{\kappa - \zeta}{\sqrt{\psi}} \right] + \operatorname{erf} \left[ \frac{\kappa + \zeta}{\sqrt{\psi}} \right] \right\} \quad (45)$$

where E is the deposited energy

For surface sources, the corresponding modified solution for instantaneous sources is :

$$T = \frac{E}{\tau} \cdot \frac{P_A}{2\alpha\rho\pi r_B C} \cdot \frac{1}{\sqrt{\pi\psi}} \cdot \frac{1}{1 + \psi} \cdot \exp \left[ \frac{-\zeta^2}{\psi} \right] \text{ where} \quad (46)$$

$$\tau \equiv \frac{r_B^2}{4\alpha}, \quad \psi \equiv \frac{t}{\tau}$$

The time will be taken as 50ns for all calculations. The figure below shows the specific energy deposition as a function of the kinetic energy of the source. Note that this relation is independent of source radius, since the size of the volumetric source is precisely equal to the size of the affected region. Thus the deposited energy and the affected mass both scale with volume, making the specific energy deposited a volume - independent quantity (as the name implies).

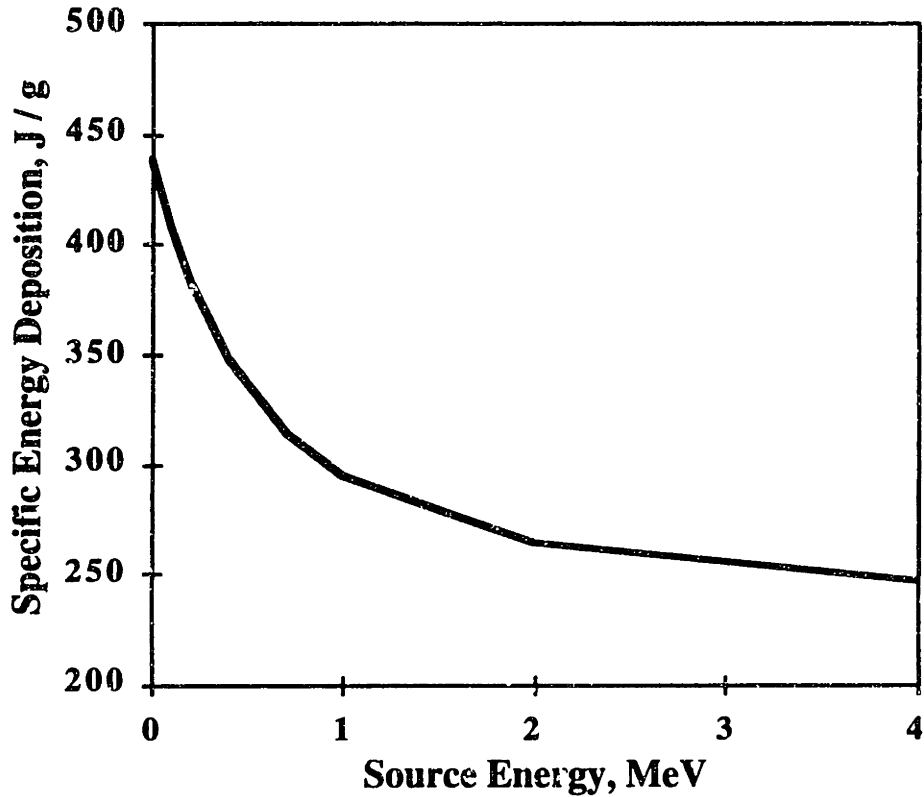


**FIGURE 5.18**  
**Specific Energy Deposition as a Function of Source Energy,**  
**Target Material is Aluminum,  $\Delta T=100\text{ }^\circ\text{C}$**

The pressure is now calculated using the relations of Equation 38. The pressure wave speed is again assumed to be 1000 m/s, so that the distance traveled by this wave during the pulselength is 0.005 cm. For all the HEEB energies of interest, the electron range is larger than this number. For the case of surface sources, the assumed "range" based on heat conduction length will be smaller than the wave travel distance. The maximum compressive stress as a function of source energy is shown below.

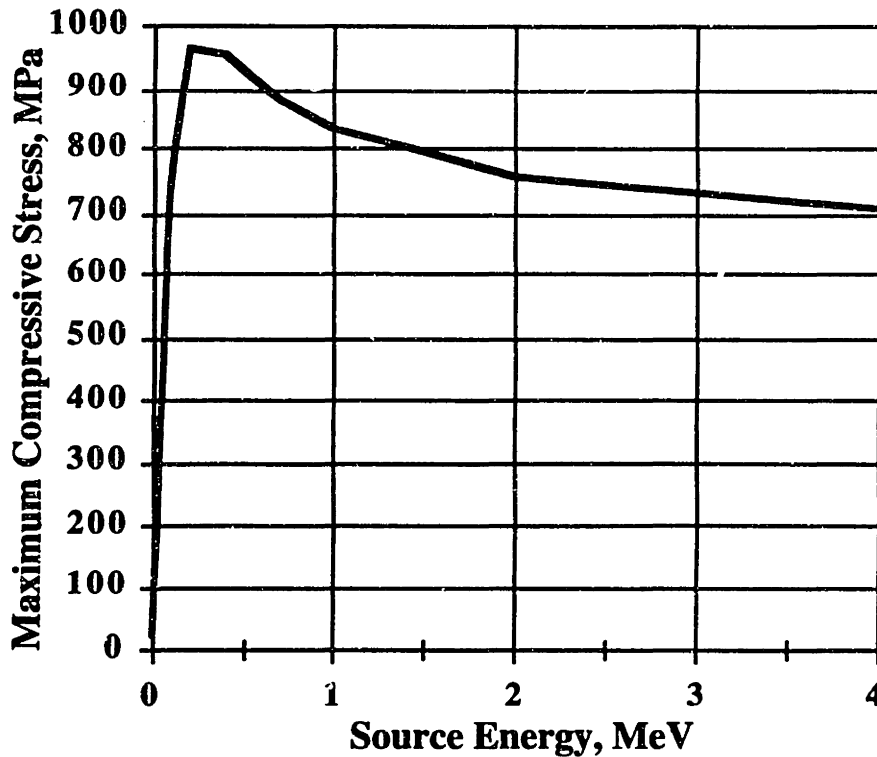


**FIGURE 5.19**  
**Maximum Compressive Stress as a Function of Source Energy,**  
**Material is Aluminum**

This result is apparently contradictory to the specific energy deposition data presented earlier. This result may be explained by simple physical considerations. First consider the case of surface sources, which also applies to volumetric sources with very small ranges (electron range smaller than the wave propagation distance). In this case, the amount of energy carried away by the pressure waves during irradiation is very significant, since the distance that these waves will travel during the deposition interval is longer than the source depth itself. This will result in lower pressures. This explains the reason why the pressure developed by a laser pulse is lower than the pressure developed by a 0.1 MeV pulse even though the electron beam produces a lower specific energy deposition. In the case of volumetric sources where the source depth is greater than the wave propagation distance, most of the energy is still contained within the affected region (the source region) after the pulse, and the effect of attenuation during the pulse is minimized. This effect eventually saturates, and then the maximum pressure generated is determined by the specific energy deposition. This term will go down with increasing energy, and thus the curve of maximum compressive stress as a function of source energy will go through a maximum. For aluminum, this maximum is around 0.5 MeV, and the exact value will depend on the sound speed and electron penetration characteristics for a given material.

### 5.4.8 Future Prospects of E-Beam Shock Processing

Pulsed beam shock processing may be useful in several applications. Two potential application areas are listed below.

- Shock hardening can be used to impart harden surfaces through plastic work, impart compressive residual stresses, and thereby improve fatigue resistance in welds or other parts. This can also lead to *non-contact "shot - peening"* techniques for residual stress relief and surface compressive stress development. The surface is not damaged if done correctly, and this is a potential advantage over conventional shot - peening.
- Combination shock processing / thermal treatments can be used to enhance near-surface mechanical properties. Potential applications to Ti - alloys. Currently, such applications are being pursued by surface rolling prior to heat treatment [WAGNER & GREGORY (3/94 and 7/94).

With regards to the latter application area, the following table is adapted from WAGNER and GREGORY (3 / 94), and it indicates the influence of surface properties on fatigue life.

**TABLE 5.9**  
**Effects of Various Surface Properties on Fatigue Life**

Property	Effect on Crack Nucleation	Effect on Crack Propagation
surface roughness	accelerates	no effect
cold work	retards	accelerates
residual compressive stresses	minor or no effect	retards

Pulsed beam irradiation will induce cold work and compressive residual stresses. If care is taken, surface damage can be minimized. The potential use of such combination surface treatments are numerous. For example, WAGNER & GREGORY (7/94) have produced variations in microstructure morphology in Ti - 6Al - 4V. In  $\alpha+\beta$  and near- $\alpha$  alloys such as Ti - 6Al - 4V and Ti - 6242, fine surface microstructures were developed while keeping the core of the material lamellar. This is significant since the lamellar structure is required for good creep resistance, but has poor LCF (low cycle fatigue ) properties. Such location - specific phase morphology control could result in significant properties improvement. Lasers and e-beams, being essentially non-contact "shot-peening" devices, can treat parts of complex geometry that are difficult at best to treat via rolling. Also, as mentioned before, shock deformation induces greater deformation (dislocation) structure for an equivalent amount of plastic strain.

In comparing pulsed e-beams to pulsed lasers, pulsed lasers may be easier to implement using currently available technology. There are atmospheric low

energy beams, but their pulsing capabilities are limited to pulselengths of one millisecond. Pulsed low energy e-beams using a triode have been built for experimental purposes [HSU, LAWRENCE, & FERRARIO (1991)]. HEEBs are certainly a possibility, but they require further development before commercial implementation is practical. Lasers offer the additional advantage of using fiber optic lines to precisely direct the shock pulses to hard-to-reach areas. The one main disadvantage of lasers is the potential for surface spall damage. This will limit the effective energy per pulse, thus requiring a greater number of pulses to reach a desired level of induced deformation.

HEEB shock processing does have great potential as far as process efficiency is concerned. As discussed in the previous sections, intermediate energy HEEBs are much more efficient at generating large pressures than are surface sources or low energy beams. Ideally, a HEEB machine operating in the range 0.5 MeV - 1.0 MeV offers the best processing characteristics as far as shock processing is concerned. The limited experimental evidence to date does support this contention. Laser irradiation at similar power levels would have caused extensive surface damage. In the previous example, the maximum pressure rise in the Al target was limited to 100 °C. Under these conditions, a 0.5 MeV HEEB will produce a pressure that is 30 - 40 times larger than that produced by a surface source, and the specific energy deposition for the HEEB is 20% lower. The key to successfully exploiting this potential lies in the construction of a robust, commercially viable HEEB unit with a source energy in the range from 0.4 MeV to 1.0 MeV. The SRL SNOMAD IV represents a significant step towards this goal, with further improvements necessary.

## **5.5 Summary of HEEB - Based Materials Processing**

This present work has examined several potential HEEB materials processing applications. Joining of C / C composites can benefit from the use of localized heat sources, but lasers and IR lamps could do an equally good job. The volumetric penetration aspect of HEEBs is not as significant or relevant as originally thought with respect to C / C joining. Similarly, for ceramic strengthening, conventional quenching will produce a greater extent of hardening. HEEBs do however offer significant advantages over surface heat sources as far as shock processing is concerned. HEEB sources will at least in theory be much more efficient, resulting in much larger pressures at lower temperature rises. This means that large shock pressures can be generated without excessive sample heating and without extensive surface damage.

Perhaps the greatest potential application of HEEBs is in the area of polymer crosslinking / curing. Here, full use is made of the volumetric penetration capabilities of HEEBs together with the fact that *electron beams* will produce physically different effects than lasers. An investigation of HEEB - based polymer curing was outside the scope of this present work, but this application area does deserve more attention as an application which is well - matched to the physical features of HEEBs.

## CHAPTER 6 CONCLUSIONS AND FUTURE WORK

### 6.1 Overview

This thesis has achieved three significant experimental objectives and one noteworthy analytical contribution. EB deposition of alloys of real engineering interest has been demonstrated as a viable SFF technique for the buildup of new parts or the repair of old ones. This technique is limited in scope to those applications which place a high premium on processing speed and would therefore warrant the high cost of processing. A new technique for the reaction synthesis of aluminides was independently discovered. This technique could be effectively used in coating applications, or as part of an SFF scheme for intermetallics. It may well be applicable to other reaction synthesis applications, such as ceramics (SiC). High energy electron beams (HEEBs) were examined at length for applications in shock processing, ceramic strengthening, and C/C joining. One of the more promising HEEB materials processing applications, polymer crosslinking, was not investigated. This application makes full use of the volumetric penetration effects and high potential for atmospheric use offered by current HEEB devices. In the analytical realm, a model was developed to account for the differences between HEEBs, low energy EBs, and surface heat sources. The technique extended existing models to examine moving, distributed volumetric heat sources.

### 6.2 EB Deposition Processes - Performance and Cost

The discussion below focuses of EB - based SFF options and strategies. The figure below recapitulates the performance of e-beams as compared to arc welding processes. Arc welding power input is effectively limited to 30kW by considerations of arc stability and arc blow. The corresponding limiting deposition rate will be approximately 100 lbs. / hr. For low energy electron beams, the envelope of deposition rates as a function of travel velocity is contained within the region that is attainable with conventional arc welding processes. The main difference is the deposition efficiency, with the EB processes requiring about 450 W for every lb. / hr. of deposition rate, whereas arc processes require close to 1000 W. Lasers are expected to fall within the low energy EB regime, depending on surface reflection losses. For high energy electron beams (HEEBs), the total possible deposition rates achievable are much higher than those physically possible through arc processes. The deposition efficiency does not change much for electron beams with energies in the range from 100 kV to 1 MV. The assumptions made in deriving this figure were that beam radii for e-beams were no smaller than 0.15 cm and no larger than 0.75 cm. This covers most cases of practical interest.

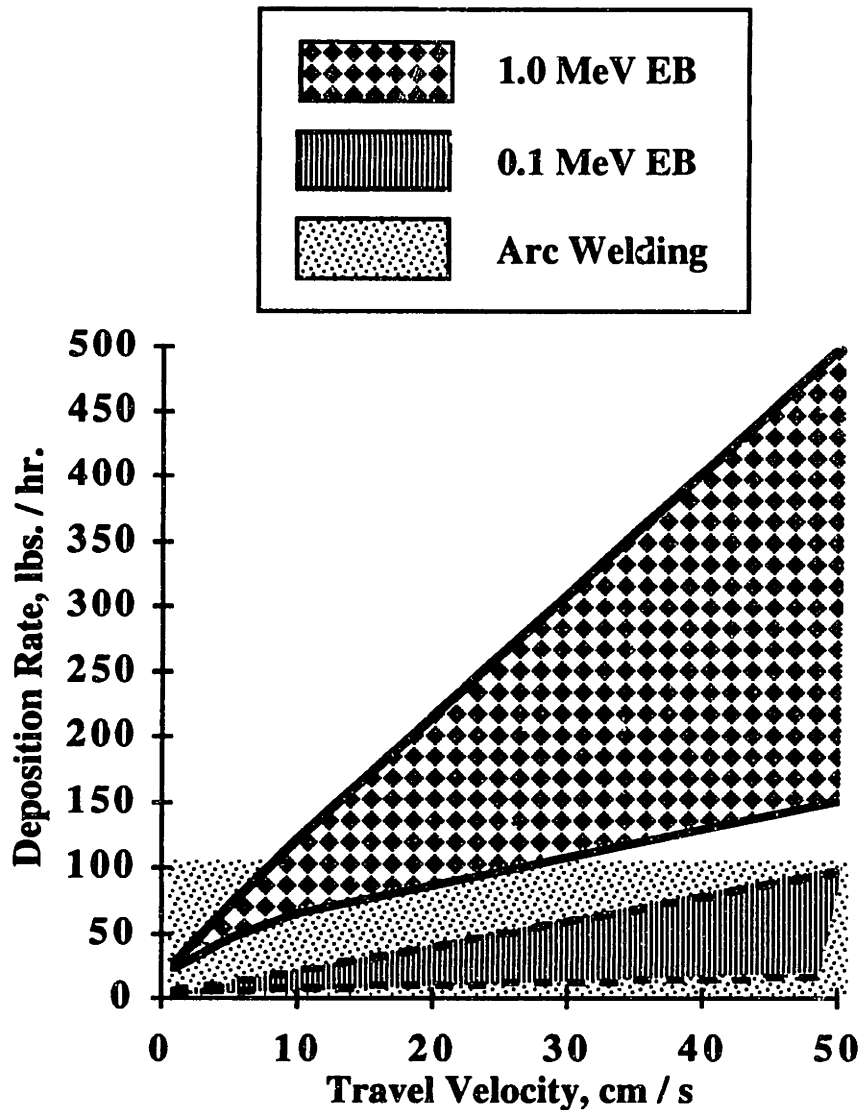


**FIGURE 6.1**  
**Processing Regimes for Low Energy EBs,**  
**High Energy EBs, and**  
**Arc Welding Processes.**

The processing range achievable by e-beams may also be represented as a three-dimensional surface, provided that either the beam radius or beam travel velocity is held constant (converts the four dimensional processing space to a three dimensional one). In the example below, the beam radius is held fixed at 0.25 cm. Although the axes are not drawn to scale, this three-dimensional representation of the processing space is useful for illustrating the effect of increasing beam energy. The deposition rate would also follow such a plot, since the deposition rate will be proportional to the difference between the melting power and the vaporization power. The melting power is shown in Figure 6.2,

and the vaporization power would be another surface above the surface of melting power. The deposition rate would therefore exhibit the same general trends.

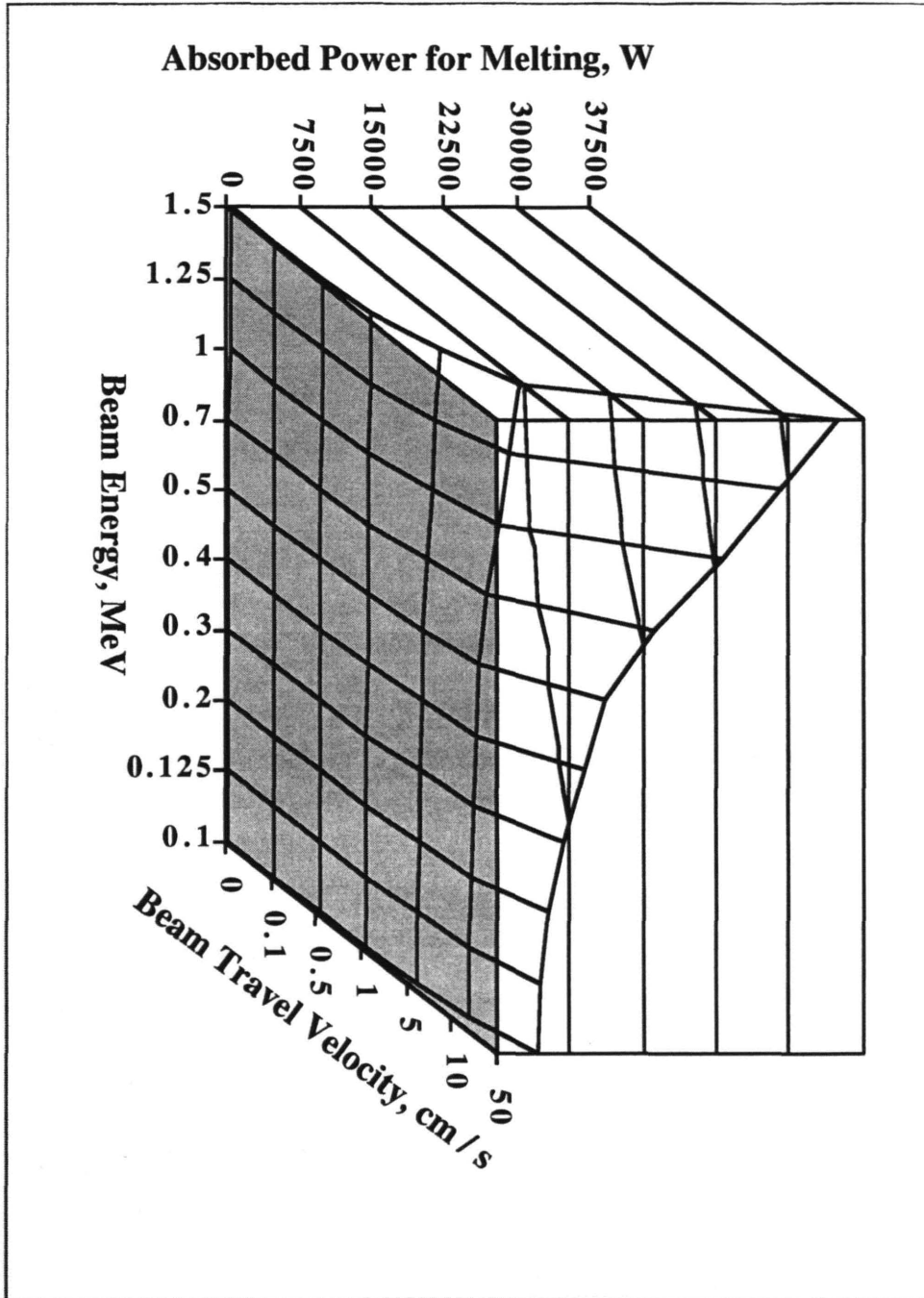


**FIGURE 6.2**  
Power Required to Melt 304 SS,  
Beam Radius is 0.25 cm



The two graphs above concisely illustrate one of the central messages of this work with regards to EB deposition processes : electron beams are capable of higher deposition rates than conventional arc processes by virtue of their increased deposition efficiency, and this advantage improves with increasing electron kinetic energy (HEEB regime). From a practical standpoint, a robust and reliable EB accelerator with high average power at operating voltages above 1000 kV (1 megavolt ) has yet to be achieved. The SNOMAD IV accelerator at Science Research Labs, Inc. is perhaps the device that is presently closest to this objective. The current power limits of this machine are between 2 and 5 kW. To realize the very high deposition rates that are possible using HEEBs, these power ratings would have to be increased by a factor of ten. Using conventional low energy electron beams, the highest deposition rates achievable would not be much more than 100 lbs. / hr. due to vaporization limitations. Such a process is possible with currently existing equipment, and this does represent an *immediate* opportunity for repair and SFF work on large parts.

From an economical standpoint, EB systems are obviously much more expensive than arc welding operations. A typical arc welding repair apparatus costs on the order of \$ 100, 000.00, whereas an EB system capable of similar tasks is on the order of \$ 1, 000, 000.00. Using the deposition rate data presented in Figure 6.1, it is possible to compare the various deposition processes on the basis of cost as follows.

**TABLE 6.1**  
**Costs Associated with Various**  
**Deposition Processes -**  
**Capital Costs Normalized with**  
**Deposition Rates**

Technology	Capital Cost, \$	Max. Deposition Rate, lbs. / hr.	Normalized Cost, \$ / lbs. / hr.
Arc Welding Processes	100, 000	100	1, 000
Low Energy EB and Lasers	1, 000, 000	100	10, 000
High Energy EB (1.0 MeV)	1, 000, 000	500	2, 000

It is seen that HEEBs have the potential to make EB processing competitive with arc processes. Current low energy EBs would be approximately ten times more expensive than conventional arc processes on the basis of capital cost required to attain a certain level of performance (deposition rate). Further improvements in HEEB technology could result in increased competitiveness of EB processes, but currently their application would be limited to situations in which the cost is warranted by the improved process performance (less heat input required to achieve a certain deposition rate or better metallurgical properties of deposit). As mentioned in Chapter 2 - Part II, emergency repairs on ship components would qualify as such an application.

The other main advantage of HEEBs in deposition and SFF processes is their superior shock generation capabilities. HEEBs can produce significantly higher shock pressures for a given amount of temperature rise as compared to surface sources. The figure below from Chapter 5 reiterates this point.

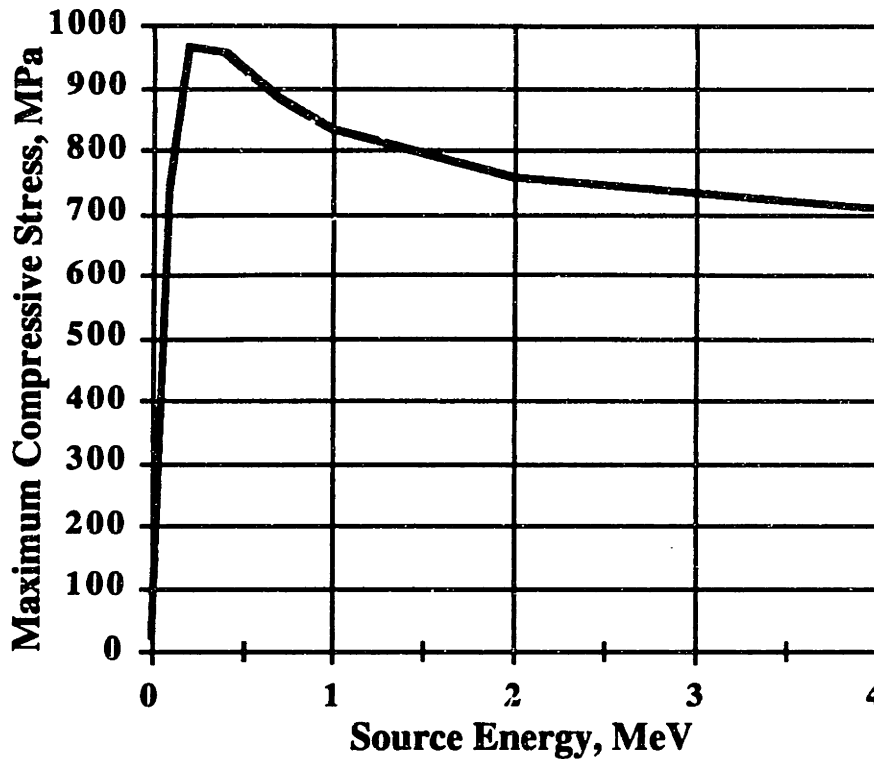


**FIGURE 6.3**  
**Maximum Compressive Stress as a Function of Source Energy,**  
**Material is Aluminum**

Shock processing is expected to play an important role in EB-based SFF, since high deposition rates will require an effective means of *in-situ* stress relief. HEEB "shot peening" is such a process : the same beam performing the deposition process can be used for stress relief by simply focusing the beam and reducing the pulse repetition rate.

In summary, the potential advantages of HEEBs in EB-based SFF are listed below.

- HEEBs offer high deposition rates that are unique : *thermal conduction limitations prevent surface sources or lower energy EBs from reaching deposition rates approaching 500 lbs / hr.*
- HEEBs are far more efficient at shock generation than surface heat sources. Shock pulses with greater pressures can be produced without surface damage.

- Both of the above-mentioned advantages can be achieved with an EB machine with a source energy of 0.7 MeV - 1.0 MeV. Energies higher than 1.0 MeV will offer higher deposition rates, but their shock generation performance will remain essentially constant. *It is therefore the opinion of this author that HEEB machines with energies in the range from 0.7 MeV - 1.0 MeV are the best for SFF applications.*

Future work in the area of EB deposition should explore three general areas :

- thick section ( several cm on the radius ) deposition and the manufacture of actual structural parts
- reaction synthesis for coating applications and intermetallic SFF
- manufacture of FGM (functionally gradient material) parts

Of course there can be combinations of these three areas to produce for example FGMs that have an intermetallic phase, or actual SFF parts made from EB deposition that have reaction synthesized corrosion-resistant coatings. In conventional materials, stainless steel, Al-Bronze, and Ni-based alloys can be explored. For reaction synthesis applications, nickel, iron, and titanium aluminides are of interest. These can be used for coating applications or for the fabrication of aluminide parts via SFF. FGM systems can include metal / intermetallic systems, such as Ni - NiAl or Ti - TiAl, etc. FGMs can also be MMC ( metal matrix composite) materials with continuously graded amounts of the reinforcing phase.

### **6.3 HEEB Materials Processing - Processes other than Deposition**

The HEEB processing applications such as C/C joining and ceramic strengthening were of questionable utility. The basic feasibility of these processes was established, but using HEEBs did not offer significant advantages to other processing routes. One application of HEEBs which was not discussed during this thesis is polymer curing and crosslinking. Radiation crosslinking and polymerization can compete with other techniques of the basis of quality, cost, and speed. It also is capable of producing material properties which are not easy to match by means of purely chemical or thermal processing. Some applications that have been successfully commercialized are shown below.

**TABLE 6.2**  
**EB Radiation Processing of Polymers - Applications**  
**Adapted from SINGH & SILVERMAN (1992)**

Application	Est. Number of Commercial Accelerators in Use in US
crosslinked film, pipe, and tubes	110
wire and cable insulation	110
coatings	125
rubber products	30
polyethylene foam	20

Polymer matrix composites (PMCs) have also successfully been manufactured using e-beam curing. The application of e-beams to these processes has resulted in reduced stresses (stresses associated with curing), shorter curing times, improved materials handling, and lower overall processing costs [SAUNDERS et al. (1993)]. The potential for continued use of e-beams to process thick - section PMC parts is very high, and is being investigated by several groups in the United States, Canada, and France. An example of such a part is a carbon fiber - reinforced motor case made by AECL of Canada using a 10 MeV, 1 kW EB system. The total thickness of parts that can be processed by such a system is 11 cm for single - sided exposure, and 22 cm for double - sided irradiation. HEEBs can perform extremely well in curing of such thick sections due to the volumetric penetration capabilities of the high energy electrons.

#### 6.4 Reaction Synthesis

As mentioned above, a technique of selective reaction synthesis using e-beams was independently discovered during the course of this work. The potential applications of this process have not been fully explored, but there are many such opportunities :

- selective application of corrosion and wear resistant coatings
- SFF of intermetallic parts
- manufacture of FGM components that are continuously graded from intermetallics to metals

The coating applications include medical implants, automotive engine parts (cylinder heads, firewalls, exhaust manifolds), aeroengine parts (TBCs, selective wear-resistant deposits), and others. Since the e-beam allows individual layers of intermetallic material to be produced, it may be possible to build an intermetallic component layer - by - layer. This offer a means of rapid prototyping and SFF applied to structural intermetallic materials. In a similar process, intermetallics could be incorporated into a metallic component, or a graded structure could be fabricated with continuously varying composition and properties.

## 6.5 Conclusions Regarding EB Fabrication

- HEEBs are the **ONLY** means of achieving high deposition rates (500 lbs. hr.) Techniques using lower energy beams or surface sources are limited by conduction and vaporization.
- For EB fabrication, in-situ stress relief will be needed to relieve residual stresses during deposition. This can be accomplished using a pulsed beam, either laser or e-beam. If the constraint of minimum surface damage is imposed, e-beams will always have superior performance. Additionally, if a limitation on the allowable temperature rise per pulse is imposed, then e-beams are again far more efficient at generating large pressures without excessive temperature rise and surface damage. For most materials of engineering interest, the best e-beam energy lies in the range 750kV - 1500 kV. *There is no advantage to going to higher energies as far as EB deposition and fabrication processes are concerned.*
- The melting efficiency of EBs ( low and high energy) is very good : it takes 1 kW of beam power to achieve a deposition rate of 2.5 - 3.0 lbs./hr. In comparison, most arc processes have a corresponding efficiency of 1kW of input power for every 1 lb. / hr. of material deposited.
- EB deposition has been demonstrated as a viable technique for the repair and fabrication of components made from *materials of real engineering interest*. This is in contrast to much of the laser sintering work, which looks at model material systems or plastics.

## 6.6 Guidance for Future Work

The following "take-home" messages from this work are expected to have a significant impact on future HEEB metals processing and fabrication applications.

- **Beam energies in the range 0.5 MeV - 1.0 MeV are necessary** to achieve deposition rates of several hundred pounds per hour. **Surface sources will not attain these deposition rates due to inherent physical limitations imposed by thermal conduction and vaporization.**
- **Beam energies in the range 0.5 MeV - 1.0 MeV offer the best shock generation capabilities : going to higher energies will not improve shock processing capabilities.** The shock generation efficiency of beams in this energy range is **superior** to those of lasers with the absence of surface damage.

- A pulsed HEEB (either linear induction accelerator or Marx-based design) with energies in the range from 0.5 MeV - 1.0 MeV is achievable with existing accelerator technology. Further improvements in accelerator reliability will result in a potentially viable commercial system. Such a system will be able to deposit material **and** perform in-situ stress relief **with a single beam**. This capability would be unique.

The overall recommendation of this work as far as HEEB materials fabrication is concerned is to build a **dedicated HEEB materials fabrication facility**. Emphasis should be placed on the following areas.

- Simplicity and robustness of accelerator design should be an overriding consideration. A suitable system must be able to provide at least 20kW of average beam power continuously for several hours.
- Operation at near-atmospheric pressures under inert gas should be a design consideration from the very beginning. The proposed applications for large parts will be impossible even in very large vacuum chambers.
- Maximum flexibility of the system will necessitate extensive computer control of tooling and material handling. The use of adaptive control may be necessary to eliminate process variability. Feedback control based on feedstock position, weldpool size, and weldpool temperature represents a minimum configuration control system. The use of more sophisticated techniques such as machine vision and optical position sensing may be needed for more complex geometries. The goal of all these systems is to ensure uniformity and repeatability of deposit geometry and microstructure.
- An overall part handling strategy must be established. This process will be different for repairs as opposed to new parts, but some common elements will include : part preparation, development of deposition schedules, process monitoring and data acquisition, post - processing inspection, repair of defects from first pass operations, and final part inspection and validation. It is clear that the better the in-situ monitoring and control, the less time and labor intensive the inspection and validation process will become. The use of diagnostic expert systems and statistical process control will greatly aid in overall process quality assurance.

Based on the above discussion, it is clear that the current state of development of HEEB-based fabrication is very rudimentary. Manufacturing considerations such as processing schedules and inspection procedures have not been considered to date, and these must be considered from the very start in the development of a new deposition system. Substantial improvements are also needed in on-line process monitoring and control. To date, low energy beams have been successfully used to deposit thick sections, but they lack suitable shock generation capabilities for in-situ stress relief. HEEBs do possess the requisite abilities for shock generation, but they currently lack the power capabilities to reach high deposition rates. HEEB reliability is also an issue, and there remains

room for improvement on this front. In light of the current shortcomings of HEEB technology and the lack of shock generation capabilities for conventional low energy beams, an alternate EB deposition system is also proposed.

- This system would utilize currently available low energy beams to deposit material. The ability to work with a 20kW beam at atmospheric pressure under inert gas already exists.
- Stress relief could be provided by induction heating or mechanical vibration. Induction heating would generate thermal stresses without material melting, and these stresses would counteract and eliminate residual stresses associated with the deposition process. Mechanical techniques would essentially try to impose compressive residual near-surface stresses to counteract the tensile stresses resulting from deposition.
- The advantage of this system is that it can be implemented with existing hardware. The disadvantage is that very high production rates (above 100 lbs. / hr.) **will not be possible** due to the previously mentioned conduction and vaporization limitations.

Despite the fact that conventional EB deposition will never be capable of high deposition rates, it is a viable process that could be demonstrated in the near term. A low energy system can also serve as a test bed to develop process schedules and process controls. These advances could easily carry over to HEEB deposition once HEEB power capabilities are high enough to make it a reality. Low energy systems could also handle a wide range of components despite their production rate limitations. Another recommendation of this work is therefore to pursue low energy deposition as a means of identifying and testing potential applications, developing suitable process controls, and establishing procedures for part handling and inspection. The lessons learned from such an endeavor could then be applied to HEEB-based processing upon the availability of a capable HEEB unit.

## CHAPTER 1

### References

- ADVANCED MATERIALS AND PROCESSES 1994 "Technical Bulletins," *Advanced Materials & Processes*, Vol. 146 , August Issue, p. 15
- ARATA, Y  
TOMIE, M. 1970 "100kW Class Electron Beam Welding Technology - Welding Apparatus and Some Aspects as a Heat Source," *JWRI*, vol. 2, p. 17.
- BAKISH, R. (ed.) 1962 *Introduction to Electron Beam Technology*, John Wiley & Sons, New York
- EAGAR, T.W. 1994 MIT Materials Engineering Department, Cambridge, MA, Private Communication.
- ELMER, J.W.  
NEWTON, M.A.  
SMITH, A.C. JR. 1993 "Rapid Thermal Processing of Steel Using High Energy Electron Beams," *The Laser and Electron Beam in Welding, Cutting, and Surface Treatment - State of the Art*, 5th Biannual Conference, Nov. 1993.
- LaFAVE, R. 1994 "Economical Repair of Turbomachinery Shafts by SAW," *Welding Journal*, 73(4), pp. 39 - 44.
- LaFLAMME, G. 1994 PTR - Precision Technologies, Enfield, CT, Private Communication.
- LUNDIN, C.D.  
DANKO, J.C.  
SHI, C.  
KHAN, K.K.  
GREENWELL, B. 1992 "Material Interaction and Joining with High Energy Electron Beam Exposure," *AWS Conference on High Energy Electron Beam Welding and Materials Processing*, Cambridge, MA, pp.123 - 137.
- MARCUS, H. L.  
BEAMAN, J. J.  
BARLOW, J. W.  
BOURELL, D. L. 1990 "From Computer to Component in 15 Minutes : The Integrated Manufacture of Three-Dimensional Objects," *JOM*, April Issue, pp. 8 - 10.



- POWERS, D. E.                    1992    "Overview of Laser/Electron Beam Technology : A Global Perspective," *AWS Conference on High Energy Electron Beam Welding and Materials Processing*, Cambridge, MA, pp. 187-203.
- SACHS, E.  
CIMA, M.  
CORNIE, J. ET AL                1990    "Three Dimensional Printing : Rapid Tooling and Prototypes Directly from CAD Representation," *Solid Freeform Fabrication Symposium Proceedings*, Austin, TX, pp. 27 - 47
- SCHEY, J.A.                        1987    *Introduction to Manufacturing Processes*, McGraw-Hill, New York.
- SMITH, A.C. JR.  
FAWLEY, W.M.  
NOLTING, E.E.                    1992    "An Overview of High Energy Electron Beam Science," *AWS Conference on High Energy Electron Beam Welding and Materials Processing*, Cambridge, MA, pp. 1 - 43.
- ZONG, G. ET AL                    1992    "Direct Selective Laser Sintering of High Temperature Materials, " *Solid Freeform Fabrication Proceedings*, Austin, TX , pp. 72 - 85.

## CHAPTER 2

### References

- |  |      |  |
|--|------|--|
| BLOCK-BOLTEN, A<br>EAGAR, T.W.                   | 1984 | "Metal Vaporization from Weld Pools," <i>Metallurgical Transactions - B</i> , 15B, pp. 461 - 469.  |
| CARLSLAW, H.S.<br>JAEGER, J.C.                   | 1959 | <i>Conduction of Heat in Solids</i> , Clarendon Press, Oxford.   |
| CHAN, C.   | 1985 | "Thermocapillary Convection During Laser Surface Heating," Ph.D. Thesis, University of Illinois at Urbana - Champaign  |
| CHOO, R.T.C.<br>SZEKELY, J.                      | 1992 | "Vaporization Kinetics and Surface Temperature in a Mutually Coupled Spot Gas Tungsten Arc Weld and Weld Pool," <i>Welding Journal</i> , 71(3), pp. 77s - 93s. |
| CHRISTENSEN, N.<br>DAVIES, V.<br>GJERMUNDSEN, K. | 1965 | "The Distribution of Temperature in Arc Welding," <i>British Welding Journal</i> , 12(2), pp. 54 - 75.   |
| EAGAR, T. W.<br>TSAI, N.S.                       | 1983 | "Temperature Fields Produced by Traveling Distributed Heat Sources," <i>The Welding Journal</i> , 62(12), pp. 346s - 355s                                      |
| ELMER, J. W.                                     | 1988 | "The Influence of Cooling Rate on the Microstructure of Stainless Steel Alloys," Ph.D. Thesis, Massachusetts Institute of Technology.                          |
| FUERSCHBACH, P.W.<br>KNOROVSKY, G.A.             | 1991 | "A Study of Melting Efficiency in Plasma Arc and Gas Tungsten Arc Welding," <i>Welding Journal</i> , 70(11), pp. 287s - 297s.                                  |
| GEIGER, G.H.<br>POIRIER, D.R.                    | 1973 | <i>Transport Phenomena in Metallurgy</i> , Addison - Wesley, Reading.  |
| HULTGREN, R. ET AL                               | 1973 | <i>Selected Values of the Thermodynamic Properties of Binary Alloys</i> , American Society for Metals, Metals Park.  |
| ION, J. C.<br>SHERCLIFF, H. R.<br>ASHBY, M. F.   | 1992 | "Diagrams for Laser Processing," <i>Acta Metallurgica</i> , 40(7), pp. 1539 - 1551.  |
| JONES, L.  | 1994 | MIT Welding and Joining Group, Cambridge, MA, Private Communication.   |

- MUNDRA, K.  
DEBROY, T. 1993 "Toward Understanding Alloying Element Vaporization during Laser Beam Welding of Stainless Steel," *Welding Journal*, 72(1), pp. 1s - 9s.
- OREPER, G.  
EAGAR, T.W.  
SZEKELY, J. 1983 "Convection in Arc Pools," *The Welding Journal*, 62(11), pp. 307s - 312s.
- ROSENTHAL, D. 1946 "The Theory of Moving Sources of Heat and its Application to Metal Treatments," *Transactions AIME* 43(11), pp. 849 - 866
- SMITHELLS, C.J.  
BRANDES, E.A. 1976 *Metals Reference Book - 5th Ed.*, Butterworths, London.
- SWIFT-HOOK, D.T.  
GICK, A.E.F. 1973 "Penetration Welding with Lasers," *Welding Journal*, 52(11), pp. 492s-499s.
- THOMAS, P. H. 1957 "Some Conduction Problems in the Heating of Small Areas on Large Solids," *Quarterly Journal of Mechanics and Applied Mathematics*, 10(4), pp. 482 - 493.
- TSAI, N.S. 1983 "Heat Distribution and Weld Geometry in Arc Welding," Ph.D. Thesis, Massachusetts Institute of Technology.

### CHAPTER 3

#### References

- ABBOUD, J.H.  
WEST, D.R.F. 1990 "Laser Surface Alloying of Titanium with Aluminum," *Journal of Material Science Letters*, Vol. 9, pp. 308 - 310.
- ALLEN, S.M.  
CAHN, J.W. 1975 "Coherent and Incoherent Equilibria in Iron-Rich Iron-Aluminum Alloys," *Acta Metallurgica*, Vol. 23, pp. 1017-1026.
- CULLITY, B.D. 1978 *Elements of X-Ray Diffraction*, Addison - Wesley Co., Reading.
- DIEHM, R. S.  
MIKKOLA, D.E. 1987 "Effects of Mo, Ti, and Si Additions on High Temperature Compressive Properties of Iron Aluminides," *Materials Research Society Symposium Proceedings, MRS Vol. 81*, pp. 329-334.
- DUNAND, D. C. 1994 "A Review of Reactive Synthesis of Aluminide Intermetallics," in *Processing and Fabrication of Advanced Materials III*, The Minerals, Metals & Materials Society.
- FORTNUM, R.T  
MIKKOLA, D.E. 1987 "Effects of Mo, Ti, and Si Additions on the DO<sub>3</sub> - B<sub>2</sub> Transition Temperature for Alloys Near Fe<sub>3</sub>Al," *Material Science and Engineering*, vol. 91, pp. 223-231.
- GERMAN, R. M.  
BOSE, A.  
STOLOFF, N.S. 1989 "Powder Processing of High Temperature Aluminides," *Materials Research Society Symposium Proceedings, MRS Vol. 133*, pp. 403 - 414.
- HIROSE, A.  
UEDA, T.  
KOBAYASHI, K.F. 1993 "Wear and Oxidation Properties of Titanium Aluminides Formed on Titanium Surface by Laser Alloying," *Materials Science and Engineering*, vol. A160, pp. 143 - 153.
- JOHNSON, M  
MIKKOLA, D.E. et al 1990 "The Resistance of Nickel and Iron Aluminides to Cavitation Erosion and Abrasive Wear," *Wear*, vol. 140, pp. 279 - 289.
- LIU, C. T. 1993 "Recent Advances in Ordered Intermetallics," *Materials Research Society Symposium Proceedings, MRS Vol. 288*, pp. 3 - 19.

- MASAMUNE, S  
SMITH, J. M. 1963 "Thermal Conductivity of Beds of Spherical Particles," *I&EC Fundamentals*, 2(2), pp. 136 - 143
- MASSALSKI, T.B. 1990 *Binary Alloy Phase Diagrams*, ASM International, Metals Park.
- METALS  
HANDBOOK - DESK  
EDITION 1985 *Metals Handbook - Desk Edition*, ASM International, Metals Park
- OHLAI, S.  
OYA, Y.  
SUZUKI, T. 1984 *Acta Metallurgica*, Vol. 32, pp. 289 - 298
- PORTER, W.D.  
MAZIASZ, P.J. 1993 "Thermal Expansion Data on Several Iron- and Nickel- Aluminide Alloys," *Scripta Metallurgica et Materialia*, vol. 29, pp. 1043-1048.
- SIKKA, V. K.  
LIU, C.T. 1994 "Iron - Aluminide Alloys for Structural Use," *Materials Technology*, 9(7/8), pp. 159-162.
- TIBBETTS, D. 1994 Cummins Engine Co., Columbus, IN. Private Communication.
- TORTORELLI, P.F.  
DeVAN, J.H. 1992 "Behavior of Iron Aluminides in Oxidizing and Oxidizing / Sulfidizing Environments," *Materials Science and Engineering*, vol. A153, pp. 573-577.
- VEDULA, K.  
STEPHENS, J.R. 1987 "B2 Aluminides for High Temperature Applications," *Materials Research Society Symposium Proceedings - MRS Vol. 81*, pp. 381 - 391.
- VEDULA, K. ET AL 1985 "Alloys Based on NiAl for High Temperature Applications," *Materials Research Society Symposium Proceedings, MRS Vol. 39*, pp. 411 - 421.

## CHAPTER 4

### References

- |   |      |  |
|---|------|--|
| CULLITY, B.D.                                 | 1978 | <i>Elements of X-Ray Diffraction</i> , Addison-Wesley, Reading.  |
| DAVID, S. A.<br>VITEK, J. M.<br>HEEBLE, T. L. | 1987 | "Effect of Rapid Solidification on Stainless Steel Weld Metal Microstructures and Its Implications on the Schaeffler Diagram," <i>Welding Journal</i> , 66(10), pp. 289s - 300s.   |
| DIETER, G.E.                                  | 1986 | <i>Mechanical Metallurgy</i> , McGraw-Hill, New York.  |
| ELMER, J.W.                                   | 1988 | <i>The Influence of Cooling Rate on the Microstructure of Stainless Steels</i> , MIT Ph.D Thesis.  |
| EVANS, N.S.                                   | 1980 | Ph.D. Thesis, University of Bristol.   |
| LaFAVE, R.<br>WIEGAND, R.                     | 1994 | "Economical Repair of Turbomachinery Shafts by SAW," <i>Welding Journal</i> , 73(4), pp. 39 - 44.  |
| MARSHALL, P.                                  | 1984 | <i>Austenitic Stainless Steels : Microstructure and Mechanical Properties</i> , Elsevier, Essex.   |
| MATSUDA, F.<br>LEE, J-B.                      | 1990 | "A New Model of Weld Solidification and Its Application to Crack Susceptibility for Stainless Steels," in <i>Advanced Joining Technologies - Proceedings of the Intl. Welding Congress on Joining Research</i> , Chapman Hall, London. |
| METALS<br>HANDBOOK - DESK<br>ED.              | 1985 | <i>Metals Handbook - Desk Edition</i> , ASM International, Metals Park   |
| SCHAEFFLER, A.L.                              | 1949 | "Constitution Diagram for Stainless Steel Weld Metal," <i>Metals Progress</i> , 56, p. 680.  |
| SETTY, S.K. et al                             | 1957 | "Stresses Alter Hardness," <i>Mechanical Engineering</i> , Vol. 79, pp. 1127 - 1129.   |
| STEFANSSON, H.                                | 1995 | Bird - Johnson, Inc. Walpole, MA<br>Personal Communication.  |

- VITEK, J.M.  
ET AL. 1992 "Examination of 308 and 308 CRE after Interrupted Creep Testing," *Welding Journal*, 71(11), pp. 421s - 435s.
- WEINER, J.H.  
BOLEY, B.A. 1963 "Elasto-Plastic Thermal Stresses in a Solidifying Body," *J. of the Mechanics and Physics of Solids*, 11, pp. 145 - 154.
- WELDING JOURNAL 1992 " Welding Wire Selection Critical to Jet Engine Repair Work," *Welding Journal*, 71(11), pp. 57 - 59.

## CHAPTER 5 REFERENCES

- ADVANCED MATERIALS & PROCESSES 1994 "Tech Spotlight - Improved Process for Manufacturing Carbon/Carbon Composites," *Advanced Materials & Processes* vol 145, pp. 35-36.
- BAILEY, V.L. 1994 Pulse Sciences, Inc., San Leandro, CA, Personal Communication.
- BANAS, G. ET AL. 1990 "Laser Shock-Induced Mechanical and Microstructural Modification of Welded Maraging Steel," *Journal of Applied Physics*, Vol. 67(5), pp. 2380 - 2384.
- BOITSOV, B.V. ET AL 1988 "The Influence of Shock Wave Treatment on Strengthening of D16 Aluminum Alloy in the Case of Aging," *Vestnik Mashinostroeniya*, Vol. 68(5), pp. 7 - 10.
- BOLEY, B.A. WEINER, J.H. 1960 *Theory of Thermal Stresses*, Krieger, Malabar.
- BUCKLEY, J.D. 1992 "Carbon - Carbon Overview," *Carbon-Carbon Materials and Composites* NASA RP 1254, pp. 1-18
- BUESSEM, W.R. GRUVER, R.M. 1972 "Computation of Residual Stresses in Quenched Al<sub>2</sub>O<sub>3</sub>," *Journal of the American Ceramic Society*, Vol. 55, pp. 101 - 104.
- CLAUER, A.H. FAIRLAND, B.P. WILCOX, B.A. 1977 "Laser Shock Hardening of Weld Zones in Aluminum Alloys," *Metallurgical Transactions A*, Vol 8A, pp. 1871 - 1876.
- COTTRELL, A.H. 1953 *Dislocations and Plastic Flow in Crystals*, Oxford University Press.
- COURANT, FRIEDRICHS 1948 *Supersonic Flow and Shock Waves*, Interscience, New York.
- DUBRUJEAUD, B. 1992 Ecole des Mines de Paris, Centre des Matériaux, France, Personal Communication.
- DUVALL, G.E. FOWLES, G.R. 1963 "Shock Waves," in *High Pressure Physics and Chemistry*, Academic Press, London.



- FAIRLAND, B.P.  
ET AL. 1972 "Laser Shock-Induced Microstructural and Mechanical Property Changes in 7075 Aluminum," *Journal of Applied Physics*, Vol. 43(9), pp. 3893 - 3895.
- HERRING, C. 1950 *J. of Applied Physics*, Vol. 21, p. 437
- HOLMAN, J.P. 1986 *Heat Transfer*, McGraw-Hill, New York
- HSU, C.  
LAWRENCE, G.  
FERRARIO, J.D. 1991 "Electron Beam Drilling Produces Clean Holes in a Single Pulse," *Welding Journal*, Vol. 70(7), pp. 49 - 52.
- ILER, R.K. 1955 *The Colloid Chemistry of Silica and Silicates* Cornell University Press, Ithaca
- INAL, O.T.  
MURR, L.E. 1978 "Laser Shock-Induced Microstructural Changes and a Comparison with Explosive Shock-Induced Phenomena in Metals : Field Ion and Electron Microscopic Studies," *Journal of Applied Physics*, Vol. 49(4), pp. 2427 - 2434.
- KINGERY, W.D.  
BOWEN, H.K.  
UHLMANN, D.R. 1976 *Introduction to Ceramics - 2nd Ed.*, Wiley - Interscience, New York.
- KIRCHNER, H.P. 1979 *Strengthening of Ceramics*, Marcel Dekker, New York.
- KOFSTAD, P. 1972 *Nonstoichiometry, Electrical Conductivity, and Diffusion in Binary Metal Oxides*, John Wiley & Sons, New York.
- KRÖGER, F.A.  
VINK, V.J. 1956 "Relations between the Concentrations of Imperfections in Crystalline Solids," *Solid State Physics*, Vol. 3, Academic Press, New York, pp. 307 - 435.
- LESLIE, W.C. 1973 "Microstructural Effects of High Strain Rate Deformation," in *Metallurgical Effects at High Strain Rates*, Plenum Press, New York, p. 571.
- LUNDIN, C.D.  
DANKO, J.C.  
SHI, C.  
KHAN, K.K.  
GREENWELL, B. 1992 "Material Interaction and Joining with High Energy Electron Beam Exposure," *AWS Conference on High Energy Electron Beam Welding and Materials Processing*, Cambridge, MA, pp.123 - 137.

- McMANUS, H. 1994 MIT Aeronautics and Astronautics Department, Private Communication.
- NABARRO, F.R.N. 1947 *Report of Conference on Strength of Solids*, University of Bristol, Bristol, pp. 75 - 90.
- NARAYANASWAMY, O.S. 1969 "Calculation of Residual Stresses in Glass," *Journal of the American Ceramic Society*, Vol. 52, pp. 554 - 558.
- GARDON, R.
- RUBIN, L 1992 "Applications of Carbon-Carbon," *Carbon-Carbon Materials and Composites* NASA RP 1254, pp. 267 - 281
- SHEEHAN, J.E. 1992 "High Temperature Coatings on Carbon Fibers and Carbon-Carbon Composites," *Carbon-Carbon Materials and Composites* NASA RP 1254, pp. 223 - 266
- SPENCER, L.V. 1959 *Energy Dissipation by Fast Electrons* NBS Monograph 1.
- SUHIR, E. 1989 "Interfacial Stresses in Bimetal Thermostats," *Journal of Applied Mechanics* vol. 56, pp. 595 - 600.
- SWEENEY, C.B. 1992 *Analysis of Residual Stresses in Ceramic / Metal Braze Joints Using Finite Element Methods* MIT Masters Thesis.
- WAGNER, L. 1994 "Improve the Fatigue Life of Titanium Alloys - Part II," *Advanced Materials & Processes*, Vol. 146(1), pp. 50hh - 50jj.
- GREGORY, J.K.
- WAGNER, L. 1994 "Improve the Fatigue Life of Titanium Alloys - Part I," *Advanced Materials & Processes*, Vol. 145(3), pp. 36v - 36z.
- GREGORY, J.K.

## CHAPTER 6

### References

- SAUNDERS et al.            1993    " Electron Curing of Fiber - Reinforced Composites : Recent Developments," *Proceedings of 38th SAMPE Conference, Anaheim, CA.*
- SINGH, A.  
SILVERMAN, J  
(editors)                    1992    *Radiation Processing of Polymers*, Oxford University Press, New York.

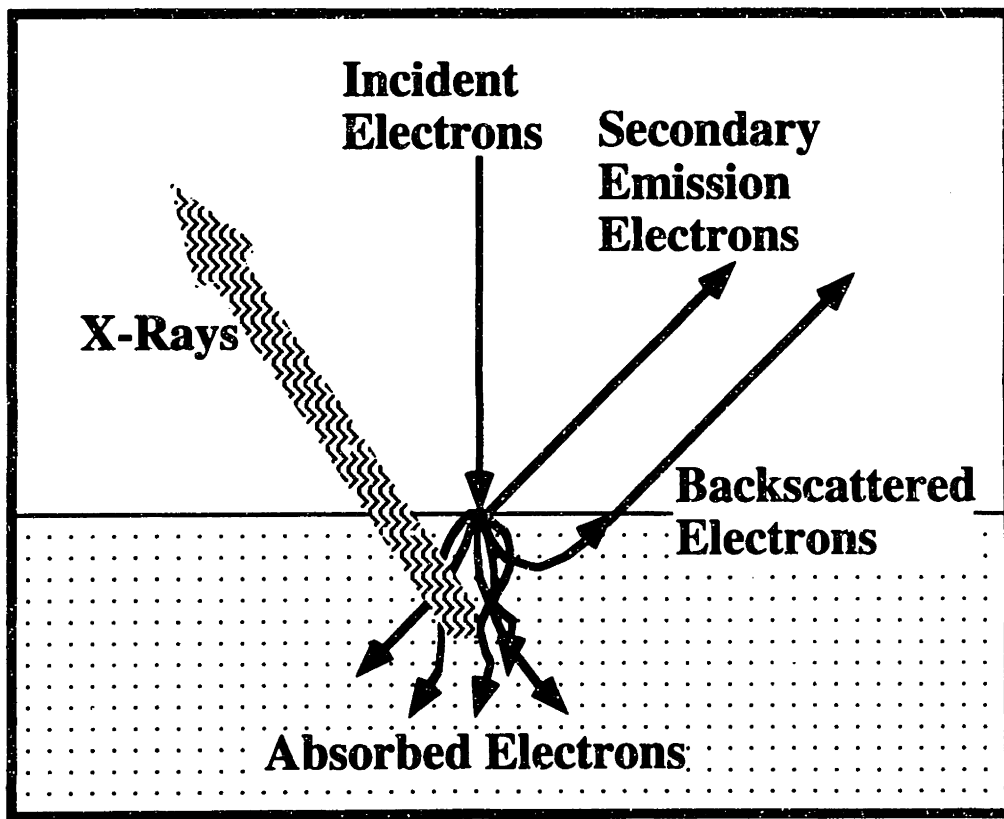
## APPENDIX A BACKGROUND PHYSICS AND BEAM TECHNOLOGY

### A.1 Electron Beams and their Interaction with Matter

An understanding of electron - material interactions is necessary to correctly describe the thermomechanical effects of electron beams. The essential features of these interactions include such phenomenon as absorption, backscattering, and X-ray production. There are several mechanisms by which electrons can transfer energy to a workpiece, and for each mechanism there are several analytical / phenomenological models used to quantify these interactions. The final practical application of these models to materials processing is the description of electron beam-material interactions in terms of an e-beam heat source model.

#### A.1.1 Types of Electron - Material Interactions

The variety of electron interactions with matter may be concisely represented in the following schematic diagram [TANIGUCHI (1989)] :



(shown above)

## **FIGURE A.1**

### **Basic Electron - Material Interactions**

**Adapted from TANIGUCHI (1989)**

For electron beam processing, we will be primarily concerned with collisional and radiative interactions and backscattering losses. Collisional processes result in sample heating, and radiative processes produce X-rays. At very high electron energies and in targets with large atomic numbers, radiative losses can become significant. Secondary emission will be ignored, but backscattering can represent a significant loss term. Its net effect is to lower the effective power of the incident beam.

#### **A.1.2. Backscattering**

Although the backscattered current can be as high as 50% of the incident current, the actual backscattered power will be much lower. The backscattered current consists of secondary electrons of low energy in addition to directly backscattered primary electrons. In this work, the backscattered power will be computed using a Monte Carlo simulation of electron trajectories in the target material. The specific code used is known as TIGER ITS 3.0, and was developed at Sandia National Laboratory [ HALBLEIB et al. (1992)]. A detailed discussion of Monte Carlo codes will be presented later in this work.

The graphs below show the backscattered current and power as a function of incident electron energy for 304 stainless steel as the target material. Complete tables of backscattered power and current for other materials are presented in Appendix B. Note that the reflected current is as high as 25 % at low energies, whereas the reflected power never exceeds 16% or so.

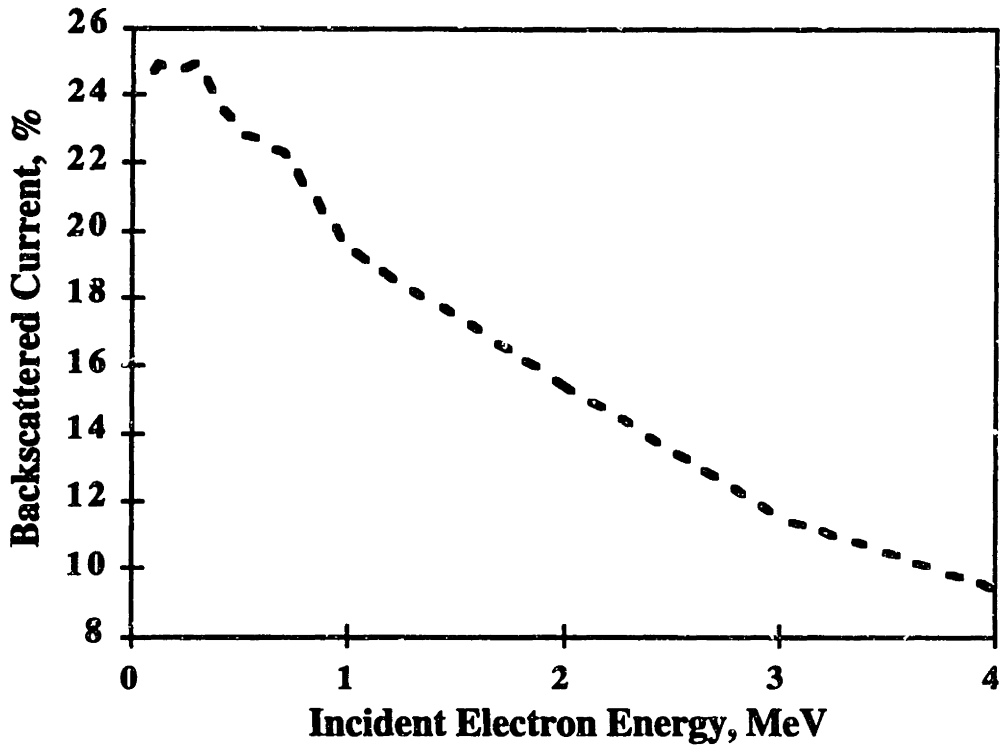
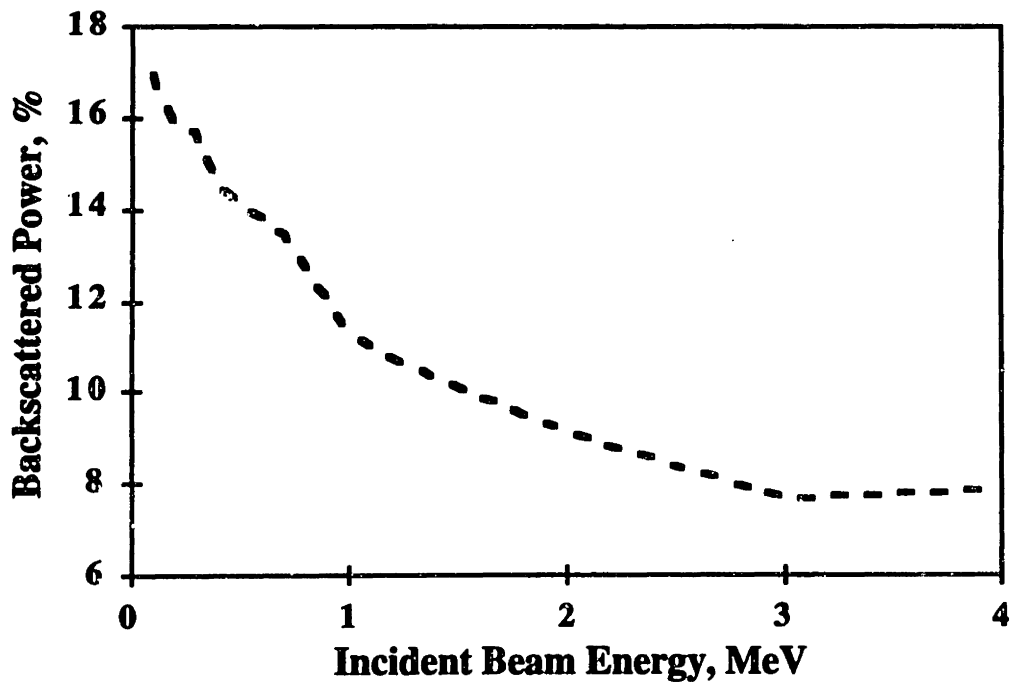


**FIGURE A.2**  
**Backscattered Current as a Function of**  
**Incident Electron Energy, 304 SS is Target**



(shown above)  
**FIGURE A.3**  
**Backscattered Power as a Function of**  
**Incident Electron Energy, 304 SS is Target**

It must be noted that the above treatment of backscattering assumes a perfectly flat surface. In such cases, it is seen that backscattering can represent a significant loss term. The effect is however very regular and predictable. It is important to note that the calculations shown above DO NOT apply to deep penetration, or "keyhole" type processes. In these operations, the steep-walled melt region will result in greater re-absorption of backscattered electrons, and hence a lower overall backscattering coefficient. To take this effect into account, a modified treatment that considers surface roughness must be considered. Suppose that the surface has a cylindrical depression in it, as shown in the figure below :

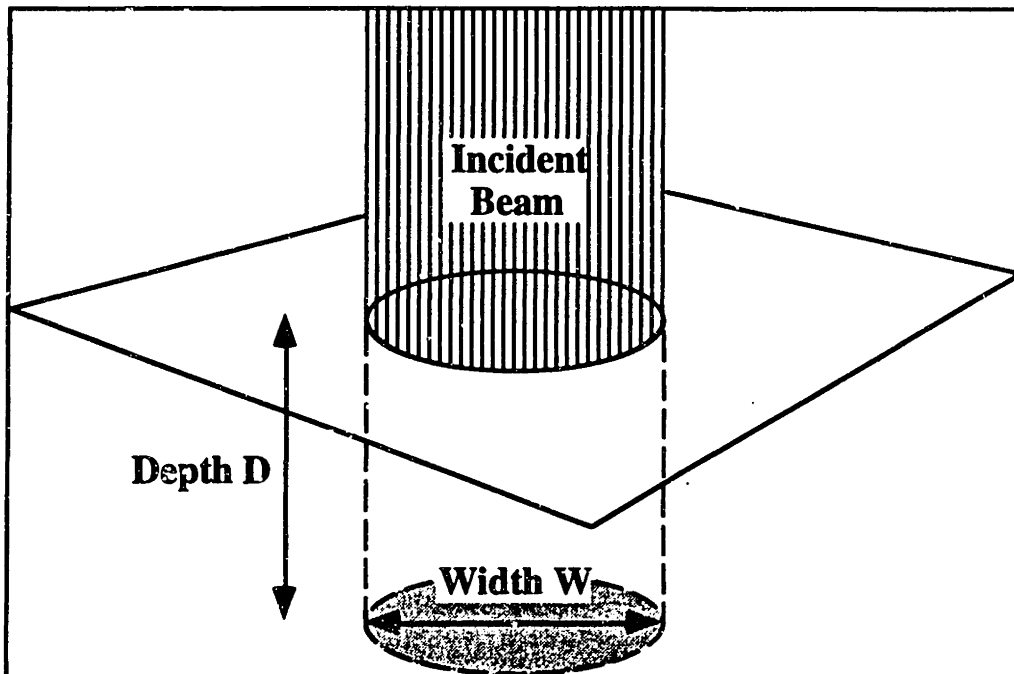


**FIGURE A.4**  
**Beam Impinging Upon a Cylindrical Surface Indentation**

The backscattering coefficient will now be modified to account for re-absorption at the walls. Suppose the beam reaches the bottom of the pit and gets partially absorbed. Suppose also that the incident beam is perfectly straight and parallel to the walls of the pit. Suppose also that the backscattered electrons are mostly emitted from the bottom of the pit, and that the flux of backscattered electrons has a uniform angular distribution. This means that each point on the bottom of the pit acts like an isotropic point source and emits electrons uniformly in all directions up and away from the surface. The walls will intercept some of these electrons, and this fraction is found with the aid of the diagram shown below.

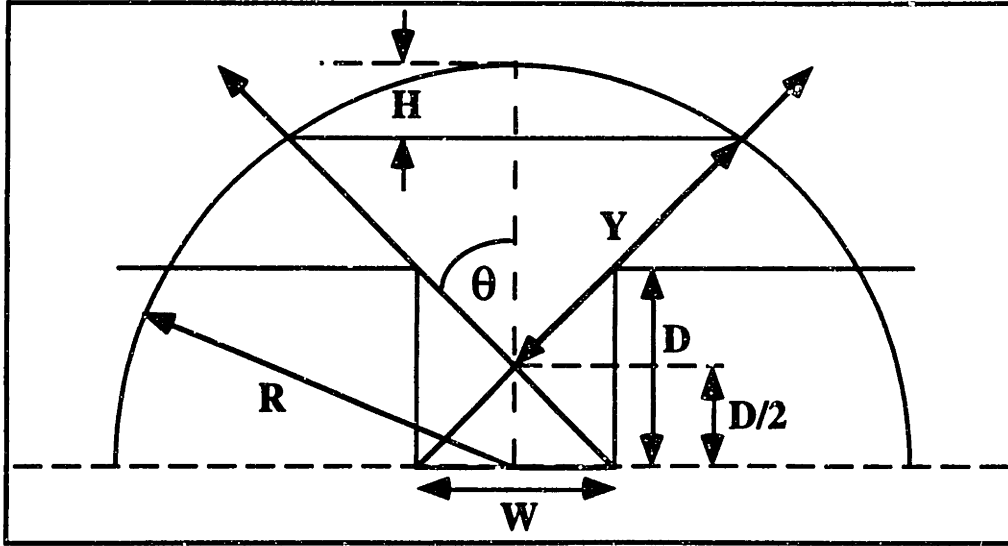


**FIGURE A.5**  
**Diagram Used to Find Backscattering**  
**from a Surface Depression**

The semicircle represents a hemisphere centered on the center of the pit. The bottom of the pit emits backscattered electrons, some of which are absorbed by the walls. *It will be assumed that the walls do not re-emit electrons.* The rays extending from the bottom corners of the pit and just touching the edges therefore define a cone that will contain all the trajectories of electrons able to escape from the pit. The additional attenuation caused by the presence of the surface depression is simply the ratio of the surface area of the spherical cap of radius R and height H to the area of the hemisphere of radius R. This calculation is shown below.

Area of Cap :

$$A_1 = 2\pi RH = 2\pi R \cdot \left( R - \frac{D}{2} - Y \cos \theta \right)$$

Area of the Hemisphere :

$$A_2 = 2\pi R^2 \tag{A.1}$$

Ratio of the two Areas :

$$\frac{A_1}{A_2} = \left( 1 - \frac{D}{2R} - \frac{Y}{R} \cdot \cos \theta \right)$$

In the limit as R get infinitely large, this ratio of areas is the ratio of the electrons able to escape as compared to emission from a flat surface. In this limit, the above expression becomes :



$$\frac{A_1}{A_2} \rightarrow 1 - \cos \theta = 1 - \frac{D}{\sqrt{D^2 + W^2}} = 1 - \frac{1}{\sqrt{1 + (W/D)^2}}$$

This ratio is the amount by which the backscattering coefficient for a flat surface is attenuated. Write this additional factor as : (A.2)

$$\eta_{WD} \equiv 1 - \frac{1}{\sqrt{1 + (W/D)^2}}$$

The overall backscattering coefficient may now be written as :

$$\eta_{TOT} = \eta_{WD} \cdot \eta_B \quad (A.3)$$

This last expression assumes that the beam diameter is the same size as the width of the surface depression. If the beam is narrower than the surface depression, then the modified expression for  $\eta_{WD}$  becomes :

$$\eta_{WD} = 1 - \frac{D}{\sqrt{D^2 + (r_B + W/2)^2}}, \quad \text{where} \quad (A.4)$$

$r_B$  is the beam radius.

If the beam is larger than the surface depression, or if there are many surface depressions, then the following method can be used to evaluate the overall backscattering coefficient.

Case 1 : single surface depression, oversized beam.

Suppose the area surrounding the surface depression is flat.

The total area from which backscattered electrons may emerge is  $\pi r_B^2$ . The fraction of this area that is at the bottom of the

surface depression is  $\frac{W^2}{4r_B^2}$ . The fraction of this area that is

perfectly flat is  $1 - \frac{W^2}{4r_B^2}$ . The total fraction of backscattered

electrons is then given by :

$$\begin{aligned} \left(1 - \frac{W^2}{4r_B^2}\right)\eta_B + \frac{W^2}{4r_B^2}\eta_{WD}\eta_B &= \left[1 + \frac{W^2}{4r_B^2}(\eta_{WD} - 1)\right]\eta_B \\ &= \left[1 - \frac{(W^2/4r_B^2)}{\sqrt{1 + (W/D)^2}}\right] \cdot \eta_B \end{aligned}$$

Case II : many small surface depressions.

Suppose that there are  $N_{WD}$  cylindrical surface depressions per unit area of surface. The total area fraction occupied by

these depressions is then  $N_{WD} \cdot \frac{\pi W^2}{4}$ . The fraction of the surface

that is perfectly flat is  $1 - N_{WD} \cdot \frac{\pi W^2}{4}$ . Going through

a calculation similar to Case I we get :

(A.5)

$$\eta_{TOT} = \left[1 - \frac{(N_{WD}\pi W^2/4)}{\sqrt{1 + (W/D)^2}}\right] \cdot \eta_B$$

For the purposes of making numerical estimates, it is useful to consider some values of the additional backscattering correction term. These values are shown in the table below.

**TABLE A.1**  
**Values of Additional Backscattering Attenuation Factor**  
**as a Function of the Depression Aspect Ratio**

VALUE OF DEPRESSION ASPECT RATIO : W/D	$1 - \frac{1}{\sqrt{1+(W/D)^2}}$
0.10	0.005
0.25	0.03
0.50	0.106
0.75	0.200
1.0	0.293
1.5	0.375
2.0	0.445
2.5	0.553
5.0	0.804
10.0	0.900

For comparison, it is useful to look at laser reflection losses for typical materials processing applications of interest [ION, SHERCLIFF and ASHBY (1991)]. It should be kept in mind that the absorbtivity / reflectivity of a surface with respect to laser radiation will vary widely depending on surface conditions and will in general vary as the process proceeds. The values shown here are intended as approximate and representative figures.

**TABLE A.2**  
**Absorbtivities for Laser Processing**  
**ION, SHERCLIFF, and ASHBY (1991)**

PROCESS DONE WITH LASER	ABSORBTIVITY
Annealing	0.5
Cladding	0.5
Hardening	0.5
Conduction Welding	0.3
Keyhole Welding	0.8
Melting	0.3

### A.1.3 Material Stopping Power, Energy Deposition, and Electron Range

Electron beams will cause sample heating by losing and depositing energy within a target through elastic and radiative interactions. The collisional interactions will dominate the energy loss. The (linear) stopping power of an absorber is defined as the energy loss per unit length experienced by an incident particle along its trajectory. The stopping power may be generically represented by :

$$\text{Stopping Power} = -\left. \frac{dE}{dx} \right|_{\text{trajectory}} \quad (\text{A.6})$$

The trajectory of an electron will be much longer but more tortuous than that of a heavy ion. The electron is thousands of times less massive than ions, and it has the same mass as the orbital electrons it will mostly encounter. Also, the nuclei are tremendously more massive than an incident electron. These factors will result in large possible angular deflections and large possible energy losses in individual collisions (catastrophic collisions).

The overall stopping power is the sum of the collisional interactions and the radiative interactions :

$$\text{Stopping Power} = - \left\{ \frac{dE}{dx} \Big|_{\text{collisional}} + \frac{dE}{dx} \Big|_{\text{radiative}} \right\} \quad (\text{A.7})$$

There has been much effort over the past eighty years or so in deriving theoretical expressions for the stopping power. The theoretical treatment of this problem requires a great deal of sophistication due to the number and complexity of the possible interactions. Here is a list of the effects that must be taken into account to get a complete physical picture [adapted from BERGER (1963)]:

- elastic scattering by atomic nuclei
- inelastic scattering by electron "cloud"
- production of secondary (knock-on) electrons
- bremsstrahlungen
- possible nuclear interactions

A complete description of electron scattering is beyond the scope of this introductory section. An excellent overview may be found in Handbuch der Physik BIRKHOFF (1958). Some of the essential features of scattering theory will be briefly presented, starting with the classical theory [THOMSON (1912) & BOHR (1948)]. This simple approach considers the collision between a moving electron and an electron at rest. This is shown in the figure below.

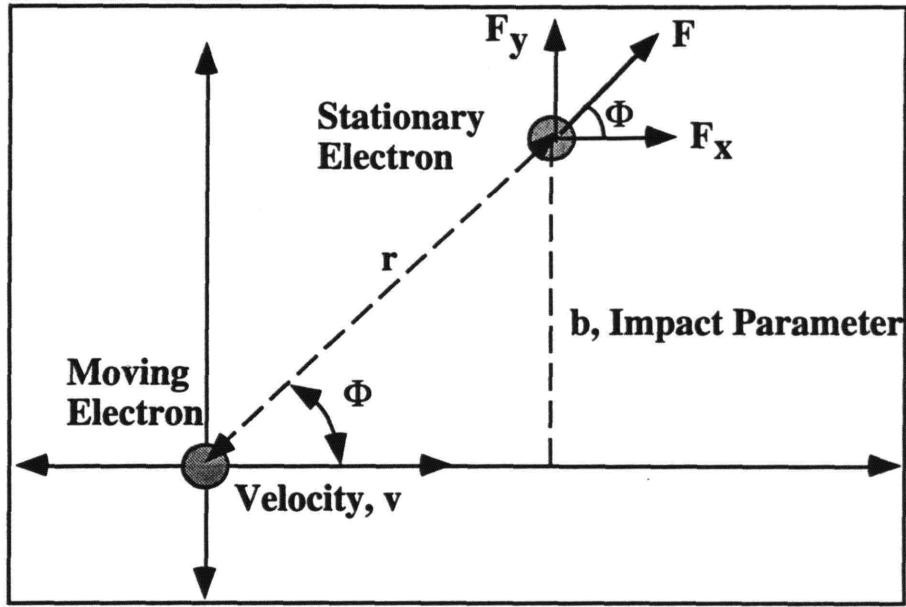


**FIGURE A.6**  
**Electron - Electron Scattering : Classical Theory**  
 Adapted from JACKSON (1962)

From elementary mechanics, the Coulombic repulsion forces may be written. Also, the momentum transfer and energy transfer may be expressed in terms of the impact parameter. The energy transfer can also be expressed in terms of the incident kinetic energy of the moving electron. These relations are shown below :

Coulombic Forces :

$$F = \frac{e^2}{r^2}, \quad F_x = \frac{e^2}{r^2} \cos \Phi, \quad F_y = \frac{e^2}{r^2} \sin \Phi \quad (\text{cgs units})$$

$e$  is the charge of an electron.

Momentum Transfer :

$$P_x = 0, \quad P_y = \frac{2e^2}{bv} \quad (\text{A.8})$$

Energy Transfer :

$$W = \frac{e^4}{Eb^2}, \quad \text{where } E = \frac{1}{2}m_0v^2 \quad (\text{non - relativistic KE})$$

The next important concept is that of the scattering cross-section. for the problem shown above, this quantity may be defined as [BIRKHOFF (1958)] :

$$d\sigma \equiv 2\pi b db$$

$d\sigma$  is the differential scattering cross - section,  
and  $b$  is the impact parameter. (A.9)

For case of classical electron - electron scattering, this expression is :

$$d\sigma = \frac{\pi e^4}{E} \cdot \frac{dW}{W^2} \quad (A.10)$$

A much more sophisticated treatment was done by Möller, who took into account relativistic effects and electron spin interactions. Möller's scattering cross-section is given by [MÖLLER (1932)] :

$$\frac{d\sigma}{dW} = \frac{2\pi e^4}{m_0 v^2} \cdot \left\{ \frac{1}{W^2} + \frac{1}{(E-W)^2} + \frac{1}{(E+m_0 c^2)^2} - \frac{1}{W(E-W)} \cdot \frac{m_0 c^2 (2E+m_0 c^2)}{(E+m_0 c^2)^2} \right\}$$

$W$  is the energy transfer,

$m_0$  is the rest mass of an electron, (A.11)

$E$  is the kinetic energy,

$v$  is the electron velocity, and

$e$  is the charge of an electron.

The stopping power may now be obtained from the scattering cross-section. The basis for this evaluation depends on the following argument. First, consider the energy transfer between two interacting electrons. Now find the energy transfer as an incident electron moves a distance  $dx$  into an absorbing material and interacts with many electrons. Suppose there are  $N$  atoms per unit volume (atomic number density), and  $Z$  electrons per atom (atomic number). Then as the incident electron moves through a region  $dx$  of the absorbing material, it interacts with  $dn$  number of electrons, where  $dn$  is given by :

$$dn = (NZ) \cdot (2\pi b db \cdot dx) \quad (A.12)$$

This number of interactions is simply the number of electrons with impact parameters between  $b$  and  $b+db$ . Therefore the total loss in energy of the incident electron is :

$$dE = \int W \cdot dn = 2\pi NZ \cdot dx \int Wbdb$$

or

$$\frac{dE}{dx} = 2\pi NZ \cdot \int Wbdb = NZ \cdot \int d\sigma \tag{A.13}$$

Using the Möller scattering cross-section as a basis, Bethe derived the following relation for stopping power for electron-electron interactions with the incident electron having relativistic speeds [BETHE (1930)]:

$$\left. \frac{dE}{dx} \right|_{\text{collisional}} = \frac{2\pi e^4 NZ}{m_0 v^2} \left[ \ln \frac{m_0 v^2 E}{2I^2(1-\beta^2)} - \ln 2(2\sqrt{1-\beta^2} - 1 + \beta^2) + (1-\beta^2) + \frac{1}{8}(1-\sqrt{1-\beta^2})^2 \right]$$

$\beta$  is the relativistic factor  $v/c$ ,

$N$  is the number density of the absorbing material,

$Z$  is the atomic number of the absorbing material,

$v$  is the velocity of the electron,

$e$  is the charge of the electron,

(A.14)

$I$  is the average excitation / ionization potential of the absorbing material, and

$m_0$  is the rest mass of the electron.

Radiative interactions have also been considered in terms of scattering cross-section. These can occur from electron - nuclear scattering interactions during which the deflection angle of incident electrons could be very large. The basic aspects of nuclear scatter may be examined in a manner similar to electron - electron interactions. Such a presentation will not be shown here. The radiative interactions are generally known as *Bremstrahlungen* ( from the German words "bremen," or to brake, and "Strahlung," or ray). It will be seen that such radiative losses become significant only at very high electron energies and in targets with large atomic numbers. The *Bremstrahlungen* energy spectrum is continuous and extends up to the incident electron energy.

This continuous spectrum is very different from characteristic X-rays, which are the result of excited orbital electrons "falling" back to lower energy shells. Since the jumps between electron energy levels are discrete, these characteristic X-rays will appear at specific and discontinuous energies. characteristic X-rays can be produced when orbiting electrons are excited by an incident electron beam. A hypothetical X-ray spectrum which combines continuous and characteristic X-ray emission is shown below.

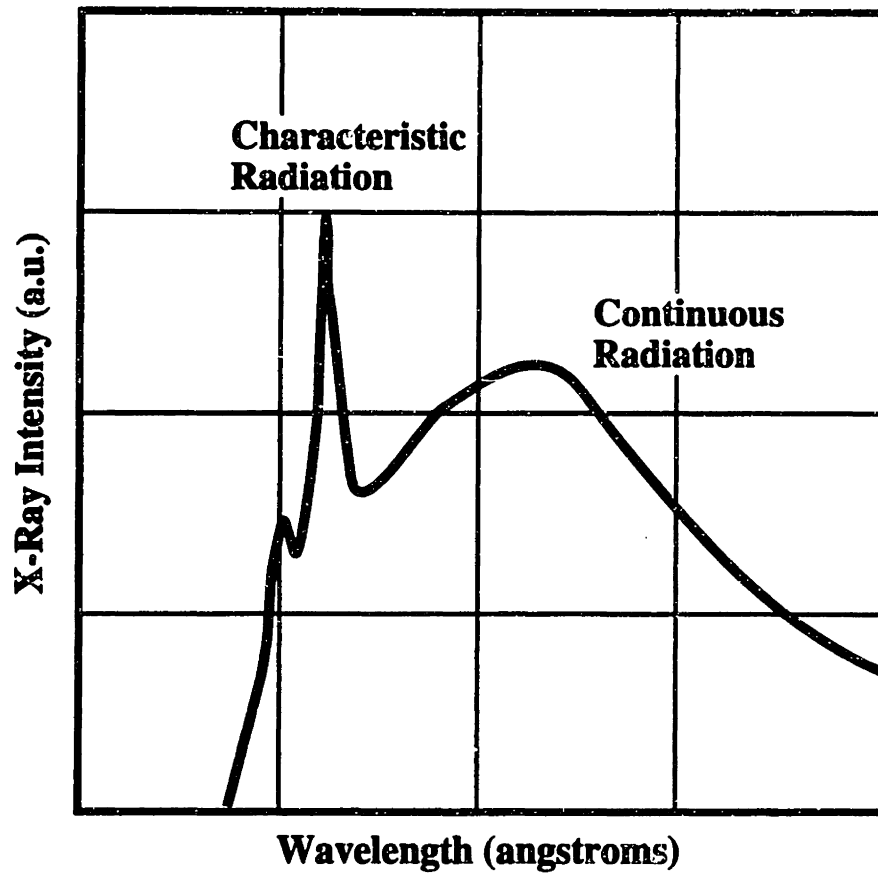


**FIGURE A.7**  
**Schematic X-Ray Spectrum**  
 Adapted from CULLITY (1978)

BETHE and HEITLER (1934) derived a scattering cross section for bremsstrahlungen. More significant than the exact form is the fact that this radiative contribution is a small part of the overall energy losses. Bethe and Heitler compared these two terms :

$$\frac{(dE/dx)_{radiative}}{(dE/dx)_{collisional}} \approx \frac{EZ}{800} \quad (A.15)$$

The actual fraction of energy lost to radiative processes has been tabulated for specific materials and different electron energies [BERGER and SELTZER (1982)]. Some typical numbers are shown in the table below.



**TABLE A.3**  
**Percent of Incident Beam Lost to Bremstrahlungen**  
**Adapted from BAILEY (1992)**

TARGET MATERIAL	PERCENT OF INCIDENT BEAM LOST TO BREMSTRAHLUNGEN	
	AT 1 MeV	AT 10 MeV
ALUMINUM	0.8 %	7.4 %
IRON	1.7 %	14 %
MOLYBDENUM	3 %	20 %
TUNGSTEN	6 %	30 %

In addition to stopping power, the range is an important parameter in describing e-beams as a heat source. As the name implies, the range is a measure of the penetration of electrons into a target material. High energy electrons can have ranges of several millimeters in most metals, making high energy electron beams volumetric heat sources.

The treatment of stopping power and scattering up to this point has focused on single events. Electrons penetrating into a thick medium will experience many thousands of collisions before stopping. An estimate of the number of these collisions is shown below [BERGER (1963)]. This calculation assumed an original electron energy of 0.5 MeV. The number of collisions occurring as the particles lose energy is estimated for different energy ranges.

**TABLE A.4**  
**Number of Collisions Experienced by**  
**an Incident Electron**  
**Adapted from BERGER (1963)**

ENERGY RANGE (MeV)	NUMBER OF COLLISIONS	
	ALUMINUM	GOLD
0.5 - 0.25	29, 000	170, 000
0.25 - 0.125	34, 000	170, 000
0.125 - 0.0625	42, 000	150, 000

To effectively deal with such situations, there has been much effort in developing multiple scattering theories. A good overview of many of these developments is given in BIRKHOFF (1958) and BERGER (1963). Most of these theories are based on several basic components. Firstly, an overall transport equation describes the relationship between the flux of electrons, the probability of interaction with the medium, and the potential outcomes of scattering events. The individual scattering events are still based on fundamental physical considerations, but a specific form for a scattering cross-section may or may not be adopted. The component of these multiple scattering theories that forms the link between energy deposition and stopping power is the continuous slowing-down approximation [see BERGER (1963)]. This assumes that the energy of the penetrating electron is a function of the pathlength traveled, and that electrons lose energy continuously along their trajectories. This assumption may be modified to account for catastrophic collisions, but the basic form is :

$$E(\zeta) = E_0 - \int_0^\zeta \left| \frac{dE}{d\zeta}(\zeta') \right| d\zeta'$$

$E(\zeta)$  is the particle energy at position  $\zeta$ , (A.16)

$E_0$  is the incident particle energy, and

$\frac{dE}{d\zeta}(\zeta')$  is the stopping power at position  $\zeta'$ .

Spencer has extensively dealt with this problem [SPENCER (1955) & SPENCER (1959)], and has compiled extensive data on energy deposition as a function of penetration for a variety of materials and a range of incident electron energies [SPENCER (1959)]. Some of this data will be used later to estimate the energy deposition profiles due to HEEB irradiation. These deposition profiles will subsequently serve as heat source terms for thermal models of e-beam processing.

It should be kept in mind that electron transport through an absorber is an inherently stochastic process on a microscopic level. Statistical correlations of average behavior will show general trends that are repeatable, and these are the parameters such as range, energy deposition, etc. that will be used in further calculations. On the microscopic level however, not all particles with the same incident energy will have the same range. Also, as the particles penetrate, the originally monoenergetic beam will have a spread in energies [FANO (1953) & WILKEN and FRITZ (1976)]. The variability in range is known as *range straggling*, and the spread in energy with penetration distance is known as *energy straggling*. Actually, these two concepts are related, and range straggling may be considered as a consequence of energy straggling. There are several theories that calculate the distribution of energies in straggling [LANDAU (1944), FANO (1953)]. These phenomena will only be of importance in describing the precise shape of the three-dimensional energy deposition profile. In subsequent calculations, simplifications will be made, and the exact profiles will not be considered.

#### A.1.4. Monte Carlo Simulations of Electron Transport

As mentioned in the previous section, electron transport processes are stochastic on the microscopic level. In fact, the term electron diffusion is often applied to such transport processes [BERGER (1963)]. By calculating the statistical characteristics of these random processes, macroscopic parameters may be obtained. The Monte Carlo Method is precisely this technique of extracting statistical information by observing a random process. Its use in simulating electron transport will be briefly discussed. Some of the energy deposition information used in later calculations in this work was derived from such numerical simulations [HALBLEIB et al. (1992)].

As a matter of introduction, consider a simple example of the applicability of this method [SHREIDER (1964)]. The main point illustrated by this example is the use of random sampling. Suppose we want to evaluate the following definite integral :

$$\int_0^1 f(x)dx, \text{ where the condition} \\ 0 \leq f(x) \leq 1 \text{ is imposed. Clearly} \quad (\text{A.17}) \\ 0 \leq x \leq 1.$$

Now suppose we have access to pairs of random numbers,  $\alpha$  and  $\beta$ . Suppose that all pairs of random numbers thus selected obey the inequalities  $0 \leq \alpha \leq 1$  and  $0 \leq \beta \leq 1$ . Now suppose that we evaluate the quantity  $f(\alpha)$ . Clearly if the inequality  $f(\alpha) > \beta$  holds, then the pair  $(\alpha, \beta)$  lies below the curve  $f(x)$ . The probability that a point will lie below the curve is simply the area under the curve. By sampling a large number of pairs  $(\alpha, \beta)$ , suppose it is found that  $K$  of these pairs lie under the curve. As the number of pairs sampled,  $N$ , gets very large, the ratio  $K/N$  gives a better and better approximation to the probability that a pair will be located under the curve. But this quantity is just the integral of the function over the interval  $(0, 1)$ , so the integral is also estimated. This simple example shows how sampling a random event can give the answer to a mathematical problem by taking statistical information from the trials and relating that to a relevant parameter of the problem. The simulation of particle trajectories is of course more complicated. Only the bare essential features will be presented here. A full treatment is well beyond the scope of this work, but BERGER (1963) is a more general introduction. The treatment shown here is on the level of SHREIDER (1964).

Consider an electron entering a medium and experiencing multiple scattering events. This will be referred to as a case history. There are many events which could occur, some of which have been discussed above : electron - electron scattering, electron - nuclei scattering, bremsstrahlungen, secondary electron production, and backscattering. Suppose it is possible to describe the physics of all these separate processes by their appropriate scattering parameters. Then, it is possible to construct probabilities of occurrence for these events as follows. Suppose that the atomic density of the absorber material is  $N$ . Suppose further that the scattering cross-sections for the individual processes are given by  $\sigma_1, \dots, \sigma_k$  where there are  $k$  separate processes. Macroscopic cross-sections are then defined as

$$\Sigma_j = N \cdot \sigma_j \quad (\text{A.18})$$

The total cross-section is the sum of the individual cross-sections :

$$\Sigma_T = \Sigma_1 + \dots + \Sigma_k \quad (\text{A.19})$$

The probability that any one of the events occurs is then given by :

$$p_j \equiv \frac{\Sigma_j}{\Sigma_T} \quad (\text{A.20})$$

Suppose now that the  $p_j$  are arranged along the interval (0,1). This is schematically shown below [adapted from SHREIDER (1964)].

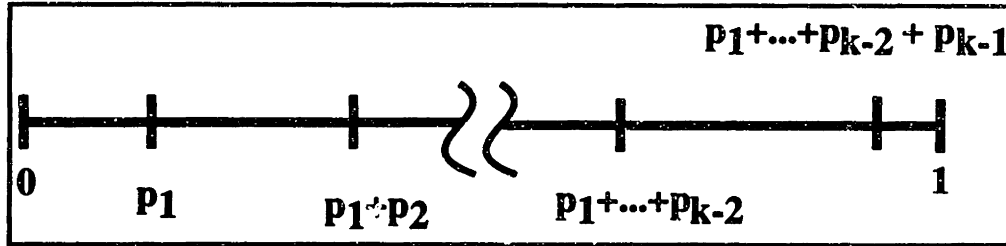


**FIGURE A.8**  
**Event Probabilities Arranged on Interval (0, 1)**  
**Adapted from SHREIDER (1964)**

If we have available random numbers  $\zeta_j$  that lie in the interval (0, 1), then clearly the following holds :

$$\begin{aligned} &\text{Given } \zeta_j \text{ such that } 0 \leq \zeta_j \leq 1, \text{ if} \\ &p_1 + \dots + p_{j-1} \leq \zeta_j \leq p_1 + \dots + p_j, \text{ then} \quad (\text{A.21}) \\ &\zeta_j \text{ determines the occurrence of event } j. \end{aligned}$$

This concept is very important, because it forms the basis of the sampling technique. Using this scheme, any given random number that is selected will indicate the occurrence of a specific event. Many case histories can then be run, keeping track of parameters such as particle energy, particle direction, and total distance traveled after each collision. In practice, this would require far too many steps in light of the huge number of collisions that will occur during the electron travel. What is usually done instead is to consider different "condensed" histories [BERGER (1963)], which are a sequence of "snapshots" of the moving particle. Between each "snapshot," the particle executes a random walk. For these random walks, several rules need to be fixed so as to properly set up the problem. These rules include the determination of a pathlength, the energy change between stages, and the spatial and angular displacements between stages. There are great intricacies involved in the selection of these various rules, and the details will not be presented here. The essential feature is that some aspect of the stages is initially specified, the energies or the pathlengths, for example. Then the rules governing fluctuations in angular and spatial displacement are formulated, together with energy or pathlength fluctuations due to catastrophic (large energy loss or scattering angle) collisions. The fluctuations are treated as random variables, and their values are sampled over some distribution of random numbers. Many histories are run, and statistical averages are calculated. The

program then tracks particle energies, energy deposition to the absorbing material, pathlength, etc. Modern Monte Carlo codes, such as the TIGER / ITS Series of codes [HALBLEIB ET AL (1992)], are very easy to use, run on PCs, and give fairly accurate results. Some of the results of this code are shown in Appendix B.

## **A.2 Numerical Data and Source Modeling**

In order to simulate the physical effects of e-beam irradiation, the actual form of the energy deposition profile must be known. For thermal and shock calculations, it is desirable to know the radiation dosage as a function of penetration depth. This quantity is measured in J / g (or W / g), and when multiplied by the material density, this term becomes a volumetric heat source term for thermal calculations. There are two approaches used in this work to estimate the energy deposition profile. The first utilizes the tabulated data of SPENCER (1959). The second uses the TIGER ITS Series of Monte Carlo Codes for coupled electron / photon transport [HALBLEIB et al (1992)]. The Spencer data exists only for certain materials and certain incident electron energies. If alloys are to be considered, or energies other than those presented in Spencer's report, interpolation can be used, but is not desirable. A more general approach is the use of Monte Carlo programs.

### **A.2.1. Spencer's Report - NBS Monograph 1, 1959**

Based on his theory of electron penetration, Spencer has compiled extensive tables of energy deposition by fast electrons. These numerical values generally agree well with experiments. The data presented in this report was converted into a form useful for subsequent calculations. The assumptions made in Spencer's report are :

- no energy / range straggling
- 1-D problem considered
- backscattering not really dealt with - there are irregularities in the representation for electrons going behind the source plane

In light of these approximations, the following approach was taken :

- Only use dissipation data for regions in front of the source plane.
- To account for 2-D effects, assume that the radial beam profile is Gaussian. Also, take the 1 / e power point as the effective beam radius (the other choice is Full Width at Half-Maximum, FWHM).
- To account for backscattering, use reflection coefficients as discussed earlier.

The Spencer data gives dimensionless energy deposition as a function of dimensionless penetration. In this work as in Spencer's report, the electron range at initial source energy will be used as the length scale for penetration. The overall mathematical framework used to derive the source representation will now be presented.

### A.2.2. Form of Source Function

It will be assumed that the energy source term for EB-material interaction has the following form :

$$\begin{aligned} f &= f(r', x'), \quad \text{and} \\ f(r', x') &= A_o \cdot u(r') \cdot v(x') \end{aligned} \tag{A.22}$$

This assumed form means that the source term has no time dependence, and that it can be decoupled into a product of r-dependent and x-dependent terms. the radial coordinate is  $r'$ , and the axial coordinate (parallel to the direction of penetration) is  $x'$ . Primed quantities are used to refer to heat source coordinates. This is done so as to distinguish them from other material points within the target. Now  $u$  and  $v$  must be evaluated to get the form of the expression, and  $A_o$  is determined by a normalization criterion. It will be assumed that the radial dependence is Gaussian in form. Range and energy straggling will be ignored. Furthermore, the form of the source distribution function chosen implies that this radial dependence is the same at all values of  $x'$ . This eliminates such beam profiles as the "tophat," in which the radial dependence of the profile changes with penetration depth. This assumption means that  $u$  has the form :

$$u(r') = \exp\left(\frac{-r'^2}{2\sigma^2}\right) \tag{A.23}$$

$\sigma^2$  is the variance

This form can be rewritten to express it in terms of the effective beam radius. There are two ways of defining an effective beam radius : in terms of the 1/e power point or the so-called full width at half-maximum (FWHM). These two criteria may be used to define an effective beam radius as follows :

1 / e Power Point :

$$A_o \cdot v(z') \cdot \exp\left(\frac{-r_B^2}{2\sigma^2}\right) = \frac{1}{e} \cdot A_o \cdot v(z'), \quad \text{so} \tag{A.24}$$

$$r_B = \sigma \cdot \sqrt{2}$$

Full Width at Half Maximum (FWHM):

$$A_o \cdot v(z') \cdot \exp\left(\frac{-r_B^2}{2\sigma^2}\right) = \frac{1}{2} \cdot A_o \cdot v(z'), \text{ so} \quad (\text{A.25})$$

$$r_B = \sigma \cdot \sqrt{2 \cdot \ln 2}$$

For the purposes of this investigation, the 1/e power point will be selected, so that the expression for Gaussian radial variation becomes :

$$u(r') = \exp\left(\frac{-r'^2}{r_B^2}\right) \quad (\text{A.26})$$

The  $x'$  - dependence of the source function can be accounted for in several ways. A polynomial could be fitted to the form of the energy deposition profile. An example of this is shown below.

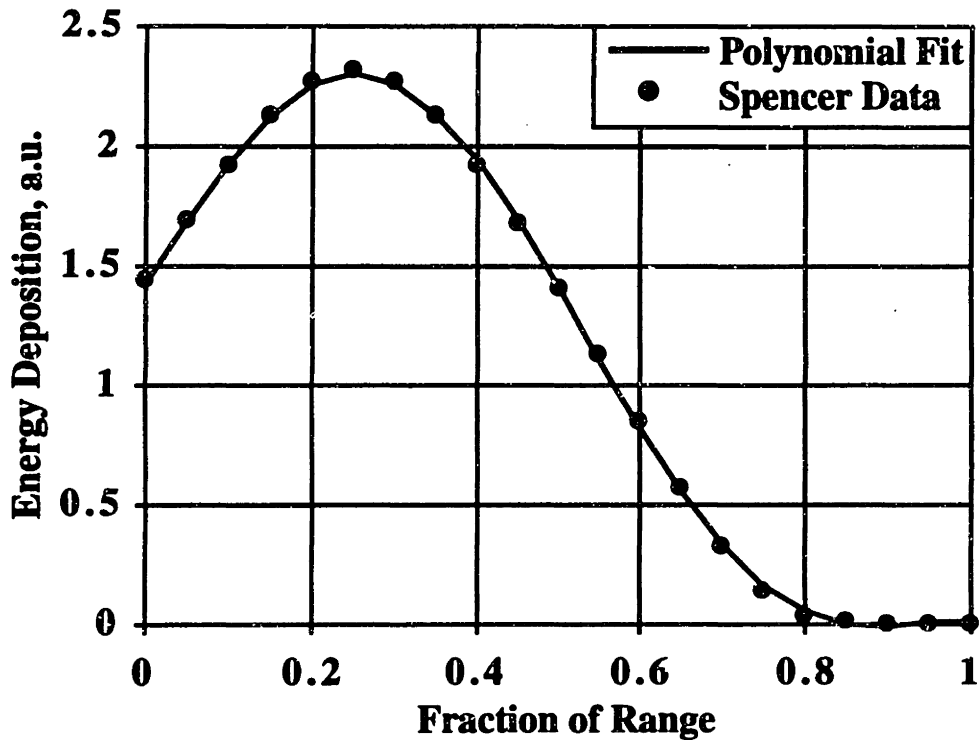


**FIGURE A.9**  
**5th-Order Polynomial Fit to Energy Deposition Profile**

For practical calculations in later sections, using such polynomial fits will be too complex an approach. The subsequent Green's function formulations

would be unduly intricate. Instead, a simplified procedure will be adopted. Imagine that the source is modeled as a cylinder imbedded into the surface of a semi-infinite solid. The source strength within the cylinder is constant. Also assume that the cylinder has dimensions as follows :

$$\begin{aligned}
 A_0 & \text{ source strength} \\
 r_B & \text{ radius} \\
 \kappa R & \text{ height}
 \end{aligned}
 \tag{A.27}$$

$\kappa$  and  $A_0$  must now be selected so that the modified cylindrical source will have a strength equal to the volumetric average of the actual source function which takes into account the spatial distribution of the deposition profile.

Consider the overall energy balance within the irradiated material :

$$\int_0^{2\pi} \int_0^R \int_0^\infty f(r', x') \cdot r' dr' dx' d\vartheta' = P_A = P_B (1 - \eta_{TOT})$$

where  $R$  is the electron range,  
 $P_A$  is the power absorbed by the target,  
 $P_B$  is the incident beam power, and  
 $\eta_{TOT}$  is the overall backscattering coefficient.

(A.28)

It is convenient to introduce the following dimensionless parameters :

$$\lambda' \equiv \frac{r'}{r_B} \quad \text{and} \quad \zeta' \equiv \frac{x'}{R}$$
(A.29)

The energy balance then becomes :

$$2\pi r_B^2 R \int_0^1 \int_0^\infty f(\lambda', \zeta') \cdot \lambda' d\lambda' d\zeta' = P_A$$
(A.30)

Introducing the proposed form of the source function, we get :

$$\pi r_B^2 R \kappa A_0 \cdot \int_0^\infty 2\lambda' \exp[-(\lambda')^2] d\lambda' = P_A$$
(A.31)

This means that the product  $\kappa A_0$  is given by :

$$\kappa A_0 = \frac{P_A}{\pi r_B^2 R}$$
(A.32)



In order to determine the source strength, the value of  $\kappa$  must be determined independently. Reconsider the energy balance shown earlier with the form of the source function given by :

$$f(\lambda', \zeta') = A_0 \exp[-(\lambda')^2] \cdot v(\zeta') \quad (\text{A.33})$$

The energy balance becomes :

$$2\pi r_B^2 R A_0 \int_0^1 v(\zeta') d\zeta' = P_A \quad (\text{A.34})$$

$$\text{this means that } \kappa = \int_0^1 v(\zeta') d\zeta'$$

SPENCER (1959) has evaluated this integral, and it may be expressed for any general energy deposition profile in terms of several physical quantities that depend on the beam energy and the target material. These are given in the relation below :

$$\kappa = \int_0^1 v(\zeta') d\zeta' = \frac{E_0}{r_0 \cdot (dE/dr)_{E_0}} \quad \text{where}$$

$E_0$  is the initial source energy in MeV, (A.35)

$r_0$  is the residual range at the source energy in  $\text{g/cm}^2$ , and

$(dE/dr)_{E_0}$  is the stopping power at the initial energy in  $\text{MeV} \cdot \text{cm}^2/\text{g}$

Thus  $\kappa$  can be specified independently, and  $A_0$  can then be determined as well. Values for the range and stopping power will be taken from SPENCER (1959) where possible. Other cases will be calculated using the TIGER series of Monte Carlo codes. These simulations are discussed at greater length below.

### A.2.3. Monte Carlo Methods - TIGER / ITS

The other approach used to calculate the energy deposition profiles due to electron irradiation utilizes the TIGER / ITS Series of computer codes [HALBLEIB et al (1992)]. These programs are sophisticated codes that can handle complex geometries and offer choices of absorber materials that include practically the whole periodic table. It is also possible to simulate alloys or compounds, and the program can accept homogeneous mixtures of any elements. In addition, it is possible to specify the density of the target, allowing gases, liquids, and porous materials to be considered.

The specific code used in this work was CYLTRAN. This code solves problems with cylindrical symmetry. The absorbing medium is defined as a disk of a certain radius and thickness, and the beam is specified as another disk that impinges on the surface of the absorber. A typical input stream includes information about target geometry, beam radius, beam energy, the number of case histories to be considered, and the number of times these case histories are to be run again to obtain good statistical information. Also, the minimum cut-off energy may be specified. This is the energy below which a trajectory is no longer monitored. This parameter is very important in practice, because having a larger cut-off greatly reduces the amount of computations required to arrive at an answer. There is a trade-off in accuracy, however, and this must be investigated by trial and error to see how much of an adverse effect results from too high a cut-off energy. The program also allows the target material to be sectioned into subzones. These subzones greatly improve the ability of the program to capture radial and axial variations in the energy deposition profile. These partitions may be thought of as bins, and accurate tallies are kept of energy and charge deposition in these subzones. Also, reflection and transmission information is calculated, and the energy losses associated with these processes are recorded.

The detail of the code is of great benefit in accurately capturing the electron - material interaction, but it must be used and interpreted carefully. In most of the work presented here, very little information from the output files is utilized. The basic issue associated with the use of the TIGER / ITS codes is that it provides too much information for the extent of process modeling presented in this work.

To better understand how the Monte Carlo output will produce the needed information, it is useful to consider the input geometry :

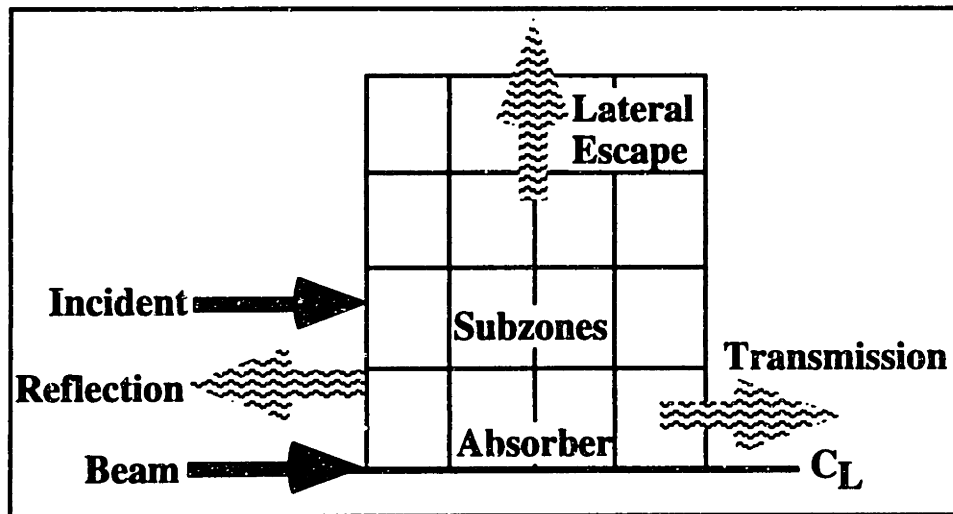


**FIGURE A.10**  
**Schematic of CYLTRAN Input Geometry**  
**and Various Calculated Energy Losses**

The output considers three loss terms : reflection, transmission, and lateral escape. These are shown in the figure above. The energy deposited in the subzones will be added up at each axial position, so that the total energy deposited as a function of penetration can be evaluated. The energy deposition is given in units of MeV per incident electron. This can be converted to joules, and upon multiplication by the beam current, the power deposited may be obtained. For use in this work, the only scaling necessary will be to convert the energy deposition profiles to dimensionless profiles. This can be done by dividing the CYLTRAN output by the incident source energy. Similarly, the reflected energy loss can be expressed as a fraction of the incident beam power, and the backscattering coefficient can thus be directly evaluated. For the purposes of the model presented in this work, only the range and stopping power as a function of incident electron energy will be relevant, and the details of the deposition profiles will not be considered. For both methods of calculating energy deposition presented here, numerical data for electron range and energy deposition are shown Appendix B. Using Spencer's data where applicable with supplemental information from CYLTRAN, source terms are generated for a wide variety of materials and beam energies.

### A.3. Electron Accelerators

This section will provide an overview of the different classes of electron devices in use for both commercial and experimental applications. Cathode materials and configurations will also be discussed. The three classes of accelerators used in this work will be described : single-shot Marx generator units, induction LINACs, and commercial DC machines. Also, magnetic focusing techniques and beam transport will be presented, and computer simulations of electron trajectories will be discussed.

#### A.3.1. Different Classes of Electron Accelerators

Electron beam devices must perform three specific tasks to successfully create a usable electron beam : beam generation, beam acceleration, and beam focusing / transport. The two main types of accelerators considered here are those based on electrostatic acceleration and those based on inductive acceleration. The difference may be simply understood by examining the mechanisms of particle acceleration in each case. Electrons will gain kinetic energy by passing through a region with electric field. This is generically indicated for a single particle by :

$$\Delta KE = e \int_c \vec{E} \cdot d\vec{s} \quad (\text{A.36})$$

where  $\Delta KE$  is the increase in kinetic energy of the electron,  $e$  is its charge, and  $\vec{E}(\vec{s}, t)$  is the electric field as a function of position and time. The path integral is to be evaluated along the particle trajectory. For electrostatic accelerators, this relation simply reduces to:

$$\Delta KE = e \cdot V_0 \quad (\text{A.37})$$

where  $V_0$  is the static potential difference across the acceleration region. Commercial EB welding machines are good examples of electrostatic accelerators. For accelerators using pulsed high voltage, the electrostatic approximation may be applied if the particle transit times and the electromagnetic wave propagation times are small compared to the pulselength [HUMPHRIES (1990)]. The Marx generator forms the basis for one kind of pulsed high voltage machine.

If the electric fields generated by time-varying magnetic fields are used in acceleration, then this type of accelerator is known as an induction accelerator. Here the basic expression is put in the form of Faraday's Law of Induction :

$$\int_c \vec{E} \cdot d\vec{s} = -\frac{1}{c} \int_s \frac{d\vec{B}}{dt} \cdot d\vec{A} \quad (\text{A.38})$$

where the flux change is evaluated over the cross-section of a toroidal core, and the path integral is again evaluated along the particle trajectory. The precise way in which flux changes in such cores produce beam acceleration will be discussed below. This type of beam acceleration forms the basis for the induction LINAC.

### A.3.2. Marx Generator-Based Accelerators

As an example of a pulsed high voltage generator, consider the Marx generator. These machines can produce truly gigantic pulses of high energy beam. The operating parameters of some of the largest ones are given below .

**TABLE A.5**  
**Operating Parameters of Some Very Large Pulsed Electron Beams**  
Adapted from MILLER (1982)

MACHINE	VOLTAGE	CURRENT	PULSE INTERVAL	POWER DURING PULSE
Aurora	14 MV	1600 kA	120 ns	22 TW
HERMES II	10 MV	100 kA	80 ns	1 TW
FX-100	8 MV	100 kA	120 ns	0.8 TW

A typical pulsed-power e-beam system has the following components:

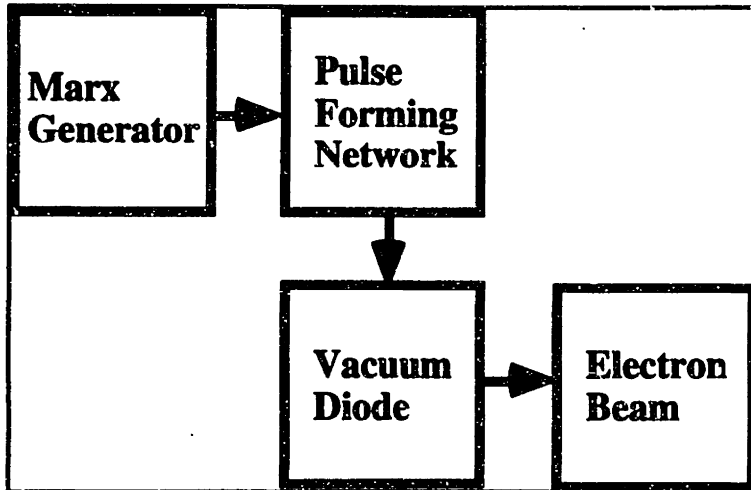


**FIGURE A.11**  
**Schematic of Pulsed High Voltage Electron Beam**  
**System Based on the Marx Generator**  
 Adapted from NATION (1979)

The basic principle of the Marx generator is fairly straightforward. The generator consists of capacitors that are charged in parallel and discharged in series. The schematic circuit diagram is shown below :

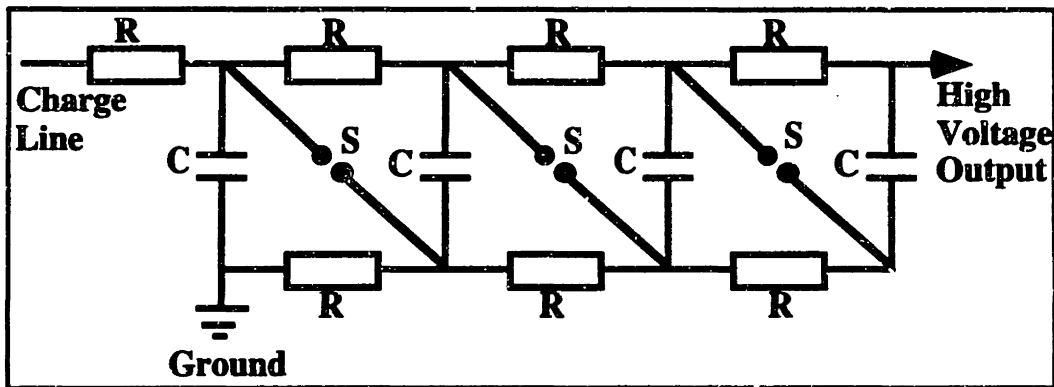


**FIGURE A.12**  
**Schematic Circuit of Marx Generator**  
 Adapted from MILLER (1982)

The switches S are sparkgaps across which controlled electrical discharges are the means for connecting the capacitors in series. The process of triggering the Marx is known as "erecting the voltage." There are also "self-erecting" Marx generators where only the first spark gap need be triggered. The remaining gaps will trigger themselves. This is possible because of the relationship between the stray capacitances across each gap and the coupling capacitance between every two gaps. This principle is illustrated below :

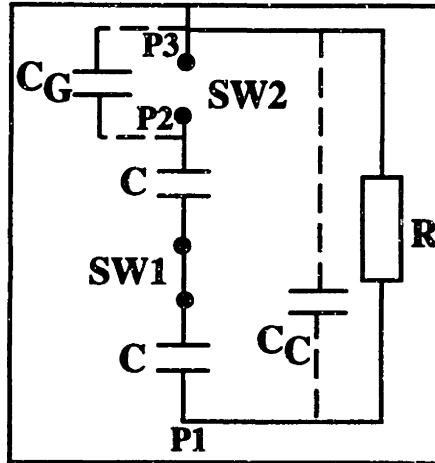


**FIGURE A.13**  
**Self-Erecting Marx Configuration**  
 Adapted from MILLER (1982)

In the figure above, only two stages of the Marx are shown. Suppose the switch SW1 fires. Suppose also that the spark gap SW2 is set so that it can withstand a voltage  $V_0 < V < 2V_0$ , where  $V_0$  is the voltage on the capacitors C. The arrangement of  $C_C$  and  $C_G$  act as a voltage divider, so that if the voltage at P2 is the voltage at P1 plus  $2V_0$ , and the voltage across the gap SW2 is given by :

$$V_{P2} = V_{P1} + 2V_0 \quad \text{and}$$

$$V_{SW2} = 2V_0 \cdot \frac{C_C}{C_C + C_G} < 2V_0 \quad (\text{A.39})$$

This potential difference is discharged however, and the RC-time constant is given by  $RC_C$ . When this potential difference discharges, the new potential difference will simply be  $2V_0$ , which will be sufficient to trigger the spark gap SW2, and thus continue the triggering. Typically, a Marx will fully trigger in about  $1 \mu\text{s}$  (NATION, 1979).

The pulse is then sent to a PFN, or pulse forming network. This may be thought of as basically a transmission line which shortens the duration of the pulse (pulse compression). The PFN will produce a fast-rising, short, low impedance pulse suitable for intense electron beam generation [NATION (1979)]. A detailed consideration of how PFNs work will not be given here. An excellent overview of this topic may be found in HUMPHRIES (1986).

The vacuum diode forms the last part of the schematic high voltage pulsed power e-beam machine shown in Figure A.11. There are several types of diodes, and these will be discussed at greater length in the section below. By convention in particle physics, the emitting surface is called the cathode, and the opposite electrode is the anode. For beams, the anode will be annular or will otherwise have a passage in it to allow the beam to propagate beyond the vacuum diode assembly.

### A.3.3. Induction LINACs (Linear Accelerators)

Induction accelerators utilize the change in magnetic flux in a ferrite core to create an electric field across an accelerating gap. The concept was originally adapted from circular betatrons for use with LINACs [CHRISTOFILOS et al (1964)]. The basic principle is illustrated in Figure A.14 below. This figure shows a single induction cell. The basic construction is that of a toroidal cavity with an inner and outer conductor. There is an acceleration gap as shown in Figure A.14. The inner conductor envelops a toroidal ferrite core. Imagine a high voltage pulse coming in on the power line. The inner conductor gets charged, and the ferrite greatly increases the inductance of the toroidal cavity. This dramatically reduces the leakage current that flows from inner to outer conductor, and creates an electric potential difference across the acceleration gap. A beam present in the gap will thus experience an increase in kinetic energy. Once a certain region of the beam passes out of the acceleration gap, it will propagate without seeing any electric fields until it encounters the next acceleration gap. In this way, the beam energy may be sequentially stepped up to very high energies. One of the HEEB accelerators used in this work, SNOMAD IV, is a linear induction accelerator.

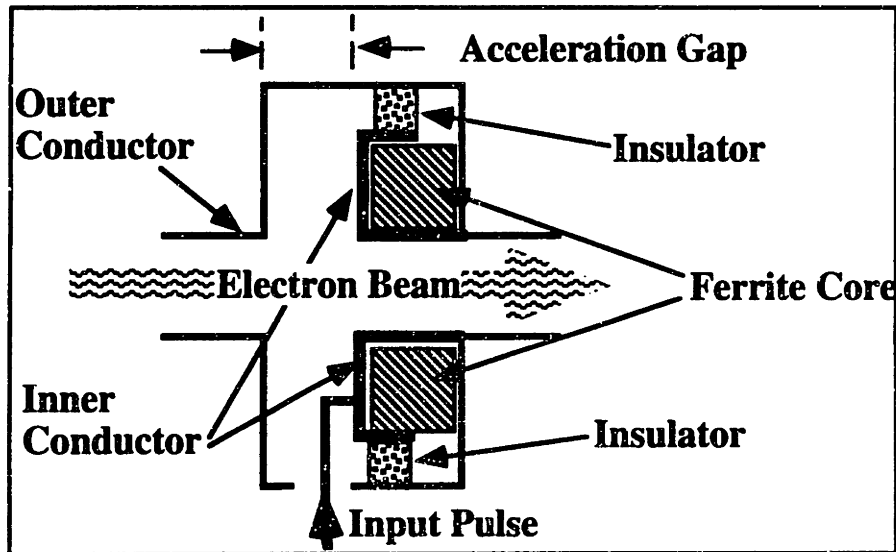


**FIGURE A.14**  
**Schematic of an Induction LINAC Acceleration Cell**  
**Adapted from HUMPHRIES (1986)**

As pointed out by HUMPHRIES (1986), the only function of the ferrite core is to greatly increase the inductance of the toroidal acceleration cavity. If this were not the case, the inductance would be so low that the acceleration pulse would not be able to sustain a great enough potential difference for a sufficient period of time to allow for electron acceleration.

### A.3.4. Conventional EB Welding Machines

Conventional EB technology is well-established in many commercial processes for welding and melting. A schematic of a vacuum EB welder is shown below.

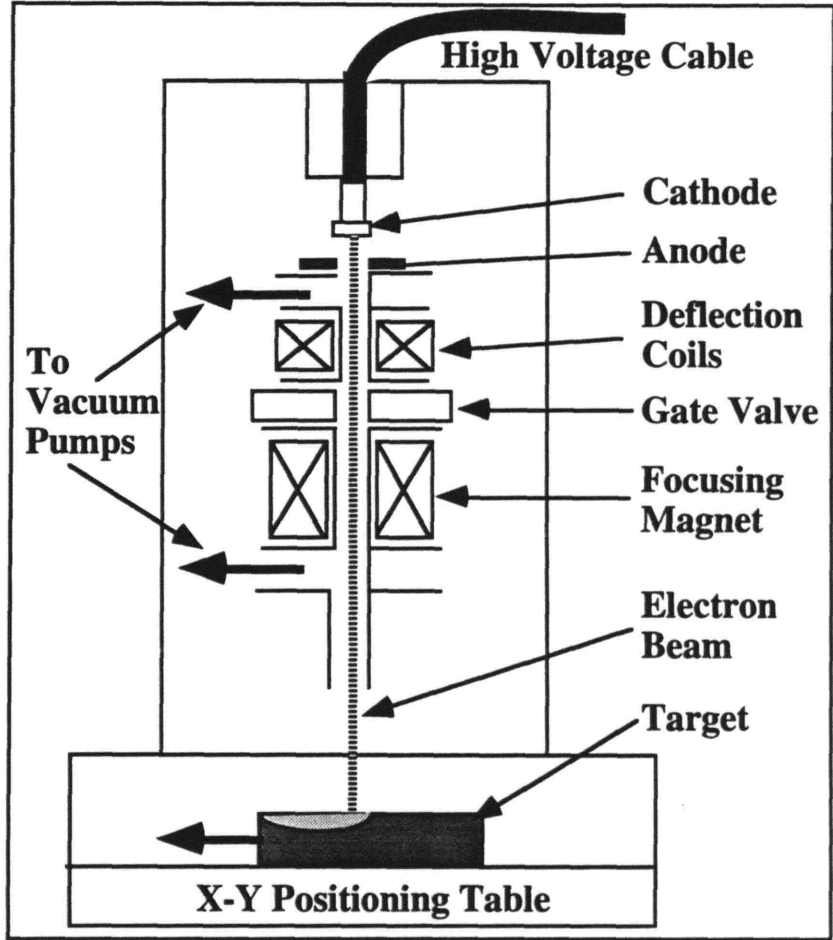


**FIGURE A.15**  
Schematic of Conventional EB Welder  
LaFLAMME (1994)

**TABLE A.6**  
Typical Operating Parameters of Conventional EB Welders

QUANTITY	VALUE
Current	0.5 - 1500 mA
Voltage	30 - 200 kV
Average Power	0 - 100 kW



The typical operating parameters of EB Welders are shown in the table above. The unit used for experiments in this work ran at a voltage of approx. 150 kV and a beam current of 10 - 50 mA. The range of powers used was therefore 1500 W - 7500 W. typical table travel speeds were 30 - 200 inches / min. The scan geometry is discussed below.

The scanning capabilities of low energy EB welding machines are extensive. Deflection coils along the acceleration column allow for beam scanning and beam rastering, and the X-Y table movement allows for target positioning. Typical table travel speeds can be as high as 250 - 1000 inches / min. The focus size of the beam can be quite small, and beam diameters of tens of  $\mu\text{m}$  are possible. The size of the interaction region on the target piece will of course be considerably larger. The fine spot may also be magnetically deflected into various patterns. Some typical scans based on circular patterns are shown below. Lines are also possible, as are rectangular regions.

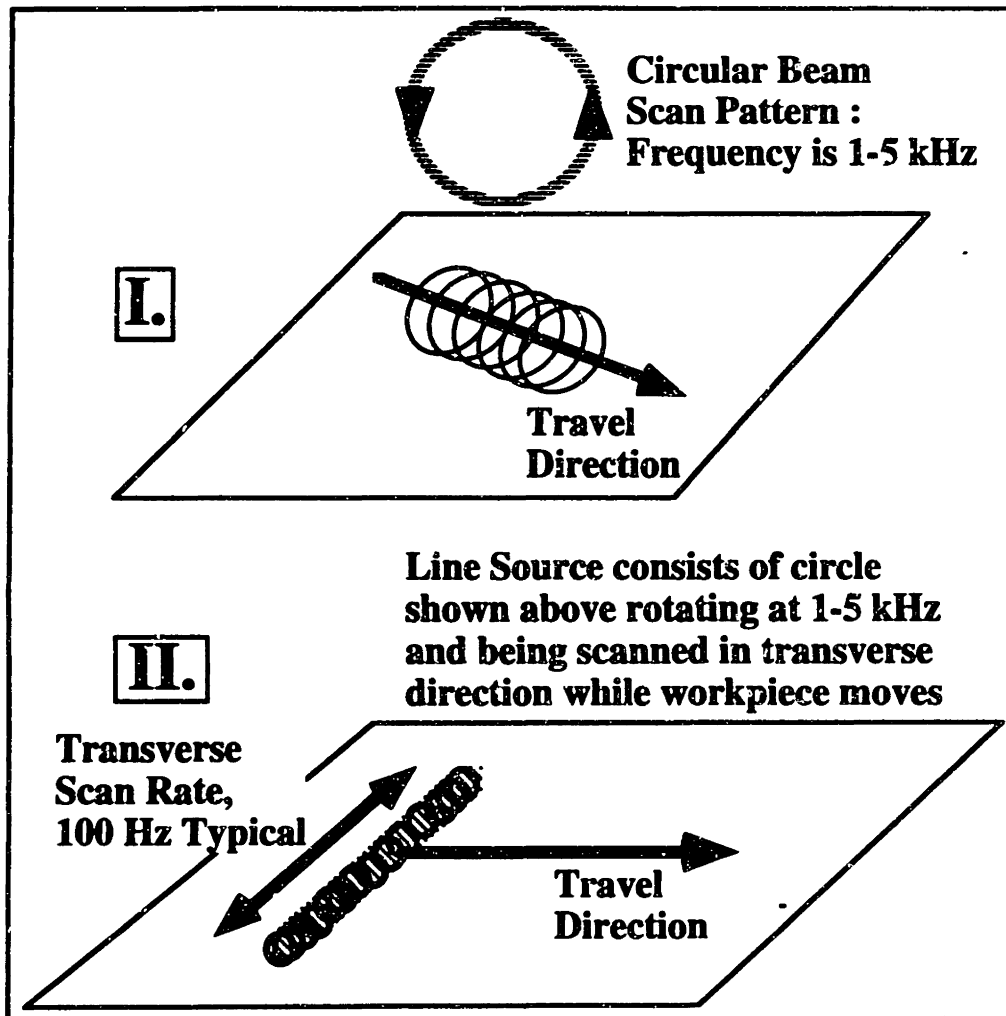


**FIGURE A.16**  
Some Possible Scan Patterns for EB Welders  
LaFLAMME (1994)

## A.4 Cathodes

As mentioned earlier, the cathode will always refer to the source of the charged particles, irrespective of the sign of these particles. In this section, we will be mainly concerned with cathodes that generate electrons. The cathode will then form half of the vacuum diode, which is the basis for electron beam generation, or launching.

There are several types of cathodes, each with different electron emission characteristics. The two that will be discussed here are the plasma cathode and the dispenser cathode. For the work done on EB welders, tungsten filament cathodes were also used, and these are very similar to those found in electron microscopes. Such cathodes are not suitable for high intensity HEEB generation. The induction LINAC SNOMAD IV uses a dispenser cathode, and the Marx-based machine used in this work relies upon a plasma (or explosive emission) cathode.

### A.4.1. Thermionic Cathodes

Thermionic emission has been the subject of study for over a century or so, and there are many excellent accounts of the historical development of the present-day theory [NOTTINGHAM( 1958)]. Only a very brief outline will be given here. The basic physics of thermionic emission will be discussed, and the technology of the dispenser cathode will be presented.

The first observations of electrons leaving heated filaments was made by Edison. The initial observations were actually a composite phenomenon, and not true thermionic emission. Richardson [RICHARDSON (1902) and (1912)] was the first to introduce the concept of the work function, or the energy required to remove an electron from the surface of a metal. His first quantitative description of thermionic emission was based of purely classical physics, and is therefore not correct. Richardson's second expression was derived on the basis of general thermodynamic arguments [RICHARDSON (1912)], and can also be explained by the theory of quantum statistics [DUSHMAN (1923)]. This equation has the form:

$$I = A_0 \cdot T^2 \cdot \exp\left[\frac{-\phi}{kT}\right] \quad (\text{A.40})$$

where  $\phi$  is the true work function

This equation is often directly applied to experimental data to obtain numerical correlations, but as pointed out by NOTTINGHAM (1958), this practice is not strictly correct. The so - called "Richardson Plot" is a plot that schematically looks like this :

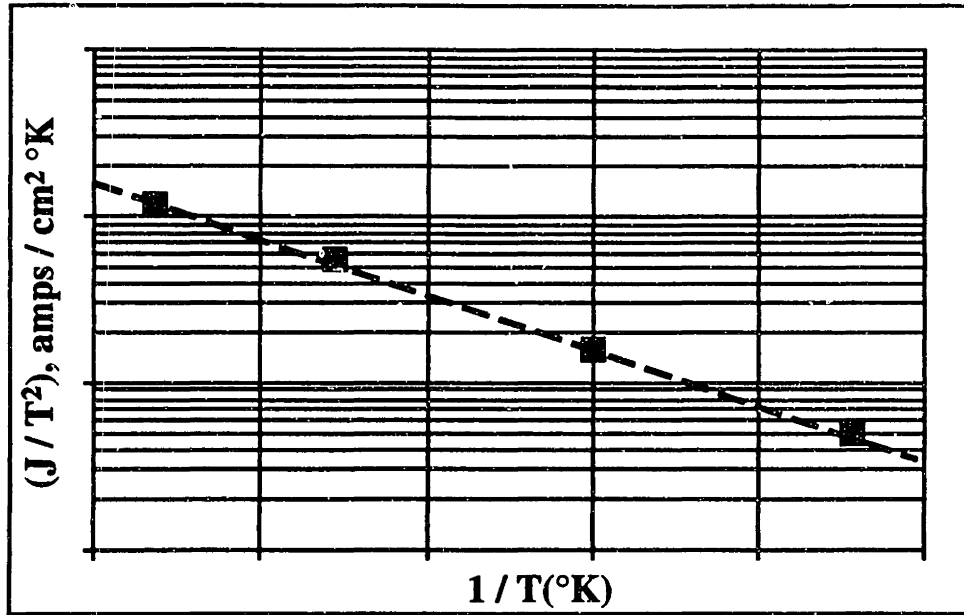
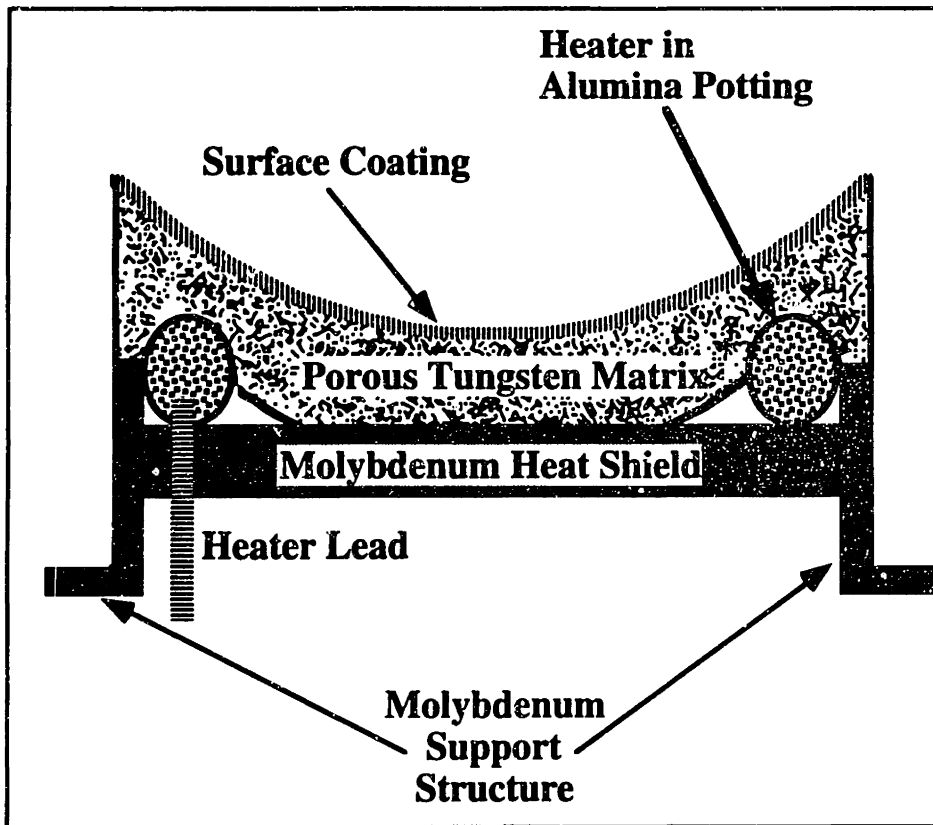


**FIGURE A.17**  
**Schematic "Richardson Plot"**

The type of cathode used in the SNOMAD IV system is a dispenser cathode. A schematic of such a cathode is shown below.



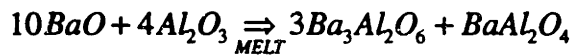
(shown above)

**FIGURE A.18**

**Schematic of a Dispenser Cathode : View of Cross - Section  
Adapted from ANONYMOUS (1977)**

The basic design of the dispenser cathode was established about fifty years ago [HULL (1939), LEMMENS, JANSEN, and LOOSJES (1950), & LEVI (1953)]. The original design consisted of a porous tungsten matrix "stuffed" with  $5BaO \cdot 2Al_2O_3$ . The mechanism of cathode operation relies on the decomposition of the Barium Aluminate compound to release gaseous Barium according to the following reactions [RITTNER, RUTLEGDE, and AHLERT (1957)].

First, there are the solidification products resulting from melting  $5BaO \cdot 2Al_2O_3$  and resolidifying it within the Tungsten matrix (impregnation process) :



Then there is the following decomposition reaction

(activation process) : (A.41)



OR



The barium then migrates to the surface of the cathode by diffusion and Knudsen flow through the porous Tungsten network. The surface of the cathode is often coated with various layers, such as Osmium and/or Ruthenium, or alloys of these materials. The surface then becomes a very "complex composite" [NOTTINGHAM (1958)] emission surface. There are many variations on the theme of the dispenser cathode, each designed for a specific application. Emission levels as high as 20-50 amps / sq. cm are possible with suitable choice of coatings and high (1100 °C) operating temperatures.

#### **A.4.2. Plasma or Explosive Emission Cathodes**

For emission levels that are substantially higher than those available from dispenser-type cathodes, plasma (explosive) emission cathodes must be used. The basis of the plasma cathode is the field intensification that occurs surrounding microscopic whiskers on the surface of the cathode material. This field enhancement can be as high as a factor of several hundred over the macroscopic field [MILLER (1982)].

When a high voltage is applied to the such a cathode surface, emission occurs from the tips of these "whiskers." The individual bursts of electron emission from adjacent whiskers combine until the entire surface of the cathode is

covered in a rapidly expanding plasma. This burst can be quite intense, since the current density associated with the individual whiskers is as high as  $10^7$  amps/sq. cm. The overall current density will be much lower, since the area of the whiskers is quite small, and their number density on a surface is typically on the order of 10 to 10,000 per sq. cm. The surface of a plasma cathode is schematically shown below.

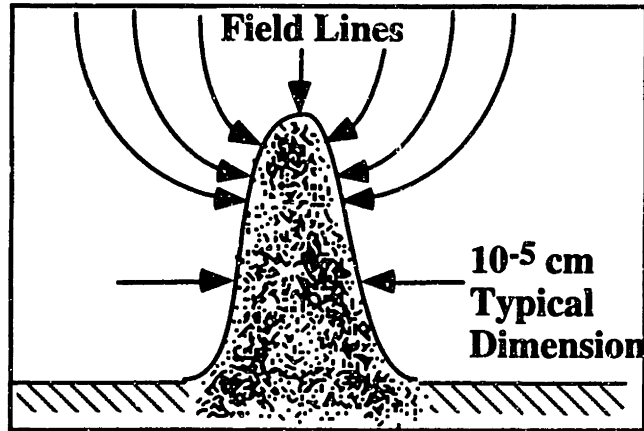


**FIGURE A.19**  
**Surface "Whisker" on a Plasma Cathode**  
 Adapted from MILLER (1982)

The following table compares the current densities that can be expected from various types of cathodes.

**TABLE A.7**  
**Current Densities for Different Types of Cathodes**  
 Adapted from TURNMAN, MAZARAKIS, and NEAU (1992)

Cathode Type	Current Density, amps / sq. cm
Tungsten metal	1 - 10
Thermionic (other than dispenser)	10 - 20
Dispenser	10 - 35
Explosive Emission	100 - 1000

It is seen that high current densities are obtainable from plasma - type cathodes. The main disadvantage of these cathodes is that they have a relatively limited life and have a practical repetition rate limit of about 50 pulses per second. They have considerable advantages over thermionic cathodes in that they do not require high vacuum conditions are practically insensitive to oxidation and contamination. The choice of cathode depends on the specific functional requirements of the system under consideration, and there are design tradeoffs in selecting the right system for the right application.

### A.4.3. Electron Guns - Vacuum Diodes

Irrespective of the choice of cathode, the cathode - anode combination may be considered as a vacuum diode. The anode will typically be annular to allow the beam to be launched beyond the initial acceleration region. This is referred to as "beam injection." There are two main factors that can determine the current flowing in a vacuum diode : emission limits or the space-charge limits. If the current is emission limited, then field effects due to the charge present in the space between the anode and cathode are not important, and the current is basically given by the appropriate relation describing emission for that given cathode. If space-charge effects are important, as is the case with most all HEEBs, then a relationship can be derived between the diode current and the voltage across the diode that depends only on the geometry of the diode and the value of the accelerating potential. This relation is often referred to as the Child - Langmuir Law [LANGMUIR and BLODGET (1924)]. This relation can be derived directly from Poisson's Equation for a diode of planar geometry :

$$\frac{d^2\phi}{dz^2} = \frac{nq}{\epsilon_0}$$

$$nq\beta c = i, \text{ where } \beta \equiv v/c, \text{ and} \quad (\text{A.42})$$

$n$  is the particle density.

If the relativistic energy factor is introduced, the equation becomes :

$$\gamma \equiv \frac{E_{TOTAL}}{m_0c^2}, \quad \gamma = 1 + \phi/\phi_0, \text{ where } \phi_0 = \frac{-m_0c^2}{q}$$

The equation becomes : (A.43)

$$\frac{d^2\gamma}{dz^2} = \frac{q}{\epsilon_0 m_0 c^2} \cdot \frac{i\gamma}{\sqrt{(\gamma^2 - 1)}}$$

This equation has the solution :

$$iz^2 = \frac{\epsilon_0 m_0 c^3}{2q} \left( \int_1^\gamma \frac{d\gamma}{(\gamma^2 - 1)^{3/4}} \right)^2$$

In the non - relativistic limit, the solution is : (A.44)

$$\frac{iz^2}{\phi^{3/2}} = \frac{4\sqrt{2}\epsilon_0\sqrt{q}}{9\sqrt{m_0}} = const. = 2.34 \times 10^{-6} \frac{\text{amps}}{\text{V}^{3/2}}$$

The non-relativistic limit shown above is usually called Child's Law for a planar diode. The noteworthy feature is the functional relationship between the current  $i$  and the voltage  $\phi$ . This relation basically establishes the I-V characteristic of the diode for conditions of space-charge limited current. The relationships implied by the Child - Langmuir Law are written in a clearer form below :

$$(\text{diode current}) \propto \frac{(\text{voltage across diode})^{3/2}}{(\text{A - K gap})^2}$$

where the A - K gap refers to the spacing (A.45)  
between the cathode and the anode.

To a good approximation, the SRL diode has the following experimentally-determined I-V characteristic :

$$I(\text{amps}) = K \cdot V^{3/2}(\text{volts})$$

$$K \approx 2.0 \times 10^{-6}$$
(A.46)

The quantity K is known as the perveance of the diode [SEPTIER (1967)].

## A.5 Beam Optics - Focusing and Transport of Electron Beams

After a beam has been launched at some kinetic energy, a beam optics system is necessary to insure delivery of the beam with the desired parameters. Beam focusing and transport can be accomplished electrostatically or magnetically. Typically, the electrostatic portion of the focusing is within the electron gun itself.

The behavior of electron beams under the influence of various electric and magnetic fields can be represented several ways. One commonly used approach for systems with axial symmetry is the paraxial ray equation [SEPTIER (1967)]. The equation is known as paraxial because it holds for particle trajectories near the axis and for situations in which the axial field components of magnetic and electric fields are independent of  $r$  and that radial components are proportional to  $r$  [SEPTIER (1967)]. The coordinate system to be used is shown below :

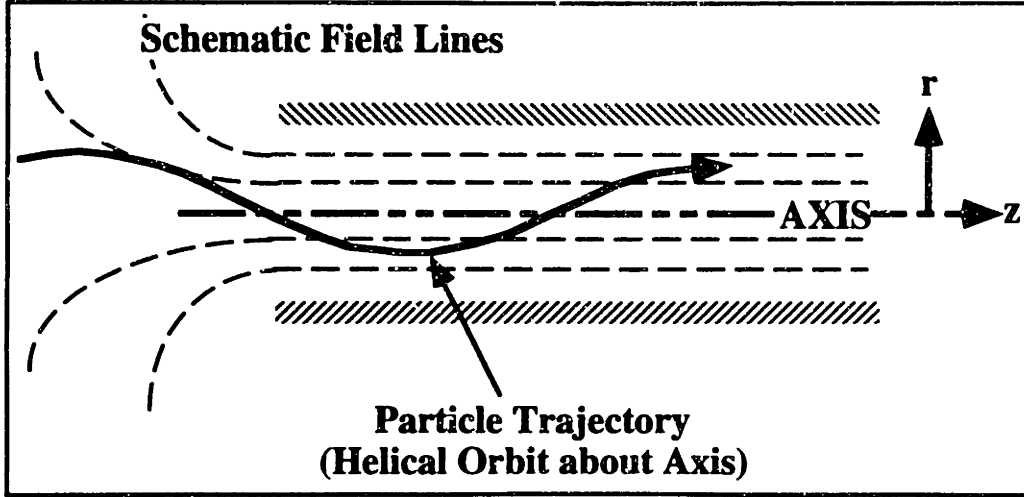


**FIGURE A.20**  
**Coordinate System for Paraxial Ray Approximation**

The details of the derivation of the paraxial ray approximation will not be presented here, but the final result may be written as [HUMPHRIES (1986)] :

$$a'' + \frac{\Omega_L^2}{\beta^2 c^2} \cdot a - \left( \frac{P_\theta}{\beta \gamma m_0 c} \right)^2 \cdot \frac{1}{a^3} - \frac{K}{a} = 0$$

$a$  is the beam envelope (outermost trajectory),

$\beta$  is the relativistic factor  $v/c$ ,

$\gamma$  is the relativistic factor  $\gamma = 1/\sqrt{(1-\beta^2)}$ ,

$\Omega_L$  is the Larmor Frequency,  $\Omega_L = -\frac{qB_z}{2\gamma m_0}$ ,

this is the angular velocity with which the particle moves in a helical orbit about the axis,

$P_\theta$  is the Canonical Angular Momentum,

$P_\theta(a) = qaA_\theta + \gamma m_0 a^2 \dot{\theta}$ , where  $A_\theta$  is the azimuthal component of the vector potential (of the magnetic field), (A.47)

and  $K$  is a constant that takes into account the self - field

of the beam,  $K = \left( \frac{a\Omega_L}{\beta c} \right)^2$

Another approach to the beam transport problem is to solve the equations of motion for a relativistic electron moving through a region with electric and magnetic fields. Some portion of the electric field is due to the self-field of the beam itself. An in-depth treatment of this approach is beyond the scope of this



introduction and will not be given here. This approach generally requires a numerical finite difference solution strategy. There are several programs that solve this problem, and the one used for this work was EGUN [HERMANNSELDT (1988)]. EGUN handles the precise geometry of the problem, including e-beam gun geometry (vacuum diode) and subsequent chamber geometry as well. Although the details of this code will not be discussed here, it was a valuable tool in the optimization of the magnetic focusing arrangement for much of the work done on SRL's SNOMAD IV.

## APPENDIX B

### Electron Energy Deposition and Source Terms for Thermal Models

#### B.1 Source Term Information

As mentioned in Appendix A, both the SPENCER NBS - 1 report and Monte Carlo techniques were used to determine necessary data in order to construct an electron beam heat source term. In this Appendix, both source term and backscattering information will be calculated. The source term is given by :

Source Strength :

constant volumetric strength  $A_0$  in  $\text{W}/\text{cm}^3$

Source Geometry :

right circular cylinder embedded into surface of  
workpiece (assumed to be a semi - infinite solid)  
height is  $\kappa R$ , where  $R$  is the electron range in cm,  
radius is  $r_B$ , which is the Gaussian radius in cm,

$A_0 = \frac{P_A}{\kappa \pi r_B^2 R}$ , where  $P_A$  is the power absorbed by the

workpiece in  $W$ , and

$\kappa = \frac{E_0}{r_0 \cdot (dE/dr)_{E_0}}$ , where  $E_0$  is the initial source energy in MeV, (B.1)

$r_0$  is the residual range at the initial source energy in  $\text{g}/\text{cm}^2$ , and

$(dE/dr)_{E_0}$  is the stopping power at the initial source energy in  $\text{MeV} - \text{cm}^2/\text{g}$

**TABLE B.1**  
**Energy Deposition Information for Aluminum**  
 adapted from SPENCER (1959)

Incident Electron Energy, MeV	Stopping Power, MeV-cm <sup>2</sup> /g	Residual Range, g / cm <sup>2</sup>	Range in cm assuming $\rho = 2.7 \text{ g / cc}$	value of kappa, $\kappa$
0.1	3.24	0.0183	0.0068	1.6866
0.2	2.22	0.0570	0.0211	1.5805
0.4	1.72	0.1620	0.0600	1.4355
0.7	1.55	0.3490	0.1293	1.2940
1	1.51	0.5450	0.2019	1.2151
2	1.51	1.2100	0.4481	1.0946
4	1.56	2.5100	0.9296	1.0216

**TABLE B.2**  
**Energy Deposition Information for Copper**  
 adapted from SPENCER (1959)

Incident Electron Energy, MeV	Stopping Power, MeV-cm <sup>2</sup> /g	Residual Range, g / cm <sup>2</sup>	Range in cm assuming $\rho = 8.92 \text{ g / cc}$	value of kappa, $\kappa$
0.1	2.7200	0.0221	0.0025	1.6636
0.2	1.8900	0.0678	0.0076	1.5608
0.4	1.4700	0.1910	0.0214	1.4247
0.7	1.3300	0.4090	0.0459	1.2868
1	1.2900	0.6390	0.0716	1.2131
2	1.3000	1.4200	0.1592	1.0834
4	1.3600	2.9200	0.3274	1.0073

**TABLE B.3**  
**Energy Deposition Information for Iron**  
 Calculated using TIGER / ITS Codes

Incident Electron Energy, MeV	Stopping Power, MeV-cm <sup>2</sup> /g	Residual Range, g / cm <sup>2</sup>	Range in cm assuming $\rho = 7.86 \text{ g / cc}$	value of kappa, $\kappa$
0.1	2.8960	0.0200	0.0025	1.7239
0.2	1.9610	0.0660	0.0084	1.5453
0.4	1.5440	0.1851	0.0235	1.3996
0.7	1.4060	0.3736	0.0475	1.3326
1	1.3710	0.6066	0.0772	1.2024
2	1.4160	1.3280	0.1690	1.0636
4	1.5710	2.6690	0.3396	0.9540

**TABLE B.4**  
**Energy Deposition Information for Titanium**  
**Calculated using TIGER / ITS Codes**

<b>Incident Electron Energy, MeV</b>	<b>Stopping Power, MeV-cm<sup>2</sup>/g</b>	<b>Residual Range, g / cm<sup>2</sup></b>	<b>Range in cm assuming <math>\rho = 4.51 \text{ g / cc}</math></b>	<b>Value of Kappa, <math>\kappa</math></b>
0.1	2.8495	0.0213	0.0047	1.6468
0.2	1.9735	0.0654	0.0145	1.5499
0.4	1.5485	0.1840	0.0408	1.4039
0.7	1.4030	0.3928	0.0871	1.2702
1	1.3740	0.6043	0.1340	1.2044
2	1.4150	1.3250	0.2938	1.0667
4	1.5570	2.6720	0.5925	0.9615

**TABLE B.5**  
**Energy Deposition Information for 304 Stainless Steel**  
**Calculated using TIGER / ITS Codes**

<b>Incident Electron Energy, MeV</b>	<b>Stopping Power, MeV-cm<sup>2</sup>/g</b>	<b>Residual Range, g / cm<sup>2</sup></b>	<b>Range in cm assuming <math>\rho = 8.0 \text{ g / cc}</math></b>	<b>value of kappa, <math>\kappa</math></b>
0.1	2.8320	0.0215	0.0027	1.6420
0.2	1.9660	0.0658	0.0082	1.5463
0.4	1.5475	0.1847	0.0231	1.3998
0.7	1.4010	0.3935	0.0492	1.2697
1	1.3730	0.6053	0.0757	1.2033
2	1.4170	1.3260	0.1658	1.0644
4	1.5700	2.6670	0.3334	0.9553

**TABLE B.6**  
**Energy Deposition Information for Monel Alloy 400**  
**Calculated using TIGER / ITS Codes**

<b>Incident Electron Energy, MeV</b>	<b>Stopping Power, MeV-cm<sup>2</sup>/g</b>	<b>Residual Range, g / cm<sup>2</sup></b>	<b>Range in cm assuming <math>\rho = 8.8 \text{ g / cc}</math></b>	<b>value of kappa, <math>\kappa</math></b>
0.1	2.8185	0.0216	0.0025	1.6392
0.2	1.9615	0.0608	0.0069	1.6770
0.4	1.5470	0.1851	0.0210	1.3969
0.7	1.4040	0.3939	0.0448	1.2657
1	1.3770	0.6052	0.0688	1.2000
2	1.4270	1.3220	0.1502	1.0602
4	1.5910	2.6490	0.3010	0.9491

**TABLE B.7**  
**Energy Deposition Information for Alloy HA-188**  
**Calculated using TIGER / ITS Codes**

<b>Incident Electron Energy, MeV</b>	<b>Stopping Power, MeV-cm<sup>2</sup>/g</b>	<b>Residual Range, g / cm<sup>2</sup></b>	<b>Range in cm assuming <math>\rho = 9.1 \text{ g / cc}</math></b>	<b>value of kappa, <math>\kappa</math></b>
0.1	2.7055	0.0226	0.0025	1.6362
0.2	1.8855	0.0688	0.0076	1.5409
0.4	1.4900	0.1925	0.0212	1.3946
0.7	1.3570	0.4089	0.0449	1.2615
1	1.3340	0.6273	0.0689	1.1950
2	1.3890	1.3660	0.1501	1.0541
4	1.5600	2.7240	0.2993	0.9413

**TABLE B.8**  
**Energy Deposition Information for Alloy INCONEL 718**  
**Calculated using TIGER / ITS Codes**

<b>Incident Electron Energy, MeV</b>	<b>Stopping Power, MeV-cm<sup>2</sup>/g</b>	<b>Residual Range, g / cm<sup>2</sup></b>	<b>Range in cm assuming <math>\rho = 8.2 \text{ g / cc}</math></b>	<b>value of kappa, <math>\kappa</math></b>
0.1	2.8190	0.0216	0.0026	1.6396
0.2	1.9605	0.0661	0.0081	1.5438
0.4	1.5450	0.1852	0.0226	1.3979
0.7	1.4030	0.3942	0.0481	1.2657
1	1.3760	0.6056	0.0739	1.2000
2	1.4250	1.3230	0.1613	1.0609
4	1.5880	2.6530	0.3235	0.9495

**TABLE B.9**  
**Energy Deposition Information for Alloy RENÉ 95**  
**Calculated using TIGER / ITS Codes**

<b>Incident Electron Energy, MeV</b>	<b>Stopping Power, MeV-cm<sup>2</sup>/g</b>	<b>Residual Range, g / cm<sup>2</sup></b>	<b>Range in cm assuming <math>\rho = 8.2 \text{ g / cc}</math></b>	<b>value of kappa, <math>\kappa</math></b>
0.1	2.8070	0.0217	0.0027	1.6391
0.2	1.9530	0.0664	0.0081	1.5434
0.4	1.5405	0.1859	0.0227	1.3971
0.7	1.3990	0.3954	0.0482	1.2654
1	1.3730	0.6073	0.0741	1.1993
2	1.4240	1.3260	0.1617	1.0592
4	1.5900	2.6550	0.3238	0.9475

## B.2 Backscattering Information

The following data was calculated using the TIGER / ITS codes. Both the absorbed current and power are shown.

**TABLE B.10**  
Backscattering Information,  
Material Is Aluminum

Incident Energy, MeV	Current Fraction Absorbed	Energy Absorbed, MeV	Energy Fraction Absorbed
0.1	0.873	0.093	0.928
0.2	0.869	0.186	0.929
0.4	0.892	0.377	0.943
0.7	0.892	0.662	0.945
1.0	0.912	0.957	0.957
2.0	0.941	1.935	0.968
4.0	0.964	3.882	0.970

**TABLE B.11**  
Backscattering Information,  
Material Is Titanium

Incident Energy, MeV	Current Fraction Absorbed	Energy Absorbed, MeV	Energy Fraction Absorbed
0.1	0.775	0.086	0.857
0.2	0.776	0.172	0.861
0.4	0.796	0.352	0.881
0.7	0.809	0.622	0.889
1.0	0.829	0.902	0.902
2.0	0.874	1.854	0.927
4.0	0.924	3.752	0.938

**TABLE B.12**  
Backscattering Information,  
Material is 304 Stainless Steel

Incident Energy, MeV	Current Fraction Absorbed	Energy Absorbed, MeV	Energy Fraction Absorbed
0.1	0.753	0.083	0.831
0.2	0.754	0.168	0.842
0.4	0.764	0.342	0.855
0.7	0.778	0.606	0.865
1.0	0.805	0.887	0.887
2.0	0.846	1.817	0.909
4.0	0.906	3.686	0.922

**TABLE B.13**  
**Backscattering Information,**  
**Material is Monel 400**

<b>Incident Energy, MeV</b>	<b>Current Fraction Absorbed</b>	<b>Energy Absorbed, MeV</b>	<b>Energy Fraction Absorbed</b>
0.1	0.722	0.081	0.813
0.2	0.731	0.165	0.825
0.4	0.740	0.334	0.835
0.7	0.764	0.599	0.855
1.0	0.780	0.866	0.866
2.0	0.827	1.789	0.895
4.0	0.897	3.672	0.918

The results for copper will be very similar to those for Monel 400, since the absorbed fraction will depend on target density and atomic number.

## Appendix C Results of Thermal Calculations

**TABLE C.1  
Thermophysical Data**

Material	Density, g / cu. cm	Melting Point, °C	Boiling Point, °C	Specific Heat, J / g°-C	Thermal Cond. , W / cm - °C
Aluminum	2.7	660	2520	1.08	2.38
Copper	8.9	1083	2560	0.427	3.41
Iron	7.9	1536	2860	0.791	0.297
Titanium	4.5	1667	3285	0.682	0.13
304 SS	8.0	1427	-----	0.50	0.215

**TABLE C.2  
Absorbed Power (W) Needed To Initiate  
Surface Melt in Aluminum : 0.1 MeV**

Beam Radius, cm	Travel Velocity, cm / s						
	0	0.1	0.5	1	5	10	50
0.15	871	876	895	918	1097	1305	2565
0.25	1428	1441	1491	1552	2015	2522	5277
0.35	1985	2009	2106	2224	3082	3978	8556
0.50	2820	2869	3063	3298	4933	6545	14353
0.75	4212	4322	4749	5260	8601	11682	25960

**TABLE C.3  
Absorbed Power (W) Needed To Initiate  
Surface Melt in Aluminum : 0.2 MeV**

Beam Radius, cm	Travel Velocity, cm / s						
	0	0.1	0.5	1	5	10	50
0.15	939	945	967	994	1207	1462	3184
0.25	1496	1510	1565	1634	2153	2740	6242
0.35	2053	2079	2183	2310	3249	4258	9863
0.50	2889	2940	3144	3392	5145	6920	16165
0.75	4281	4394	4836	5367	8890	12217	28605



**TABLE C.4**  
**Absorbed Power (W) Needed To Initiate**  
**Surface Melt in Aluminum : 0.4 MeV**

Beam Radius, cm	Travel Velocity, cm / s						
	0	0.1	0.5	1	5	10	50
0.15	1101	1108	1138	1176	1483	1874	5073
0.25	1660	1677	1745	1830	2502	3310	9121
0.35	2218	2248	2369	2520	3672	4989	13683
0.50	3053	3111	3339	3621	5680	7892	21351
0.75	4446	4568	5048	5628	9615	13590	35994

**TABLE C.5**  
**Absorbed Power (W) Needed To Initiate**  
**Surface Melt in Aluminum : 1.0 MeV**

Beam Radius, cm	Travel Velocity, cm / s						
	0	0.1	0.5	1	5	10	50
0.15	1562	1577	1639	1716	2393	3347	12672
0.25	2137	2165	2280	2425	3673	5381	21061
0.35	2702	2747	2929	3161	5097	7637	29635
0.50	3543	3621	3933	4326	7483	11385	42895
0.75	4939	5090	5692	6437	12046	18451	66155

**TABLE C.6**  
**Absorbed Power (W) Needed To Initiate**  
**Surface Melt in Aluminum : 2.0 MeV**

Beam Radius, cm	Travel Velocity, cm / s						
	0	0.1	0.5	1	5	10	50
0.15	2212	2242	2366	2525	3955	6031	25292
0.25	2829	2878	3081	3344	5751	9291	41852
0.35	3415	3487	3783	4167	7664	12723	58475
0.50	4274	4387	4850	5447	10759	18149	83468
0.75	5684	5885	6698	7737	16463	27846	125293

**TABLE C.7**  
**Absorbed Power (W) Needed To Initiate**  
**Surface Melt in Aluminum : 4.0 MeV**

Beam Radius, cm	Travel Velocity, cm / s						
	0	0.1	0.5	1	5	10	50
0.15	3308	3376	3653	4011	7171	11486	48974
0.25	4018	4118	4532	5074	10174	17514	81035
0.35	4661	4796	5357	6098	13254	23707	113215
0.50	5572	5765	6570	7641	18049	33195	161554
0.75	7029	7337	8619	10322	26467	49363	242186

**TABLE C.8**  
**Absorbed Power (W) Needed To Initiate**  
**Surface Melt in Copper : 0.1 MeV**

Beam Radius, cm	Travel Velocity, cm / s						
	0	0.1	0.5	1	5	10	50
0.15	1994	2004	2042	2089	2454	2875	5369
0.25	3304	3330	3434	3563	4526	5583	11222
0.35	4613	4664	4866	5115	6926	8822	18352
0.50	6576	6680	7090	7588	11078	14535	31021
0.75	9849	10082	10992	12084	19295	25982	56513

**TABLE C.9**  
**Absorbed Power (W) Needed To Initiate**  
**Surface Melt in Copper : 0.2 MeV**

Beam Radius, cm	Travel Velocity, cm / s						
	0	0.1	0.5	1	5	10	50
0.15	2051	2061	2102	2152	2540	2994	5788
0.25	3360	3388	3495	3629	4633	5746	11887
0.35	4670	4722	4930	5185	7054	9031	19261
0.50	6633	6739	7156	7664	11240	14814	32295
0.75	9906	10141	11063	12170	19514	26379	58395

**TABLE C.10**  
**Absorbed Power (W) Needed To Initiate**  
**Surface Melt in Copper : 0.4 MeV**

Beam Radius, cm	Travel Velocity, cm / s						
	0	0.1	0.5	1	5	10	50
0.15	2188	2199	2245	2302	2752	3291	6909
0.25	3497	3527	3644	3789	4897	6153	13636
0.35	4807	4862	5083	5354	7370	9551	21630
0.50	6771	6881	7316	7848	11637	15506	35584
0.75	10044	10285	11234	12378	20050	27361	6320?

**TABLE C.11**  
**Absorbed Power (W) Needed To Initiate**  
**Surface Melt in Copper : 0.7 MeV**

Beam Radius, cm	Travel Velocity, cm / s						
	0	0.1	0.5	1	5	10	50
0.15	2395	2408	2464	2533	3085	3770	8919
0.25	3706	3739	3871	4035	5312	6809	16713
0.35	5016	5077	5317	5615	7869	10387	25738
0.50	6981	7098	7561	8131	12263	16615	41203
0.75	10254	10506	11498	12699	20894	28928	71283

**TABLE C.12**  
**Absorbed Power (W) Needed To Initiate**  
**Surface Melt in Copper : 1.0 MeV**

Beam Radius, cm	Travel Velocity, cm / s						
	0	0.1	0.5	1	5	10	50
0.15	2593	2609	2674	2756	3418	4261	11181
0.25	3908	3944	4091	4275	5727	7484	20144
0.35	5219	5284	5546	5870	8368	11246	30274
0.50	7184	7308	7801	8408	12891	17749	47331
0.75	10458	10721	11755	13012	21738	30520	79968

**TABLE C.13**  
**Absorbed Power (W) Needed To Initiate**  
**Surface Melt in Copper : 2.0 MeV**

Beam Radius, cm	Travel Velocity, cm / s						
	0	0.1	0.5	1	5	10	50
0.15	3187	3212	3310	3435	4488	5918	19493
0.25	4518	4567	4765	5014	7080	9773	32928
0.35	5836	5918	6247	6661	9998	14155	47170
0.50	7806	7953	8539	9270	14937	21576	69991
0.75	11084	11379	12551	13992	24481	35852	111629

**TABLE C.14**  
**Absorbed Power (W) Needed To Initiate**  
**Surface Melt in Copper : 4.0 MeV**

Beam Radius, cm	Travel Velocity, cm / s						
	0	0.1	0.5	1	5	10	50
0.15	4216	4259	4432	4654	6603	9397	36671
0.25	5598	5673	5980	6372	9813	14684	60660
0.35	6940	7056	7527	8128	13318	20436	84894
0.50	8929	9121	9898	10883	19117	29835	121750
0.75	12221	12581	14025	15835	30074	47268	184878

**TABLE C.15**  
**Absorbed Power (W) Needed To Initiate**  
**Surface Melt in Iron : 0.1 MeV**

Beam Radius, cm	Travel Velocity, cm / s						
	0	0.1	0.5	1	5	10	50
0.15	247	268	349	437	902	1290	3149
0.25	408	468	675	883	1897	2713	6505
0.35	570	684	1063	1423	3109	4442	10546
0.50	813	1041	1747	2383	5261	7510	17665
0.75	1217	1714	3117	4310	9589	13671	31875

**TABLE C.16**  
**Absorbed Power (W) Needed To Initiate**  
**Surface Melt in Iron : 0.2 MeV**

Beam Radius, cm	Travel Velocity, cm / s						
	0	0.1	0.5	1	5	10	50
0.15	254	278	365	462	1011	1511	4441
0.25	416	478	696	920	2071	3068	8524
0.35	578	696	1091	1473	3348	4929	13271
0.50	820	1054	1784	2451	5596	8193	21428
0.75	1225	1730	3170	4410	10084	14678	37336

**TABLE C.17**  
**Absorbed Power (W) Needed To Initiate**  
**Surface Melt in Iron : 0.4 MeV**

Beam Radius, cm	Travel Velocity, cm / s						
	0	0.1	0.5	1	5	10	50
0.15	272	299	403	523	1301	2139	8547
0.25	434	502	748	1010	2524	4039	14781
0.35	596	722	1156	1593	3960	6232	21521
0.50	839	1084	1871	2615	6443	9982	32511
0.75	1243	1766	3292	4648	11316	17261	52915

**TABLE C.18**  
**Absorbed Power (W) Needed To Initiate**  
**Surface Melt in Iron : 0.7 MeV**

Beam Radius, cm	Travel Velocity, cm / s						
	0	0.1	0.5	1	5	10	50
0.15	300	332	464	625	1847	3369	16077
0.25	462	539	830	1160	3358	5912	26852
0.35	623	763	1261	1790	5067	8702	37768
0.50	866	1130	2009	2883	7945	13303	54537
0.75	1270	1823	3487	5032	13454	21935	83750

**TABLE C.19**  
**Absorbed Power (W) Needed To Initiate**  
**Surface Melt in Iron : 1.0 MeV**

Beam Radius, cm	Travel Velocity, cm / s						
	0	0.1	0.5	1	5	10	50
0.15	326	365	526	734	2475	4759	23569
0.25	488	575	915	1319	4316	8073	39284
0.35	650	803	1368	1998	6328	11564	55016
0.50	893	1176	2150	3163	9636	17136	78707
0.75	1297	1878	3684	5431	15825	27272	118666

**TABLE C.20**  
**Absorbed Power (W) Needed To Initiate**  
**Surface Melt in Iron : 2.0 MeV**

Beam Radius, cm	Travel Velocity, cm / s						
	0	0.1	0.5	1	5	10	50
0.15	400	460	726	1100	4589	9137	45642
0.25	564	683	1189	1857	7666	15225	76066
0.35	727	923	1715	2701	10813	21336	106491
0.50	971	1313	2605	4103	15693	30588	152128
0.75	1376	2045	4316	6750	24288	46348	228194

**TABLE C.21**  
**Absorbed Power (W) Needed To Initiate**  
**Surface Melt in Iron : 4.0 MeV**

Beam Radius, cm	Travel Velocity, cm / s						
	0	0.1	0.5	1	5	10	50
0.15	516	618	1099	1810	8259	16469	82279
0.25	687	867	1712	2928	13730	27430	137116
0.35	852	1129	2381	4111	19212	38395	191953
0.50	1098	1551	3479	5992	27458	54845	274209
0.75	1504	2334	5522	9385	41308	82281	411304

**TABLE C.22**  
**Absorbed Power (W) Needed To Initiate**  
**Surface Melt in Titanium : 0.1 MeV**

Beam Radius, cm	Travel Velocity, cm / s						
	0	0.1	0.5	1	5	10	50
0.15	119	131	175	223	478	699	1862
0.25	195	228	339	450	995	1447	3716
0.35	272	334	536	725	1622	2350	5913
0.50	387	510	882	1213	2730	3943	9738
0.75	580	845	1576	2193	4952	7128	17293

**TABLE C.23**  
**Absorbed Power (W) Needed To Initiate**  
**Surface Melt in Titanium : 0.2 MeV**

Beam Radius, cm	Travel Velocity, cm / s						
	0	0.1	0.5	1	5	10	50
0.15	125	138	189	245	585	926	3299
0.25	202	236	358	484	1165	1803	5910
0.35	279	344	561	771	1852	2832	8823
0.50	394	521	916	1277	3051	4612	13684
0.75	586	859	1624	2286	5422	8102	22906

**TABLE C.24**  
**Absorbed Power (W) Needed To Initiate**  
**Surface Melt in Titanium : 0.4 MeV**

Beam Radius, cm	Travel Velocity, cm / s						
	0	0.1	0.5	1	5	10	50
0.15	140	157	224	305	907	1646	7812
0.25	217	257	407	573	1657	2902	13056
0.35	294	367	623	889	2508	4284	18381
0.50	409	548	998	1438	3945	6571	26588
0.75	601	892	1741	2518	6700	10873	40943

**TABLE C.25**  
**Absorbed Power (W) Needed To Initiate**  
**Surface Melt in Titanium : 0.7 MeV**

Beam Radius, cm	Travel Velocity, cm / s						
	0	0.1	0.5	1	5	10	50
0.15	162	185	283	412	1539	3024	15083
0.25	239	289	488	730	2628	5072	25137
0.35	316	403	727	1095	3790	7177	35192
0.50	432	589	1136	1716	5662	10463	50285
0.75	624	943	1934	2912	9101	16300	75517

**TABLE C.26**  
**Absorbed Power (W) Needed To Initiate**  
**Surface Melt in Titanium : 1.0 MeV**

Beam Radius, cm	Travel Velocity, cm / s						
	0	0.1	0.5	1	5	10	50
0.15	183	212	344	527	2211	4404	22002
0.25	261	321	573	901	3701	7340	36669
0.35	338	438	835	1318	5229	10292	51336
0.50	453	630	1278	2014	7608	14769	73337
0.75	646	993	2133	3331	11820	22426	110009

**TABLE C.27**  
**Absorbed Power (W) Needed To Initiate**  
**Surface Melt in Titanium : 2.0 MeV**

Beam Radius, cm	Travel Velocity, cm / s						
	0	0.1	0.5	1	5	10	50
0.15	241	294	548	924	4286	8552	42732
0.25	322	417	863	1503	7129	14245	71213
0.35	401	546	1207	2114	9976	19940	99695
0.50	517	757	1768	3081	14257	28485	142417
0.75	710	1149	2811	4821	21438	42732	213621



**TABLE C.28**  
**Absorbed Power (W) Needed To Initiate**  
**Surface Melt in Titanium : 4.0 MeV**

Beam Radius, cm	Travel Velocity, cm / s						
	0	0.1	0.5	1	5	10	50
0.15	333	435	937	1655	7791	15547	77724
0.25	420	586	1434	2660	12959	25897	129497
0.35	502	741	1952	3685	18132	36249	181270
0.50	621	986	2765	5246	25895	51780	258930
0.75	817	1433	4200	7906	38836	77666	388364

**TABLE C.29**  
**Absorbed Power (W) Needed To Initiate**  
**Surface Melt in 304 SS : 0.1 MeV**

Beam Radius, cm	Travel Velocity, cm / s						
	0	0.1	0.5	1	5	10	50
0.15	166	179	228	282	573	817	1986
0.25	275	310	436	565	1204	1718	4108
0.35	383	452	684	909	1972	2814	6664
0.50	547	684	1119	1517	3336	4757	11168
0.75	818	1119	1989	2741	6079	8661	20162

**TABLE C.30**  
**Absorbed Power (W) Needed To Initiate**  
**Surface Melt in 304 SS : 0.2 MeV**

Beam Radius, cm	Travel Velocity, cm / s						
	0	0.1	0.5	1	5	10	50
0.15	171	185	237	296	634	942	2708
0.25	280	317	449	587	1302	1919	5238
0.35	388	459	700	937	2107	3089	8192
0.50	552	692	1140	1557	3525	5143	13282
0.75	823	1128	2019	2798	6359	9231	23236

**TABLE C.31**  
**Absorbed Power (W) Needed To Initiate**  
**Surface Melt in 304 SS : 0.4 MeV**

Beam Radius, cm	Travel Velocity, cm / s						
	0	0.1	0.5	1	5	10	50
0.15	183	199	261	333	803	1304	5066
0.25	292	332	480	641	1566	2482	8829
0.35	400	476	740	1008	2464	3845	12930
0.50	564	711	1192	1654	4020	6184	19657
0.75	836	1151	2092	2938	7080	10736	32218

**TABLE C.32**  
**Absorbed Power (W) Needed To Initiate**  
**Surface Melt in 304 SS : 0.7 MeV**

Beam Radius, cm	Travel Velocity, cm / s						
	0	0.1	0.5	1	5	10	50
0.15	201	220	299	395	1120	2015	9486
0.25	310	356	531	730	2050	3562	15864
0.35	419	502	803	1125	3107	5272	22357
0.50	582	740	1275	1812	4894	8106	32391
0.75	854	1186	2208	3165	8327	13448	50004

**TABLE C.33**  
**Absorbed Power (W) Needed To Initiate**  
**Surface Melt in 304 SS : 1.0 MeV**

Beam Radius, cm	Travel Velocity, cm / s						
	0	0.1	0.5	1	5	10	50
0.15	218	241	336	458	1474	2805	13825
0.25	327	379	581	822	2590	4784	23044
0.35	436	527	866	1245	3819	6886	32283
0.50	599	768	1358	1974	5849	10265	46228
0.75	871	1220	2323	3394	9669	16457	69865

**TABLE C.34**  
**Absorbed Power (W) Needed To Initiate**  
**Surface Melt in 304 SS : 2.0 MeV**

Beam Radius, cm	Travel Velocity, cm / s						
	0	0.1	0.5	1	5	10	50
0.15	267	302	457	673	2699	5364	26784
0.25	378	448	744	1135	4517	8939	44638
0.35	487	603	1071	1652	6389	12537	62493
0.50	651	855	1625	2517	9311	18005	89275
0.75	923	1323	2693	4157	14500	27381	133917

**TABLE C.35**  
**Absorbed Power (W) Needed To Initiate**  
**Surface Melt in 304 SS : 4.0 MeV**

Beam Radius, cm	Travel Velocity, cm / s						
	0	0.1	0.5	1	5	10	50
0.15	344	404	681	1089	4858	9680	48346
0.25	459	565	1054	1755	8072	16119	80568
0.35	570	733	1462	2466	11295	22562	112791
0.50	735	1003	2134	3603	16150	32229	161124
0.75	1009	1501	3393	5670	24335	48362	241681

**Appendix D**  
**Acronyms Used in this Work**

<b>ACRONYM</b>	<b>MEANING</b>
ACC	Advanced Carbon Composite
AECL	Atomic Energy of Canada, Ltd.
AMS	Aerospace Materials Specification
C/C or CCC	Carbon - Carbon Composite
CTE	Coefficient of Thermal Expansion
D.E.	Deposition Efficiency (measured in lbs./hr./kW)
D.M.E.	Deposition Melting Efficiency (dimensionless)
EB	Electron Beam
EBSFF	Electron Beam Solid Freeform Fabrication
FCAW	Flux Cored Arc Welding
FGM	Functionally Graded (or Gradient) Material
FWHM	Full Width at Half Maximum
GMAW	Gas Metal Arc Welding
GTAW or GTA	Gas Tungsten Arc Welding
HEEB	High Energy Electron Beam
HY (as in HY-100)	High Yield
IMC	Intermetallic Matrix Composite
IN or INCO	Inconel, or referring to an alloy from INCO, Inc.
LIA	Linear Induction Accelerator
LINAC	Linear Accelerator
MMC	Metal Matrix Composite
NDE	Non - Destructive Evaluation
NDI	Non - Destructive Inspection
NSWC	Naval Surface Warfare Center
O.M.E.	Overall Melting Efficiency (dimensionless)
PAW	Plasma Arc Welding
PFN	Pulse Forming Network
PMC	Polymer Matrix Composite
PTR	Precision Technologies, Inc.
RCC	Reusable Carbon Composite
SAW	Submerged Arc Welding
SFF	Solid Freeform Fabrication
SLS	Selective Laser Sintering
SNOMAD IV	SRL's HEEB Accelerator
SRL	Science Research Laboratory, Inc.
THOR	NSWC's single-pulse HEEB

## APPENDIX A

### References

- |                                 |      |   |
|---------------------------------|------|---|
| ANONYMOUS                       | 1977 | " Osmium - Ruthenium Coating Improves Cathode Life," <i>Design News</i> , July 4 Iss.   |
| BAILEY, V.L.                    | 1992 | " High Energy Electron Beam Interaction with Materials," <i>AWS Conference on High Energy Electron Beam Welding and Materials Processing</i> , Cambridge, MA, pp. 92 - 114. |
| BERGER, M. J.<br>SELTZER, S. M. | 1982 | <i>Stopping Powers and Ranges of Electrons and Positrons</i> NBSIR 82 - 2550  |
| BERGER, M.J.                    | 1963 | " Monte Carlo Calculation of the Penetration and Diffusion of Fast Charged Particles," in <i>Methods in Computational Physics - Vol. 1</i> , Academic Press, New York.      |
| BETHE, H. A.<br>HEITLER, W.     | 1934 | <i>Proceedings of the Royal Society of London</i> , Serial A, Vol. 146, p. 83.  |
| BETHE, H. A.                    | 1930 | <i>Ann. Physik</i> , Vol. 5, p. 325.  |
| BIRKHOFF, R.D.                  | 1958 | "The Passage of Fast Electrons Through Matter," in <i>Handbuch der Physik</i> , Springer - Verlag, Berlin.  |
| BOHR, N.                        | 1948 | <i>Kgl. danske Vid. Selsk., mat.-fys. Medd.</i> 18(8)   |
| CHRISTOFILOS, N. C.<br>et al.   | 1964 | " High Current Linear Induction Accelerator for Electrons," <i>Review of Scientific Instruments</i> , Vol. 35(7), pp. 886 - 890.  |
| CULLITY, B. D.                  | 1968 | <i>Elements of X-Ray Diffraction</i> , Addison - Wesley, Reading.   |
| DUSHMAN, S.                     | 1923 | <i>Physical Review</i> , Vol. 21, p. 623  |
| FANO, U.                        | 1953 | <i>Physical Review</i> , Vol. 92(2), pp. 328 - 349  |
| HALBLEIB, J.A. et al            | 1992 | <i>ITS Version 3.0 : The Integrated TIGER Series of Coupled Electron / Photon Monte Carlo Transport Codes</i> SAND - 1634   |

- HERRMANNSELDT, W.B. 1988 *EGUN - An Electron Optics and Gun Design Program*, Stanford Linear Accelerator Center.
- HULL, A. W. 1939 *Physical Review*, Vol. 56, p. 86.
- HUMPHRIES, S. 1986 *Charged Particle Beams*, John Wiley and Sons, New York.
- ION, J. C.  
SHERCLIFF, H. R.  
ASHBY, M. F. 1992 "Diagrams for Laser Processing," *Acta Metallurgica*, 40(7), pp. 1539 - 1551.
- JACKSON, J.D. 1962 *Classical Electrodynamics*, John Wiley & Sons, New York.
- LaFLAMME, G. 1994 PTR - Precision Technologies, Inc. Enfiled, CT. Private Communication.
- LANDAU, L. 1944 *J. of Experimental Physics USSR*, Vol. 8, p. 201.
- LANGMUIR, I.  
BLODGET, K. 1924 *Physical Review*, Vol. 24, p. 49.
- LEMMENS, H. J.  
JANSEN, M. J.  
LOOSJES, R. 1950 *Phillips Technical Review*, Vol. 11, p. 341.
- LEVI, R. 1955 *J. of Applied Physics*, Vol. 26, p. 639.
- MILLER, R. B. 1982 *An Introduction to the Physics of Intense Charged Particle Beams*, Plenum Press, New York.
- MÖLLER, C. 1932 *Ann. Physik* Vol. 14, p. 531.
- NATION, J. A. 1979 "High - Power Electron and Ion Beam Generation," *Particle Accelerators*, Vol. 10, pp. 1 - 30.
- NOTTINGHAM, W. B. 1958 "Thermionic Emission," in *Handbuch der Physik*, Springer - Verlag, Berlin.
- RICHARDSON, O. W. 1902 *Proceedings of Cambridge Philosophical Society*, Vol. 11, p. 286.
- RICHARDSON, O. W. 1912 *Philosophical Magazine*, Vol. 23, p. 263.

- RITTNER, E. S.                    1957    *J. of Applied Physics*, Vol. 28(12),  
RUTLEDGE, W. C.                    pp. 1468 - 1473  
AHLERT, R. H.
- SEPTIER, A. ed.                    1967    *Focusing of Charged Particles - Vols I & II.*  
Academic Press, New York.
- SHREIDER, Y. A.                    1964    *The Monte Carlo Method*, Pergamon Press,  
New York.
- SPENCER, L. V.                    1955    "Theory of Electron Penetration," *Physical*  
*Review*, Vol. 98(4), pp. 1597 - 1615.
- SPENCER, L. V.                    1959    *Energy Dissipation by Fast Electrons* NBS  
Monograph 1.
- TANIGUCHI, N. et al                1989    *Energy Beam Processing of Materials*,  
Oxford University Press, London.
- THOMSON, J.J.                    1912    *Philosophical Magazine*, 6(23), p. 449
- TURMAN, B. N.                    1992    " Fundamentals of High Energy Electron  
Beam Generation," *AWS Conference on High*  
*Energy Electron Beam Welding and*  
*Materials Processing*, Cambridge, MA,  
pp. 44 - 57.
- WILKEN, B.                        1976    *Nuclear Instruments and Methods*, Vol.  
FRITZ, T. A.                        138, pp. 331 - 343.

## **Biographical Sketch**

### *Educational / Occupational*

1995 -present	Methods Engineering Specialist, Metal Joining Manufacturing Technology Group, UIC / Pratt & Whitney, East Hartford, CT.
1992-1995	Ph.D. in Materials Engineering, Massachusetts Institute of Technology, Cambridge, MA.
1991-1992	Research Assistant, Department of Materials Science and Engineering, Massachusetts Institute of Technology, Cambridge, MA.
1989-1991	S.M. in Materials Engineering, Massachusetts Institute of Technology, Cambridge, MA.
1985-1989	S.B. in Engineering & Applied Science, California Institute of Technology, Pasadena, CA.
1982-1985	High School, Phillips Academy, Andover, MA.
1981-1982	High School, St. Mary's-in-the-Mountains, Littleton, NH.

### *Professional Affiliations*

- ASM
- TMS
- AWS
- Sigma Xi
- Corporate Member, EWI / TWI